Electronic Thesis and Dissertation Repository

10-16-2013 12:00 AM

Potassium Metasomatism at the Polymetallic NICO Deposit, Northwest Territories, Canada

Gregory B. Robinson, *The University of Western Ontario*

Supervisor: Norman A. Duke, *The University of Western Ontario*
A thesis submitted in partial fulfillment of the requirements for the Master of Science degree in Geology
© Gregory B. Robinson 2013

Follow this and additional works at: https://ir.lib.uwo.ca/etd

Part of the Geology Commons

Recommended Citation

POTASSIUM METASOMATISM AT THE POLYMETALLIC NICO DEPOSIT,
NORTHWEST TERRITORIES, CANADA

by

Greg Robinson

Graduate Program in Geology
Department of Earth Sciences

Submitted in partial fulfillment
of the requirements for the degree of
Master of Science

The School of Graduate and Postdoctoral Studies
The University of Western Ontario
London, Ontario, Canada

© Greg Robinson, 2013

ABSTRACT

High temperature K-metasomatism pervasively replaced Paleoproterozoic volcanic and metasedimentary rocks at Lou Lake NWT. This replacement developed primarily at the structural interface juxtaposing non-metamorphosed Lou Lake volcanic rocks over Treasure Lake Group metasedimentary rocks. This crustal-scale fault developed coeval with the emplacement of anorogenic magmatism within a post-collision extensional setting. Emplacement of porphyry dykes into the fault breccia coincided with K-metasomatism at peak upper-greenschist to amphibolite-facies thermal conditions.

The K-metasomatism resulted from co-mingling of descending crustal fluids and ascending potassic magmatic fluids along the decollement surface. Pervasive K-metasomatism resulted in complete replacement of precursor rocks by potassium feldspar. The pronounced element liberation and SiO_2-Al_2O_3-K_2O enrichment resulted in the homogenization of diverse rock types into brick-red potassium feldspar metasomatite characterized by high K_2O/Na_2O ratios and up to 13.4 wt%, K_2O. The secondary microcline approaches end member orthoclase composition. Petrographic and isotopic evidence indicate associated iron oxide is an inherited component from precursor rocks. Oxidizing conditions were superimposed by continued flux of crustal fluids during a prolonged retrograde cooling history.

Keywords: Great Bear Magmatic Zone, Lou Lake, Treasure Lake Group, metasiltstone, meta-arenite, calcsilicate rocks, plagioclase-phyric porphyry, feldspar-phyric porphyry, K-metasomatism, hydrothermal alteration, detachment fault, brecciation

ACKNOWLEDGEMENTS

TABLE OF CONTENTS

LIST OF TABLES

LIST OF FIGURES

LIST OF PLATES

LIST OF APPENDICES

CHAPTER 1 – INTRODUCTION

1.1   Introduction and Thesis Statement

The iron oxide copper-gold (IOCG) family was defined by Hitzman et al. (1992) as Proterozoic iron oxide deposits affiliated with low titanium, iron rich igneous or sedimentary host rocks, and occurring within extensional tectonic environments. Universal recognition of an IOCG deposit family remains elusive due to an exceptional diversity in terms of host rock setting, structural control, geophysical and geochemical signatures, alteration styles, and diversity of ore mineral assemblage (Hitzman, 2000; Williams et al., 2005; Corriveau and Mumin, 2009; Williams, 2009). Prominent Proterozoic examples include Olympic Dam and Earnest Henry of Australia, Phalborwa of South Africa, Kiruna of Sweden, and Bayan Obo of China.

Ore systems within the IOCG family are characterized by hydrothermal copper deposits associated with a minimum of 15-20% iron oxide (Williams et al., 2005). However, direct correlation between iron oxide and copper mineralization is not necessary (Corriveau and Mumin, 2009) as sulphide mineralization often overprints earlier iron oxides (Pollard, 2000). These ore systems exhibit intense regional to deposit scale calcic, sodic, potassic and iron alteration (Hitzman et al., 1992), strong structural and lithologic control, and abundant hydrothermal and/or structural breccia (Corriveau and Mumin, 2009). Williams et al. (2005) proposed that skarn and Cu-Au porphyry exhibiting definitive causative relationships with igneous centers be excluded from the family. These same authors note that copper-deficient iron oxide-rich deposits may constitute an affiliated deposit of the IOCG system although are not recognized as bona fide IOCG deposits.

A descriptive classification suggested by Williams (2009) divides members into three distinct groups, including: (i) "Kiruna-type" Fe oxide ± apatite deposits occurring in districts, (ii) "Olympic Dam-type" Fe oxide-hosted and associated low Fe oxide Cu-Au, low Cu-U-(Fe oxide) and low-Cu Co-As ± U(Fe oxide) deposits, and (iii) "Bayan Obo-type" Fe oxide ± apatite ± Cu ± Au ± rare metals deposits. Globally, IOCG's have been demonstrated to form within districts where regional scale hydrothermal systems form a discontinuous band of deposits that correlates with crustal-scale fault zones, e.g. the Cloncurry district (Corriveau et al., 2009). A paragenetic framework based upon alteration zonation suggested by Corriveau et al. (2009) characterizes IOCG deposits with having a predictive sequence of alteration evolved from early higher temperature sodic-calcic to intermediate temperature potassic-iron to late-stage lower temperature potassic-iron alteration.

The NICO Deposit is one of several known sites identified as an IOCG within the Great Bear magmatic zone (Goad et al., 2000). This magnetite-group IOCG deposit has demonstrated economic concentrations of cobalt, gold and bismuth (Goad et al., 2000; Corriveau et al., 2009). Mineralization is hosted within amphibole-magnetite-biotite metasomatic rock within Treasure Lake Group metasedimentary basement capped by potassium feldspar metasomatite. The potassium feldspar metasomatite is developed at the boundary between where overlying non-metamorphosed Faber Lake Volcanic Group rocks are juxtaposed against transitional greenschist to amphibolite-facies Treasure Lake Group metasedimentary rocks.

A multiparameter airborne geophysical survey completed by the Geological Survey of Canada as part of the Canada-Northwest Territories Minerals Initiative Program (1991-1996) detected a strong potassium anomaly over a 3 x 4 km area centered over the NICO deposit

(Charbonneau et al., 1994). The potassium anomaly is coincident with a high magnetic anomaly and a low eTh/K ratio anomaly (Gandhi et al., 1996). The nature of the source potassium feldspar metasomatite has never been formally addressed. Previous investigations have interpreted the monominerallic rocks within the potassium anomaly as K-Fe rich volcanics (Mulligan, 1995) and felsite (Goad et al., 2000; Sidor, 2000; Goad et al., 2001), however textural evidence clearly suggests a metasomatic origin. It is this controversy that comprises the main focus of this thesis. A thorough investigation of the potassic alteration at Lou Lake is crucial for the determination of the origin of the alteration. A better understanding of the mode of origin for the potassium feldspar metasomatite will shed light on the role of potassic alteration during mineralization, and this has implications for future IOCG exploration.

At NICO, the zone of K-feldspar replacement coincides with local porphyry dykes and this replacement intensifies at dyke margins to produce a characteristic pink to brick red metasomatic aureole. The relationship between dyking and K-feldspar replacement will be critically evaluated. The nature of the contact between the Lou Lake volcanic rocks and Treasure Lake Group metasedimentary rocks remains controversial, with conflicting interpretations including an unconformity (Thomas and Olson, 1978; Gandhi and Lentz, 1990; Duke, 1996) and a major detachment fault (Duke, 1998; Duke et al., 1998a; Duke et al., 1998b). Although not a primary focus of this investigation, the study of K-feldspar replacement at the boundary may provide additional insight into this unresolved debate.

1.2   Methodology

A total of five months over two field seasons were devoted by the author toward

detailed mapping of K-feldspar-replaced lithology at surface and the NICO ramp, and core logging at the Lou Lake camp. Approximately 3.5 kilometers of core were examined, and an additional 1.5 kilometers of core stored on-site from previous years of drilling were re-examined to document evidence of K-metasomatism. A representative sample suite was collected from the surface, decline and core for detailed petrographic analysis. Thirty nine polished and 57 thin sections were prepared for petrographic analysis. Forty two samples were analysed for major and trace mineral geochemistry using ICP-OES Perkin Elmer model Optima 3000 operated by the Centre – Eau Terre Environment located at the Institute Nationale de la Reserche Scientifique (INRS) in Quebec City, QC.

Mineral chemical analyses were carried out on a select suite of samples collected from the potassium feldspar metasomatite and potassic altered porphyry dykes. These were analysed by a JEOL JXA-733 electron microprobe equipped with 5-wavelength-dispersive spectrometers (WDS) and an energy-dispersive spectrometer (EDS) at Renaud Geological Consulting Limited in London, Ontario. The grain mounts were covered with a thin film of analytical grade carbon using a vacuum carbon evaporator. The microprobe is operated using an Advanced Microbeam "Probe for Windows" operating system to drive the Tracor Northern TN-5600 spectrometer and stage automation system. Chemical compositions were measured using a 15 kV accelerating voltage and 11 nA probe current.

A reconnaissance suite of whole rock oxygen isotopes were analyzed to determine the $O^{18/16}$ signature of the potassium feldspar metasomatite. These were determined by the Geology Isotope Laboratory at the University of Western Ontario. Calculated values were determined by K. Law at F. Longstaffe Isotope Laboratory in the Earth Science Department at the University of Western Ontario. Values were determined relative to the internationally

accepted standard Vienna Standard Mean Ocean Water (VSMOW). The following calibration standards were used: NBS-30 (biotite), KGa-1 (laboratory standard kaolinite), and ORX (laboratory standard quartz).

1.3 Location, Access and Topography

The Fortune Minerals Limited NICO Project is located within the Mazenod Lake District of the Northwest Territories. It occurs in the National Topographic System (NTS) quadrant 85 N/10 at 63^o33'N and 116^o45'W. Originally staked as a group of 12 claims around Lou Lake, the property currently consists of 10 mining leases covering an area of approximately 5140 hectares. Two of the original claims have been allowed to lapse (Hennessey et al., 2007). This study is primarily focused on the immediate area of the NICO deposit centrally located within portions of NICO Leases 1, 2, 3, 4 and 5. Access to the study location is available year-round by float or ski-equipped aircraft or helicopter from Yellowknife, 160 km to the southeast of Lou Lake (Figure 1.1). A government-maintained ice road from the town of Bechoko to local communities Wha'Ti and Rae Lakes provides winter land-based access. Planned development of an all weather road will provide all-season access to Yellowknife via Edzo in the future (Fortune Minerals Limited, 2007).

The immediate study area is characterized by moderate relief between 250 to 340 meters above sea level. Outcrops are generally well exposed with minimal tree cover limited to low lying bog and muskeg areas. The area provides adequate habitat for a local population of black bears. The study area is further populated with a number of small lakes that sustain a moderate stock of pickerel and pike.
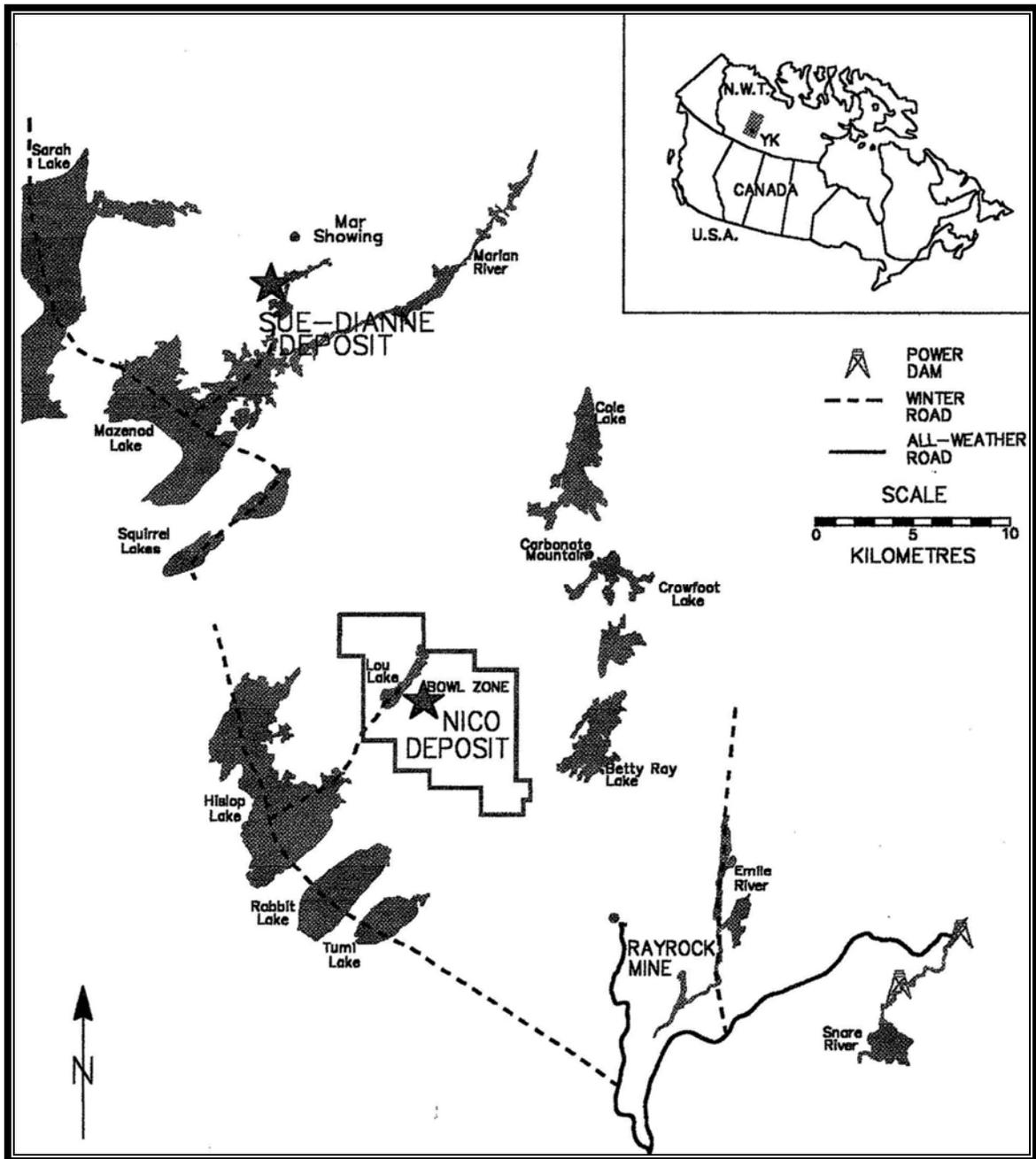
Figure 1.1 - Location of Lou Lake and the NICO study area in Northwest Territories (after Sidor, 2000).

1.4   Previous Study

Regional mapping was initiated by the Geological Survey of Canada in the 1930's (Kidd, 1936). Initial exploration in the southern part of the Great Bear Magmatic Zone was focused on U, Ag and Cu vein mineralization (Kidd, 1932).   The Rayrock uranium deposit sited about 20 kilometers east of NICO was initially discovered as part of the regional mapping efforts by the Geological Survey (Lang et al., 1962). These early mapping efforts identified Snare Group metasediments intruded by porphyries of felsic composition within the Lou Lake vicinity (Lord, 1942).

At NICO, polymetallic Co-As-Au-Bi-Cu veins were discovered in 1965. Precambrian Mining Services Limited bulk sampled one of these veins on the CAB claim (Mathieu, 1966). After optioning 12 claims covering the polymetallic vein mineralization in the Lou Lake area, New Athona Mines Limited mapped the local geology, conducted magnetic and electromagnetic surveys, trenched, and drilled 21 diamond drill holes between 1968 and 1969 (Hoefer, 1989). Exploratory results from trenching and drill core revealed considerable polymetallic ore (Byrne, 1968; Hall, 1969). New Athona Mines Limited relinquished the CAB claims at the end of 1969.

Aeromagnetic surveys conducted by the Geological Survey of Canada in 1973 resulted in the discovery of the Sue Dianne occurrence 25 km north of Lou Lake. This was staked by Noranda Exploration Company Limited in 1974 (Climie, 1976). Eldorado Nuclear Limited explored for uranium resources between 1976 and 1978.   They discovered several uneconomic pitchblende and uranium oxide occurrences (Hoefer, 1989).   Noranda Exploration Company Limited acquired the previous New Athona Mines Limited claims in

1978, and added the GAR Claim Group to encompass new occurrences in the Burke Lake area (Bryan, 1981 and 1982). Noranda's exploration of the GAR claims included detailed mapping, trenching and re-sampling of New Athona trenches. Noranda's results were similar to those previously reported by New Athona, and reconfirmed high grade Co-As-Au-Bi-Cu mineralization. Noranda allowed the GAR claims to lapse in 1989 (Gandhi and Lentz, 1990).

The Geological Survey of Canada conducted airborne magnetic and gravimetric surveys in the Mazenod Lake area between 1987 and 1991. In 1993, they extended the multiparameter geophysical survey to complement ongoing metallogenic studies in the southern Great Bear magmatic zone. The multiparameter survey covered a surface area of 1500 square kilometers, and highlighted several highly anomalous magnetic and radiometric anomalies, the largest coinciding with the Lou Lake Co-As-Au-Bi-Cu occurrence (Charbonneau et al., 1994).

Fortune Minerals acquired the previous Noranda claims around Lou Lake in June of 1994, renaming them the NICO Claim Group (Mulligan, 1995). Fortune Minerals has since pursued detailed geological mapping, geophysical surveys, trenching and diamond drilling coupled with an aggressive multi-element assay program. The bulk of this work has determined proven and probable mineral reserves of nearly 31 million tonnes grading 0.91 g/t Au, 0.12% Co, 0.16% Bi and 0.04% Cu (Fortune Minerals Limited, 2009). Potential to expand the reserves and further define the resource are expected from the 7000 m infill drill program conducted during the summer of 2010.

Fortune Minerals has supported a number of academic studies. The BSc thesis by Mulligan in 1995 described the iron oxide and arsenopyrite vein hosted mineralization at Lou

Lake. A BSc by D'Oria in 1998 described the nature of the Faber Lake rapakivi granite and bordering porphyries, including petrographic, textural and geochemical investigations of the intrusive and extrusive phases. A BSc by Shepley in 1999 investigated evidence supporting a detachment fault hypothesis between Faber Lake Volcanic Group and Snare Group metasedimentary rocks. An MSc by Sidor in 2000 investigated the nature of "black rock" alteration hosting the polymetallic mineralization at Lou Lake. An MSc by Camier in 2002 investigated the nearby Sue Dianne Deposit.

1.5   Thesis Format

An overview of the regional geology of the Great Bear Magmatic Zone and the local geology of the NICO deposit are presented in Chapter 2. Detailed petrography of the deposit scale K-metasomatism of wall rock metasedimentary, volcanic and porphyry rocks, as well as associated brecciation are described in Chapter 3. Major and trace element geochemistry and oxygen isotopes are reported in Chapter 4. In addition, mineral chemical analyses of the key minerals involved in the K-metasomatism are presented in Chapter 4. The results of analysis on mass balance conducted on samples sourced from feldspar porphyry dyking demonstrating strong spatial and temporal relationships to K-metasomatism are documented in Chapter 5. Collective evidence relevant to K-metasomatism and deposit-scale brecciation is further discussed in Chapter 6. The results of this study is concluded and summarized in Chapter 7.

CHAPTER 2 – GEOLOGY OF THE STUDY AREA

2.1 Introduction

The study area occurs within the Wopmay Orogen, an early Proterozoic north-south trending domain of metamorphosed sedimentary, volcanic and plutonic rocks that collectively form the southern portion of the triangularly-shaped Bear Province (see Figure 2.1). The Bear encompasses approximately 80,000 square kilometers and forms the northwestern corner of the Canadian Shield (Fraser et al., 1972). Its eastern boundary is defined by an unconformity with the Coronation Supergroup overlying the western edge of the Archean Slave Province (Hoffman, 1973). It is onlapped by Paleozoic platformal carbonates to the west (Stockwell et al., 1970).

The Bear structural province is divided into two major regions, the Amundsen Basin and the aforementioned Wopmay Orogen. The Amundsen Basin comprises the northwestern portion. Its boundary is defined by unconformably overlying westward-dipping strata of the Neoproterozoic Coppermine Homocline (Wilson, 1949; Fraser et al., 1972). It is characterized by a substantial thickness of shallow marine and continental sedimentary rocks (Fraser et al., 1972). The Wopmay Orogen developed on the western margin of the Slave Province ca. 2.1 to 1.84 Ga (Hoffman, 1973; Hoffman, 1980; Housh et al., 1989). It is further divided into five principal zones that parallel the trend of the orogen. From east to west these zones include: the Coronation Supergroup, the Turmoil Klippe, the Medial or Wopmay Fault Zone, the Great Bear Magmatic Zone, and the Hottah Terrane (Hoffman, 1988; Gandhi et al., 2001; Hildebrand et al., 2010).

The Hottah Terrane is composed of metamorphosed crystalline Archean basement

overlain by amphibolite facies volcanic and sedimentary rocks. It is intruded by metaluminous to peraluminous plutonic rocks with individual dates that range between 1919 and 1885 Ma (Hildebrand et al., 1983 and 1984; Bowring and Grotzinger, 1992; Hildebrand et al., 2009). These composite intrusives are collectively referred to as the Hepburn Batholith (or Hepburn Intrusive Suite) east of the Great Bear Magmatic Zone, though remain unnamed to the west. The Hottah terrane has been interpreted as an exotic east-facing continental magmatic arc that was accreted above a westward dipping subducting plate along the western margin of the Slave craton during the Calderian Orogeny (Hoffman, 1988; Hildebrand et al., 1991; Bowring and Grotzinger, 1992). Interpretations of the Hepburn are conflicting. St. Onge and King (1987) suggest the deformed and allochthonous nature place plutonism prior to the Calderian. Conversely, Hildebrand et al. (2009) has suggested that post-collisional extension of the arc, and crustal melting resulting from asthenospheric upwelling during contemporaneous failure and consequent roll-back of the subducted slab, generated the Hepburn intrusive suite.

The Coronation Supergroup is a Paleoproterozoic sedimentary succession that developed contemporaneous with, though independently of, the Hottah terrane. The supergroup is comprised of: (i) basal bimodal volcanic and clastic rocks of the Melville Group, interpreted by Hoffman and Pelletier (1982) as rift-facies; (ii) shallow marine siliciclastic and carbonate formations of the Epworth Group, which have been interpreted as a west-facing passive continental margin succession by Hoffman (1973); and (iii) deep water siliciclastics of the basal Recluse Group, interpreted as a collision-related foredeep facies by Hoffman (1973). A volcanic ash bed near the base of the foredeep succession marks the transition between passive margin and foredeep at approximately 1882 Ma, and dates the onset of collision
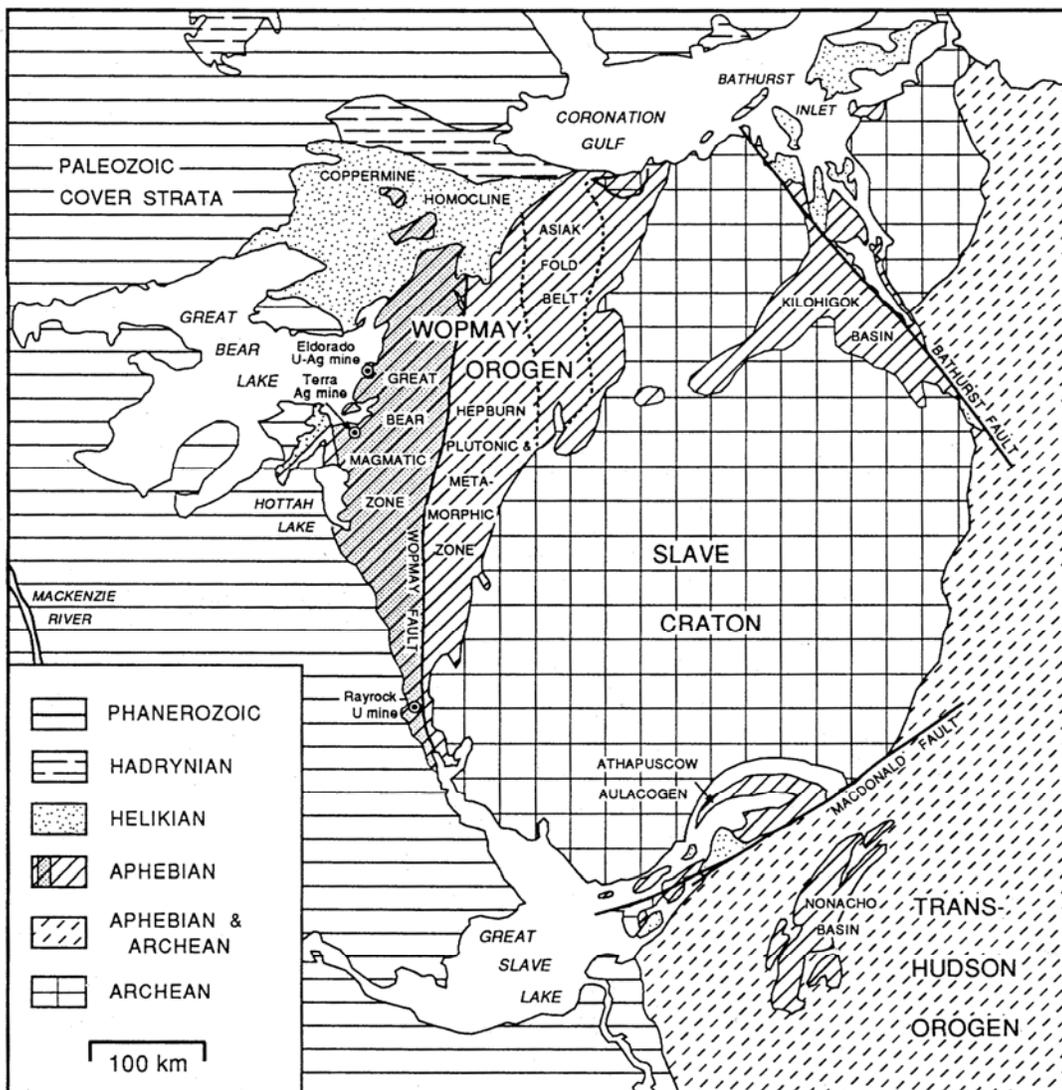
Figure 2.1 – The general geology of the structural provinces of the northwestern Canadian Shield, after Gandhi (1994). The Bear Province comprises the area denoted as the Wopmay Orogen.

(Bowring and Grotzinger, 1992). The supracrustal rocks were detached from the original basement, folded, and transported eastward onto the western margin of the Slave craton. Prior to detachment and subsequent deformation, the supergroup was intruded by gabbroic to granitic plutons from the Hepburn Intrusive Suite (Hildebrand et al., 1987).

The Turmoil Klippe is composed of metamorphosed crystalline basement rocks unconformably overlain by metamorphosed sedimentary and volcanic rocks. Previously interpreted to be displaced initial rift facies (Easton, 1981; Hoffman and Bowring, 1984), the Turmoil klippe is currently interpreted to be a relic of the Hottah Terrane (Hildebrand et al., 2009) despite inconsistent geochronological evidence (Hildebrand et al., 1991). Structurally, the klippe overlies the western edge of the Coronation margin, and is itself structurally overlain by the Great Bear Magmatic Zone (Hildebrand et al., 1990 and 1991). The boundary between the klippe and underlying rocks is marked by basal mylonitic gneiss. Rocks of the klippe have been intruded by the Hepburn intrusive suite.

The Wopmay Fault Zone divides the Wopmay Orogen and forms the eastern margin of the Great Bear Magmatic Zone. It forms a 10 kilometer wide north-trending belt of mylonitized rock encompassing a diverse assemblage derived from the Archean basement, the Hottah Terrane, the Turmoil Klippe and the Great Bear Magmatic Zone (Hoffman, 1988). The zone is presently tightly folded about northerly trending axes, with the folding post-dating Great Bear magmatism and earlier structural components (Hildebrand et al., 1990). Isotopes and field relations suggest the western edge of the Slave reaches the Wopmay Fault Zone (Housh et al., 1989; Hildebrand et al., 1990). Conjugate transverse thrusts related to collisional tectonics focused west of the Great Bear Magmatic Zone reflect east-west shortening and north-south extension (Hoffman, 1984 and 1988). Regional transcurrent

faulting is suggested between 1843 to 1810 Ma (Hildebrand et al., 1987).

2.2 Great Bear Magmatic Zone

The Great Bear Magmatic Zone (GBMZ) is an approximately 100 kilometer wide volcano-plutonic arc exposed over a distance of 450 kilometers along strike (Figure 2.2). The zone can be further traced by a positive magnetic anomaly for a further 400 to 500 kilometers south under thin, gently westward-dipping Paleozoic platform (Coles et al., 1976; Hildebrand et al., 1987), and 300 kilometers north-west under gently dipping Proterozoic cover (Gandhi et al., 2001; Hildebrand et al., 2009).   It is characterized by intermediate to felsic plutonic, volcanic and volcaniclastic rocks that have been weakly to moderately deformed and metamorphosed to sub-greenschist facies (McGlynn, 1979; Gandhi, 1989; Hildebrand et al., 2009). The Great Bear Magmatic Zone has been interpreted as a continental arc that formed on the western margin of the of the Wopmay Orogen ca. 1880 to 1840 Ma, post-dating the accretion of the Hottah terrane (Hoffman, 1980; Hildebrand, 1986; Gandhi et al., 2001). Emplacement was a potential consequence of subduction reversal to form an eastward facing subduction zone west of the Hottah.   Reactivation of an earlier zone is suggested by Hildebrand et al. (2009). The Great Bear Magmatic Zone tectonically overlies the Hottah terrane to the west, Turmoil klippe to the east, and parts of the western Coronation margin (Hoffman and McGlynn, 1977; Hildebrand et al., 1990). The Great Bear Magmatic Zone has been intruded by several generations of Neoproterozoic gabbroic dykes (Park et al., 1995).

The GBMZ is comprised of dominantly felsic volcanic and plutonic rocks of Paleoproterozoic age. The volcanic and volcaniclastic rocks of the GBMZ are divided into four groups collectively referred to as the McTavish Supergroup (Hoffman and McGlynn,

1977; Hoffman, 1980). The Faber Group located in the southern portion of the GBMZ has an aggregate thickness of approximately five kilometers. The north-eastern Dumas Group, the north-central Sloan Group and the north-western Labine Group have a cumulative thickness of more than 10 kilometers. Basement lithology is poorly exposed in the GBMZ, and includes metasedimentary and plutonic rocks of the Hottah terrane and Bell Island Bay Group volcanic and sedimentary rocks. Exposures between basement and volcanic cover reveal a basal unconformity at the base of both the Labine and Faber Groups (Hoffman et al., 1977; Gandhi et al., 2001). The GBMZ is approximately synclinal, with younger rocks more commonly exposed within the center, and older rocks more commonly exposed on the limbs. Dumas, Sloan and Labine rocks are gently folded with plunging NW-trending axes (Hoffman and McGlynn, 1977). Though the volcanic stratigraphy of the GBMZ is relatively complex, primary volcanic textures are generally well preserved, with weak to moderate deformation and metamorphism limited to sub-greenschist facies (Gandhi et al., 1996). The nearly horizontal Faber Group forms a monocline, dipping moderately northward north of Lou Lake (Gandhi and Lentz, 1990).

2.3 Treasure Lake Group Metasedimentary Rocks

The Treasure Lake Group is a recently defined sequence of deformed and metamorphosed platformal sedimentary rock west of the Wopmay Fault Zone originally recognized as the Snare Group. The sequence is greater then three kilometers thick (Gandhi et al., 2001). Deformation and regional upper greenschist facies metamorphism occurred coeval with accretion of the Hottah Terrane, with increasing metamorphic intensity proximal to the Wopmay Fault Zone. Current interpretations suggest deposition on the Paleoproterozoic basement of Hottah terrane; however, this cannot be verified as the

basement is not exposed (Gandhi et al., 2005). Exposures of the Treasure Lake Group only occur in the southern part of the GBMZ, commonly in the Wopmay fault zone. Treasure Lake Group metasedimentary rock is intruded by granitic and subvolcanic GBMZ plutons and unconformably overlain by GBMZ volcanics. The Treasure Lake Group is distinguished from previously recognized Snare Group on the basis of several criteria. Stratiform occurrences of iron oxide (commonly magnetite) west of the Wopmay fault zone do not occur in Snare Group stratigraphy (Gandhi, 1994; Gandhi et al., 2001). Additionally, Gandhi and van Breeman (2005) demonstrated contrasting provenances of Treasure Lake Group and Snare Group rocks. An 18 kilometer long, northwest-trending belt between Lou Lake and Rayrock mine provides the best exposure of the group (Gandhi and van Breeman, 2005).

The Treasure Lake Group is comprised of four main units: (i) a basal siltstone unit; (ii) a lower carbonate unit; (iii) a middle quartz arenite unit; and (iv) an upper siltstone unit (Figure 2.3). The basal siltstone is of unknown thickness, though estimated to be approximately one kilometer. It is dominated by quartzo-feldspathic fine-grained sediments intercalated with argillaceous and variably magnetic siltstone (Gandhi et al., 2001). A boundary of intercalated calcareous siltstone and mudstone marks the transition to an approximately 100 meter thick finely-bedded stromatolitic carbonate unit (Gandhi and van Breeman, 2005). The carbonate unit is comprised of limestone and dolomite with sparse calcareous argillite, calc-silicate and magnetite-rich beds.   The carbonate unit is typically metamorphosed to marble and laterally discontinuous at the northwestern end of the exposed belt.

Overlying the carbonate unit is a 300 to 500 meter thick quartz arenite. This massive, well bedded unit is intercalated with quartzo-feldspathic and argillaceous siltstone. Grading upward, the arenite gradationally transitions into a 300 meter thick upper siltstone unit
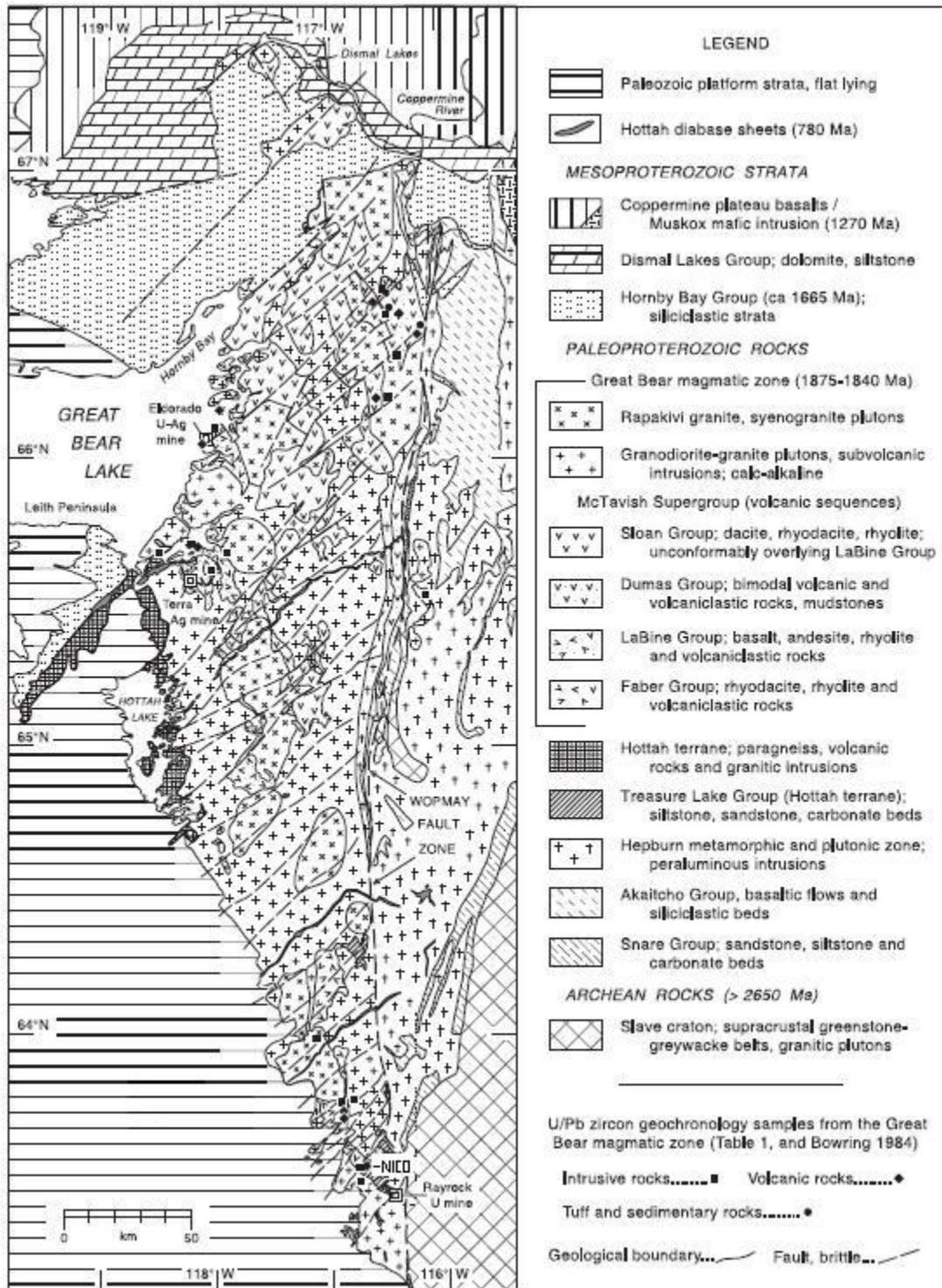
Figure 2.2 – Simplified geological map of the Great Bear Magmatic Zone showing the general location of the Lou Lake study area (from Gandhi et al., 2001).

Figure 2.3 – General geology of the Lou Lake area. Locations of U-Pb zircon dating of the local lithology are highlighted (modified after Gandhi et al. 1996).

(Gandhi et al., 2005). This argillaceous unit is interbedded with quartzo-feldspathic siltstone with common units of argillite and carbonate. The upper siltstone unit is locally cordierite-bearing proximal to Marion River plutonism. Duke (personal communication) noted the cordierite porphyroblasts can be traced from the north end of Peanut Lake northwest of Lou Lake, through Bea Lake to the east side of Dianne Lake. Gandhi (1994) and Gandhi et al. (2001) have interpreted the platform-shelf sequence as a transition from low-energy to high energy sedimentation, with a subsequent variable depositional environment.

A minimum age for the Treasure Lake Group of 1873 Ma has been determined by U-Pb dating of zircons sampled from a sodic leucogranite pluton emplaced within the lower siltstone strata (Gandhi et al., 2001). All significant geochronology are listed in Table 2.1. Detrital zircons from the medial quartz arenite indicate a maximum age of 1895 Ma, with a weighted mean average age of 1886 Ma for sedimentation (Gandhi et al., 2005). This pre-dates U-Pb geochronology of zircons sampled from basal Recluse Group ash beds which have been used by Bowring and Grotzinger (1992) to infer the Hottah-Slave collision at 1883 Ma, and confirms Treasure Lake Group deposition pre-collision. Ar-Ar dating of annite obtained from drill core (NICO DDH-97-054, interval 101.81 to 102.20 m) from Treasure Lake Group medial biotite-amphibole-magnetite metasomatic rock hosting cobalt mineralization gave an age of 1832 Ma. Gandhi et al. (2001) have interpreted this younger date as indicative of the timing of the intense potassium metasomatism characterized by the Lou Lake potassium anomaly, with possible ties to late stage magmatic-hydrothermal activity within the magmatic arc. This age likely signifies the timing of black rock alteration described by Sidor (2000).

2.4 Great Bear Volcanic Rocks

Magmatic activity within the GBMZ began with emplacement of sodic leucogranite plutons into folded metasedimentary basement ca. 1873 Ma (Gandhi et al., 2001). Field relations and geochronology suggest that extrusion of the basaltic to rhyolitic Labine Group and rhyodacitic to rhyolitic Faber Group were coeval with the Marion River Batholith at approximately 1867 Ma (Bowring, 1984; Bowring et al., 1984). The Labine Group is composed of subaerial sedimentary rock intercalated with variable basic, intermediate and acidic volcanic and volcaniclastic rocks (Hildebrand, 1981). The oldest exposed volcanic rocks of the western GBMZ belong to the Labine Group, where they unconformably overlie Bell Island Group pillow basalts (Hoffman et al., 1976). Thick sequences (up to 2600 meters) of andesitic tuff dominate the upper-Labine, outcropping in the Echo Bay and Camsell River regions (Badham, 1973; Hoffman and McGlynn, 1977). The Labine Group has previously been interpreted as post-collapse caldera-fill and stratovolcano facies (Hildebrand et al., 1987). Potentially coeval and lithologically similar to the Labine Group, the Dumas Group is composed of bimodal volcanics and volcaniclastics intercalated with lacustrine mudstones (Hildebrand et al., 1987). The Dumas Group forms a narrow belt along the eastern margin of the GBMZ. Ash-flow tuffs of the Dumas Group have been interpreted as outflow facies and alluvial braid-plains deposited behind the main volcanic front of the Labine (Hildebrand et al., 1987).

The central Sloan Group forms the youngest supracrustal rocks of the GBMZ. Their age is best constrained by subvolcanic porphyry cross-cutting the group dated at 1867 ± 7 Ma (Bowring, 1984). They are dominated by dacite-rhyodacite-rhyolite flows and ignimbrites

Table 2.1 - Geochronology for several lithologies in the Lou Lake area.

LITHOLOGY	DATE (Ma)	RANGE	DATING TECHNIQUE	SAMPLE SOURCE	REFERENCE
Quartz Monzonite Porphyry	1831	-11 / +11	Ar-Ar	biotite separate from potassium metasomatized quartz feldspar porphyry	Gandhi et al. (2001)
Biotite Amphibole Magnetite Metasomatic Rock	1832		Ar-Ar	annite separate from drill core intersection (NICO DDH-97-054, interval 101.81 to 102.20 m)	Gandhi et al. (2001)
Summit Peak Metasomatite	1851	-16 / +18	U-Pb	poor quality zircon from banded potassium feldspar metasomatite	Gandhi et al. (2001)
Faber Lake Rapakivi Granite	1856	-3 / +2	U-Pb	zircons from Faber Lake rapakivi granite	Gandhi et al. (2001)
Marion River Batholith	1866	-2 / +3	U-Pb	zircons from Marion River batholith (two sources: gneissic granodiorite and massive granodiorite)	Gandhi et al. (2001)
Quartz Monzonite Intrusives	1867	-1.5 / +1.6	U-Pb	zircons from quartz monzonite plutons emplaced within volcanic rock at Lou Lake	Gandhi et al. (2001)
Mazenod Lake Volcanic Assemblage (Faber Group)	1868.6	-1.2 / +1.2	U-Pb	zircons from Mazenod Lake rhyodacite ignimbrite	Gandhi et al. (2001)
Sodic Leucogranite Plutons	1873	-2 / +2	U-Pb	zircon from sodic leugranite pluton emplaced in lower siltstone post-deformation/metamorphism	Gandhi et al. (2001)
Basal Recluse Group Ash Bed	1883	-3.5 / +3.5	U-Pb	zircons from basal ash bed	Bowring & Grotzinger (1992)
Medial Quartz Arenite	1886	-8 / +8	U-Pb	detrital zircons from quartz arenite	Gandhi & van Breeman (2005)

intercalated with andesite (Hoffman and McGlynn, 1977). Intercalated sedimentary rock within the volcanic sequence is relatively rare when compared to other volcanic sequences to the east and west. The Sloan disconformably overlies the caldera-stratovolcano sequences of the Labine, but only occurs in tectonic contact with the Dumas Group (Hildebrand et al., 1987). These same authors suggest the region is strongly populated with coalesced and superimposed caldera complexes based upon the dense welding and high crystal content of the thick ash flow succession, which may be indicative of prolonged and voluminous volcanic activity.

Though geochronology suggests a coeval relation between the Labine and Dumas groups, the temporal relationship between the southern Faber Group and the remaining members of the McTavish Supergroup are not exposed (Gandhi, 1994). The southern group is a volcanic belt dominated by rhyodacitic-rhyolitic ignimbrites and associated flows, tuffs and volcaniclastics (McGlynn, 1979; Gandhi, 1989). Andesitic volcanism is absent in the Faber Group, a significant contrast to the northern groups (Hildebrand et al., 1987). The Faber Group has been subdivided into three separate assemblages based on stratigraphic relationships: (i) the rhyolitic Lou Lake assemblage (Gandhi et al., 1996); (ii) the rhyodacitic Mazenod Lake assemblage (Gandhi, 1994); and (iii) the rhyodacitic Bea Lake assemblage (Gandhi and Lentz, 1990). U-Pb geochronology from zircons hosted in rhyodacite ignimbrite show a date of 1868.6 Ma for the Mazenod Lake assemblage (Gandhi et al., 2001). This date represents the timing of regional calc alkaline volcanism and therefore correlative to the Lou Lake assemblage; however field relations between the two are ambiguous. Timing of Lou Lake volcanism is best constrained by U-Pb zircon geochronology of 1867 Ma obtained from quartz monzonite plutons intrusive to rhyolite ignimbrite and volcanic tuffs and agglomerates

sampled by Gandhi et al. (2001) at the southwestern end of Lou Lake.

2.5 Great Bear Intrusive Rocks

A-type plutonism within the GBMZ commenced post-ash tuff volcanism and was active between 1875-1840 Ma (Bowring, 1984; Gandhi et al., 2001). Granitic plutonism dominated the intrusive activity, with minor, smaller diorite intrusions. Two temporally and compositionally distinct granitic intrusive suites are recognized. The earlier granodiorite-monzogranite plutonism may be compositionally related to the volcanic rocks. Later syenogranite plutonism was emplaced post-regional folding. Northwest trending regional folds parallel the former, and the latter form substantial, oval-shaped discordant units (Hildebrand et al., 1987).

The earliest intrusive rocks of the GBMZ are of intermediate composition associated with andesitic stratovolcanoes of the western Labine Group. They are dominantly monzonitic, monzodioritic and dioritic plutons of variable diameter between five and 25 kilometers (Hildebrand et al., 1987). Commonly metasomatically altered, the plutons occur within alteration haloes up to a kilometer thick, characterized by an inner albite zone, a central magnetite-apatite-actinolite zone, and a marginal pyritic zone (Hildebrand, 1986). Hildebrand et al. (1987) has advocated emplacement at two to three kilometers depth. Hildebrand (1981) has observed that several plutons of this suite were unroofed by succeeding ash-flow volcanism, indicating significant vertical displacement coincident with volcanic activity.

The granodiorite-monzogranite plutonic suite was emplaced prior to regional folding of the GBMZ (Hildebrand et al., 1987). This interpretation is indicated by the orientation of the plutons which parallel the northwest-trending fold axes in conjunction with the spatial

arrangement of compositional zoning within individual plutons. Several plutons within this suite exhibit temporal and spatial relationships to Labine Group calderas. Generally, however, the majority of the early granitic intrusions are potentially syn-Sloan Group volcanism. Individual plutons are typically heterogeneous, composite (Hildebrand et al., 1987), and range in size up to 100 kilometers in diameter with variable two to four kilometer thickness (Hildebrand et al., 1990). In the area east of Lou Lake (see Figure 2.3), the early granodiorite plutonic suite is represented by the extensive Marion River Batholith. The Marion River Batholith is characterized by coarse euhedral feldspars in a medium- to coarse-grained groundmass (Gandhi et al., 2001). These authors have dated both it and its metamorphosed gneissic equivalent using both U-Pb zircon and titanite at 1866 +3/-2 Ma. Marginal domains of the batholith are characterized by monzonite and quartz-monzonite phases (Mumin, 2000).

A less voluminous, post-folding syenogranite suite is compositionally the most uniform of the GBMZ. Member plutons are commonly porphyritic and exhibit contacts that are consistently discordant to folding of the earlier extrusive McTavish Supergroup (Hildebrand et al., 1987). North-northeast trending siliceous dyke swarms compositionally similar to the granites are spatially and temporally associated with this intrusive suite (Hildebrand, 1982). The syenogranite plutons intrude, and are intruded by volumetrically insignificant linear to ovoid shaped hornblende-quartz diorite, diorite and monzodiorite intrusions in the eastern part of the magmatic arc, indicative of active post-folding intermediate magmatism (Hildebrand et al., 1987).

The youngest intrusive unit of the Faber Lake Group is a rapakivi granite suite. These are comprised of four texturally distinct phases defined by grain size and phenocryst abundance

(Gandhi et al., 2001). They are generally characterized by a moderately high K_2O content (D'Oria, 1998). Gandhi et al. (2001) have dated the rapakivi granite using U-Pb zircon dating at 1856 +2/-3 Ma, and suggest the date is likely close to the time of emplacement and igneous crystallization. However, discordant U-Pb zircon results suggest an inheritance in the zircon population of one of the analyzed fractions.

2.6 Geology of the Lou Lake Area

The Lou Lake area is located at the southernmost exposure of the Great Bear Magmatic Zone. The lake itself is situated on one of the numerous major northeast-trending transverse faults that post-date magmatic activity (Figure 2.3). The Lou Lake fault extends through Hislop Lake to the southwest, and is truncated by the regional Wopmay Fault Zone to the northeast. Faber Lake volcanic rocks on the northwestern side of the fault are downthrown with slight dextral displacement (Gandhi and Lentz, 1990). The Faber Lake volcanic belt extends a further 30 kilometers, trending northwest. Paleoproterozoic Treasure Lake metasedimentary rocks on the southeastern side of the fault strike 105° to 120° and dip variably between 40° to 90° to the northeast (Plate 2.1). The metasedimentary rocks are intruded to the east by Betty Ray Lake granodiorite and monzonite gneiss. Foliation of the gneiss trends to the northwest (Gandhi et al., 1996). Granite-granodiorite of the Marian River Batholith borders the volcanic assemblage to the northeast, and hornblende-biotite granitic rock form a southwestern boundary to the belt of Faber Lake volcanic and Treasure Lake metasedimentary rock.

Shallow north-dipping (20° to 40°) non-metamorphosed Faber Lake volcanic rocks striking 100° to 110° overlie the metasedimentary succession (Plate 2.2). The Lou Lake

volcanic assemblage ranges from massive to flow-banded rhyolite-rhyodacite, interbedded ash-flow, lapilli- and lithic-tuff, and volcaniclastics. Metasedimentary and potassium feldspar metasomatic rocks south of the deposit have been intruded by east-west trending porphyritic dykes. These predominantly quartz-feldspar and feldspar porphyries are variably altered by potassium metasomatism. A giant late-stage quartz vein striking east-northeast parallel to the late cross faults outcrops for approximately four kilometres. Late stage, local-scale unaltered dykes of intermediate composition and undetermined age strike at various orientations, cross-cutting earlier lithology and alteration.

2.6.1 Treasure Lake Group

Until recently the metasedimentary rocks exposed at Lou Lake have been universally recognized as Paleoproterozoic Snare Group, defined by Lord in 1942. However, Gandhi et al. (2001) regarded the occurrence of stratiform iron oxide within the sequence as distinct. Further geochronological evidence determined from U-Pb zircon dating from samples of quartz arenite (middle unit) suggest a maximum age for the Treasure Lake Group of 1886 ± 8 Ma (Gandhi and van Breeman, 2005). This evidence indicates the Treasure Lake Group is temporally distinct from the Snare Group, which was deposited on the Archean Slave craton as a passive margin sequence ca. 1970 to 1890 Ma.

In the immediate Lou Lake vicinity, the Treasure Lake Group comprises a coarsening upward succession of basal siltstone, intercalated lower-middle biotite-amphibole and amphibole-magnetite metasomatic rock, upper-middle arenite, and an overlying upper siltstone. The local amphibolitic rocks occupy the same stratigraphic level as the regional carbonate unit, which pinches out in the northwestern portion of the metasedimentary belt

between Peanut Lake and Lou Lake. Metasedimentary rocks within the vicinity of Bowl Zone mineralization are deformed, pervasively altered and locally brecciated. Polymetallic mineralization within the NICO deposit is hosted by amphibole - biotite $\pm$ magnetite $\pm$ clinopyroxene assemblages that show a strong association to pervasive black rock amphibole-biotite and infiltrational magnetite alteration (Sidor, 2000).

Basal Siltstone

The basal siltstone is locally exposed over a large expanse to the south and west of the NICO deposit. It is fine grained and predominantly grey-to-dark grey, with centimeter-scale layering that has been interpreted as primary bedding by Gandhi and Lentz (1990). Stratiform disseminated magnetite occurs locally within argillaceous layers. This siltstone is intermittently replaced by variably weak to intense potassium metasomatism. The potassium metasomatism most commonly occurs as stratabound pink-colored layers and lenses between five and 15 millimeters thick. It is also typically locally overprinted by potassium metasomatism or silicification where brecciated. Veins of steel-grey magnetite commonly cross-cut both layering and earlier styles of alteration.

Medial Biotite-Amphibole and Biotite-Amphibole-Magnetite Metasomatic Rock

As revealed in drill core, the contact between basal siltstone and overlying amphibolitic rock is transitional over several meters marked by intervals of dark grey siltstone variably overprinted by olive-green amphibole and chlorite. The biotite-amphibole metasomatic rock is generally massive or banded. Where massive, compositions are predominantly marked by fine-grained amphibole overprinting a fine-to-medium grained quartz matrix. Banding is marked by heterogeneous compositions and grain sizes, with highly

variable quartz, clinopyroxene, amphibole, biotite and chlorite. Rose-pink K-feldspar + quartz bands are locally preserved. These have thicknesses that range from millimeter- to centimeter-scale. In diamond drill core, these bands are variably spaced on a centimeter to decimeter-scale over intervals measuring 10's of meters. Fresh exposures revealed in the decline indicate the banding is discontinuous over several meters.

Biotite-amphibole and amphibole-magnetite metasomatic rocks are commonly intercalated. Together they host the Fe-oxide associated mineralization and largely encompass the Bowl zone of the NICO deposit. Differentiation between them is broadly marked by the absence or presence of magnetite; otherwise both are macroscopically massive or banded. Magnetite occurs in three distinct modes. Fine disseminations occur most commonly where the rock is massive. Thick grey-black centimeter- and decimeter-scale magnetite bands characterize banded intervals. Steel-grey discordant to semi-concordant veins locally cross-cut earlier alteration styles. Biotite and chlorite laminations are common. Individual laminae range in thickness up to several millimeters, are frequently wavy to crenulated, and are variably concordant to discordant to compositional banding.

As revealed in drill core and the decline, where biotite-amphibole alteration intensity is reduced, transitions into arenite, wacke, and calc silicate rock are common. Precise boundaries are often ambiguous due to amphibole and chlorite overprinting. Psammitic intervals show marginal preservation with moderate fine grained amphibolitic overprints. Less commonly, discrete horizons of medium grained carbonate rock occur intercalated within the biotite-amphibole and amphibole-magnetite succession. These intervals are of variable thickness though generally no greater than two meters. They are characterized by wavy mm-scale laminations of biotite and chlorite that cross-cut brecciated matrix.

Upper-Middle Quartz Meta-Arenite

Upper-middle quartz meta-arenite outcrops east of the NICO deposit, and west of Peanut Lake. The contact between meta-arenite and underlying units is not well exposed in this area. The greenish-grey medium-grained meta-arenite weathers to a pinkish green, and is massive to well-bedded on a decimeter to meter scale. Ripple marks, graded- and cross-bedding observed locally within the unit indicate the meta-arenite is stratigraphically upright (Gandhi and van Breeman, 2005). As demonstrated by an overall increase in matrix content, meta-arenite maturity decreases proximal to the Bowl Zone. Here the meta-arenite is fine grained and increasingly heterogeneous in composition. Though fresh surfaces are dark grey to nearly black, they weather to a light grey to pinkish grey. Locally, microcrystalline K-feldspar is incipient within the meta-arenite matrix or occurs as solitary pseudoclasts as revealed by fresh rock faces exposed in the decline.

In the Peanut Lake vicinity, the arenite is locally intercalated with medium grained blue-green Ca-Fe amphibolite with variable thickness on a decimeter- to meter-scale. These Ca-Fe silicate units strike 285° and dip 35° to the northeast. They can be traced intermittently northwest along strike into the southern edge of the Bowl Zone. They are weakly magnetic and characterized by clinopyroxene + calcic hornblende + potassium feldspar + chlorite ± biotite ± quartz ± magnetite assemblages. They are massive to subtly banded, with banding generally marked by grain size and compositional variations. A local planar fabric resulting from alignment of biotite is oriented parallel to the strike and dip of the individual beds.

Upper Siltstone

Northwest of Nico Lake, a gradational transition into upper siltstone is characterized

by quartz arenite interbedded with cordierite-bearing metapelites. The variably thin- to thickly bedded upper siltstone has an aggregate thickness of over 300 meters. Gandhi and van Breeman (2005) have characterized it as argillaceous with quartzo-feldspathic siltstone interbeds. These quartzo-feldspathic beds are noted for the presence of disseminated magnetite, and have been compared mineralogically to the Lou Lake felsic tuffs and flows (Gandhi and van Breeman, 2005).

Further to the south, the cordierite-bearing basal portion of the siltstone is exposed west of Peanut Lake. Here massive medium grained quartz-rich bands are intercalated with cordierite-bearing fine grained siltstone beds. Cordierite-bearing layers range in thickness on a decimeter-scale. The beds are defined by the presence or absence of cordierite knots. Individual cordierites are spherical to ovoid in shape, with diameters ranging from millimeter- to centimeter-scale. The Peanut Lake exposure locally exhibits biotite alteration incipient into cordierite-bearing matrix proximal to porphyry dyking.

2.6.2 Lou Lake Volcanic Rocks

The Lou Lake assemblage comprises a coherent succession of subaerial ash tuffs and volcaniclastic rocks with an aggregate thickness of approximately one and a half kilometers. Ten felsic volcanic and volcaniclastic units have been recognized and described in some detail by Gandhi and Lentz (1990) and Gandhi at al. (2001). The succession of volcanic rocks can be broadly characterized as meter-scale cooling units defined by basal agglomerate- and lithic tuffs that grade upward into massive to flow-banded tuffs and subporphyritic to porphyritic coherent flows. Regionally, the Lou Lake volcanic rocks range from rhyolite to dacite in composition as determined by Gandhi and Lentz (1990) through whole rock petrochemical

analysis using the total alkali silica classification (LeMaitre, 1989).

Seven of the volcanic and volcaniclastic units recognized by Gandhi and Lentz (1990) occur in the immediate Lou Lake area. The basal unit, a heterolithic breccia, has conflicting interpretations that include: i) polymictic volcanic conglomerate (Thomas and Olson, 1978), (ii) laharic breccia (Bryan, 1982), (iii) agglomerate-lithic tuff-conglomerate (Gandhi and Lentz, 1990), and (iv) fault breccia (Duke, 1998). Gandhi et al. (1996 and 2001) recognize the basal unit as being deposited upon the erosional surface of folded metasedimentary rocks. It is exposed at the south-western end of Lou Lake, and can be traced discontinuously to the east where the creamy orange-pink weathered surface is conspicuous within domains of reddish-brown K-metasomatism. Though the matrix supported breccia is poorly sorted with respect to clast size, preferential orientation of clasts between 100° and 110° is comparable to the strike of overlying volcanic beds. The angular to sub-round clasts are largely comprised of a variety of metasedimentary source rocks. However, a common fraction of potassic altered fragments suggests the origin occurred syn- or post-K metasomatism (Plate 2.4).

Gandhi and Lentz (1990) documented that the basal unit is overlain by a porphyritic flow banded rhyolite. This rock has been alternatively interpreted as potassium feldspar felsite (Sidor, 2000). It is conspicuous in that this rock is pervasively metasomatically altered to reddish pink-to-maroon potassium feldspar. It is best exposed south-east of Lou Lake at Summit Lake, and can be traced eastward north of the giant quartz vein (Plate 2.3). Outliers of similarly altered rock occur both south of the main eastward trending exposure and south of the giant quartz vein. Though these rocks have collectively been considered volcanic historically, where a relationship to a specific protolith is ambiguous they are recognized here as metasomatic rock. Their uncertain nature and metasomatic origin defines the focus of this

investigation.

Where demonstrably volcanic, the lower-most units are concordantly overlain by well bedded volcaniclastic siltstone-tuff exposed centrally along the east and west sides of Lou Lake. Gandhi and Lentz (1990) described the siltstones as grey to buff-white, with centimeter-scale bedding, and interbedded with meter-scale agglomerate beds and thin aphyric rhyolites. These are overlain by buff-white, porphyritic massive to flow laminated rhyolite exposed centrally along the east side of Lou Lake, and at the northwestern corner of Lou Lake (Gandhi and Lentz, 1990). A feldspar-phyric rhyolite with well developed banding is exposed at the north end of Lou Lake. Also north of Lou Lake, massive aphanitic rhyolites extend north-northwest to Mazenod Lake, and porphyritic dacite extends to the north-east (Gandhi et al., 2001).

2.6.3 Intrusive Rocks

The oldest intrusive rocks in the Lou Lake area are exposed over several kilometers south of the deposit. Dated at 1873 ± 2 Ma by Gandhi et al. (2001), the sodic leucogranite predates Faber Lake Group volcanism. This leucogranite intrudes Treasure Lake metasedimentary rock and commonly encompasses xenoliths of metasedimentary rock. The leucocratic granite is characterized by graphic and myrmekitic intergrowths, with a low potassium (1-2.5% K_2O) and high sodium content (6-7% Na_2O) (Gandhi et al., 2001).

Quartz monzonite-monzodiorite intrusions form northeast trending dykes that outcrop at the southern end of Lou Lake. Gandhi et al. (2001) have dated the quartz monzonite at 1867 +1.6/-1.5 Ma, indicating these may be apophyses off the Marion River Batholith. The quartz monzonite is medium grained, with variable proportions of plagioclase, quartz,

feldspar and hornblende phenocrysts. Locally, the quartz monzonite has been overprinted by patches of orange-pink potassium feldspar.

Large calc-alkaline granitic plutons of the Marion River Batholith dominate the area south and east-northeast of Lou Lake. Gandhi et al. (2001) have dated several samples of the massive granodiorite and gneissic granodiorite at 1866 +3/-2 Ma and 1866 ± 2 Ma respectively. The granite is characterized by perthitic alkaline feldspar phenocrysts with thin rims of plagioclase, with a groundmass of sericitized plagioclase, quartz, alkaline feldspar and minor chloritized biotite (McGlynn, 1979). The granite is commonly porphyritic and massive, and grades to an equidimensional finer grain-size near contacts with volcanics.

Younger quartz-feldspar and feldspar porphyry dykes at the NICO deposit are discordant to Treasure Lake Group metasedimentary rock and intrude potassium feldspar metasomatite. These dykes trend to the east, and have variable widths up to 50 meters. The quartz-feldspar porphyries weather to a pinkish-orange. Prominent quartz eyes range up to a centimeter in diameter (locally up to 2 centimeters). The quartz-feldspar porphyry is pink to grey-pink where fresh, with a fine-grained groundmass and abundant quartz and plagioclase phenocrysts. Feldspar porphyries have variable proportions of plagioclase, biotite, relict hornblende and minor to absent quartz phenocrysts within a fine-grained to aphanitic, purple-brown to purple-grey groundmass. In both, plagioclase phenocrysts exhibit variable incipient to pervasive alteration to potassium feldspar. Though dyke contacts are generally razor sharp, immediate contacts often exhibit a metasomatic aureole characterized by intense potassium feldspar replacement. Where biotite-amphibole metasomatic rock is intruded, replacement within porphyry margins and immediate exocontact zones are texturally and compositionally

Plate 2.1

North-facing view of steeply dipping Treasure Lake Group upper middle quartz meta-arenite. Outcrop located northwest of Peanut Lake.

Plate 2.2

Gently dipping tuffaceous Lou Lake volcanic rocks located southeast of Lou Lake as viewed facing east.

Plate 2.3

North-facing view of an exposure of potassium feldspar metasomatic rock at Summit Lake.

Plate 2.4

Angular fragment of pink potassium feldspar metasomatic rock hosted within heterolithic breccia observed within outcrop east of Summit Lake.
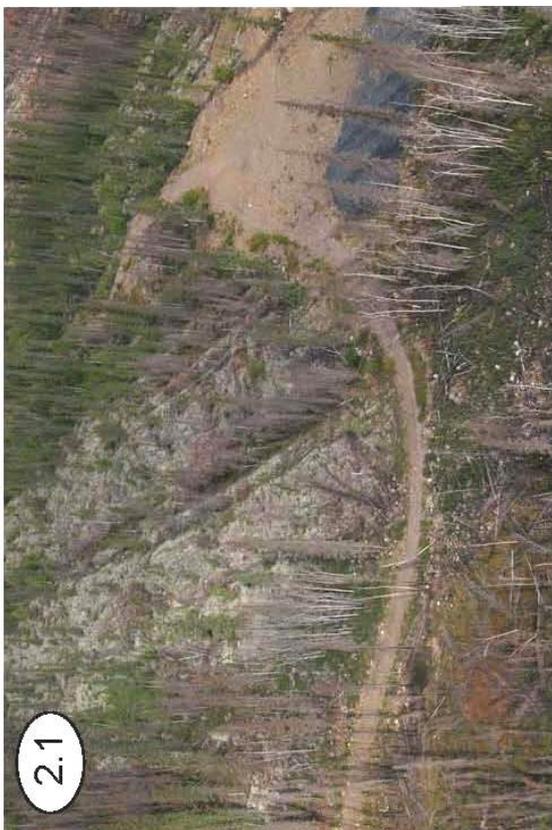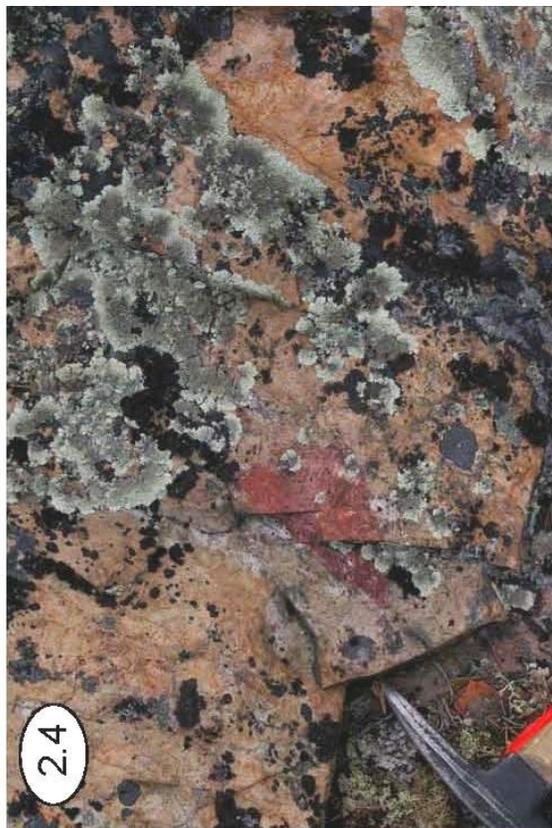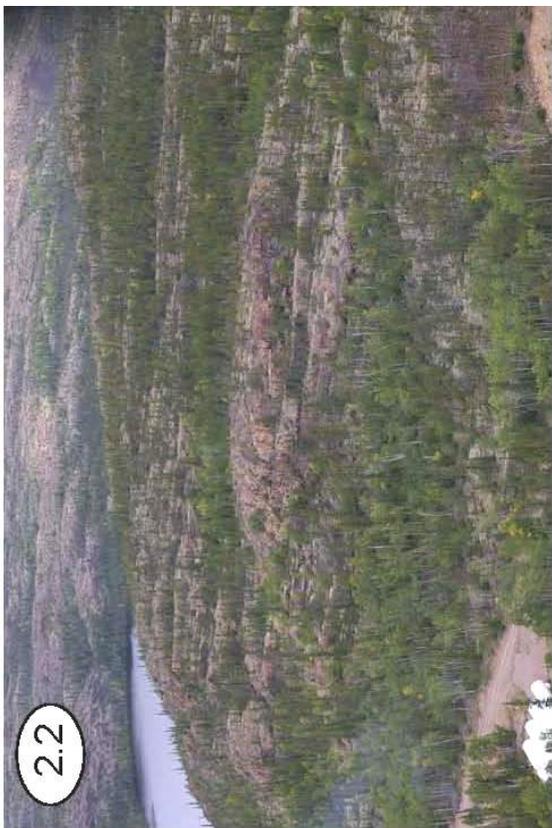
similar. Exogenous inclusions of Treasure Lake Group metasedimentary rock are commonly hosted within the porphyries. Neither type of porphyry has been dated.

The youngest intrusive rocks of the GBMZ outcrop in the Mazenod Lake area north of Lou Lake. The Faber Lake rapakivi granite is comprised of a suite of four texturally distinct, potassium rich phases that include: i) rapakivi texture with a high concentration (up to 60%) of zoned potassium feldspar phenocrysts 1-2 cm long rimmed by plagioclase; (ii) more dilute rapakivi textured porphyry with larger (2-5 cm) plagioclase-rimmed potassium feldspar phenocrysts; (iii) equigranular to seriate textured phase; and (iv) a younger fine-grained granite-aplite phase (Gandhi et al., 2001). These authors have dated the rapakivi granite at 1856 +2/-3 Ma. Thalenhorst and Farquharson (2002) have suggested that the rapakivi granite stocks are coeval with Lou Lake volcanism, though this was disproven by Gandhi et al.'s (2001) date of 1867 Ma for quartz monzonite intrusive to the volcanic rocks.

2.6.4 Local Mineralization

A number of mineralized occurrences have been recognized within the metasedimentary rocks and potassium feldspar metasomatite at Lou Lake, with showings extending south-east as far as Burke Lake. The main As-Co-Au-Bi±Cu occurrence is hosted within amphibole-altered metasedimentary rock of the Treasure Lake Group (Sidor, 2000). The polymetallic mineralization is strongly associated with arsenopyrite, which in turn exhibits a close spatial association with both stratabound magnetite and discordant magnetite veins. Arsenopyrite veins range in thickness from sub-cm to several decimeters, with vein off-shoots commonly migrating along metasedimentary structures.

Fortune Minerals Limited diamond drill exploration program has delineated the main

occurrence (designated as the NICO Deposit) into four approximately parallel lenses with economic concentrations. The lenses can be traced along an approximate two kilometer strike length that trends parallel to the 110° strike of the metasedimentary host. The main minerals of the deposit include magnetite, arsenopyrite, pyrite, pyrrhotite, chalcopyrite and bismuthinite with minor cobaltite, cobaltian arsenopyrite, native bismuth and native gold (Sidor, 2000). Gold mineralization is largely restricted to a central corridor within more extensive cobalt-bismuth mineralization in the lower two lenses. Fortune Minerals Limited (2009) report proven and probable reserves totaling nearly 31 million tonnes grading 0.91 g/t Au, 0.12 % Co, 0.16 % Bi and 0.04 % Cu (Fortune Minerals, 2007). Similar, smaller Bi-Cu-Co-Au-As occurrences are documented to the southeast in the East and Burke Lake zones (Goad et al., 2000).

Occurrences of Cu mineralization have been documented south-west of Lou Lake at Summit Peak, and due south of Lou Lake at Chalco Lake. Fortune Minerals Limited have reported assays as high as 0.7% Cu over 44 meters for the copper-rich Summit Peak zone, with some assays as high as 0.5% W and 1 ppm Au (Fortune Minerals, 1995 and 1996a and b). Summit Peak and Chalco Lake mineralization occur as chalcopyrite and bornite-rich matrix hosted within brecciated potassium feldspar metasomatite.

CHAPTER 3 – PETROGRAPHY

3.1 Introduction

The petrographic investigation focused on the mineralogy and texture of K-metasomatized rock east of Lou Lake. Samples for detailed study were selected from a representative suite collected from the decline, surface outcrop, and diamond drill core. A comprehensive catalogue of brief sample descriptions and locations is provided in Appendix 1. In total, 39 polished and 57 thin sections were examined. Petrographic descriptions of units and associated K-metasomatism encompass the following: i) Treasure Lake Group metasedimentary rocks; (ii) Lou Lake Volcanic rocks; (iii) local intrusive rocks; (iv) potassium feldspar metasomatic rocks; (v) brecciation associated with K-metasomatism; and (vi) veins. For the purpose of this investigation, those rocks where the relationship between pervasive metasomatic replacement of a specific protolith is poorly defined are identified as either metasomatic rock or 'metasomatite' - as prescribed by the IUGS subcommission on the systematics of metamorphic rocks (Zharikov et al., 2007). The intensity of alteration is defined on the basis of observed destruction of primary minerals and textures, the degree of neocrystallization, and the degree of pervasiveness of microstructural and textural alteration.

3.2 Treasure Lake Group Metasedimentary Rocks

Previous investigations have described Treasure Lake Group metasedimentary rocks at Lou Lake which host the Fe-oxide associated mineralization of the NICO deposit, including: i) basal metasiltstone; (ii) medial biotite-amphibole-magnetite metasomatic rock; (iii) local carbonate units; and (iv) upper quartz meta-arenite. The effects of "black rock" Ca-Fe alteration and sulphide mineralization have been previously documented by Sidor (2000).

Accordingly, petrographic examination of these units and the nature of Ca-Fe alteration are excluded from the current study. However, the effects of K-metasomatism of metasedimentary rocks have not been rigorously documented. Extreme potassic alteration overprints many units of the Treasure Lake succession. Pervasive stratabound replacement is similarly preserved within basal metasiltstone and medial biotite-amphibole-magnetite metasomatic rock, alteration effects of variable intensity overprint metapsammite matrix, and incipient alteration occurs locally within cordierite-bearing basal beds of the upper-most metasiltstone. Petrographic descriptions of the effects of potassium feldspar replacement within metapelitic and metapsammitic units are presented below. Because of the similarity of replacement within basal metasiltstone and medial biotite-amphibole-magnetite metasomatic rock, the effects of potassic alteration are described together.

3.2.1 Basal Metasiltstone

The basal metasiltstone has been previously described by Sidor (2000) and Gandhi and van Breeman (2005), and it is briefly described here to highlight the effects of potassium metasomatism. It is primarily exposed south of the NICO deposit and is conformably overlain by amphibole metasomatic rock. This fine grained unit is characterized by alternating light to dark grey and minor pale pink centimeter-scale bands (Plate 3.1). Both Sidor (2000) and Gandhi and van Breeman (2005) characterize this banding as preserved primary bedding. Sidor (2000) notes the compositional nature is marked by modal variation in mosaic quartz, biotite, magnetite and coarse plagioclase-biotite. Though the siltstone in general is non to weakly magnetic, moderate magnetism is locally observed in dark bands where magnetite is most concentrated. As revealed in thin section, magnetite occurs as stratabound disseminations and locally as discordant veins.

3.2.2 Medial Biotite-Amphibole-Magnetite Metasomatic Rock

The medial unit is a metasomatic rock that has been described in detail by Sidor (2000) as amphibolitic ironstone. It is best exposed along the southern rim of the Bowl zone where it conformably overlies the basal metasiltstone. East of the Bowl Zone, it is conformably overlain by quartz meta-arenite and discordantly overlain by Lou Lake metavolcanic rocks or potassium feldspar metasomatite. These contacts are further discussed in subsequent sections below. In core the biotite-amphibole-magnetite metasomatic rock ranges from pale to dark olive green. At surface it weathers to dark green-black. It is commonly intercalated with brecciated and silicified basal metasiltstone beds or variably preserved arenaceous and subarkosic metapsammite beds showing variable thickness and amphibole overprinting. Sidor (2000) distinguished between non-banded and banded varieties, with the non-banded type characterized by fine to medium grained radiating mosaics of amphibole, quartz and minor feldspar and the banded type characterized by similarly composed bands interlayered with weakly foliated biotite-rich layers. Magnetite is commonly heavily disseminated or layered within the banded variety, though discordant magnetite veins locally infiltrate both varieties.

K-Metasomatism of Basal Metasiltstone and Medial Biotite-Amphibole-Magnetite Metasomatic Rock

Potassium feldspar replacement of basal metasiltstone and medial biotite-amphibole-magnetite metasomatic rock give rise to rose-pink stratabound bands on a millimeter to centimeter-scale. These potassicly altered bands form concordant discontinuous layers within both units and are thus described here together. Stratabound replacement is particularly well-developed in metasiltstone exposures approximately 500 meters south of the Bowl Zone

(Plate 3.1). Here K-metasomatized laminations and thin lenses have lateral continuity on a meter-scale, and contacts with bounding non-K metasomatized layers are sharp.

Similar bands within biotite-amphibole-magnetite metasomatic rock are best observed intersected in drill core (Plate 3.2). They most commonly occur proximal to the lower boundary with basal metasiltstone. In contrast to those observed in metasiltstone, K-metasomatized bands in the biotite-amphibole-magnetite metasomatic rock are frequently insitu-brecciated. Band fragments show diffuse to transitional margins into amphibolitic matrix indicating amphibole growth post potassium feldspar replacement. Intervals of biotite-amphibole-magnetite metasomatic rock hosting frequent replacement bands show comparatively low magnetite content. This is best observed in the NICO decline where cross-cuts reveal markedly well preserved pink bands over significant intervals. Drill core intersections show these successions either transition into lower banded biotite-amphibole metasomatic rock or basal metasiltstone where effects from K-metasomatism are not exhibited. Upper transitions are commonly into amphibolitized quartz arenite.

In thin section K-metasomatized bands exhibit two modes of occurrence, distinguished by matrix grain size and mineral assemblage. These include coarse grained bands comprised by a quartz + potassium feldspar ± magnetite assemblage and very fine grained bands consists of a quartz + potassium feldspar + chlorite + hematite assemblage.

The matrix of coarse grained bands shows a relatively homogeneous, inequigranular composition marked by quartz (50-55%) and potassium feldspar (40-45%) with minor magnetite (2-5%). Less commonly these bands are weakly overprinted with trace chlorite. The matrix of altered bands are comprised of irregular, xenoblastic grains with diameters up

to 150 μm that exhibit deeply sutured and sometimes diffuse boundaries indicative of grain coarsening and recrystallization. These are nearly an order of magnitude coarser than matrix from adjacent fine grained non-K-metasomatized layering (Plate 3.3). Grain size coarsening was apparently domainal, with sub-grain recrystallization common at margins and within cores. Idioblastic magnetite occurs as octahedral disseminations within grain-coarsened bands. These show characteristic trapezoidal and diamond-shaped cross sections, and are commonly finer than 50 μm in diameter. Less commonly, xenoblastic magnetite occurs as anhedral grains or forms aggregates. Grain coarsened effects were more commonly observed in replaced bands from basal metasiltstone.

Very fine grained band compositions are dominated by an ultra-fine equigranular matrix of mosaic-textured quartz (45-55%) and hematite-dusted potassium feldspar (35-40%). Trace zircon (<1%), fine disseminations of secondary biotite (2-3%) and amphibole (<1%), and trace chlorite (3-5%) persist, but these minor and trace accessory minerals are relatively depleted within altered bands when compared to adjacent non-metasomatized layering (Plate 3.4).

Though uncommon, quartz porphyroblasts and feldspar porphyroblasts are preserved within the neocrystallized very fine grained band matrix. Quartz porphyroblasts range from sub-angular to sub-round with diameters up to 200 μm. Randomly dispersed pale green chlorite inclusions throughout the coarser examples support neogenesis over a detrital origin. Less commonly, microcline and orthoclase are preserved as irregularly shaped porphyroblasts less than 50 μm in diameter. The feldspar phases are distinguished by characteristic cross-hatched twinning in the former and simple twinning in the latter. Diffuse grain margins are defined by sub-grains that transition into the finer grained matrix indicating the coarser grains

are a product of recrystallization. Both potassium feldspar species have chlorite and lesser sericite inclusions.

Euhedral zircons up to 100 μm in length within these very fine grained bands are readily distinguished by their high relief and third order yellow interference colours. Subhedral overgrowths developed on rounded cores suggest secondary growth on original detrital grains. Light green to blue-green pleochroic amphibole occur as aggregates or form subhedral blades up to 150 μm in length. Biotite forms randomly oriented microlites and tan brown to dark green pleochroic laths which attain lengths up to 140 μm. Both amphibole and biotite show chlorite alteration at grain margins and along cleavage planes. Otherwise pale green chlorite microlites and ultra-fine hematite dusting is ubiquitous within the very fine grained altered matrix.

3.2.3 Interbedded Calcsilicate Rock

Calcsilicate domains are a poorly understood and rarely documented lithologic component within the Treasure Lake Group metasedimentary succession. Sidor (2000) petrographically described amphibolitic marl occurring within medial biotite-amphibole-magnetite metasomatic rock, and Gandhi and van Breeman (2005) briefly noted their occurrence within Treasure Lake group medial carbonate. However, as similar calc-silicate rock occurs as discrete horizons within basal metapsammite, the minor lithological unit likely marks the stratigraphic transition from biotite-amphibole-magnetite metasomatic rock to meta-arenite. They are described here to demonstrate the effects of K-metasomatism.

The calc-silicate rocks form a semi-continuous horizon that can be traced at surface along a northwest-southeast trend from Peanut Lake into the south-western edge of the Bowl

Zone. These occur as deformed and locally boudinaged horizons interbedded within metamorphosed arenite near Peanut Lake (Plate 3.5). Here, calc-silicate domains weather to blue-green and are characterized by a prominent planar fabric oriented parallel to unit boundaries. Northwest of Whale Lake and within exposures immediately west of the Peanut Lake road, similarly oriented calc-silicate rock form local domains within a succession of banded biotite-amphibole-magnetite metasomatic rock. Here and within exposures along the south-western ridge of the Bowl Zone, these domains weather to green-black and are much richer in banded magnetite. The subtle planar fabric is due to alignment of 1 to 3 mm black biotite. They are locally banded on a millimeter- to centimeter-scale marked by variable amphibole composition. Where calc-silicate domains are cross-cut in the decline, they are intercalated with meta-arenite. At surface the boundaries with meta-arenite are sharp.

Calc-silicate rocks comprise a markedly heterogeneous metamorphic mineral assemblage including clinopyroxene (15-40%), potassium feldspar (0-40%), quartz (5-30%), magnetite (<1-30%), chlorite (5-20%), biotite (3-8%), amphibole (2-10%), and minor epidote (1-2%), with trace calcite (1%), rutile (<1%), ilmenite (<1%) and zircon (<1%). Calc-silicate units do not have a matrix component. Xenoblastic clinopyroxene forms irregular masses or coarse grained mosaics that poikiloblastically enclose other grains. The clinopyroxene is distinguished by a weak colourless to pale green pleochroism, a well developed imperfect prismatic cleavage, high positive relief and 2nd order yellow birefringence. Though Sidor (2000) reported hedenbergite and augite compositions for clinopyroxene found in amphibolitic rock, pyroxene species obtained from samples interbedded with meta-arenite have not been verified by electron microprobe or X-ray diffraction. Clinopyroxene is commonly partly replaced on grain margins, fractures, and cleavage planes by amphibole,

biotite and chlorite pseudomorphing biotite. Locally, clinopyroxene is replaced by patches of epidote or calcite, or entirely pseudomorphed by amphibole. The sub-round to round quartz inclusions within clinopyroxene poikiloblasts have sharply defined boundaries and range in size up to 300 μm. Comparatively, quartz enclosed within clinopyroxene poikiloblasts exhibit sub-grain development similar to that observed in quartz metawacke. Secondary quartz is readily distinguished by its vuggy appearance and irregular habit.

Poikiloblastic amphibole metacrysts also include quartz grains, and are locally rich in magnetite. Amphibole pseudomorphs after clinopyroxene are distinguished by characteristic 56° and 124° cleavage, and 2nd order interference colours. Amphibole porphyroblasts range in diameter from 100 to 900 μm, with smaller grains exhibiting diamond shaped cross sections. Larger grains are commonly altered to biotite and chlorite along cleavage planes and grain boundaries. Tabular tan to dark brown biotite laths up to 1 mm in diameter are commonly altered by patches of green pleochroic chlorite. Unaltered biotite cleavage planes show traces of reddish brown rutile, and less commonly ilmenite. Both biotite and chlorite pseudomorphs after biotite host local sphene inclusions. Rare 20-30 μm colourless anhedral zircon grains form pleochroic halos within biotite and in the chlorite replacing biotite. Magnetite occurs as isolated anhedral and octahedral grains up to 50 μm.

Subtle to moderately intense incipient chlorite and sericite microveinlets locally infiltrate the Ca-Fe silicate rocks. The chlorite microveinlets occur as replacement of amphibole after clinopyroxene domains. Retrograde chlorite forms as randomly oriented masses, and coarser porphyroblasts show weak green to olive green pleochroism and well developed cleavage. Chlorite is locally partially overprinted by incipient sericite, and sericite disseminations are common within strongly chlorite altered domains.

K-Metasomatism of Calcsilicate Rock

Potassium feldspar replacement of calc-silicate rock is well exposed in the decline, though only occasionally recognized in core. Here, potassium feldspar locally comprises up to 40% of the unit, forming coarse heteroblastic metacrysts that include chlorite, amphibole, clinopyroxene and ankerite. These poikiloblasts range up to 500 μm in diameter, with turbid cores and rims rich with hematite inclusions (Plate 3.6). Potassium feldspar replacement is generally domainal, and sub-grain recrystallization is ubiquitous. Boundaries between adjacent feldspar grains are commonly diffuse, or interdigitate where more distinct. Crisp, angular boundaries of potassium feldspar grains enclosed within metacrysts suggest a fragmental origin for an earlier phase. Triple point junctions evidenced within homogenous aggregates suggest textural equilibrium was locally attained. Less commonly, well developed microcline porphyroblasts exhibit tartan twinning. Banded to lamellar intergrowth textures are locally developed within larger potassium feldspar grains.

Weak foliation is also locally developed within intervals of potassium feldspar replaced calc-silicate rock. This anisotropic fabric is defined by the alignment of quartz and preferred orientation of chlorite ± sericite. Elongate domains of equigranular potassium feldspar parallel the chlorite, forming cryptic discontinuous lenses. Similar crystallographic orientation for potassium feldspar is confirmed by use of a gypsum plate. As the domains comprise independent grains of potassium feldspar, similar crystallographic orientation is indicative of dynamic potassium feldspar replacement. Similarly oriented mafic bands are characterized by aggregates of elongate, pleochroic blue-green amphibole ± clinopyroxene locally replaced by randomly oriented scales of pleochroic biotite and chlorite.

Relict potassium feldspar and hematite are commonly preserved as macroscopic reddish pink spots within calc-silicate domains. In thin section these spots show clinopyroxene poikiloblasts heavily included with amphibole, quartz, microcline and hematite. Here, amphibole partly replaces clinopyroxene on grain margins and cleavage planes. Quartz and microcline show sharp angular boundaries indicative of a fragmental origin (Plate 3.7). Hematite occurs as discrete irregularly shaped masses similarly enclosed by clinopyroxene. The optical continuity of microcline clasts as revealed by characteristic cross-hatch twinning suggests the pre-fragmental source was relatively coarse grained. Fe-oxide species are conspicuously absent within microcline fragments. Both quartz and feldspar fragments are weakly included by chlorite.

3.2.4 Upper Medial Quartz Meta-Arenite

This metapsammitic unit at Lou Lake shows a westward transition from compositionally mature and least-altered meta-arenite which outcrops south and east of the Grid Lakes to variably Ca-Fe and K-metasomatized meta-subarenite exposed proximal to and east of the Bowl zone. Metapsammite intersected by drill core commonly show intercalations of amphibole metasomatic rock and meta-arenite, with variable potassium feldspar overprints. These "subarkosic" units are best observed in drill core. Quartz arenite has been previously described by Sidor (2000), however, it is briefly described here to illustrate the effects of potassium metasomatism.

The metapsammite is generally macroscopically massive, with local fine laminations defined by marked variation between moderately well sorted very fine-to-fine and fine-to-medium grain sizes. It typically weathers to a pale pink-brown, though fresh surfaces in the

decline are variably grey to dark grey (Plate 3.8). The subarenite is composed of angular to sub-round porphyroclasts occurring within a silty matrix. The sand-sized fraction of the sub-arenite comprises between 65 to 85% of the unit, the silty matrix ranges between 15 to 35%. The dominant fraction of detrital grains is quartz (80-95%), occasionally forming polycrystalline aggregates, with trace ilmenite (<1%), martite (<1%), and pyrite (<1%) (Plate 3.9). Metacrysts of microcline (1-2%), orthoclase (1-2%), and calcite (<1%) are less common.

Inclusion-rich quartz clasts range in diameter from 50 μm to nearly 1 mm, though granules of 2-3 mm diameter do occur. Undulose extinction of quartz grains is ubiquitous and sub-grain recrystallization along grain boundaries and within grain cores is common. Quartz granules vary from multi-grain aggregates to sub-round to round monocrystalline quartz clasts. The corroded margins of quartz clasts are mantled by randomly oriented chlorite, while unmantled quartz contacts are commonly sutured. Occasional polycrystalline aggregates of annealed quartz and chlorite microlithons may be of tectonic origin.

The meta-arenite matrix is predominantly composed of platy green chlorite with very fine-to-fine grained silt-sized quartz, biotite, sericite, disseminated pyrite and iron oxide. Reddish-brown patches of hematite are spatially associated with the chlorite. Polygonal martite pseudomorphs after magnetite occur up to 100 μm in diameter. These and trace ilmenite and pyrite form anhedral grains and fine grained aggregates up to 200 μm in diameter. Rare ankerite grains range in size between 50 to 400 μm, with anhedral to subhedral forms, and abundant chlorite and sericite inclusions. Earthy hematite commonly occurs as red amorphous masses within the matrix.

K-Metasomatism of Meta-Arenite

In general, effects of K-metasomatism are least-developed within metapsammitic rock indicating the resistance of quartz to replacement. Potassic alteration is recognized in drill core by a variably incipient to pervasive pinkish coloration of the matrix. Well preserved textures indicate an arenite protolith; however intervals showing replacement are generally characterized as "subarkosic" to reflect the secondary potassium feldspar component of the matrix. Here, porphyroblasts of microcline and orthoclase distinguished by characteristic cross-hatch twinning in the former and lack of twinning in the latter occur as minor components within the meta-arenite. The equant but anhedral grains range in diameter from 150 to 600 μm. Corroded margins of the potassium feldspar grains are commonly mantled by chlorite matrix. Boundaries of remnant quartz clasts are commonly sharp and rich in inclusions of apatite, zircon and chlorite. Recrystallization of detrital quartz grains is more pronounced within intervals of intense alteration, resulting in development of sub-grains at grain boundaries and within grain cores.

At surface and where exposed by decline cross-cuts, potassium feldspar replacement occasionally produces a brecciated appearance in metapsammites. Pseudobrecciated layering is best observed at surface south of Chalco Lake where metasedimentary bedding can be traced along strike (Plate 3.10). Here, pervasive potassium feldspar replacement extends along individual layers evidenced by elongate replacement spots that produce a pseudobrecciated appearance. Both completely replaced layering and pseudoclasts are of similar pink potassium feldspar composition. Replacement is confined to individual beds, with bounding layers apparently unaffected.

Lone-stones, as defined by Laznicka (1989), are best observed along decline cross-cuts where their pink color contrasts against darker grey matrix. These range in size on a centimeter-scale. They exhibit semi-parallel elongate or distorted shapes. In thin section, grain size reduction and potassium feldspar replacement of matrix is pervasive. Modification of quartz porphyroclasts ranges from incipient potassium feldspar cross cutting grain boundaries to complete replacement of grains. Typically quartz shows partial replacement with sub-grain development along boundaries (Plate 3.11). The pseudobrecciation of metasedimentary layering and formation of lone-stones within massive beds provides strong evidence of selective hydrothermal replacement. Local development of rolling structures preserved by quartz porphyroblasts is indicative of shear, suggesting this replacement occurred syn-deformation.

3.2.5 Upper Metasiltstone

The upper metasiltstone is well exposed in outcrop northwest of NICO Lake. It can be readily traced at surface from the Rayrock Mine in the south to north of Lou Lake. Cordierite-bearing beds and interbedded arenite mark a gradational transition from underlying sandstone. Their regional extent is demonstrated by exposures that can be traced at surface from Lou Lake through Bea Lake to Sue Dianne 20 km north of the NICO deposit (N. Duke, personal communication). Metasiltstone bedding is of variable thickness, ranging from several millimeters to a decimeter-scale. Layering is defined by colour and compositional changes, varying from light to pale pink-grey and quartzo-feldspathic, to dark grey and argillaceous where biotite and magnetite content is greater. Though composition and grain size fluctuate on a layer by layer basis, the matrix is generally comprised of quartz, biotite, microcline, chlorite, magnetite and mixed aggregates of unidentified phyllosilicate minerals.

Metapelite bedding is generally variably grey and argillaceous. These are predominantly silty with clay-sized fractions composed of phyllosilicate minerals (40-60%), biotite (10-20%), quartz (5-15%), and magnetite (2-10%). Colourless to pale grey-green phyllosilicate minerals form cement that largely supports remaining granular components. Though the ultra-fine grain-size is difficult to optically resolve (< 10 μm), varied birefringence suggests mixed compositions. Individual species have not been determined by electron microprobe or X-ray diffraction. Weakly pleochroic brown-green biotite laths range in size up to 110 μm. These are commonly weakly included by very fine magnetite. Biotite grains are generally aligned parallel to bedding planes. Where this is better developed, they impart a weak foliation to layering.

Quartz porphyroclasts within argillaceous layers show sub-round to round shapes and diameters ranging up to 120 μm. Rare larger grains persist up to 600 μm. Though boundaries are sharp, larger grains exhibit cuspate embayments and porphyroclasts are commonly dusted with fine inclusions suggesting local instability and recrystallization. However, square biotite-quartz interfaces are nearly ubiquitous, indicating equilibrium metamorphic recrystallization progressing toward reduced surface energy. Fine to very fine magnetite is generally evenly disseminated within these layers, though modal populations are variable.

Quartzo-feldspathic layers show mixed silt and sand sized fractions comprised of quartz (80-85%), biotite (5-10%), magnetite (2-5%), unidentified phyllosilicate minerals (2-5%) and microcline (1-2%). They are dominated by inequigranular sub-angular quartz porphyroclasts that range in size from 10 to 120 μm. These commonly exhibit a granoblastic-polygonal texture showing well-defined straight boundaries, sutured contacts and triple point junctions indicative of textural stability. Though undulose extinction is widespread, it is most

Plate 3.1

Exposure of fine grained metasiltstone south of the Bowl Zone showing alternating compositional bands of light grey (quartz-dominant), dark grey (magnetite-rich) and pink (stratabound potassium feldspar replacement). Photo from sample location GR-10-107.

Plate 3.2

Interval of biotite-amphibole-magnetite metasomatic rock from diamond drill core showing the preservation of rose pink bands. Photo from NICO-10-314(154 to 157m interval).

Plate 3.3

Xenoblastic grains of quartz and potassium feldspar exhibiting sutured contacts and grain size coarsening (upper field) an order of magnitude larger than adjacent non-coarsened layering (lower field). Photomicrograph of GR-10-107 taken under crossed polars.

Plate 3.4

Very fine grained band composition dominated by an ultra-fine equigranular matrix of mosaic-textured quartz and hematite-dusted potassium feldspar showing diffuse minor and trace accessory mineral content (left hemisphere) when compared to adjacent non-metasomatized layering (right hemisphere). Photomicrograph of GR-06-011W taken under crossed polars.
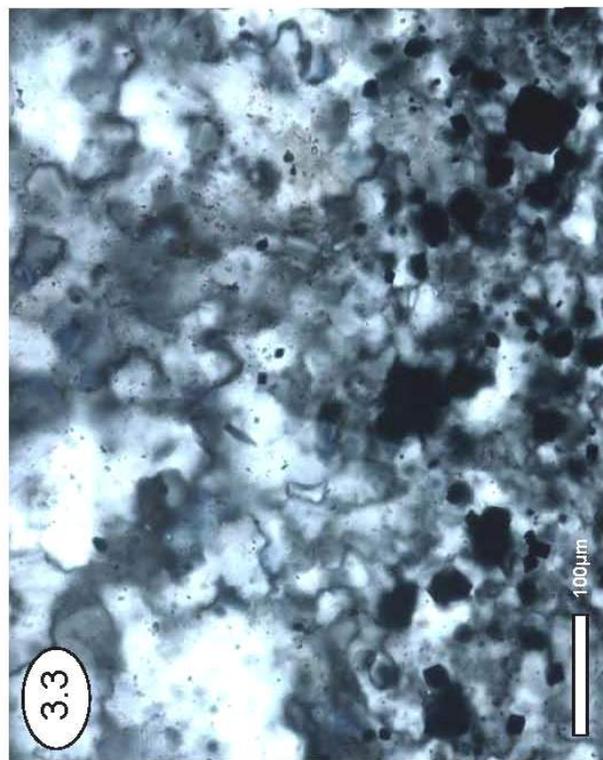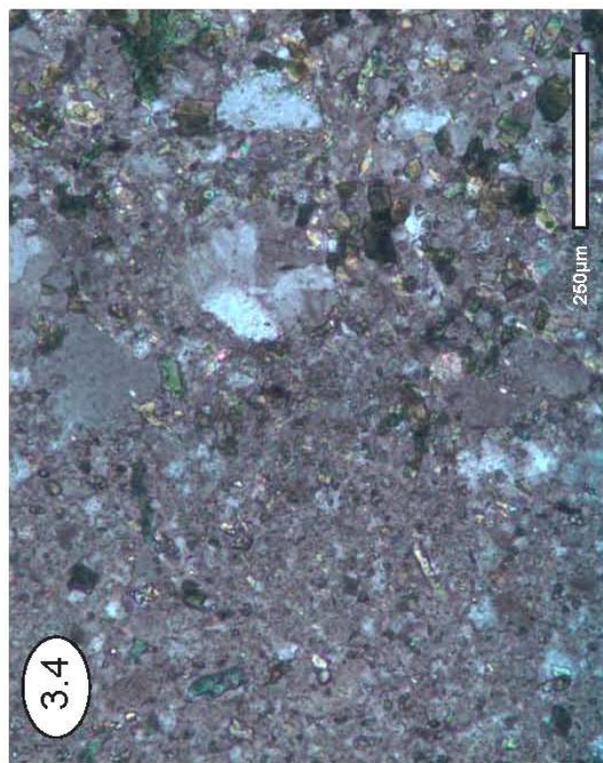
Plate 3.5

Boudinaged calc-silicate rocks interbedded within metamorphosed arenite near Peanut Lake. Photo from sample location GR-10-123.

Plate 3.6

Poikiloblastic potassium feldspar marked by moderate hematite turbidity and trace chlorite and ankerite inclusions. Partially included clinopyroxene (lower half of left hemisphere) indicates potassium feldspar was a later phase. Crisp angular boundaries exhibited by potassium feldspar enclosed within the metacrysts suggests they originated from an earlier fragmental phase (indicated by yellow arrows). Photomicrograph of GR-07-084 taken under crossed polars.

Plate 3.7

Angular grains of quartz and microcline (tartan twinning), both indicated by yellow arrows, are enveloped by a large clinopyroxene poikiloblast. Photomicrograph of GR-06-013 taken under crossed polars.

Plate 3.8

Exposure of massive meta-arenite weathered to a pale pink-brown. White edging along left of photo = 30cm. Photo taken east of the Bowl Zone.

3.6

3.8

3.5

3.7
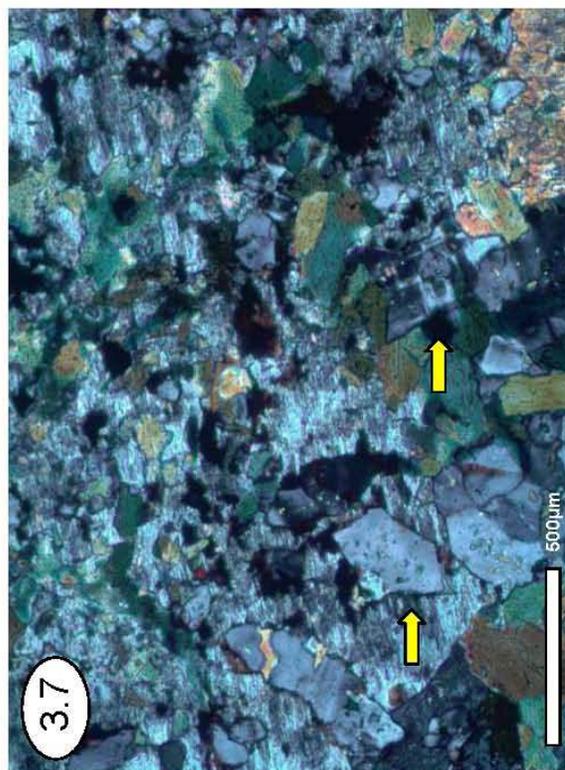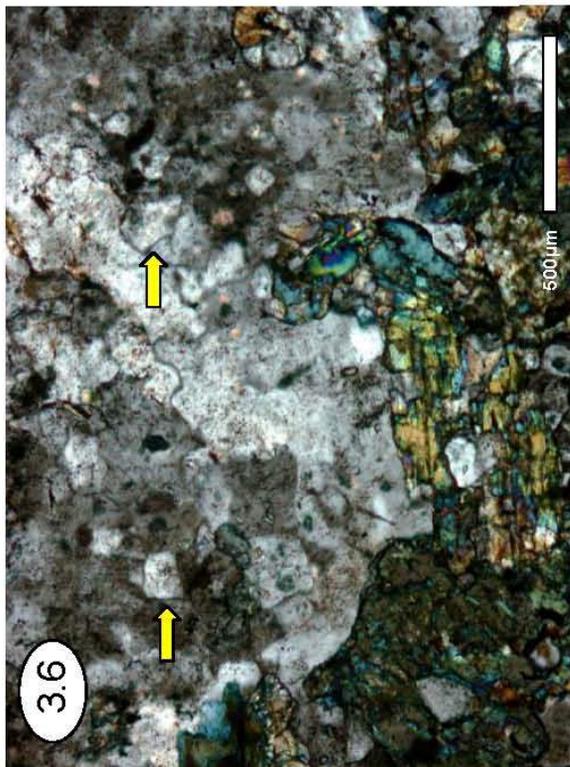
Plate 3.9

Medium grained subarenite showing a clastic composition dominated by quartz with rare microcline (tartan twinning) within a matrix of fine grained chlorite. Photomicrograph of GR-06-002W taken under crossed polars.

Plate 3.10

Pseudobrecciated layering bounded by meta-arenite observed south of Chalco Lake. Pervasive potassium feldspar replacement extends along individual layers (top hemisphere)) evidenced by elongate replacement spots that produce a pseudobrecciated appearance. Photo from sample location GR-10-141.

Plate 3.11

Grain size reduction and textural destruction of meta-arenite resulting from K-metasomatism. Here a quartz porphyroclast preserves a rolling structure suggestive of shear. Sub-grain recrystallization is evidenced at grain boundaries of the porphyroclast. Photomicrograph of GR-06-008W taken under crossed polars.

Plate 3.12

Incipient orange-pink alteration into cordierite-bearing beds observed west of Peanut Lake proximal to emplacement of a porphyry dyke. Photo from sample location GR-10-127. Hammer used for scale.
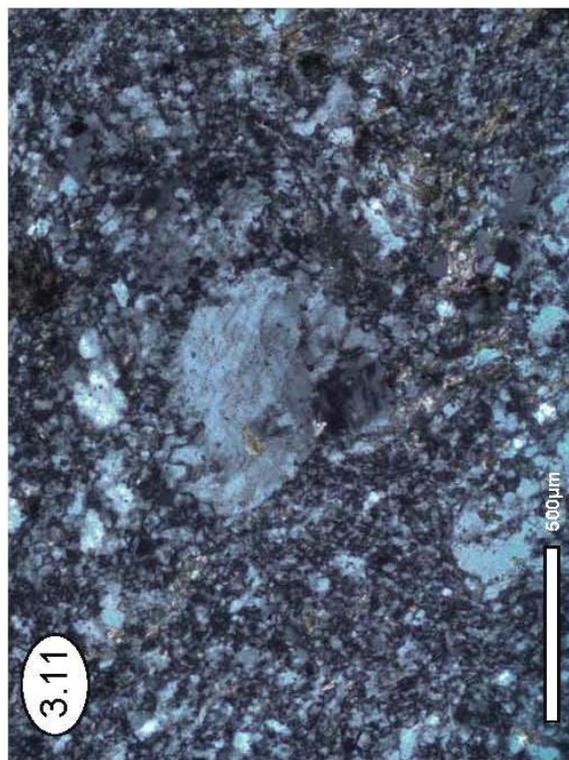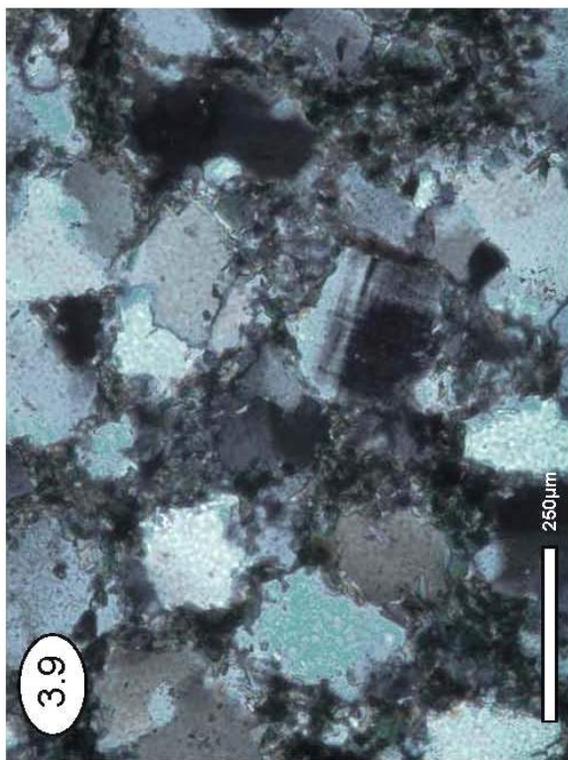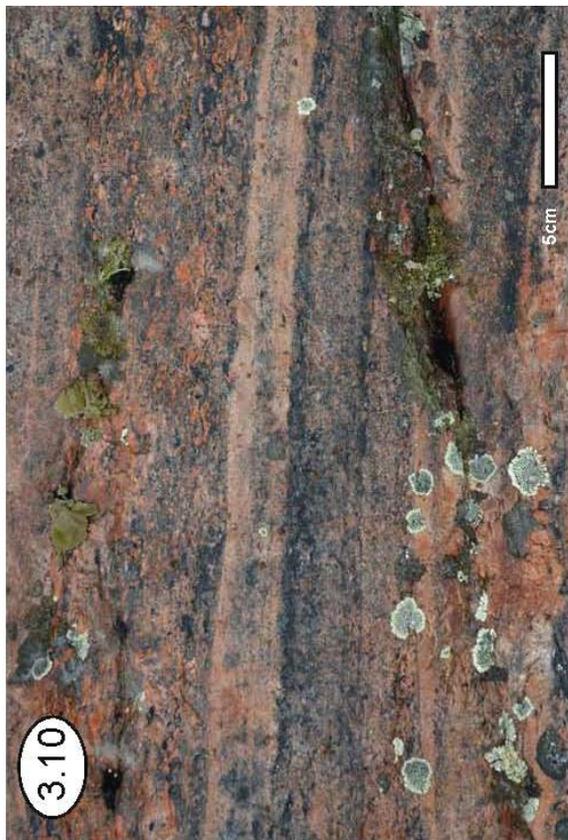
frequently developed near grain boundaries. Green-brown biotite laths range in length up to 100 μm. However randomly distributed, preferred orientations impart a subtle foliation. Microcline porphyroclasts identified by tartan twinning are similarly distributed and show grain size and shapes comparable to quartz. They have well defined boundaries suggesting textural equilibration through recrystallization. Magnetite grains range in size from 2 to 10 μm. They are evenly distributed and show characteristic triangular and trapezoidal forms. Quartzo-feldspathic layers are cemented by very fine grained phyllosilicate aggregates.

Cordierites are common within basal beds of the upper metasiltstone, identified by spherical to ovoid shapes and distinctive grey-blue color. Individual diameters range from millimeter- to centimeter-scale. Though former shapes are markedly well preserved, pervasive replacement of matrix by very fine grained phyllosilicate aggregates is ubiquitous. Pinite is distinguished by a yellowish green color. Minor quartz and magnetite porphyroclasts are preserved near former margins.

K-Metasomatism of Upper Metasiltstone

Cordierite-bearing beds proximal to porphyry dykes exhibit an incipient orange-pink alteration (Plate 3.12). This effect is best observed west of Peanut Lake where cordierite-bearing beds are interbedded with arenite. In thin section, the "pinkification" of metasiltstone matrix is marked by biotite and hematite infiltration. Invading biotite displays pleochroic dark green colors commonly masked by hematite dusting. Biotite growths form irregularly shaped mats of fine grained randomly oriented arrangement. Quartz grains remain largely unchanged within biotite growths. Hematite forms reddish brown clouds that are both concentrated with, and extend beyond, the biotite. Alteration is matrix selective, leaving relic

cordierite knots well preserved. These textures indicate cordierite formation prior to dyke emplacement.

3.3 Lou Lake Volcanic Rocks

The Lou Lake Group comprises a succession of subaerial pyroclastic and volcaniclastic rocks with an aggregate thickness of approximately 1.5 km (Gandhi et al., 1996). Ten felsic volcanic and volcaniclastic units have been recognized and described in some detail by Gandhi and Lentz (1990) and Gandhi at al. (2001). The succession can be broadly characterized as decameter-scale cooling units defined by basal crystal ash tuff that grades upward into massive to flow-banded tuff and crystal ash-flow tuffs. Using the total alkali silica classification of LeMaitre (1989), the whole rock petrochemical analysis reported by Gandhi and Lentz (1990) suggests the Lou Lake volcanic rocks range from rhyolite to dacite in composition. However, the volcanic rocks proximal to Lou Lake show anomalous secondary alkali content and the referenced classification system is unsuitable for altered rocks.

An exhaustive petrographic examination of the volcanic rock suite is beyond the scope of this study. However, the volcanic rocks that directly overlie the Treasure Lake Group show effects of K-metasomatism. Drilling by Fortune Minerals (DDH NW-00-01) intersected the basal volcanic-metasedimentary rock contact, thus provides an extended interval across the volcanic succession which exhibits the effects of variable potassium metasomatism (Figure 3.1). The boundary is marked by xenoltih-bearing basal ash tuff directly overlying weakly K-metasomatized subarkosic metasedimentary rock. The immediately overlying volcanic succession intersected by 175 meters of diamond drill core is dominated by units
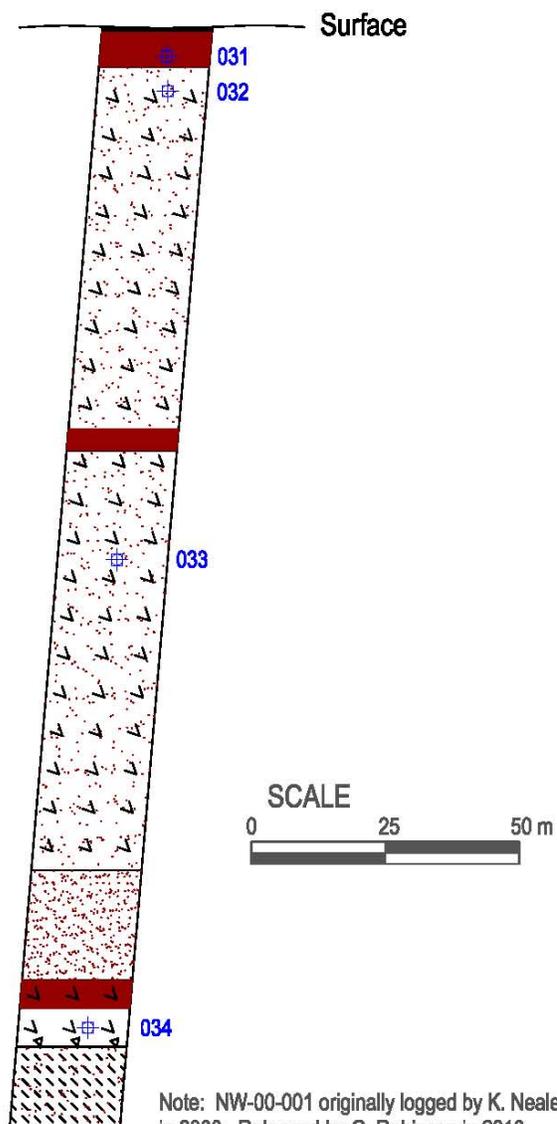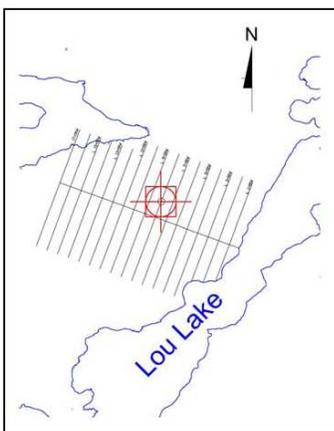
Figure 3.1 – Graphic core illustrating K-metasomatism overprinting a volcanic interval intersected by drilling (DDH NW-00-001). Inset shows location of drilling.

10's of meters thick of thinly banded plagioclase-phyric crystal ash tuff interlayered with thinner meter-scale units of massive ash tuff. Intervals of intense potassium metasomatism characterize the horizons of massive ash tuff, with extensive zones of weak to moderate pervasive potassium feldspar alteration of the crystal ash tuff. The present detailed petrographic analysis of samples selected from this interval is accompanied by whole rock geochemical analysis discussed in Chapter 4. The description of unaltered tuff is supported by additional representative samples obtained from surface outcrop north and southeast of Lou Lake. Sampled surface exposures of crystal ash and lapilli ash tuff both show variable effects of potassium metasomatism.

3.3.1 Massive and Banded Crystal Ash Tuffs

The basal crystal ash tuff of the Lou Lake volcanic field is banded to massive, and weathers to a pale grey-green (Plate 3.13). Centimeter-scale banding is marked by laminations and thin beds of ash tuff interlayered with crystal ash tuff. The tuff is predominantly ash rich with inconsistent phenocryst content and occasional centimeter-scale lapilli. Interlayered very fine-to-fine ash tuff is virtually crystal-free. Crystal-bearing beds occur as non-graded or normal graded in terms of both groundmass and crystal grain size. Phenocryst populations within these layers are comprised of variable plagioclase (1 to 6%), orthoclase (1 to 2%), biotite (<1 to 2%) and quartz (1%). Primary plagioclase and orthoclase phenocrysts indicate a rhyodacite composition.

Plagioclase is the most abundant phenocryst, generally occurring as subhedral to euhedral grains, and locally as sub-round to angular isolated grain fragments or mosaics due to in situ brecciation. Polysynthetic twinning of plagioclase exhibit tapered terminations

indicative of deformation. Plagioclase phenocrysts show limited degrees of replacement by sericite, chlorite and traces of epidote. Boundaries of plagioclase grains are generally sharp, and occasionally exhibit overgrowths of different crystallographic orientation. Such overgrowths are accompanied by mantles of coarser recrystallized potassium feldspar groundmass. Simple twinned subhedral to euhedral orthoclase phenocrysts are generally tabular, and range in size up to 2.5 mm (Plate 3.14). Crystal outlines commonly exhibit degrees of brittle fracture. These are incipiently sericitized, unzoned and distinguished by simple-twinning. Quartz occurs as rare embayed phenocrysts and equant grains with diameters up to 1 mm, and as sub-angular grains and crystal fragments. Quartz grains are weakly to moderately overprinted by sericite and very fine grained potassium feldspar.

Relict perlitic fractures show variable preservation within both ash and crystal-bearing beds. These textures range from concentric arcuate to elongate and sub-parallel, and typically originate from devitrification of glass. Here they are typically altered to quartz and lined with very fine grained chlorite or sericite. Fine-grained pleochroic green chlorite also occurs as an alteration of biotite phenocrysts. These align parallel to primary bedding within elongate anastomosing aggregates. Relics of euhedral tabular biotite phenocrysts are pseudomorphed by chlorite rich in opaque inclusions. Magnetite and ilmenite occur as anhedral to euhedral accessories within the elongate mafic aggregates, as well as inclusions within the remnant biotite.

K-Metasomatism of Crystal Ash Tuff

Though metasomatic effects within the crystal ash and ash tuff are variable, the volcanic succession intersected by DDH NW-00-01 shows pervasive metasomatic

replacement is best developed within intervals of ash tuff. This is evidenced by massive salmon pink to brick red rock generally confined to stratigraphic units lacking phenocrysts. Crystal ash tuff overlying the immediate metasedimentary-volcanic boundary is markedly unaltered. Groundmass of metasomatized horizons are predominantly comprised of ultra-fine potassium feldspar (75 to 85%) with minor quartz (8 to 12%), trace magnetite (<1%), ilmenite (<1%) and pyrite (<1%), and local porphyroblasts of ankerite (<1%).

Plagioclase phenocrysts exhibit partial to nearly complete replacement by fine grained incipient potassium feldspar. Though diffuse grain boundaries are overprinted by recrystallized groundmass, polysynthetic twinning is preserved. Limited replacement of orthoclase results in the preservation of sharp boundaries and incipient fine grained recrystallization within phenocryst cores. Biotite phenocrysts are inferred by the preservation of tabular-shaped fine grained chlorite + magnetite aggregates. Very fine grained halos of ultrafine hematite commonly infiltrate into groundmass along biotite boundaries. Quartz characteristically marks the most resistant phase, with replacement limited to local overprinting by fine grained potassium feldspar.

Pervasive potassium feldspar replacement results in completely adularized sheafy textured groundmass (Plate 3.15). The randomly oriented potassium feldspar is ubiquitously ultra-fine to very fine grained. A pseudo-microbrecciated appearance results from coarser grained potassium feldspar replacement along anastomosing microbrecciated boundaries. Recrystallization is evidenced by the development of diffuse grain boundaries detected by optical discontinuities within the coarser masses. These larger grains exhibit triple point boundaries indicative of local textural equilibrium (Plate 3.16). Pervasive chloritization and infiltrational sericitization of phenocrysts and groundmass suggest retrogressive alteration

overprints during post-potassium metasomatism cooling. Ankerite porphyroblasts occur as rare rhombs within chlorite and sericite altered groundmass.

Locally, perlitic fractures are suggested by coarser grained aggregates of potassium feldspar and quartz. These are partially outlined by chlorite and exhibit strong pervasive infiltration by very fine grained sericite within concentric interstices. Commonly, evidence for perlitic fractures is ambiguous where obscured by pervasive sericite alteration of the groundmass. Locally intense sericitization is generally oriented parallel to bedding. Groundmass within crystal-bearing units is also moderately sericitized. Hematite occurs as micron-sized inclusions and local patches within the groundmass.

3.4 Local Intrusive Rocks

Massive plagioclase-phyric porphyry occasionally intersected by drilling has been variably identified as subvolcanic or porphyritic volcanic rock. However, drill intersections southeast of Lou Lake (DDH NICO-10-317) show plagioclase-phyric porphyry sills intrusive to metasedimentary rock. Therefore they are described here as a porphyritic intrusions. Sill intersections illustrated on the cross section for NICO grid line 14+50W demonstrate emplacement was both concordant and discordant to metasedimentary layering (Figure 3.2 – back pocket). No surface outcrops are documented and the overall extent of plagioclase-phyric porphyry is not known. However, texturally similar enclaves are variably preserved within potassium feldspar metasomatite. Both the enclaves and sills exhibit pervasive alteration, though sills show greatest intensity of replacement at boundaries. Replacement is marked by pronounced colour change from least altered brown groundmass to pink or reddish brown (Plate 3.17). Border zones between dacite porphyry and amphibolitic rock exhibit a

Plate 3.13

Beds of gently dipping massive grey-green ash tuff hosting a volcanic bomb (center of image). Photo from sample location GR-10-130D located on the north side of Lou Lake. Hammer used for scale.

Plate 3.14

Simple twinned subhedral to euhedral orthoclase phenocrysts from crystal ash tuff beds. Photomicrograph of GR-06-034 taken under crossed polars.

Plate 3.15

Adularized sheafy textured groundmass where potassium feldspar replacement is most pervasive. Photomicrograph of GR-06-029 taken under crossed polars.

Plate 3.16

Coarser grained secondary potassium feldspar incipient into microbrecciated layering. Well developed triple point boundaries are indicative of local textural equilibrium. Photomicrograph of GR-06-028 taken under crossed polars.
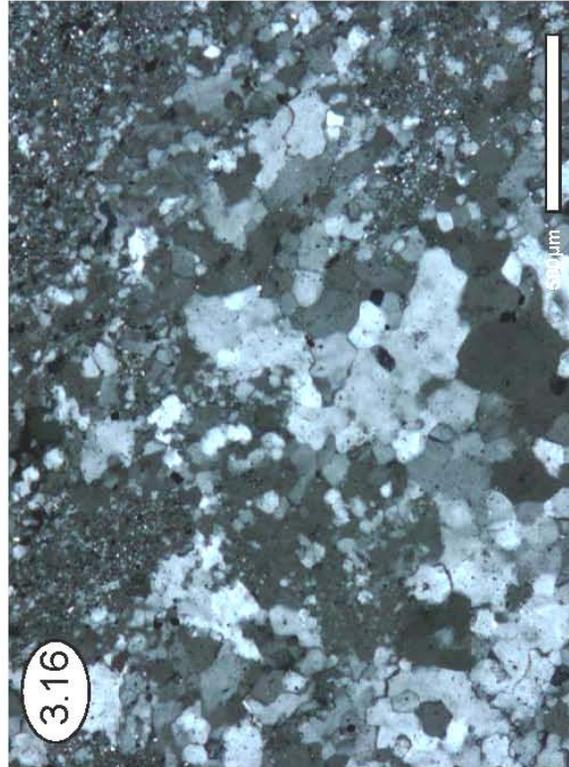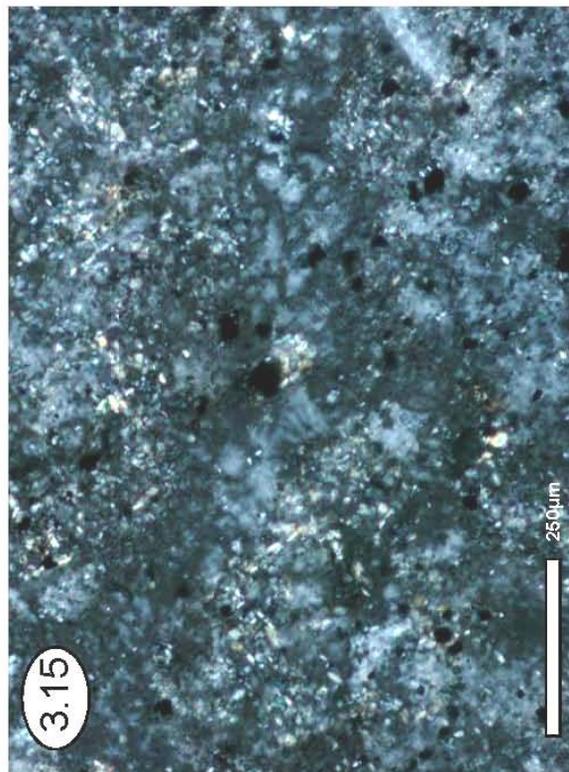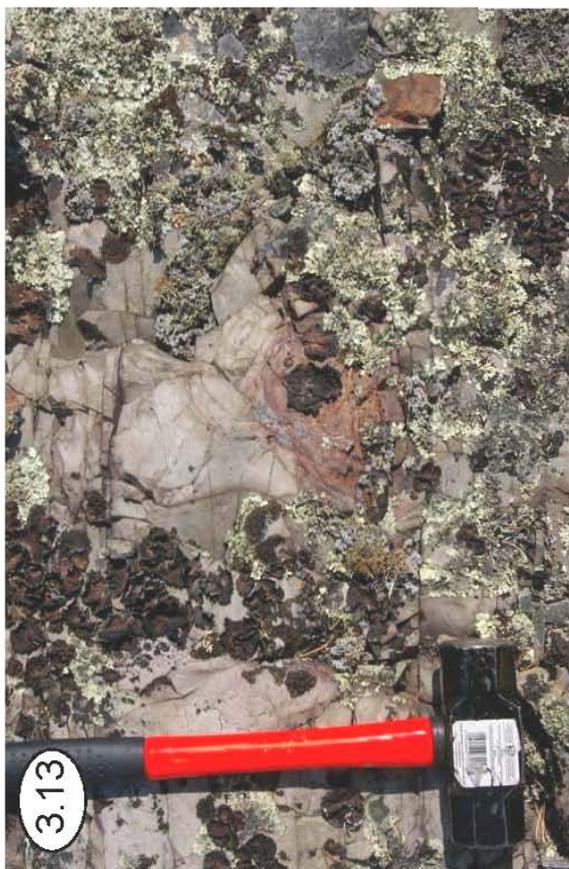
complex interface gradational on a centimeter to decimeter scale marked by complex permeation textures suggesting sill emplacement syn-amphibolite facies conditions. A pre-metasomatite emplacement for the plagioclase-phyric porphyry is clearly indicated by fragments of the latter hosted by the former.

A suite of vertical to sub-vertical porphyry dykes south of Lou Lake trend east-southeast to west-northwest. They range in thickness from less than a meter to over 50 meters, and individual dykes can be traced along strike for over a kilometer. The dykes vary widely in terms of phenocryst abundance, with individual dykes distinguishable by phenocryst grain size and population density. Dykes are commonly identified as quartz, quartz-feldspar, feldspar, and feldspar-amphibole porphyry. In weathered orange to orange-pink exposures, quartz and quartz-feldspar porphyries are distinguished from feldspar-phyric varieties by prominent "quartz eyes" as illustrated in Plate 3.19. In thin section they are distinguished by quartz phenocryst abundance. Field relationships between quartz-phyric and feldspar-phyric intrusives demonstrate the quartz-phyric variety is an earlier generation as these are clearly cross-cut by later feldspar porphyry.

All varieties of quartz- and feldspar-phyric dykes are discordant to the metasedimentary rocks of the Treasure Lake Group and intrusive into potassium feldspar metasomatite. Dyke contacts with meta-arenite are sharp and show no evidence of chilling or baking. Contacts with amphibolitic or calc-silicate rock are commonly marked by intensification of potassium feldspar replacement along immediate boundaries and show permeation effects or infiltration into bordering rock. Dyke contacts with potassium feldspar metasomatite typically exhibit a similar intensification of potassium feldspar and hematite within the endocontact of the porphyry as demonstrated in Plate 3.21, with comparable

replacement extending into exocontact zones developed in wall rocks. Where feldspar-phyric porphyry intrudes dacite enclaves hosted by metasomatite, contacts are sharp and lack apparent potassium feldspar replacement.

Dyke boundary relationships are most clearly demonstrated along decline cross-cuts (Figure 3.3 – back pocket). Here, feldspar porphyry dykes are immediately bordered by hydrothermal breccia within the enveloping metasomatic aureole. Though brecciation generally appears monolithic due to pervasive potassium feldspar and hematite replacement of fragment matrix, where replacement is less intense, heterolithic brecciation is more readily recognized. Where quartz-phyric dykes intrude similar brecciation, chilled margins are exhibited (Plate 3.19). Brecciation is characterized by a fine grained to aphanitic matrix with a highly variable composition of amphibole ± clinopyroxene ± biotite ± magnetite. Fragments are angular to sub-angular, light pink to reddish brown and range in size on a centimeter to decimeter scale. Brecciation transitions from crackle brecciated metasomatite margins through fragment-rich matrix-supported to fragment-poor matrix-dominant domains.

3.4.1 Plagioclase-phyric Porphyry

Fine crystalline groundmass with primary phenocryst populations showing dominance of plagioclase over alkali feldspar is characteristic of dacite porphyry dykes. These rocks have a high proportion of groundmass with phenocrysts marked by plagioclase (6 to 8%) and trace orthoclase (<1%) with relic ferromagnesium minerals (1-2%).

Plagioclase phenocrysts are subhedral to euhedral. Those in least altered core samples show preservation of sharp well defined grain boundaries. They have a continuous range of grain size up to 2 mm in diameter. Individual grains are generally isolated and randomly

oriented; glomerocrysts are rare and appear fragmental. Most exhibit either Carlsbad or Pericline polysynthetic twinning but occasionally are untwinned. Both Carlsbad and Pericline twins are indicative of intermediate plagioclase composition; however this has not been verified by electron microprobe. Tapered and stepped Carlsbad twin terminations are common, the former indicative of deformation. Larger grains exhibit micropoikilitic textures, hosting chadacrysts of biotite, amphibole, magnetite and apatite.

The simply twinned orthoclase grains form euhedral tablets with diameters similar to plagioclase. These are micropoikilitic, including biotite, amphibole, quartz and apatite, and are variably dusted with reddish brown hematite. Boundaries are poorly preserved due to sub-grain development along margins.

Relict ferromagnesium minerals are suggested by fine grained bladed and diamond shaped aggregates of biotite, amphibole and magnetite. The 56° and 124° angularity exhibited by rare bladed shapes is indicative of former amphibole. Relic amphibole grains within these aggregates are pleochroic green and yellow-green. They are readily identified by high relief and characteristic cleavage. Randomly oriented fine-grained green-brown biotite and very fine-grained granular magnetite overgrow these aggregates. Both the mafic aggregates and the dacite groundmass are weakly altered by chlorite.

K-Metasomatism of the Dacite Porphyry Sills

Potassium metasomatism of the dacitic sills is most strongly developed near sill margins, however microscopically these effects appear less pronounced than similar replacement described for other volcanic rock or porphyry dykes. Diffuse phenocryst boundaries result from recrystallized groundmass overprinting plagioclase margins. Where

grains are transgressed, grain morphologies are irregular and twinning is simple or indistinct (Plate 3.18). Fine grained calcite form randomly as intergrowths within the plagioclase-rich groundmass. Less commonly calcite occurs as partial overgrowths at phenocryst margins.

Polymineralic aggregates are conspicuous within the alteration envelope. These occur within feldspar cores mantled by quartz, ankerite and recrystallized groundmass, or as irregularly shaped clots of quartz with sub-round feldspar phenocryst relics, ankerite and chlorite. The feldspar cores and relics are untwinned and of an indeterminate composition. Overprinting of quartz and feldspar margins by groundmass is common. Quartz is characterized by lobate interdigitating boundaries. Rare triple point junctions suggest textural equilibrium was locally achieved. Chlorite forms bundles of radiating fibres readily identified by anomalous bluish interference colours which signify an iron-rich composition. The fine grained ankerite component is distinguished by colourless grains with high birefringence and moderate relief. Ankerite aggregates are commonly widespread within altered groundmass.

3.4.2 Quartz and Quartz-Feldspar-phyric Porphyry

Quartz-phyric porphyry dykes demonstrate variable feldspar phenocryst distributions in outcrop but appear relatively uniform in thin section. Phenocryst populations of quartz porphyries are characterized by orthoclase (<5 to 20%), quartz (5 to 10%), plagioclase (<2 to 5%), biotite (2 - 5%), and rare amphibole pseudomorphs (1-3%). These porphyries are locally glomeroporphyritic with polymineralic aggregates of orthoclase, quartz and plagioclase. The brown-pink groundmass is microcrystalline and composed of very fine grained orthoclase with traces of albite and quartz. Minor and trace mineral species include primary magnetite and apatite with secondary hematite and chlorite.

Simple twins readily distinguish orthoclase from other feldspars. Orthoclase phenocrysts are inequigranular, subhedral to euhedral, and range from <1 to 9 mm in diameter. These feldspars have inclusion-rich cores and are commonly overgrown by weakly included untwinned albite. Coarse-grained orthoclase is characterized by poikilitic texture, commonly enclosing fine-grained chadacrysts of orthoclase and inclusions of biotite, quartz and apatite. Apatite inclusions are colourless to weakly blue coloured, euhedral to subhedral with elongate habit. More rarely, inclusion-free cores are marked by strongly included margins. Orthoclase is commonly partially altered to sericite, with sericitization occurring both uniformly distributed and concentrated within grain cores.

Quartz phenocrysts range from <1 to 19 mm, with a median diameter of 8.7 mm. These are typically "eye-shaped" and granular, though equant hexagonal grains are not uncommon in the coarser population. Undulatory extinction is ubiquitous, indicating variable degrees of strain. Quartz phenocrysts are generally embayed by groundmass suggesting disequilibrium with the melt.

Plagioclase phenocrysts are subhedral to euhedral with tabular grains exhibiting rectangular cross-sections. Diameters range from <1 to 5 mm. These exhibit polysynthetic twinning with abrupt and tapered terminations, and sector extinctions. Plagioclase phenocrysts are generally inclusion-rich and apparently lack the overgrowth textures and multiple zoning of orthoclase. Occasional grains show incipient replacement to potassium feldspar (Plate 3.20). Sericite alteration of plagioclase occurs both uniformly distributed or localized within grain cores.

Dark brown to tan pleochroic biotite phenocrysts range from <1 to 9 mm in diameter.

Grains occur as tabular forms or with irregular outlines. Coarser laths commonly exhibit kink-bands indicated by bends in the cleavage and wavy extinction. They are typically mantled by very fine grained randomly oriented platy chlorite, and locally by fine grained quartz fibres perpendicular to grain margins. Complete topotactic replacement to pleochroic green chlorite is common. Rare zircon inclusions give rise to pleochroic haloes.

Rare amphibole pseudomorphs range from <1 to 2mm. The pseudomorphs are identified by anomalous brown pleochroic chlorite demonstrating preservation of characteristic 56° and 124° cleavage of amphibole. Amphibole pseudomorphs are generally mantled by randomly oriented pleochroic green chlorite. These fine grained aggregates of biotite and chlorite form irregularly-shaped clots and streaks within the groundmass may also represent replaced amphibole. They are partially bordered by halos of earthy hematite inclusions, though similar "clouds" of hematite populate the groundmass showing no apparent association to other phenocrysts. Locally, discrete magnetite grains comprise a small fraction of the mafic aggregates.

3.4.3 Feldspar (± Amphibole ± Quartz)-phyric Porphyries

Phenocryst populations of feldspar-phyric porphyries vary greatly. They are typified by albite (<5 to 15%), orthoclase (<5 to 10%), biotite (2 to 10%), amphibole pseudomorphs (<2 to 5%), and quartz (0 to 5%). These porphyries are locally glomeroporphyritic with monomineralic glomerocrysts of feldspar or quartz, and polymineralic cumulocrysts of feldspar, quartz, and biotite. Domains of fragmental feldspar phenocrysts are common proximal to sheared contacts. The microcrystalline groundmass is composed of very fine grained, equigranular orthoclase with traces of albite and quartz. Minor and trace mineral

species include primary ilmenite, magnetite and apatite, and secondary chlorite, sericite, and hematite. Groundmass coloration varies from purple-grey dyke cores to pink-brown margins, characteristic of the potassium feldspar metasomatized endocontact zone (Plate 3.21). This colour variation is due primarily to an increased concentration of earthy hematite and chlorite inclusions toward dyke margins. Otherwise very fine grained chlorite occurs as fine grained aggregates or as inclusions with a relatively uniform distribution throughout the porphyry groundmass.

Albitic plagioclase phenocrysts occur as both anhedral and euhedral grains ranging from <1 to 11 mm in diameter. Coarser phenocrysts commonly exhibit characteristic polysynthetic twinning with tapered terminations indicative of deformation. Twinning is generally absent in finer grains. Multiple-zoned phenocrysts are not uncommon, and thin overgrowths of very fine grained untwinned albite are typical. The fine-to-medium grained plagioclase grains are usually inclusion-rich, and local inclusions of potassium feldspar are typical within the albitic rind. Albite phenocrysts are variably altered by domains of potassium feldspar replacement. Locally, plagioclase phenocrysts are saussuritized with patchy fine-grained aggregates of epidote, albite and sericite.

Simple twinned orthoclase phenocrysts are inequigranular and seriate-textured with diameters ranging from <1 to 11 mm. Though grain size variability is markedly evident in thin section, local equigranular populations are generally finer grained and more densely populated. Coarser phenocrysts are mostly euhedral, while finer grained phenocrysts range from anhedral to euhedral. Where richly included with hematite, orthoclase phenocrysts have cloudy to extremely turbid cores. Conversely, chlorite inclusions show greatest concentrations toward phenocryst margins. Orthoclase less commonly exhibit "rapakivi-like"

Plate 3.17

Interval of dacite porphyry from drill core showing variable effects of K-metasomatism. Pervasive replacement results in salmon pink ground mass. Incipient pale or dark pink potassium feldspar infiltrates along the selvage of cross-cutting biotite veinlets. Photo from DDH NICO-10-317 118.0 to 121.0 m interval.

Plate 3.18

Diffuse grain boundaries result from secondary K-feldspar overprinting plagioclase and feldspar phenocrysts during K-metasomatism. The margins of this simple twinned feldspar are heavily corroded from recrystallization of the groundmass. Photomicrograph of GR-10-151 taken under crossed polars.

Plate 3.19

Orange weathered exposure of quartz-phyric porphyry (top hemisphere) distinguished by the development of 'quartz eyes'. Here the porphyry exhibits a chilled margin against monolithic hydrothermal breccia (lower hemisphere). Photo taken north of Whale Lake.

Plate 3.20

Partial replacement of plagioclase lath by secondary potassium feldspar. Sericite, distinguished by high birefringence, invades the plagioclase core. Photomicrograph of GR-10-149 taken under crossed polars.

3.18

3.20

3.17

3.19
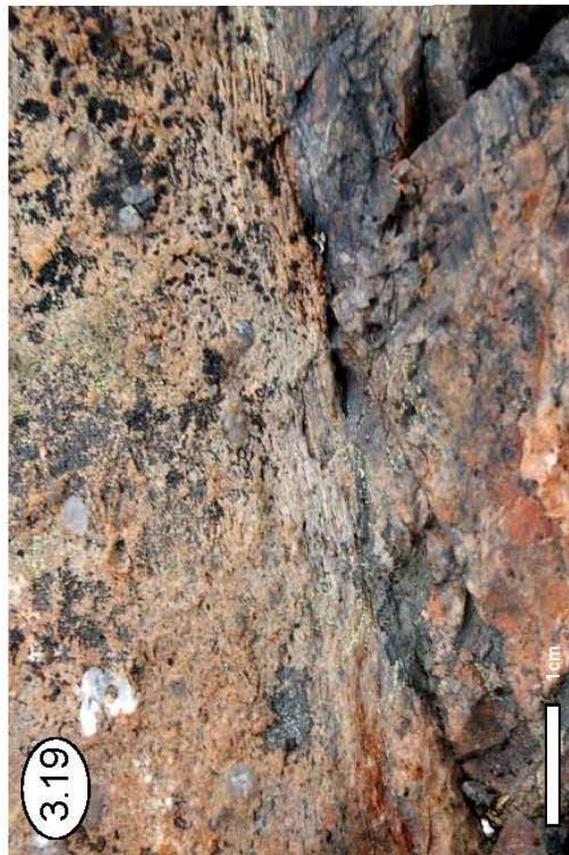
Plate 3.21

Intense K-feldspar + hematite replacement developed within the endocontact zone (upper hemisphere) of feldspar-phyric porphyry (lower hemisphere) as revealed by decline cross-cuts. Photo taken from sample location GR-06-005W.

Plate 3.22

Pseudomorphous replacement of amphibole phenocryst from feldspar porphyry. Hematite is demonstrably concentrated along the grain boundary. Photomicrograph of GR-06-024W taken under plane polarized light.

Plate 3.23

Very fine grained potassium feldspar transgresses the margins of a quartz phenocryst (approaching extinction, top right of photo) as a result of K-metasomatism. Photomicrograph of GR-06-005E taken under crossed polars.

Plate 3.24

Quartz phenocryst within very fine grained matrix of secondary K-feldspar typical of endocontact K-metasomatism of feldspar porphyry. Their preservation distinguishes pervasively replaced porphyry from altered wall rocks. Photomicrograph of GR-06-015E taken under crossed polars.

3.22

3.24

3.21

3.23
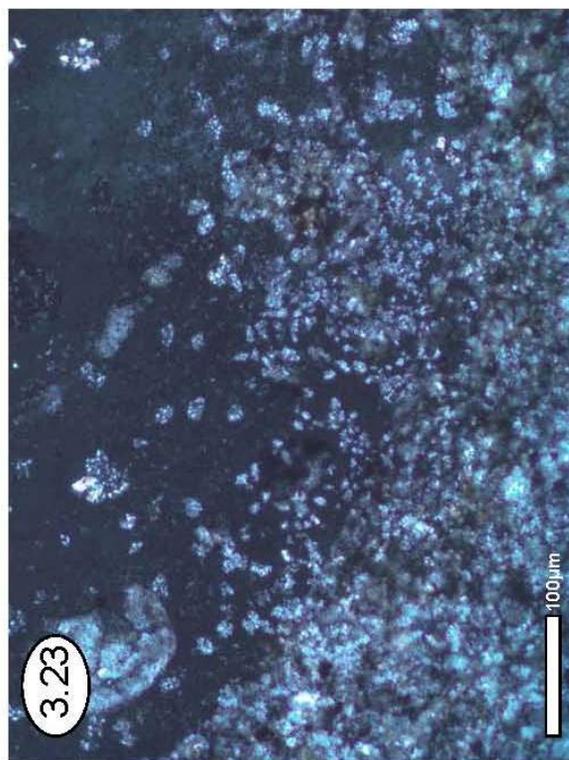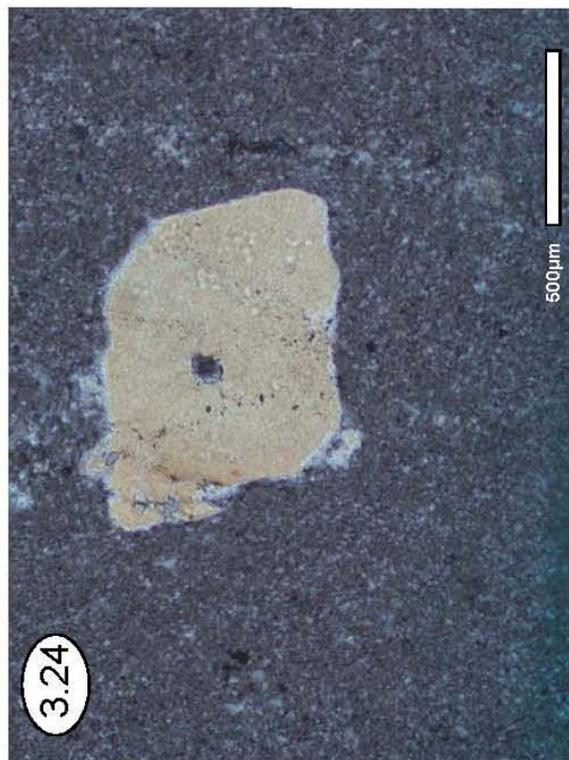
mantles of fine grained untwinned albite. Incipient sericitization of orthoclase phenocrysts is ubiquitous.

Inclusions within the feldspar population include chadacrysts of apatite, Ti-biotite, chlorite, and sericite. Apatite forms strongly blue-coloured euhedral to subhedral elongate prismatic very fine grained inclusions with hexagonal cross-sections. Ti-biotite inclusions are generally pale brown-red grains. Light green pleochroic chlorite inclusions exhibit scaly to platy habits. Sericite alteration is incipient along feldspar cleavage.

Amphibole phenocrysts are commonly pseudomorphed by anomalous green-brown pleochroic biotite (Plate 3.22). Pseudomorphed grains range in size between <1 and 5 mm, and are typically mantled by randomly oriented platy chlorite. Pseudomorphs are distinguished from other biotite grains by the preserved 56° and 124° cleavage and more rarely by well preserved prismatic shape and diamond cross sections. Relic amphibole occurring within fine grained aggregates of biotite, chlorite, magnetite and martite show characteristic blue-green coloration and 56° and 124° cleavage. Macroscopically, these aggregates appear as streaks and clots of fine grained shreddy biotite.

Quartz content is variable within feldspar-phyric porphyries. This variation is exemplified within individual dykes where quartz is locally present or absent. Where present, quartz "eyes" are fine-to-coarse grained and inequigranular. At surface these quartz eyes are indistinguishable from those evidenced by quartz-phyric dykes. Quartz grains exhibit undulose extinction, and are moderately to strongly embayed with matrix.

Pleochroic dark brown to tan biotite phenocrysts occur as subhedral tabular grains that measure <1 to 6 mm. Microprobe analysis has identified the phenocryst species as Ti-rich

annite, though these exhibit margins compositionally lower in Ti and higher in Al. Similarly lower Ti annite laths occur as very fine grained streaks and aggregates. Very fine grained ilmenite occurs along phenocryst cleavage planes. Partial to complete overprinting of biotite by pleochroic pale green to olive green chlorite is ubiquitous.

K-Metasomatism of Quartz and Feldspar-phyric Porphyry Dykes

Both quartz and feldspar-phyric porphyry dykes exhibit endocontact zones characterized by pronounced mineralogical and textural modification from less altered porphyry into massive potassium feldspar metasomatite (Plate 3.21). Observations suggest the scale of these zones is highly variable and inconsistent even within a single dyke. Drill core intersections reveal obvious endocontact replacement ranges from encompassing a small fraction of overall dyke thickness to complete dyke replacement. At surface this results in ambiguous dyke–metasomatite boundaries.

In thin section, endocontact metasomatism is typically marked by gradational alteration from recognizable porphyry textures and mineralogy outward to pervasive textural destruction and mineralogical replacement at dyke margins. Though porphyry textures and grain shapes are largely preserved within the transition, albite and plagioclase phenocryst compositions are typically completely replaced by finer grained aggregates of potassium feldspar. The degree of modification is clearly illustrated by a modal change to >95% potassium feldspar. The crystallinity of this secondary potassium feldspar is best recognized at high magnification due to extreme hematite turbidity. Quartz demonstrates a strong resistance to replacement, though infiltration at margins of select phenocrysts is evidenced (Plate 3.23). Biotite is similarly poorly preserved through the transition, being replaced by

very fine grained mafic aggregates of Fe-rich biotite, chlorite, magnetite and/or hematite. Groundmass shows increasing uniformity toward a very fine grain size indicative of recrystallization. Intensification of hematite with grain size reduction is ubiquitous. The relatively uniform groundmass distribution of chlorite within least-altered dyke cores and cross-cutting of endocontact zones evidenced by veins of similar chlorite species indicate chloritization post-dates K-metasomatism of the porphyries.

Recognition of a porphyry protolith is most ambiguous within the endocontact zones at dyke margins. Replacement intensity here is best illustrated by nearly complete destruction of porphyry textures and the homogenization of groundmass to very fine grained potassium feldspar. Though fine grained blasts of quartz and ankerite locally persist, the rare preservation of quartz phenocrysts best distinguishes the porphyry endocontact from the exocontact zone developed within adjacent wall rocks (Plate 3.24). These relict quartz grains occasionally exhibit sub-grain development along margins indicating partial recrystallization.

3.5 Potassium Feldspar Metasomatite

Potassium feldspar metasomatite is prominently exposed as very fine grained reddish-brown to pink rock south-east of Lou Lake (Plate 3.25). It occurs in three general areas illustrated in Figure 3.4; between Summit Lake and Chalco Lake, south-west of the Grid Lakes, and north of Whale Lake. Though Summit Lake rocks have been historically recognized as basal Lou Lake volcanic assemblage, their anomalous potassium content and a mineral assemblage dominated by potassium feldspar (>90%) are indicative of pervasive metasomatic replacement. They are thus described here as metasomatite. At Summit, the metasomatite is largely massive-to-banded with a cherty red-to-maroon color. Drilling here
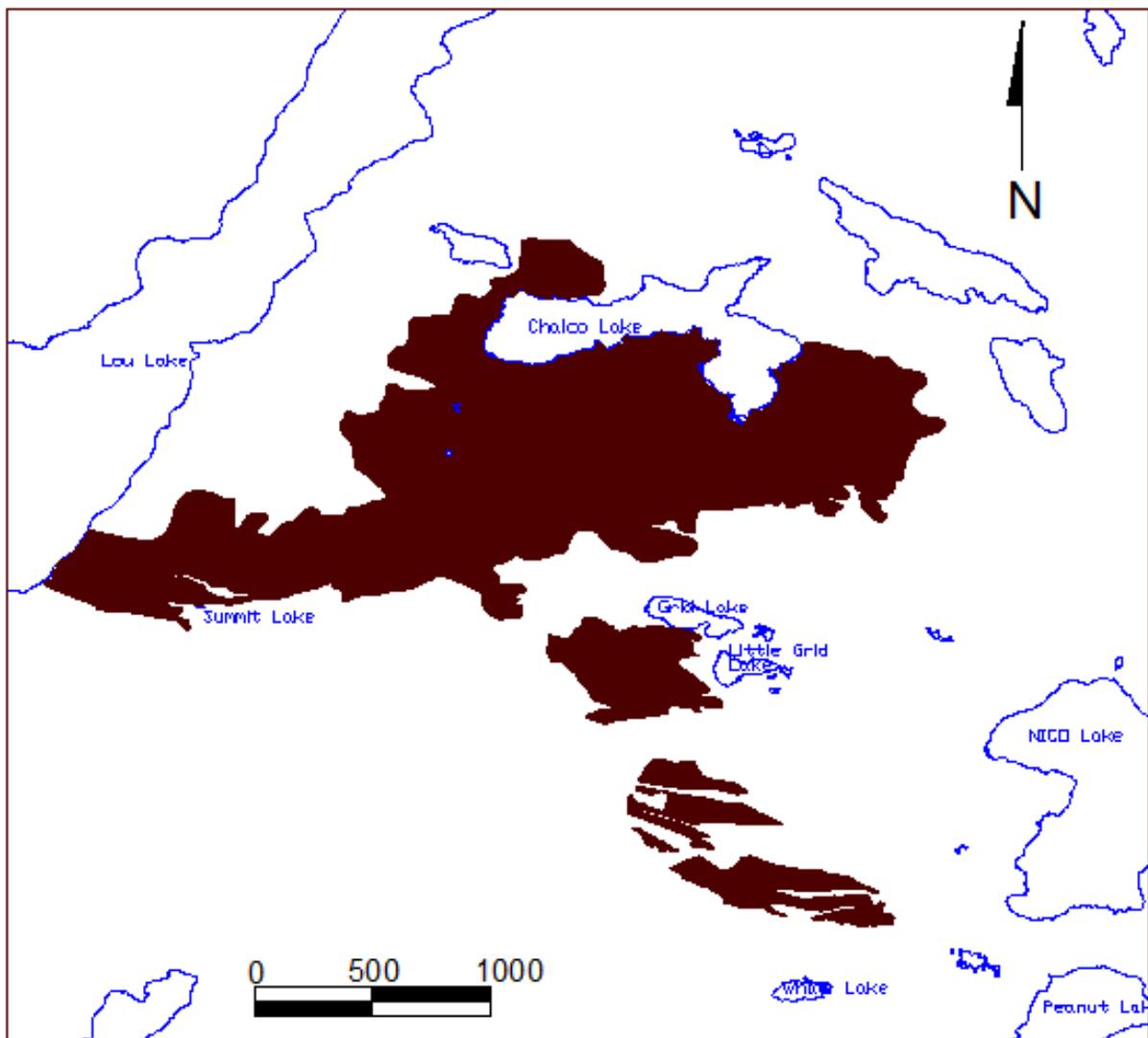
Figure 3.4 – General location of potassium feldspar metasomatite.

by Fortune Minerals (DDH NICO-96-01 to 03) demonstrated that the potassium feldspar metasomatite discordantly overlies altered Treasure Lake greywacke and siltstone. Locally at Summit, the metasomatite has been brecciated and mineralized with chalcopyrite ± pyrite ± bornite.

West of the Grid Lakes and south of Chalco Lake, the potassium feldspar metasomatite is predominantly non-banded and marked by locally unique heterogeneities, including: (i) weakly magnetic zones characterized by a concentration of magnetite aggregates (Plate 3.26); (ii) "bleached" micro- and macro-domains, occurring locally west of Grid Lake (Plate 3.27); and (iii) brecciated metasomatite hosting chalcopyrite mineralization south of Chalco Lake (Plate 3.28). Here, the contact between underlying metasedimentary rock and potassium feldspar metasomatite revealed in drill core (DDH NICO-10-325) is characterized by extensive heterolithic brecciation up to 25 meters in thickness. As illustrated in the cross section for NICO grid line 21+00W (Figure 3.5), this disaggregation regime is commonly overprinted by K-metasomatism.

North of Whale Lake, massive potassium feldspar metasomatite directly overlies amphibolitic and metapsammitic units of the Treasure Lake Group. Here the metasomatite is discordant to metasedimentary layering and is intruded by several generations of porphyry dykes. Metasomatite-metasedimentary contacts are either characterized by permeation effects or brecciation. The former contaminated boundaries are indicative of high temperature interaction between adjacent chemically different replacement regimes. Revealed in drill core, they occur solely between metasomatite and amphibolitic rock (DDH NICO-10-317). Brecciated contact relationships intersected by drill core are complex. These typically transition from crackle-brecciated metasomatite margins into matrix-supported monolithic

brecciation over thicknesses up to a meter (DDH NICO-10-296). Brecciated metasomatite is indicative of brittle deformation post-metasomatite formation. Here sharp amphibolite interfaces against metasomatite fragments indicates brecciation occurred under amphibolite facies conditions. Such interfaces between amphibolitic rock and metasomatite exhibited in the decline reveals contradictory evidence. Here fragments of amphibolitic rock are hosted within metasomatite matrix and metasomatite relics are hosted by amphibole matrix, indicating coeval replacement regimes.

Brecciated and strongly replaced relics exhibiting fine spotted textures occur within the expanse of metasomatite north of Whale Lake (Plate 3.29). These patches are commonly recognized at surface and intersected by drill core (DDH NICO-10-313). Textural and mineralogical characteristics determined microscopically are ambiguous, supporting either a greywacke or volcanic protolith. As such, these features are described here as relict domains within pervasive potassium feldspar replacement.

3.5.1 Banded Potassium Feldspar Metasomatite

Banded potassium feldspar metasomatite occurs in several localities but is best developed at Summit Lake where many have interpreted it as flow-banding (Gandhi and Lentz, 1990; Gandhi et al., 1996; Goad et al., 2000 and 2001; Sidor, 2001). It exhibits well developed compositional laminations characterized by fine-grained parallel streaks and discontinuous lenses defined by hornblende + biotite + quartz ± magnetite ± pyrite ± chalcopyrite. These mafic laminations measure less than a mm to several mm's thick, and are variably spaced on a millimeter to centimeter scale. Their megascopic appearance is a result of a gradational patchiness produced by the distribution of the ferromagnesian species. In thin
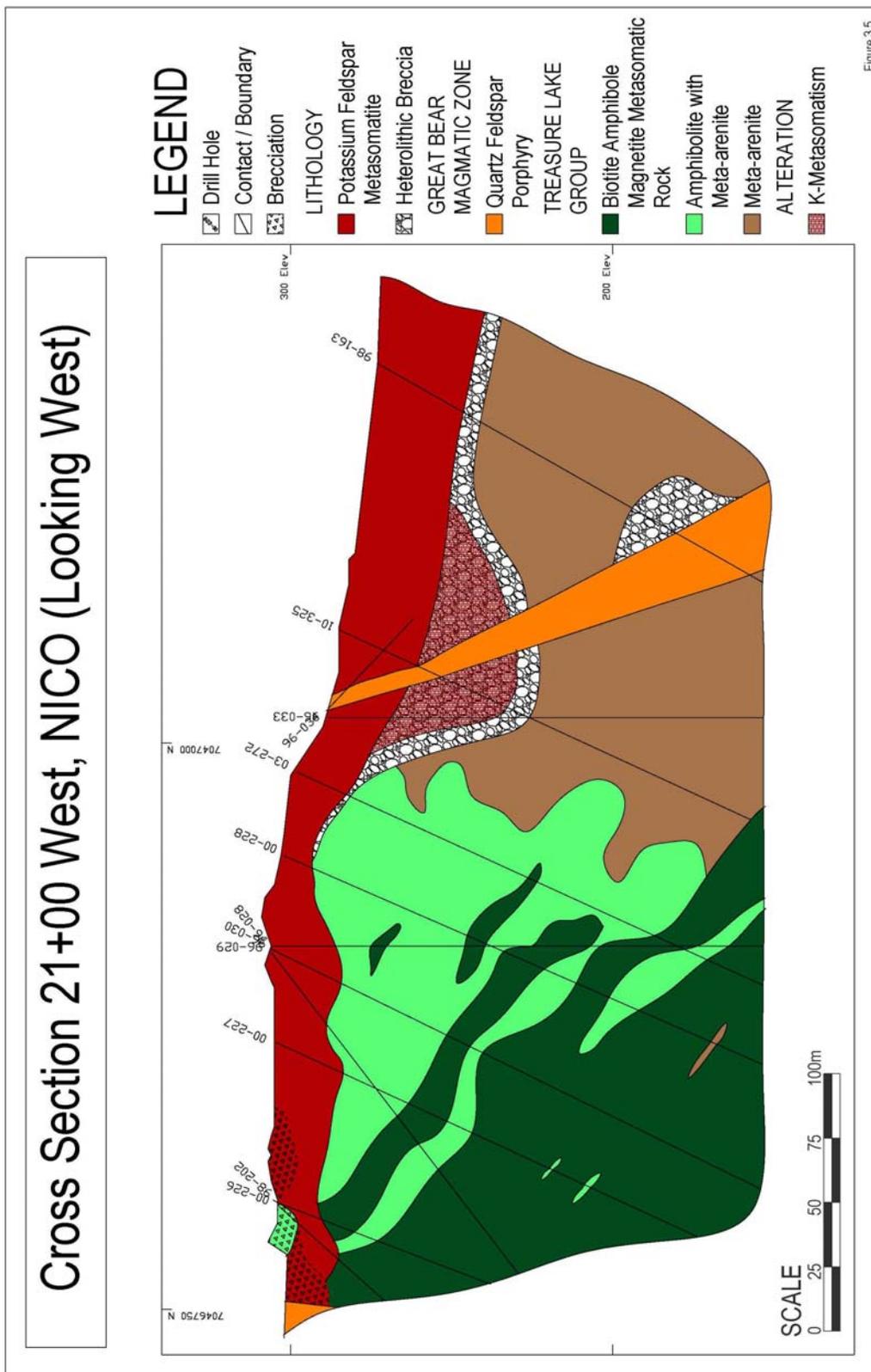
Figure 3.5 – Cross section of NICO grid line 21+00W.

section, aggregates of hornblende, biotite and occasionally magnetite form parallel clots and streaks that are largely replaced by chlorite.   Otherwise potassium feldspar comprises greater than 95% of the unit.

Two principal modes of occurrence are recognized for the matrix, distinguished by crystallinity and mineral assemblage. These include microcrystalline K-feldspar + quartz ± magnetite ± pyrite ± martite and cryptocrystalline K-feldspar + quartz + hematite.   They exhibit texturally complex relationships with each other, with both forming discontinuous elongate or lenticular domains that approximately parallel the mafic banding. Coarser grained aggregates of quartz form discrete seams or vugs that similarly approximate the fabric and contribute to the laminated appearance. Both microcrystalline and cryptocrystalline domains show weak disseminations of chlorite.

Rare subhedral to euhedral feldspar crystals up to 150 μm occur where banding is most pronounced.   These have weakly-to-moderately corroded margins and are commonly microbrecciated due to infiltration of the K-feldspar matrix. They exhibit either the simple twinning of orthoclase, or tartan twinning of microcline. Preservation of delicate structures supports an igneous origin. Locally, secondary ankerite forms anhedral growths heavily included by chlorite and overgrowing the very fine grained K-feldspar. Rarely, idioblastic rhombs decorated with biotite and chlorite inclusions occur as solitary porphyroblasts.

Where banding is poorly developed, spherulite-like patterns are preserved within the matrix (Plate 3.30). These are characterized by a radial structure in the outer envelope defined by subtle, very fine outward radiating fibres perpendicular to a coarser grained central nucleus. The radiating fibres are composed of cryptocrystalline potassium feldspar variably

dusted with earthy hematite. Less commonly, the outer envelope lacks an outward-radiating structure or is cross-cut by coarser grained K-feldspar + magnetite matrix. Preservation of spherulites and feldspar phenocrysts support interpretations for a volcanic precursor.

Chalcopyrite-Cemented Potassium Feldspar Metasomatite Breccia

Brecciated banded-to-massive potassium feldspar metasomatite hosts occurrences of chalcopyrite with variable pyrite and minor bornite at Summit Lake and along the south-eastern shore of Chalco Lake. The brecciated metasomatite is monolithic and generally clast-supported. Clasts range in size from less than a cm to greater than 5 cm's. Locally, clasts appear to exhibit a common alignment, though are predominantly of a random orientation. Though fragments are predominantly angular, clast boundaries are either coated with black chlorite or exhibit a ragged or diffuse appearance. The interfragmental spaces have been infilled by fine to coarse grained chalcopyrite + chlorite ± pyrite ± bornite. Here metasomatite is compositionally and texturally similar to the cryptocrystalline K-feldspar + quartz + hematite assemblage previously described for the banded variety. However, spherulite-like textures preserved here occur in greater abundance and are commonly marked by haloes of coarser aggregates of K-feldspar and quartz.

3.5.2 Non-Banded Potassium Feldspar Metasomatite

Cherty potassium feldspar metasomatite most commonly appears as massive pink to red brick cryptocrystalline rock. Close scrutiny reveals a mottled to semi-homogenous rock, and fine mafic streaks and clots are typical. These comprise less than 5% of the overall volume, and occasionally impart a local lineation to the rock. Streak compositions are highly variable, consisting of combinations of hornblende, biotite, quartz, chlorite, magnetite, pyrite,

pyrrhotite, arsenopyrite and/or chalcopyrite. The red brick colouration is nearly ubiquitous due to a uniform hematite turbidity developed in the matrix. Overprinting by Fe-chlorite is similarly widespread.

Massive metasomatite is exceptional for the development of domains exhibiting near complete replacement by ultra-fine equigranular K-feldspar (Plate 3.31). Though margins of individual matrix grains are often difficult to discern, development of triple point boundaries is common where grain margins are best developed. At high magnification, an intensification of hematite inclusions along grain boundaries is evidenced with secondary K-feldspar cores comparatively free of hematite. Quartz forms isolated islands of coarser grains or aggregates but lack the vuggy appearance or degree of coarseness developed in banded metasomatite. Coarser grains exhibit undulose extinction that suggests deformation post-grain coarsening. Matrix homogeneity is marred locally by heavier concentrations of disseminated hematite, martite or chlorite.

Porphyroblasts of K-feldspar and quartz up to 200 μm are rare. Though the former exhibit a lack of twinning, they can be recognized by subhedral lath shapes. The generally irregular shape and diffuse boundaries transitional into ultra-fine grained matrix indicate a secondary origin for both species. The randomly oriented mafic clots and streaks are primarily composed of chlorite ± amphibole ± biotite and range in size from less than a millimeter to several centimeters. These occur isolated, or as clusters where more concentrated. Trace ankerite occurs locally as fine grained aggregates within the matrix.

3.5.3 Magnetite Potassium Feldspar Metasomatite

South of Chalco Lake, non-banded metasomatite is locally magnetic. Overall, this

magnetic domain has a dimension at 100 meter scale. Similarly altered rock has not been observed elsewhere within K-metasomatized rock at NICO. The interface between magnetic and non-magnetic metasomatite is sharp. Here the metasomatite is distinguished by the presence of fine grained magnetite and the development of a dark purple-red colouration. Fine grained aggregates form magnetic spots that appear macroscopically to be nearly equidimensional with oval-shapes and measurements between 1-2 mm (Plate 3.26). On an outcrop scale these spots show a preferential alignment. However, spot distribution lacks uniformity. They occur collectively as patches, with significant variation in patch dimensions on a decimetre to meter-scale. Fine grained aggregates of quartz + specularite + arsenopyrite + biotite form similar clots and streaks that locally border the magnetite concentrations.

Thin section analysis reveals two contrasting mineral assemblages with uniquely developed crystallinities define this domain (Plate 3.32). The macroscopic spots result from microcrystalline aggregates comprised of K-feldspar + magnetite + quartz ± martite assemblages. The matrix of these spots is marked by hematite-free very-fine grain-sized K-feldspar. Coarse grained quartz vugs are ubiquitous within each spot. The heavy magnetite disseminations commonly concentrate at vug boundaries. These disseminations occur as octahedral grains with trapezoidal and diamond-shaped cross-sections, or as anhedral grains and granular masses. Individual grains range up to 30 μm in diameter.

In contrast to other non-banded metasomatite, K-feldspar + quartz + hematite + chlorite assemblages here comprise a coarser matrix within which these spots occur indicative of grain coarsening through recrystallization. Here, grain boundaries are characteristically diffuse and marked by a concentration of hematite inclusions around relatively clear K-feldspar cores. Less commonly hematite is uniformly disseminated within individual grains

of this coarser K-feldspar phase. Quartz is markedly finer grained and less vuggy in comparison to species within spot assemblages. Late-stage finely disseminated dark green Fe-chlorite overprints the coarser matrix.

3.5.4 Bleached Domains of Potassium Feldspar Metasomatite

Massive potassium metasomatite is locally bleached on a macro-scale. This is best developed south of Grid Lake where bleached patches develop on a meter scale (Plate 3.27). Bleaching is also commonly observed within drill core west of the Bowl Zone. Here individual patches occur on a centimetre scale. Centimetre-scale bleached patches generally form pale haloes around mafic cores. Mafic cores have not been observed within meter-scale patches. Sharp contacts between bleached and non-bleached domains are typical, though gradational boundaries do occur.

Irrespective of scale, bleached patches are characterized microscopically by a matrix of K-feldspar + quartz that is distinctly free of hematite and Fe-chlorite inclusions. Quartz occurs as coarser grained vug-like aggregates. Here grain coarsening results in diffuse boundaries marked by optical heterogeneities that transition into finer grained matrix. Inequigranular K-feldspar forms vague ovoid textures or irregularly patterned matrix that typically exhibit coarsened cores rimmed by finer grain-sizes (Plate 3.33). High magnification reveals triple point junctions are equally well developed within both fine and coarsened matrix. Mafic cores are generally fine to medium grained, black and characterized by irregular shapes. Core composition is highly variable with amphibole, biotite, or biotite pseudomorphs of amphibole with magnetite, pyrite, and/or arsenopyrite. Cores show pervasive chloritization and are commonly richly dusted with ultra-fine hematite. Magnetite is

commonly oxidized to martite or hematite.

3.5.5 Potassium Feldspar Metasomatite-hosted Relicts

Relicts hosted within the metasomatite are best exposed south-east of the Bowl Zone. Weathered to a pale or earthy brown at surface, they form meter-scale patches that show gradational boundaries into pervasive replacement. In core, they are darkly coloured, massive with no observed bedding (Plate 3.29). Pale spots are conspicuous or ghost textures are preserved within relicts. In thin section, the highly variable fine grained matrix is comprised of K-feldspar (60-90%) and magnetite (5-35%), with plagioclase (2-4%), biotite (1-2%) and quartz (1-2%) porphyroclasts, ankerite (<1%) and calcite (<1%) porphyroblasts, secondary chlorite (2-4%) and hematite (<1-2%).

In core, pervasive K-feldspar overprinting relict patches result in massive salmon pink to brick red rock. This replacement is marked by variable preservation of prior components within pervasive fine grained K-feldspar matrix. Replacement by K-feldspar becomes more prominent within intervals of greatest alteration intensity. Further recrystallization of ultrafine K-feldspar develops irregular to oval mottling patterns defined by centers of coarser grain size bordered by a transition to finer grains. Such patterns rarely exceed 500 μm in diameter, and generally range from 200 to 400 μm. High magnification reveals individual K-feldspar microlites that comprise the replaced matrix are moderately overprinted by late chlorite microlites with an intensification of micron-sized hematite inclusions along grain boundaries. Coarser feldspar cores are generally free of hematite. Coarsening of very fine grained K-feldspar matrix occasionally results in domains marked by tartan twinning, indicative of microcline.

Quartz marks the most resistant relict phase, and preservation of rounded shapes suggest a detrital origin. Quartz porphyroclasts range in diameter up to two millimeters. Their sharp grain boundaries are occasionally mantled with fine grained chlorite. Quartz notably exhibits a reduction in size by an order of magnitude within intervals of greatest replacement. Specifically, in more intensely altered intervals they approach 300 μm in diameter. These are rich with chlorite inclusions, with occasional apatite and hematite.

Plagioclase porphyroclasts are conspicuous within these relic patches, identified by polysynthetic twinning. These are most commonly preserved as individual grains up to two millimeters in diameter, however the preservation of fragile clusters persists where there is pervasive K-feldspar replacement of the matrix. Plagioclase ranges from euhedral to subhedral, with fragmentation and rounding common. Occasional simple-twinned orthoclase porphyroblasts similarly persist. Grain boundaries of both species are generally sharp and distinct, though become diffuse where partially-to-completely replaced by K-feldspar, indicating grain reduction through recrystallization (Plate 3.34). Replacement by biotite, chlorite, and sericite within intervals of moderate to strong alteration intensity is also common. Plagioclase is typically included with chlorite microlites and hematite, and locally replaced by cores of dark green tabular chlorite

Fine grained magnetite occurs disseminated throughout, though variable concentrations mark magnetite-rich and magnetite-poor domains. Compositional boundaries are sharply defined by the variable magnetite content. Individual grains are locally euhedral but predominantly anhedral, and range up to 25 μm in diameter. Coarser granular masses occur within more densely populated domains where they replaced former mafic minerals and/or lithic clasts. These coarser grained aggregates show infiltration by earthy hematite.

Hematite also occurs as micron-sized disseminations within magnetite-poor domains.

Fine grained scaly brown pleochroic biotite and amorphous green chlorite generally occur as clots and streaks, or as fine grained disseminations within the K-feldspar replaced matrix. Former mafic minerals and/or lithic grains are indicated by very fine grained aggregates of biotite, chlorite, amphibole, and magnetite. These aggregates are commonly interconnected by a mosaic of coarser grained quartz exhibiting triple point quartz-quartz boundaries and sub-grain development, with very fine grained K-feldspar infiltration. Locally, trace ankerite forms very fine grained aggregates up to 120 μm. They generally occur spatially associated with disseminated chlorite within the matrix.

3.5.6 Potassium Feldspar Metasomatite-associated Brecciation

Though the mineralogically and texturally destructive nature of the pervasive potassium feldspar replacement at NICO obscures and obliterates many vital genetic clues, examples of brecciation and discrete brecciated bodies are commonly preserved. Many breccia bodies are too small to be effectively depicted on maps or cross-sections, representing a local feature within the greater lithological context. As recognized by Sillitoe (1985) and others (see Laznicka, 1988), better understanding of breccia systems aids interpretation of the nature of deformational and hydrothermal processes that result in alteration and mineralization. However, the intent of this study is not to exhaustively document or describe all the brecciation at NICO. Brecciation exhibiting a metasomatite-association, with implications for metasomatic origins, is briefly described here. Breccia classification is based on formational regimes and descriptive petrography. Brecciation intimately associated with potassium feldspar metasomatism can be classified broadly under three main categories: i)

monolithologic to heterolithologic, (ii) metasomatite disaggregation, and (iii) pseudobrecciation.

Monolithologic to heterolithologic brecciation commonly occurs as a boundary condition to domains of pervasive potassium feldspar replacement. This relationship is best observed proximal to the interface between potassium feldspar metasomatite and porphyry dykes, and directly between metasomatite and metasedimentary rocks. Usually this style of brecciation appears monolithic due to pervasive potassium feldspar replacement of fragment matrix (Plate 3.35). Where replacement is less intense, heterolithic brecciation is more readily recognized. This style of brecciation is characterized by a highly variable matrix of fine grained to aphanitic K-feldspar ± amphibole ± quartz ± biotite ± magnetite matrix. Fragments are angular to sub-round, light pink to reddish brown and range in size up to several 10's of centimeters in length. They are generally composed of Treasure Lake Group metasedimentary rocks and metasomatite, though rare porphyritic volcanic clasts have been identified. Brecciation transitions from crackle brecciated metasomatite margins through fragment-rich matrix-supported to fragment-poor matrix-rich domains. Late stage infiltration of breccia matrix by fine grained biotite or magnetite veins is common.

A more complex metasomatite-metasedimentary rock interface was revealed within the decline. Here complexly shaped biotite amphibolite-composition fragments are hosted within a very fine grained potassium feldspar metasomatite matrix. Complex shapes are characterized by variably sub-round and smooth or rough and irregular external fragment surfaces. Amphibolitized clasts show partial white rims suggesting feldspathization and replacement of mafic components by potassium feldspar at fragment boundaries (Plate 3.36). Nebulous relicts of fragments revealed by vague and ill-defined darker shapes within the

matrix are indicative of the differential replacement process. In thin section, recrystallization of K-feldspar matrix results in rosette structures defined by grain coarsened cores with ultra fine K-feldspar haloes (Plate 3.37). Locally, recrystallization of K-feldspar and quartz produces a vermicular-like rosette texture marked by finely intermixed K-feldspar and quartz. These occur where coarse grained quartz vugs are abundant within grain coarsened K-feldspar matrix

Repeated disaggregation and replacement of potassium feldspar metasomatite is evidenced locally by preservation of patches of brecciated and rebrecciated metasomatite and incompletely replaced relics within otherwise completely potassium feldspar replaced rock. Preservation of nebulous or ghost-like fragments and brecciated or rebrecciated metasomatite are commonly encountered in drill core. Brecciated relics are best observed at surface north of Whale Lake. Though the petrography of relics has been described previously in Section 3.5.3, their general brecciation is briefly reviewed here. Metasomatite and relict fragments show angular shapes. Clast margins are variably sharp or diffusely overprinted by a very fine grained potassium feldspar matrix. Grain size variations between clast and matrix show coarser clast grain sizes hosted by a finer grained matrix.

Pseudobrecciation is most readily recognized in metasedimentary rock, and has been previously described in Section 3.2.4. The process is briefly described further here to illustrate similar brecciation processes where they show an association with K-metasomatism. Pseudobrecciation is indicated when an appearance of brecciation did not result from physical fragmentation. Where abundant relics are hosted by metasomatite, apparent clasts appear in situ without rotation. This typically results in brown spotted pseudo-fragments subdivided by cherty pink K-feldspar. Thin section petrography for relics has been previously described in

Section 3.5.5.

3.6 Veins

Though veins comprise only a very small fraction of the overall volume of rock, they can provide very useful information. Decline cross-cuts have revealed clinopyroxene veins extending from zones of brecciation that cross-cut feldspar-phyric porphyry and their well developed endocontact zones (Plate 3.38). The nature of these veins and their relationship to porphyry dykes provides significant implications for amphibolite conditions post-dyke emplacement, and therefore these veins are further described here. While late stage infiltration of metasedimentary, volcanic, intrusive and metasomatic rocks is further evidenced by examples of biotite, magnetite, carbonate, quartz-carbonate, quartz, barite, specular and earthy hematite, and chlorite veins, the collective nature of these veins is beyond the scope of this study.

3.6.1 Clinopyroxene ± Epidote ± Chlorite Veins Bordered by K-Feldspar Selvages

Feldspar porphyries and their metasomatic aureoles are cross-cut by clinopyroxene ± epidote ± chlorite veins that infiltrate from metasomatically altered brecciated borders. Similar veins cross-cutting metasedimentary or volcanic stratigraphies have not been observed. These veins are randomly oriented, exhibit pinch and swells characterized by variable thickness on a centimetre scale. Well developed selvages, also centimetre scale, are marked by an orange-red coloration and a reduction of phenocryst abundance macroscopically similar to porphyry endocontact zones.

In thin section, vein cores are dominated by coarse grained anhedral clinopyroxene that poikiloblastically enclose fragments of altered wall rock (Plate 3.39).   Though

Plate 3.25

Outcrop of red-brown potassium feldspar metasomatite showing intense but variable hematite alteration. Photo taken north-east of Summit Lake.

Plate 3.26

Outcrop of magnetite potassium feldspar metasomatite showing spots defined by fine grained aggregates of K-feldspar + magnetite ± martite ± quartz. Photo of sample location GR-10-139.

Plate 3.27

Outcrop of an intensely bleached macro-domain within massive potassium feldspar metasomatite taken west of the Grid Lakes. Lens cap used for scale (upper right corner of photo) measures 5.2cm in diameter.

Plate 3.28

Outcrop of chalcopyrite breccia hosted by potassium feldspar metasomatite at Summit Lake. Hammer used for scale. Photo of sample location GR-10-117.

Plate 3.29

Spotted relict hosted within potassium feldspar metasomatite. Photo of sample location GR-10-143.

Plate 3.30

Spherulite-like pattern preserved within banded potassium feldspar metasomatite at Summit. The radial structure in the outer envelope is defined by subtle, very fine outward radiating fibres perpendicular to a coarser grained central nucleus. The radiating fibres composed of cryptocrystalline potassium feldspar variably dusted with earthy hematite are cross-cut by coarser grained K-feldspar + magnetite matrix. Photomicrograph of GR-10-116 taken under plane polarized light.

Plate 3.31

Massive metasomatite exhibiting near complete replacement to a matrix of ultra-fine equigranular K-feldspar. Trace quartz persists (coarser grains exhibiting 1st order grey birefringence). The opaque clots are concentrations hematite. Photomicrograph of GR-06-003E taken under crossed polars.

Plate 3.32

Boundary showing the crystallinity and mineral assemblage contrast within magnetite potassium feldspar metasomatite. The left hemisphere demonstrates a portion of a macroscopic spot defined by aggregates of microcrystalline K-feldspar, vuggy quartz (bottom center) and disseminated magnetite (opaque). The right hemisphere demonstrates a bounding matrix of coarser grained K-feldspar, quartz, hematite and chlorite. Photomicrograph of GR-10-144 taken under plane polarized light.

3.30

3.32

3.29

3.31
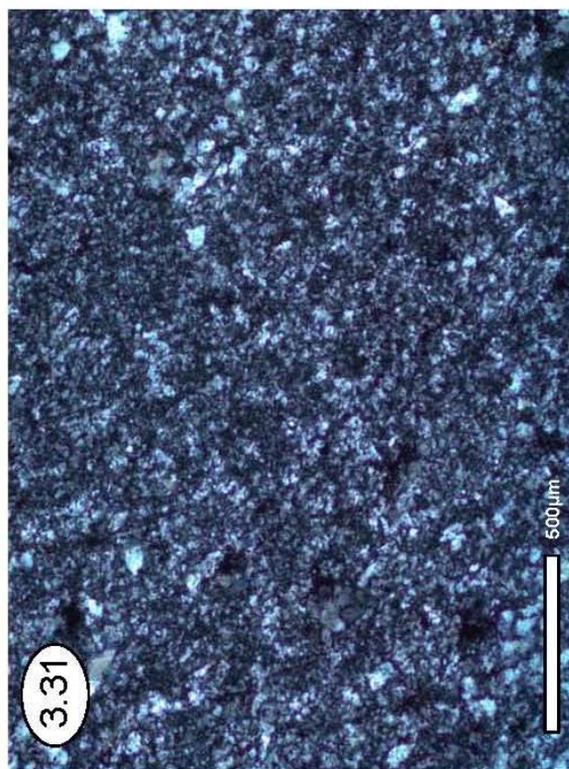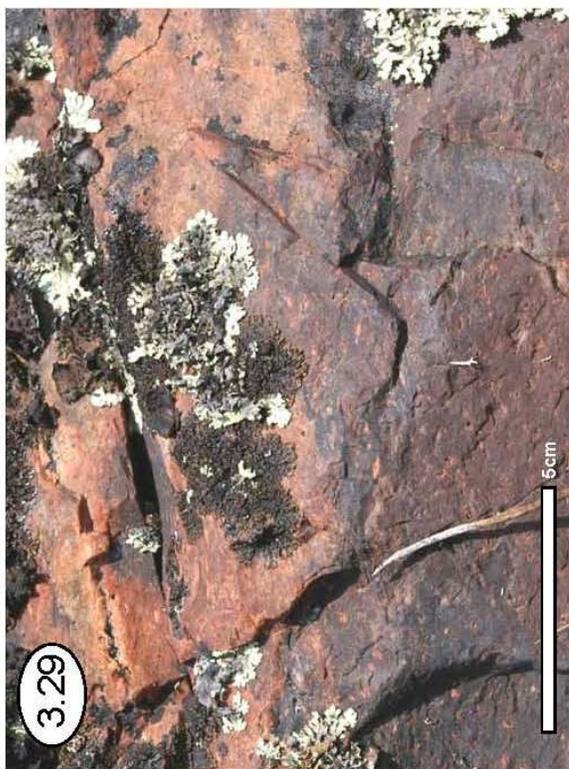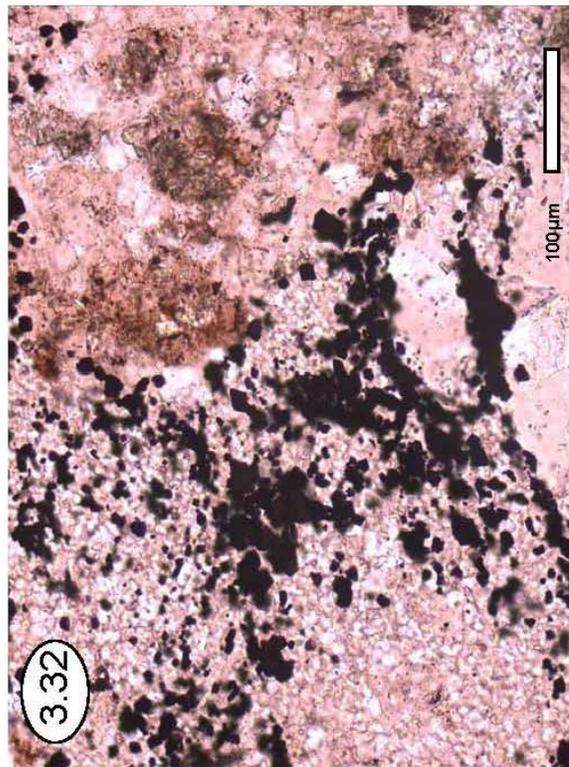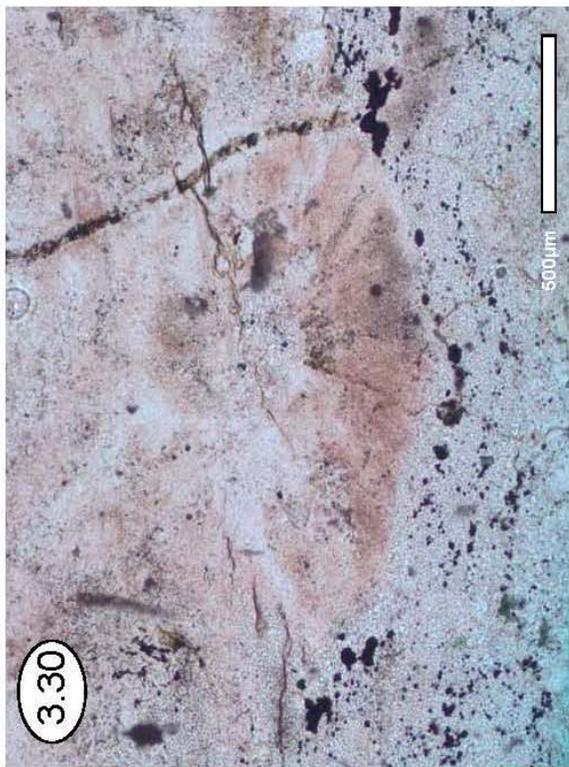
Plate 3.33

Vague ovoid textures and irregularly patterned matrix resulting from inequigranular K-feldspar. Coarser grained quartz typically exhibit vug-like textures. Photomicrograph of GR-10-154 taken under crossed polars.

Plate 3.34

Plagioclase porphyroclast shows pervasive recrystallization to K-feldspar. Photomicrograph of GR-10-143 taken under crossed polars.

Plate 3.35

Monolithic appearance resulting from pervasive potassium feldspar replacement of fragment matrix. This style of brecciation is best observed proximal to the interface between potassium feldspar metasomatite and porphyry dykes. Photo of sample location GR-10-145A.

Plate 3.36

Amphibolitized clasts showing partial white rims suggesting feldspathization and replacement of mafic components by potassium feldspar at fragment boundaries. Photo of slab sample location GR-07-085A.

.

3.34

3.36

3.33

3.35
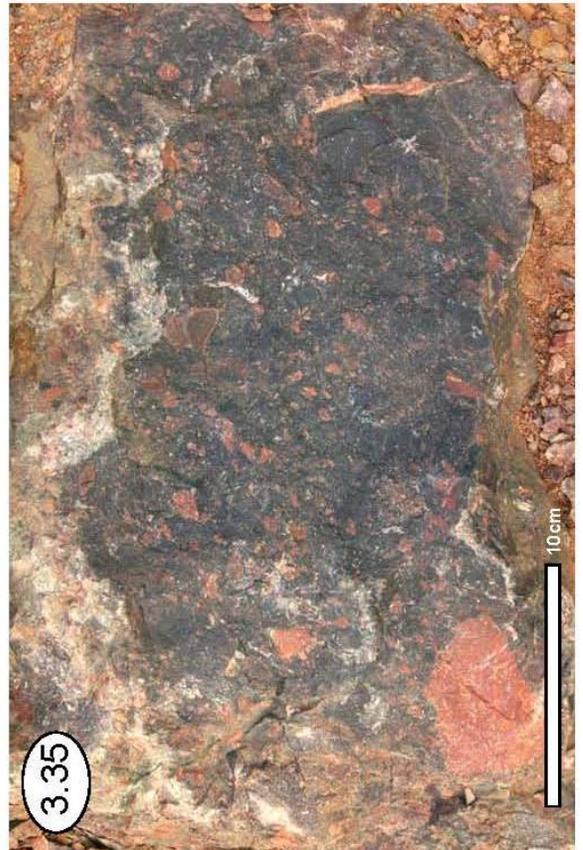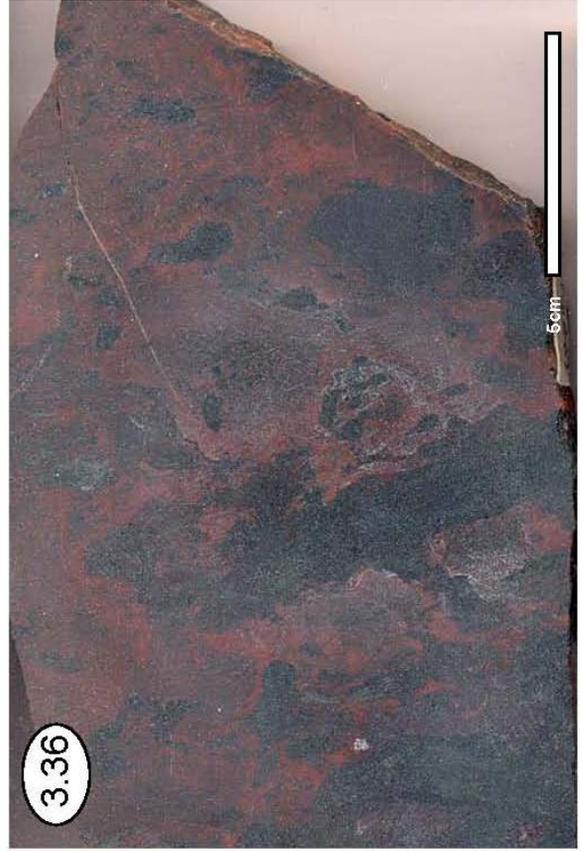
Plate 3.37

Rosette structure resulting from recrystallization of breccia matrix. These show grain coarsened cores of K-feldspar within an ultra-fine halo. Photomicrograph of GR-07-085B taken under plane polarized light.

Plate 3.38

Clinopyroxene vein cross-cutting feldspar-phyric porphyry, as revealed by wall exposures in the decline. Photo of sample station GR-07-086. Mechanical pencil used for scale measures 15.3cm.

Plate 3.39

Vein mineralogy shows clinopyroxene commonly altered to epidote or amphibole, both showing further alteration to biotite or chlorite. (bio – biotite, chl – chlorite, cpx – clinopyroxene, epi – epidote). Photomicrograph of GR-07-086 taken under plane polarized light.

Plate 3.40

Aggregate of euhedral sphene grains with (brown coloured grain with wedge cross sections) collected within altered selvage developed around clinopyroxene vein. Photomicrograph of GR-07-086 taken under plane polarized light.

3.38

3.40

3.37

3.39

clinopyroxene species from vein samples have not been identified by electron microprobe or X-ray diffraction, they exhibit similar pale brown to pale green pleochroism, prismatic cleavage and similar 2nd order birefringence as clinopyroxene species identified in calc-silicate rocks. Partial replacement along grain margins, fractures, and cleavage planes by epidote and chlorite is typical. Epidote most commonly occurs as partial overgrowths to clinopyroxene, or as islands within a chlorite matrix. Epidote is distinguished by characteristic pale yellow-green colors and pleochroism in plane polarized light, and anomalous greenish yellow birefringence under crossed polars. Cross-cutting chlorite clearly establishes it as a late stage of generation. Their strong pale green to olive green pleochroism is comparable to alteration chlorite species identified in metasedimentary and intrusive units.

The altered selvage is texturally similar though with marked mineralogical differences than the previously described porphyry endocontact zone (Section 3.4.3). Here groundmass is mostly indistinguishable from the latter. It is characterized by very fine to ultra fine potassium feldspar showing patches of hematite turbidity. Phenocrysts are also characteristically absent within the selvage indicative of textural destruction accompanying replacement and recrystallization. In contrast to endocontact zones, the vein-selvage boundary is populated by an unusual concentration of sphene and apatite, both trace minerals in porphyry (Plate 3.40). Their aggregate occurrence likely represents several meters of porphyry suggesting a residual intensification of immobile phases under extremely mobile conditions.

CHAPTER 4 - GEOCHEMISTRY

4.1 Introduction

To quantify the effects of K-metasomatism, 52 samples representative of the major rock types were submitted for whole rock geochemistry. Select samples were submitted for mineral chemistry. Bulk rock results are presented qualitatively by lithology in Sections 4.2 and 4.3 for major and trace elements respectively. Major elements are reported as weight percent oxide (wt %) and listed in order of decreasing cation valence in Appendix 2; 42 trace elements are reported in parts per million (ppm) in order of increasing cation valence. Total iron is reported as Fe_2O_3. The chemistry of specific mineral phases is reported individually in Section 4.4, with complete compositional data listed in Appendix 3. Select samples representative of the potassium feldspar metasomatite anomaly were submitted for whole rock ^{18}O isotopic analysis. Results are presented in Section 4.5.

4.2 Major Element Geochemistry

Basal and upper metasiltstone are geochemically comparable, containing between 58.9 - 63.5 wt% SiO_2 and 16.1 - 19.1 wt% Al_2O_3 with low SiO_2/Al_2O_3 ratios of 3.3 to 3.9. Their aluminous character is reflected by a mineral assemblage of quartz, feldspar, chlorite, iron oxides and cordierite. Iron oxide contents show bed by bed variation in both, with Fe_2O_3 ranging from 4.3 - 11.7 wt%. Sampled beds show consistent magnesium (avg. 2.5 wt% MgO), elevated potassium (avg. 5.6 wt% K_2O), and variable titanium (0.09 - 0.67 wt% TiO_2). Basal metasiltstone has calcium (1.3 wt% CaO) and sodium (4.65 wt% Na_2O) enrichment compared to younger cordierite-bearing upper beds (avg. 0.22 wt% CaO and avg. 1.9 wt% Na_2O), and comparatively lower K_2O/Na_2O ratios (1.1 vs. 3.1). Intervals where stratabound

potassium feldspar replacement occurs within basal metasiltstone demonstrate aluminum (12.5 wt% Al_2O_3) and sodium (0.47 wt% Na_2O) depletion, and enrichment of calcium (2.7 wt% CaO) and potassium (9.9 wt% K_2O). Changes to bulk composition are reflected by increased SiO_2/Al_2O_3 and K_2O/Na_2O ratios of 5.1 and 21.0 respectively. Silica, titanium, total iron and magnesium content of the altered rock are comparable to results from non-metasomatized beds.

Biotite-amphibole-magnetite metasomatic rocks exhibit substantial range in major oxide content largely resulting from band by band variation of amphibole, biotite, magnetite, and chlorite abundance, and their respective mineral compositions. Silicon and aluminum content is generally low, ranging from 35.1 - 49.6 wt% SiO_2 and 5.4 - 8.5 wt% Al_2O_3; SiO_2/Al_2O_3 ratios range between 4.1 and 9.1. Total iron varies from 23.2 - 37.0 wt% Fe_2O_3, exhibiting a positive trend with potassium (2.4 - 5.1 wt% K_2O) illustrated graphically in Figure 4.3B. This characteristic suggests a direct relationship between magnetite and biotite abundance. Calcium and sodium both show a positive trend with silica (2.0 to 11.4 wt% CaO; 0.12 to 0.68 wt% Na_2O) corresponding with increasing amphibole abundance. A negative trend between sodium and potassium, illustrated in Figure 4.4B, is reflected by K_2O/Na_2O ratios that range from 3.5 to 42.9. Magnesium content varies between 4.7 - 9.1 wt% MgO, with consistent titanium (0.24 - 0.40 TiO_2).

Quartz-rich meta-arenite beds have high silica (78.8 - 82.3 wt% SiO_2) and low aluminum (4.0 - 5.9 wt% Al_2O_3), with high SiO_2/Al_2O_3 ratios ranging between 13.6 and 20.7. Feldspar, chlorite and iron oxide impurities in the sandstone are reflected by moderate secondary potassium (avg. 3.3 wt% K_2O), magnesium (avg. 1.6 wt% MgO) and total iron (avg. 7.3 wt% Fe_2O_3) enrichment. Trace titanium (avg. 0.20 wt% TiO_2) and calcium (avg.

LEGEND

- K-Feldspar Metasomatite Breccia

- K-Feldspar Metasomatite

- Relics within K-Feldspar Metasomatite

- Feldspar-phyric Porphyry

- Quartz Feldspar-phyric Porphyry

- Plagioclase-phyric Porphyry

- Lou Lake Volcanics

- Upper Metasiltstone

- Meta-arenite

- Biotite-Amphibole-Magnetite Metasomatic Rock

- K-Metasomatized Basal Metasiltstone

- Basal Metasiltstone

Figure 4.1 – Legend used for Figures 4.2 – 4.4.
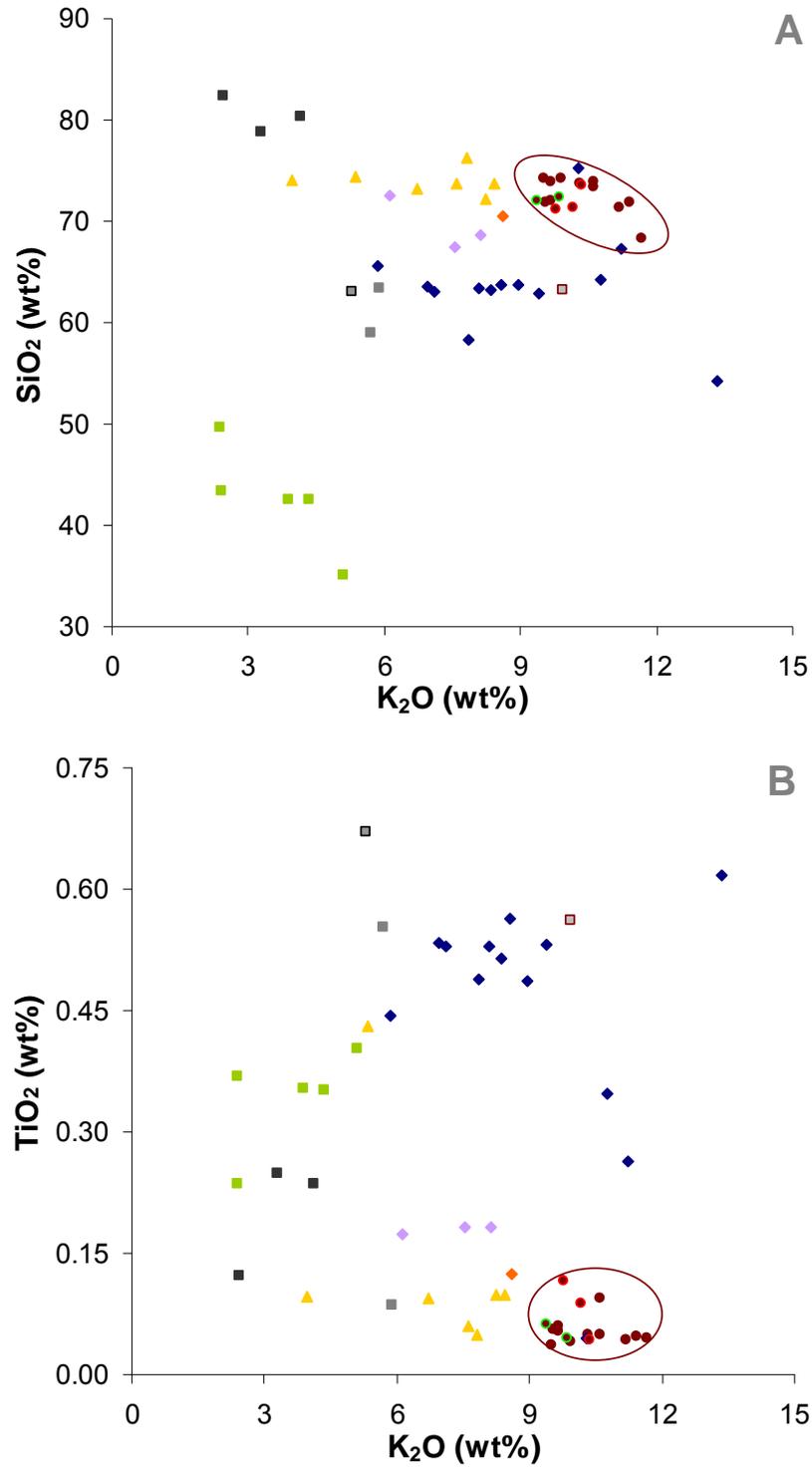
Figure 4.2 – Bivariate plots, including: a) SiO₂ vs. K₂O, and b) TiO₂ vs. K₂O. The field of intense potassium feldspar replacement is indicated on both diagrams.
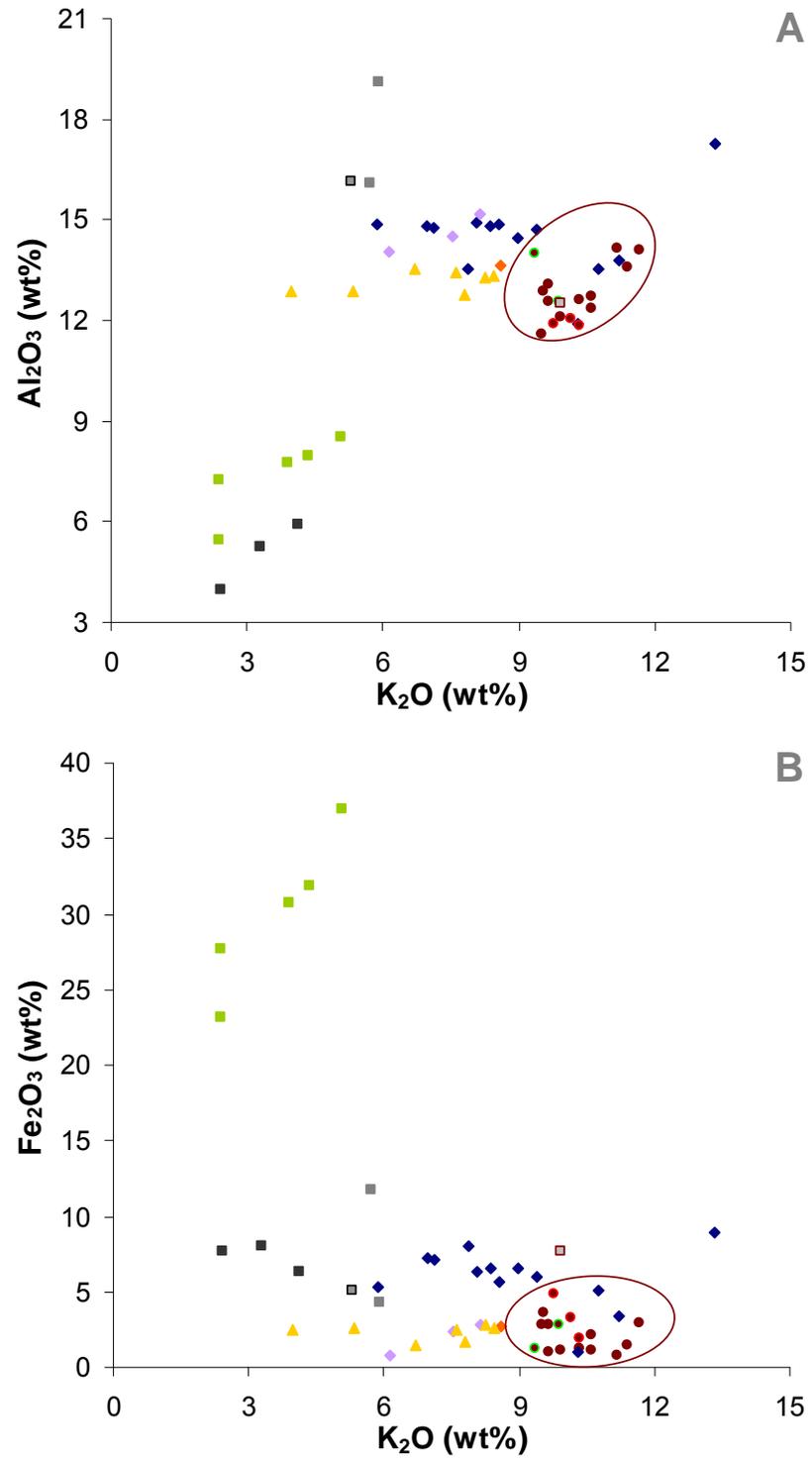
Figure 4.3 – Bivariate plots, including: a) Al₂O₃ vs. K₂O, and b) Fe₂O₃ vs. K₂O. The field of intense potassium feldspar replacement is indicated on both diagrams.
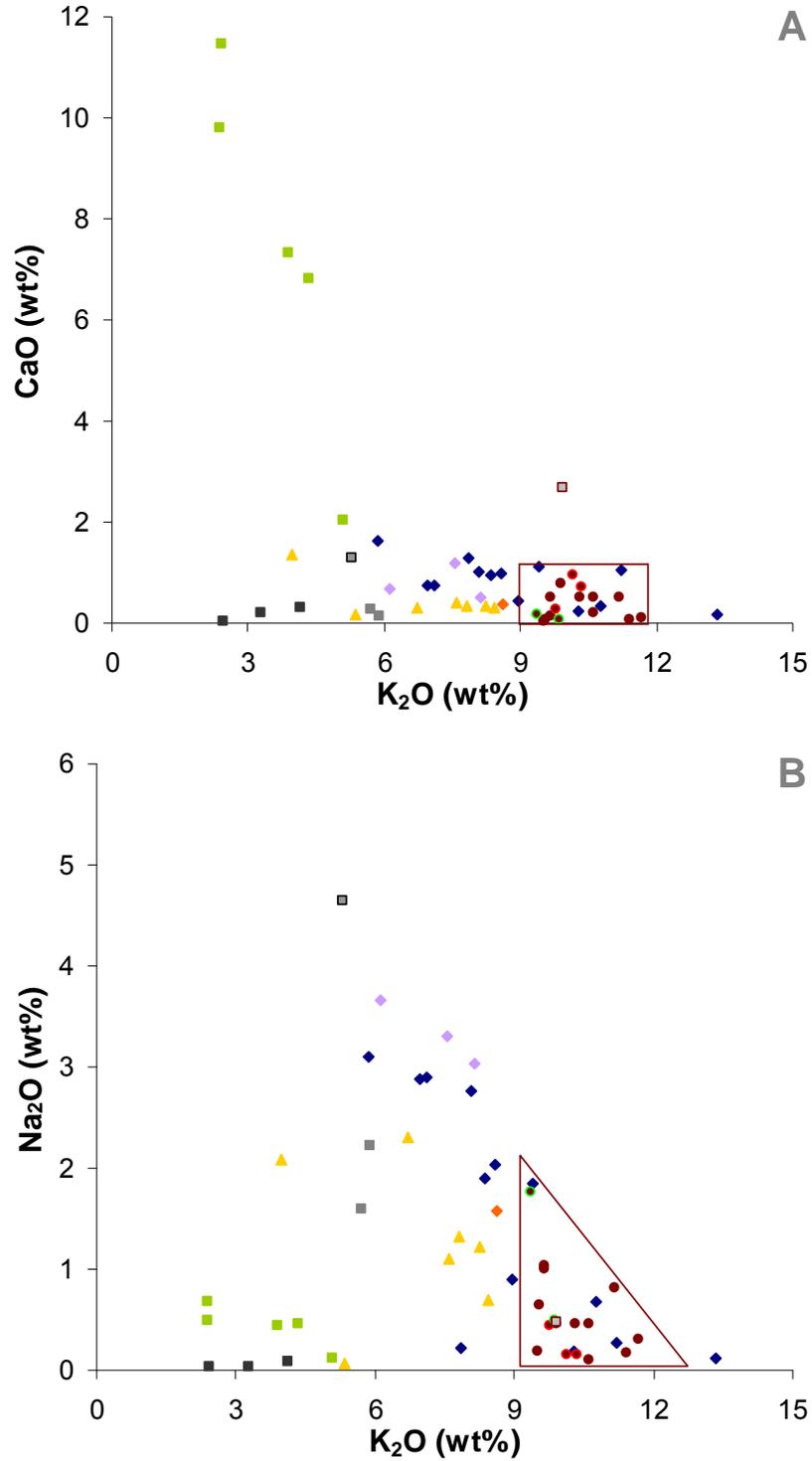
Figure 4.4 – Bivariate plots, including: a) CaO vs. K₂O, and b) Na₂O vs. K₂O. The field of intense potassium feldspar replacement is indicated on both diagrams.

0.19 wt% CaO) content are indicative of accessory rutile and local calcite replacement respectively. Very low sodium content (avg. 0.05 wt% Na_2O) translates into high K_2O/Na_2O ratios (avg. 68.7).

Volcanic rocks sampled in this study contain 72.3 – 76.3 wt% SiO_2, 0.06 – 2.3 wt% Na_2O, and 4.0 – 8.4 wt% K_2O. Total alkalis ($Na_2O + K_2O$) have been plotted against silica in Figure 4.5, demonstrating both least and moderately altered volcanic rock fall within the rhyolite field of the TAS classification diagram (after Le Bas et al., 1986). Alkaline and subalkaline rock suites can also be estimated on this diagram; however many subdivision schemes have been proposed (Rickwood, 1989). Here the recent division of Best (2003) is employed as it best represents the subalkaline character of both volcanic and subvolcanic rocks sampled at NICO. Caution is required when using this diagram to classify altered rocks due to the potential for alkali mobility. Moderately altered volcanic rock and banded potassium feldspar metasomatite were included only to illustrate the significant increase in total alkalis resulting from potassic alteration.

Although alkali mobility makes sodium and potassium generally unsuitable for classification of hydrothermally altered rock, they can be utilized effectively to indicate altered rock. Alkali compositions show all volcanic rock sampled fall within the K-altered field when plotted on the Hughes (1973) igneous spectrum diagram in Figure 4.6B. K_2O/Na_2O ratios plotted against wt% K_2O in Figure 4.6A increase from least altered 1.9 to as high as 89.2; indicating sodium depletion is coupled with potassium enrichment. For comparison, Nockolds et al. (1978) propose unaltered rhyolite typically show K_2O/Na_2O ratios less than two. Least altered volcanic rock contain 1.35 wt% CaO with a K_2O/CaO ratio of 1.9. Altered samples show calcium content varies from 0.18 to 0.40 wt% CaO.

Corresponding K_2O/CaO ratios between 1.90 and 26.7 indicate calcium depletion also occurs during K-metasomatism. Total iron shows relative consistency with least altered samples containing 2.4 wt% Fe_2O_3, while altered samples contain between 1.45 and 2.8 wt% Fe_2O_3.

Three porphyritic phases have been sampled at Lou Lake: i) plagioclase-phyric ii) quartz feldspar-phyric, and (iii) feldspar-phyric. Relative timing is best demonstrated in cross section, where the metasomatite hosting enclaves of the plagioclase-phyric variety is intruded by dykes of the remaining two. Further cross-cutting relations demonstrated at surface and in core show the quartz feldspar-phyric variety marked an earlier phase than the feldspar-phyric. Plotting total alkali vs. silica for least altered samples of each indicate a chemical composition intermediate between microsyenite and microgranite for the earliest, a granitic composition for the middle phase, and a quartz monzonite-syenite composition for the latest (see Figure 4.5). The relationships between individual volcanic and magmatic rocks are further explored in Chapter 5.

The earliest porphyritic phase shows high silica (67.5 – 72.5 wt% SiO_2) and aluminum (14.0 – 15.2 wt% Al_2O_3) content. Moderate sodium (3.0 – 3.7 wt% Na_2O and high potassium (6.1 – 8.1 wt% K_2O) result in low K_2O/Na_2O ratios between 1.7 and 2.7, suggesting this phase suffered least from the effects of alkali metasomatism. This is confirmed by the igneous spectrum diagram for porphyritic phases (Figure 4.6B) where samples plot along the right-hand side of the unaltered field. Low magnesium content (0.23 to 0.50 wt% MgO) is reflected by a mineralogy showing weak replacement by chlorite. Low titanium (0.17 – 0.18 wt% TiO_2) and iron (0.8 to 2.8 wt% Fe_2O_3) content marks this phase from coarser-grained feldspar-phyric porphyry.
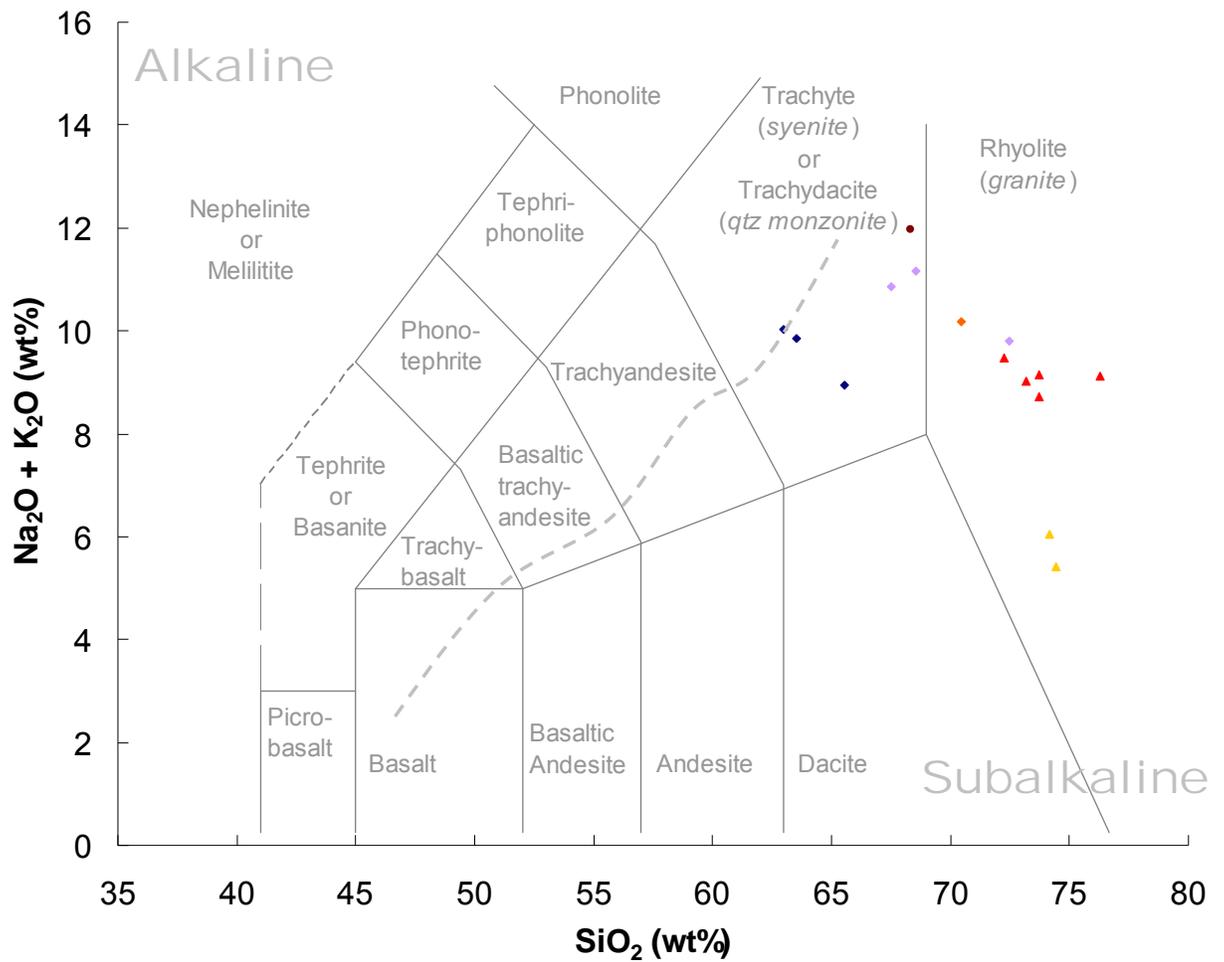
Figure 4.5 – Total alkalis vs. silica (TAS) classification diagram comparing least altered volcanic and porphyritic rock to K-metasomatized volcanics and banded potassium feldspar metasomatite. Nomenclature of plutonic variants with similar compositions have been included in parenthesis. A curved dashed line divides the TAS diagram into alkaline and subalkaline rock suites (after Best, 2003).
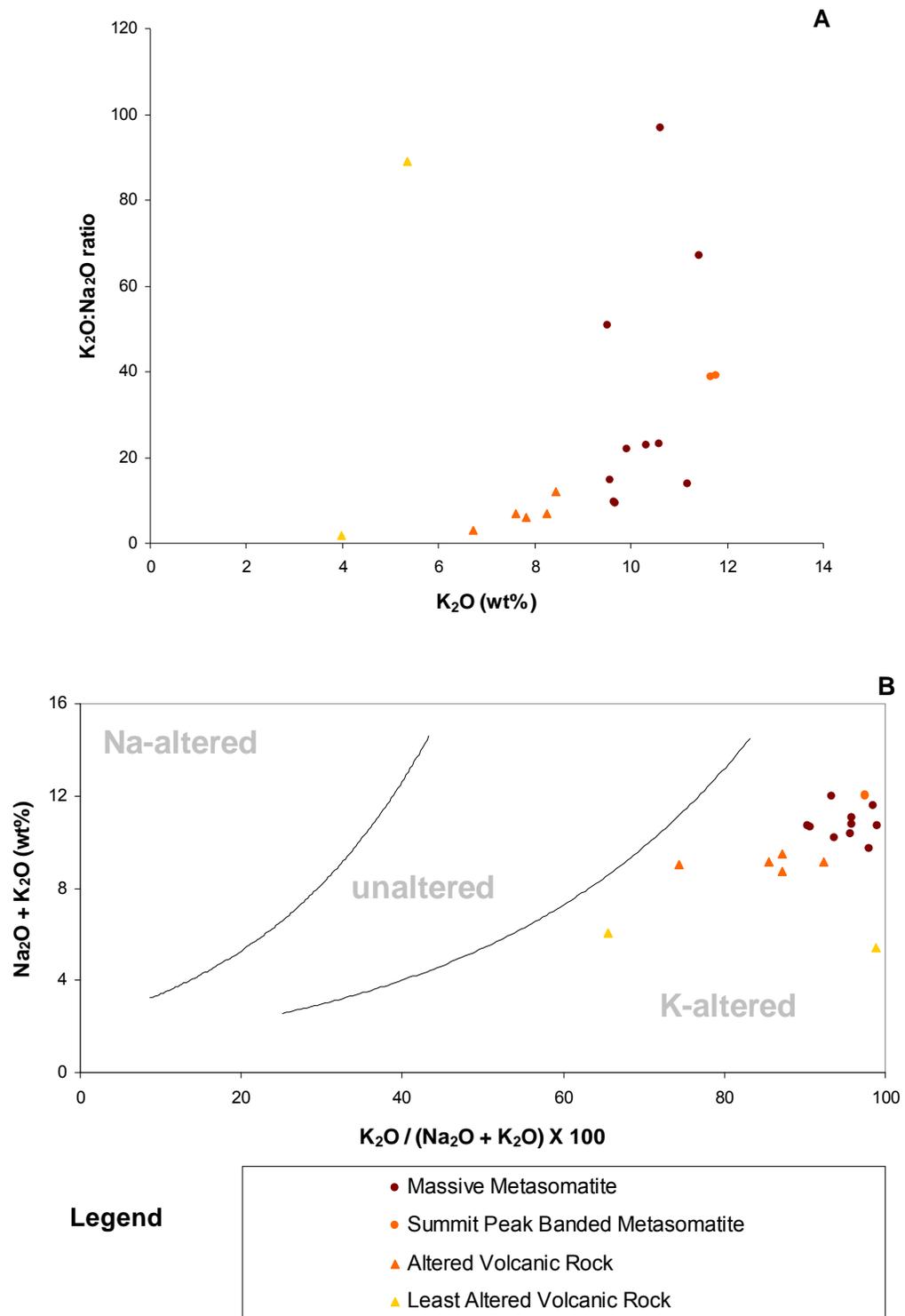
Figure 4.6 –   a) K₂O:Na₂O ratios vs. K₂O (wt%) comparing volcanic rock to metasomatite. b) Igneous spectrum diagram for volcanic rock and potassium feldspar metasomatite (after Hughes, 1973).

Quartz feldspar porphyry is rich in silica (70.4 wt% SiO_2), with low sodium (1.6 wt% Na_2O) and high potassium (8.6 wt% K_2O) resulting in a moderately high K_2O/Na_2O ratio of 5.5. Alkalis plotted on the Hughes (1973) igneous spectrum fall within the K-altered field (Figure 4.7B). The quartz feldspar porphyry contains lower titanium (0.12 wt% TiO_2), aluminum (13.6 wt% Al_2O_3), and calcium (0.38 wt% CaO) than feldspar-phyric porphyry, but contains greater magnesium (0.65 wt% MgO) than the plagioclase-phyric phase. The K_2O/CaO ratio is high at 22.8. Lower titanium and high silicon suggest this phase resulted from an early silica-rich titanium-depleted melt followed by comparatively silica-depleted titanium-enriched igneous activity.

Though both quartz and feldspar-phyric phases show a strong spatial relationship to the potassium feldspar metasomatite, construction of a decline provided an opportunity for sampling across a range of alteration within a single feldspar-phyric dyke. Silica (54.3 – 75.3 wt% SiO_2), sodium (0.1 – 3.1 wt% Na_2O), and potassium (5.9 – 13.4 wt% K_2O) exhibit considerable variation within this unit. K_2O/Na_2O ratios range from least altered 1.9 to intensely altered 119.3. Alkalis from least altered samples plot along the igneous spectrum boundary separating the unaltered and K-altered fields (see Figure 4.7B). The rightward trend towards the K-altered field exhibited by variably altered feldspar porphyry samples illustrates the increasing effects of alteration on alkali composition. The positive alteration trend depicted in Figure 4.7A suggests coupling of sodium depletion with potassium enrichment. Titanium (0.05 – 0.62 wt% TiO_2), aluminum (11.9 – 17.3 wt% Al_2O_3), magnesium (0.16 – 5.6 wt% MgO), and calcium (0.19 – 1.6 wt% CaO) show significant variation with greatest depletions coupled with greatest potassium enrichment. The geochemical effects of K-metasomatism on this phase of feldspar porphyry are further quantified in Chapter 5.
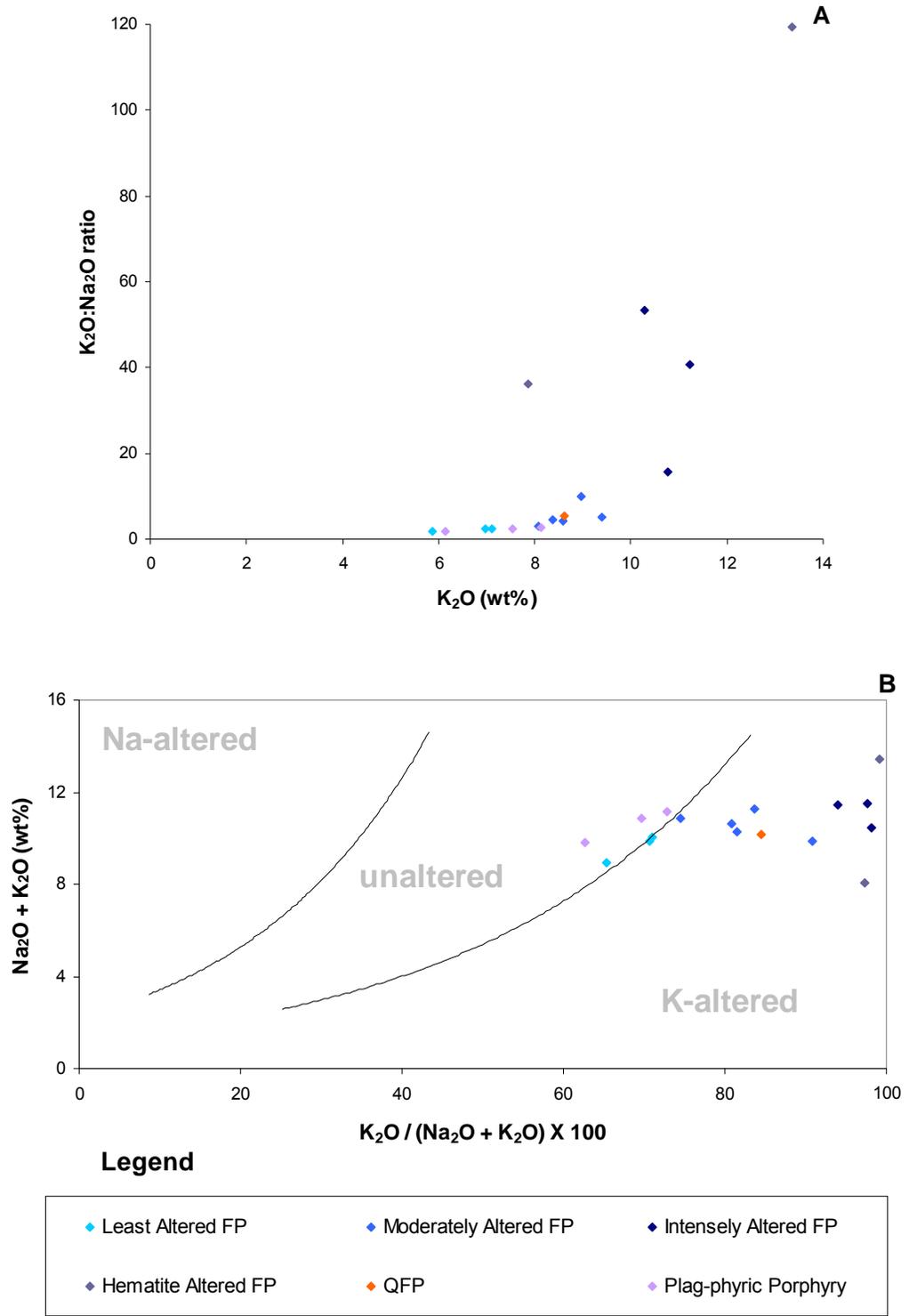
Figure 4.7 – a) $K_2O:Na_2O$ ratios vs. K_2O (wt%) comparing three porphyritic phases.
[FP = Feldspar Porphyry; QFP = Quartz Feldspar Porphyry]
b) Igneous spectrum diagram for porphyritic rock (after Hughes, 1973).

Samples of potassium feldspar metasomatite show relatively uniform compositions high in silicon (68.3 - 74.3 wt% SiO_2), aluminum (11.6 – 14.2 wt% Al_2O_3) and potassium (9.4 – 11.7 wt% K_2O). Low levels of titanium (0.04 – 0.12 wt% TiO_2), magnesium (0.13 – 1.0 wt% MgO), calcium (0.04 – 0.77 wt% CaO) and sodium (0.11 – 1.00 wt% Na_2O) are characteristic. K_2O/Na_2O ratios range from 9.3 to 97.4. Aluminum plots as a positive trend with potassium, reflecting the intense potassium feldspar replacement (see Figure 4.3A). Variable iron content (0.78 – 3.6 wt% Fe_2O_3) marks the near ubiquitous concentration of earthy hematite or magnetite in secondary potassium feldspar. Textural relics within the metasomatite contain higher sodium (0.50 – 1.8 wt% Na_2O) with comparably high potassium (9.4 – 9.9 wt% K_2O) and K_2O/Na_2O ratios (5.3 – 19.7). Greater iron (2.0 – 4.8 wt% Fe_2O_3) and calcium (0.27 – 0.95 wt% CaO) within metasomatite breccia reflect magnetite and calcite minerals preserved within digested fragments.

4.3 Trace Element Geochemistry

Normalized multi-element diagrams are employed to present and compare trace element geochemistry from igneous and K-metasomatized lithologies. The igneous rocks at Lou Lake represent evolved crustal rocks; therefore spidergrams for these rocks have been normalized to MORB values as recommended by Rollinson (1993). Volcanic rock chemistry is presented in Figure 4.8 and porphyritic rock in Figure 4.9. Though several lists of normalizing values exist, no single list provides a complete representation of all elements of interest (Rock, 1987). For this reason, MORB normalization values have been used from several sources including: i) Sc (Pearce, 1982), (ii) Sr, K_2O, Rb, Ba, Th, Ta, Nb, Ce, P_2O_5, Zr, Hf, Sm, TiO2, Y and Yb (Pearce, 1983), and (iii) La, Nb, Nd, Eu, and Tb (Bevins et al., 1984). Element ordering within diagrams presented here follows a modification of the

scheme used by Bevins et al. (1984). Elements are ordered to approximate incompatibility as determined by bulk distribution coefficients for each element between garnet lherzolite and melt. Those elements showing greatest mobility are arranged left to right and elements showing the greatest incompatibility are correspondingly arranged right to left (Rollinson, 1993). Spidergrams for potassium feldspar metasomatite samples have been similarly MORB-normalized for ready comparison (see Figure 4.10).

Patterns show consistent enrichment of mobile components and depletion of incompatible elements for volcanic and porphyritic rocks as compared to mid-ocean ridge basalt. Samples of potassium feldspar metasomatite exhibit similar patterns with several exceptions. The consistent enrichment of mobile components, demonstrated by all samples, is likely an indication of crustal contamination post-magma genesis. The spidergrams demonstrate that significant depletion of Sr, P_2O_5, TiO_2 and Sc from MORB values is common for both igneous and replaced rocks at Lou Lake. Rare earth element (REE) concentrations included on the spider diagrams show extreme enrichment over MORB levels. The degree of REE enrichment exhibited by metasomatite samples are up to an order of magnitude greater than those exhibited by volcanic or porphyritic rocks. This is perhaps best evidenced by the acute enrichment of La, Ce, Nd, Sm and Eu within outliers of the metasomatite sample population (see Figure 4.10). Metasomatite samples showing the greatest REE enrichment were collected from replaced rock south of Chalco Lake. Notably, the intensely altered porphyry boundary shows depleted REE values when compared to porphyry samples exhibiting lesser alteration effects (see Figure 4.9).

Though low Eu content is ubiquitous for igneous rock, several metasomatite samples have content equivalent to MORB values or show significant enrichment. Both
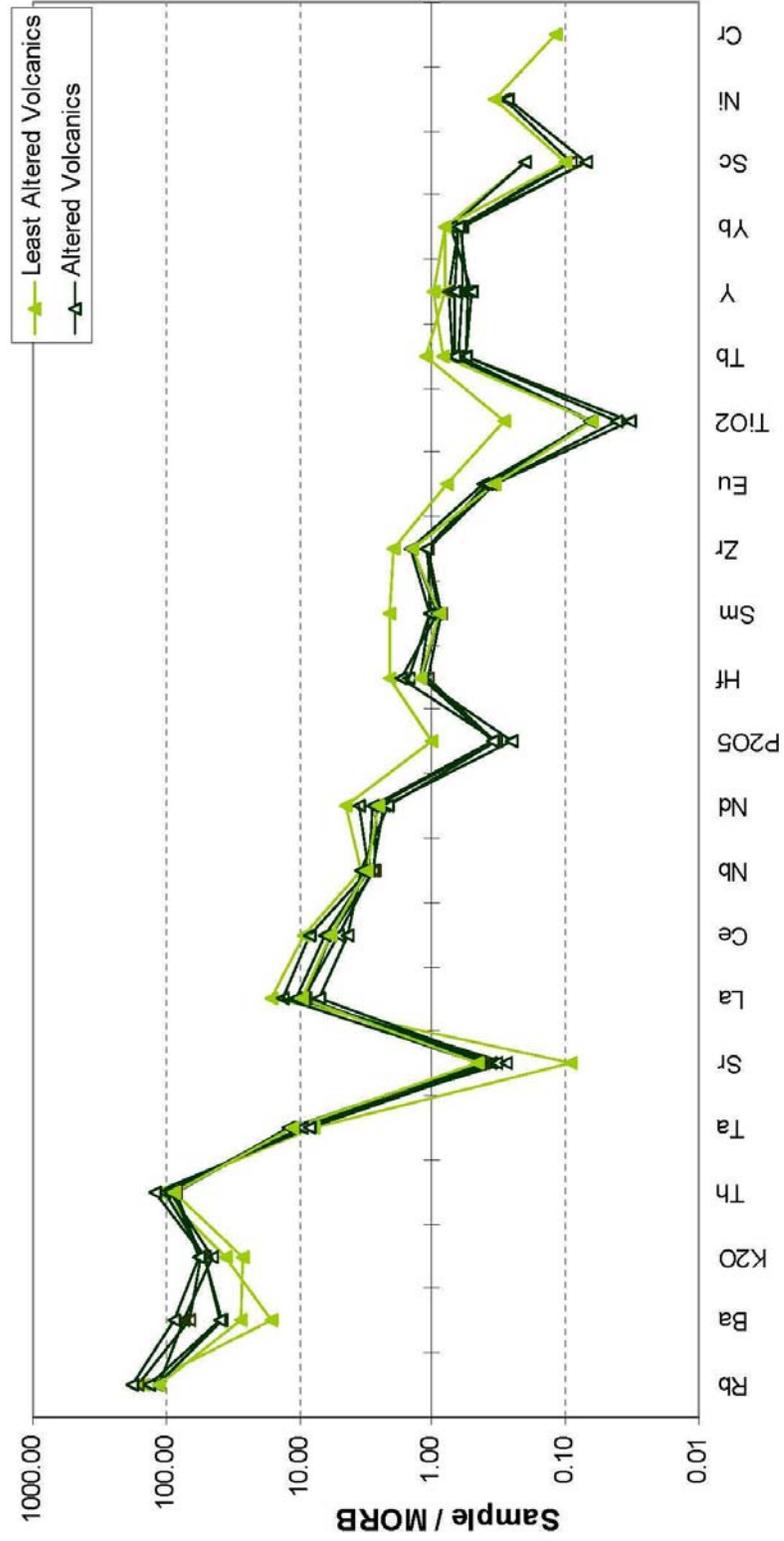
Figure 4.8 – MORB-normalized spidergrams for least altered and altered volcanic rock.
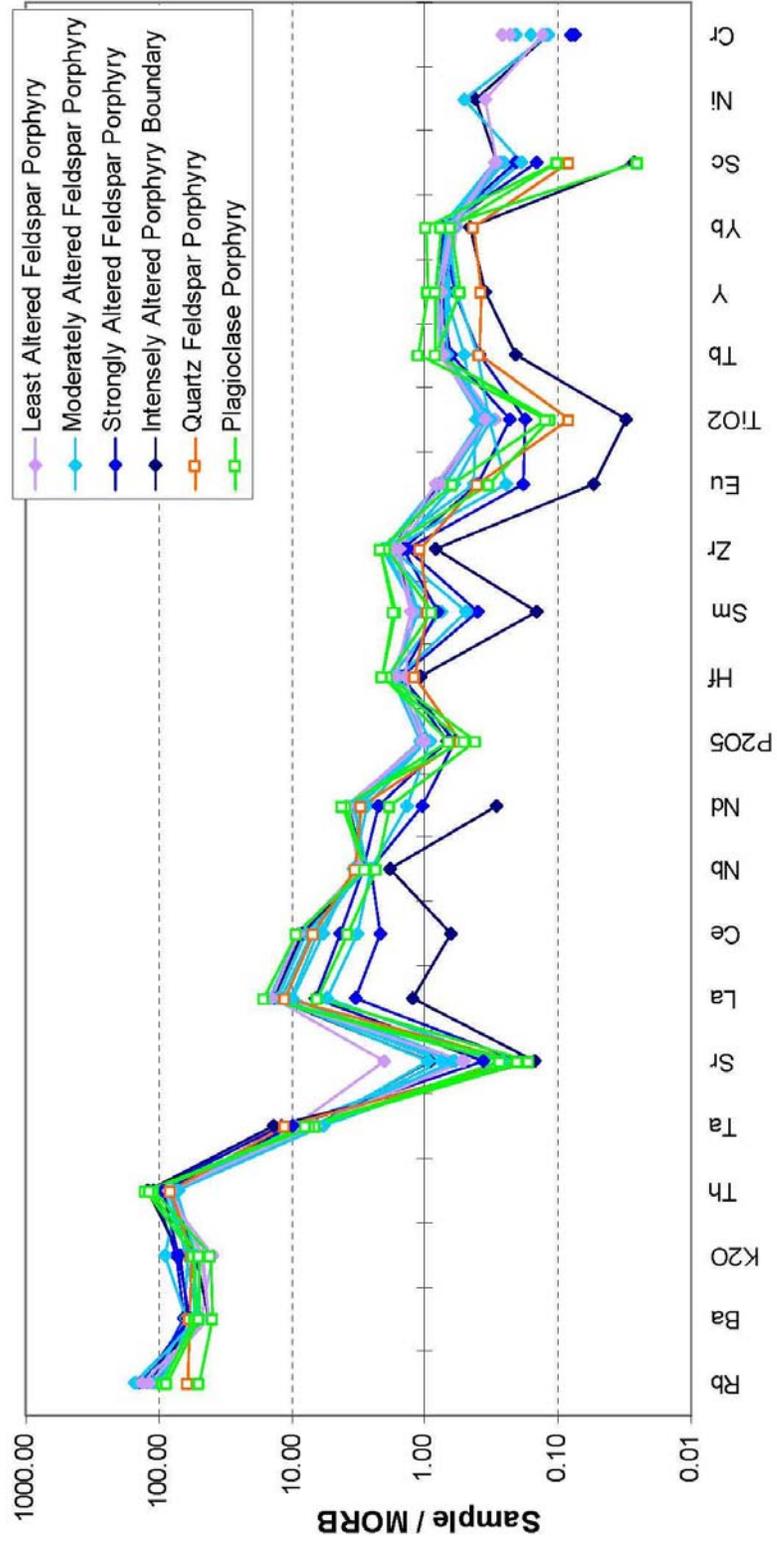
Figure 4.9 – MORB-normalized spidergrams for three porphyritic phases. Feldspar porphyry samples are separated on the basis of textural and mineralogical alteration effects.
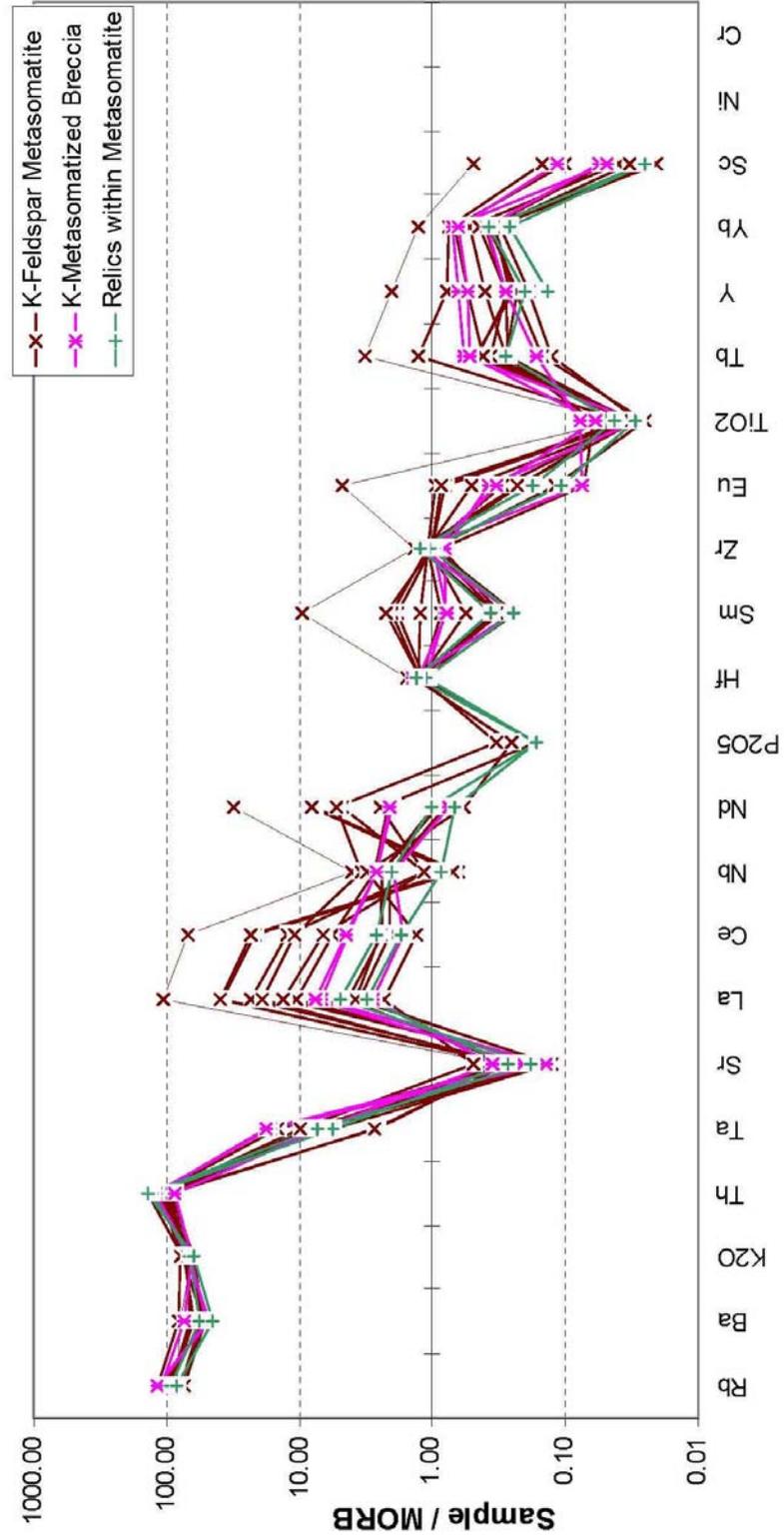
Figure 4.10 – MORB-normalized spidergrams for potassium feldspar metasomatite.

volcanic and porphyritic rock show mixed enrichment (Nb, Ta, Zr, Hf) or depletion (Y, Ti) of high field strength (HFS) element concentrations. Metasomatite samples exhibit comparable patterns for high field strength element concentrations; however several samples show inconsistencies including Nb depletion or Y enrichment. Perhaps most striking are results showing enrichments an order of magnitude greater than concentrations expressed by igneous rocks. These results suggest multiple protoliths for the metasomatite.

4.4 Mineral Chemistry

Mineral chemistry was determined by electron microprobe on thirteen specimens selected from a variety of K-metasomatized rocks at NICO. Analytical procedures are given in Section 1.2. The sample suite included K-metasomatized layering within biotite-amphibole-magnetite metasomatic rock, patchy K-metasomatism of meta-arenite, variable K-metasomatic effects overprinting feldspar porphyry and potassium feldspar metasomatite. A total of 206 analyses are reported on the following mineral species: feldspar, amphibole, biotite, chlorite, epidote, apatite and rutile. The mineral chemical analyses are presented in Appendix 3.

4.4.1 Feldspar Group Minerals

Feldspar group minerals are a ubiquitous component within altered Treasure Lake Group metasedimentary rocks, Lou Lake volcanic rocks, and Great Bear intrusive rocks, particularly within the vicinity of the NICO deposit. Compositions of feldspars from several lithologies were analyzed to constrain and compare the effects of K-metasomatism. A ternary plot of all feldspar compositions (Figure 4.11) indicates a compositional range from $An_{16}Ab_{83}$ to Or_{100}, with most results clustering near end members albite and orthoclase. To better assess

these results, compositions have been divided into two groups: a) feldspar species from feldspar porphyry exhibiting effects of K-metasomatism, and b) feldspar species from K-metasomatized metasedimentary rock and domains of potassium feldspar metasomatite.

a) Feldspar Porphyry

The highly variable effects of K-metasomatism on porphyry dyke mineralogy generally exhibit greater intensity at boundaries with lesser effects inward. To critically characterize these effects, samples were selected from least altered, moderately altered and intensely altered zones based on petrography and bulk rock geochemistry. Individual results distinguish phenocryst cores and intergrowths from overgrowth and replacement textures, and very fine grained porphyry groundmass. As illustrated in Figures 4.12 and 4.13 respectively, phenocrysts and overgrowth textures demonstrate distinct populations with compositions concentrated near end member albite and end member orthoclase. Groundmass feldspars plotted in Figure 4.14 demonstrate insignificant compositional differences between the variably altered zones.

Coarse grained plagioclase phenocrysts within least altered porphyry are characterized by oligoclase cores high in SiO_2 and Al_2O_3 with moderate Na_2O and CaO, and low K_2O and BaO (see Table 4.1, column 1). As demonstrated by backscatter imagery (see Figure 4.15), these phenocrysts transition to albite at grain margins. Coarse grained plagioclase phenocrysts within moderately altered porphyry are higher in SiO_2, Na_2O and K_2O with lower Al_2O_3 and CaO compared to least altered equivalents (see Table 4.1, column 2). This subtle Na enrichment is best demonstrated by average An:Ab:Or ratios of $An_{12}Ab_{87}Or_1$ for plagioclase phenocrysts within least altered porphyry to $An_3Ab_{95}Or_2$ for those within
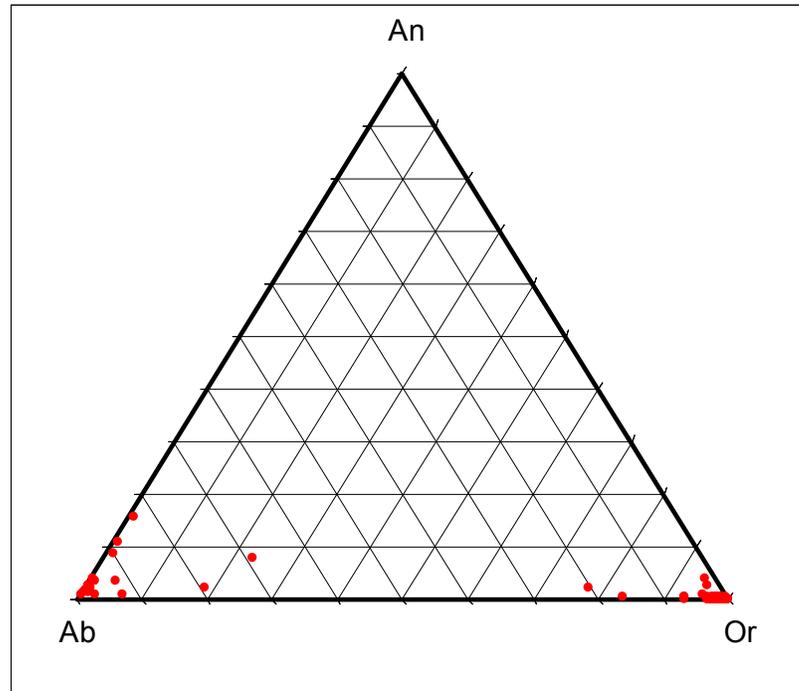
Figure 4.11 – Ternary diagram for system An-Ab-Or demonstrating the compositional range of all feldspars probed from all samples.
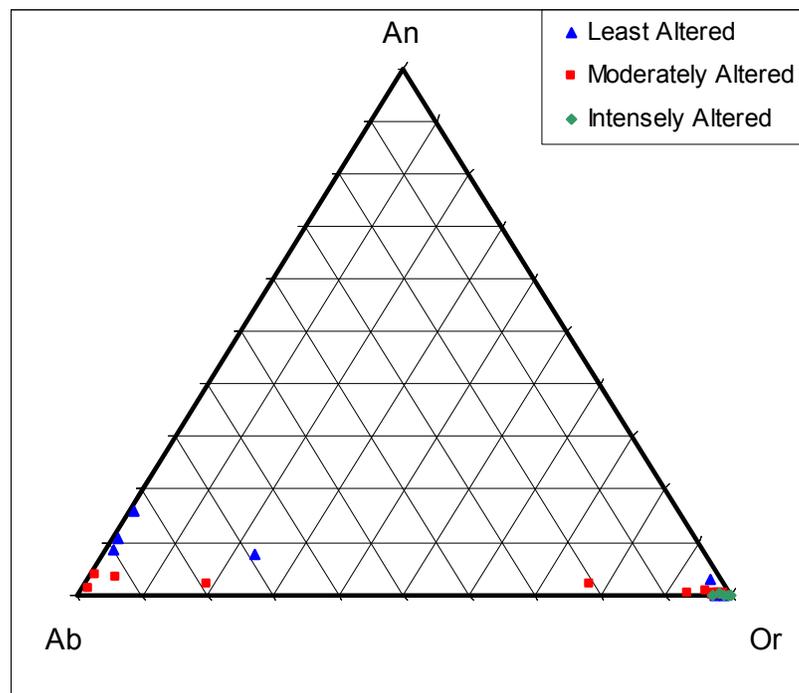
Figure 4.12 – Ternary diagram of probed feldspar phenocryst cores and intergrowths from samples of variably altered feldspar porphyry dyke, plotted within the system An-Ab-Or.
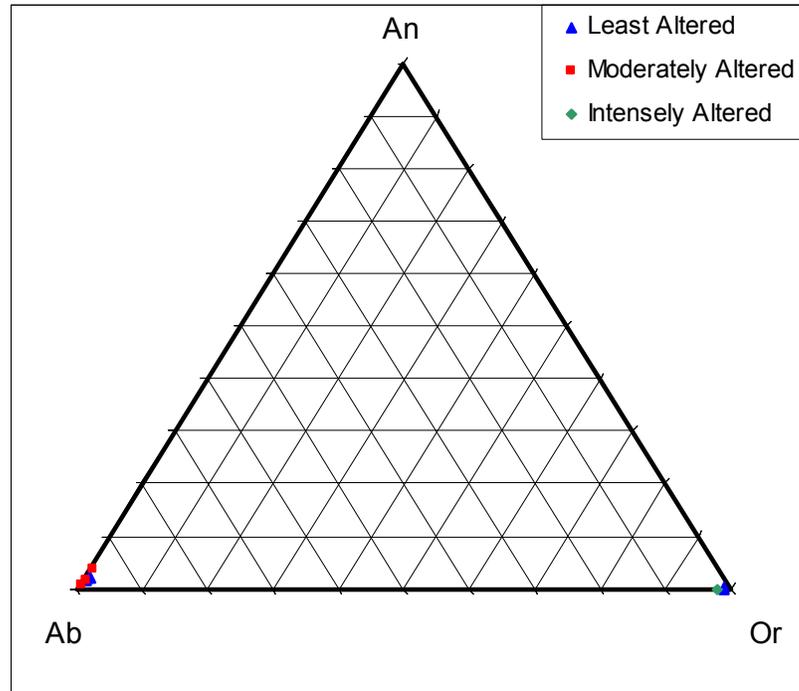
Figure 4.13 – Ternary diagram of probed feldspar phenocryst margins and overgrowths from samples of variably altered feldspar porphyry dyke, plotted within the system An-Ab-Or.
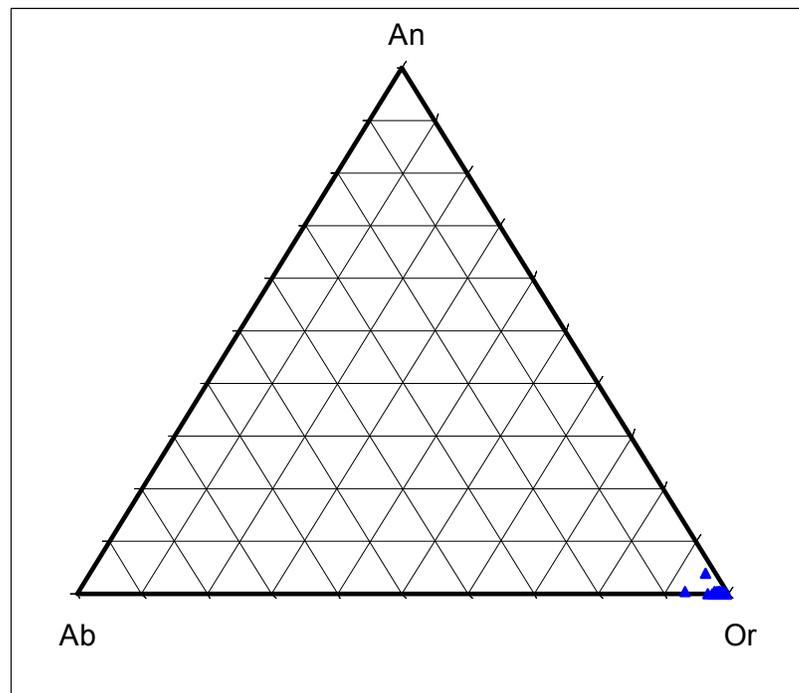
Figure 4.14 – Ternary diagram of porphyry groundmass composition plotted within the system An-Ab-Or.

Table 4.1 – Compositional details for plagioclase and alkali feldspar species.

	1	2	3	4	5
SiO_2	64.54	68.65	67.60	63.94	65.18
Al_2O_3	21.47	18.81	19.11	22.88	18.75
CaO	2.45	0.59	0.45	0.95	0.41
Na_2O	10.18	11.30	12.26	8.19	2.19
K_2O	0.21	0.40	0.15	3.54	12.54
BaO	0.09	0.00	0.01	0.06	0.45
TOTAL	98.93	99.75	99.58	99.55	99.52
Number of ions on the basis of 32 O					
Si	11.49	12.04	11.92	11.47	11.97
Al	4.51	3.89	3.97	4.80	4.06
Ca	0.47	0.11	0.09	0.18	0.08
Na	3.52	3.84	4.19	2.83	0.78
K	0.05	0.09	0.03	0.80	2.94
Ba	0.01	0.00	0.00	0.00	0.03
Z	15.99	15.92	15.89	16.02	16.00
X	4.04	4.06	4.32	4.10	3.86
Mole Percent					
An	11.58%	2.74%	1.98%	4.76%	2.12%
Ab	87.25%	95.04%	97.23%	74.18%	20.54%
Or	1.17%	2.21%	0.79%	21.07%	77.34%

1. *Plagioclase phenocryst compositions (oligoclase) sampled from least altered porphyry (average composition, n = 3).*
2. *Plagioclase phenocryst compositions (albite) sampled from moderately altered porphyry (average composition, n = 3).*
3. *Composition of albite overgrowths sampled from variably altered porphyry (average composition, n = 6).*
4. *Cryptic antiperthite intergrowths (anorthoclase) from plagioclase phenocrysts sampled from moderately altered porphyry (average composition, n = 2).*
5. *Cryptic antiperthite intergrowth (microcline) within plagioclase phenocryst (sample GR-06-011W).*

moderately altered porphyry. Chemical compositions indicate K content increases from approximately 0.05 to 0.09 atoms per unit cell from least altered to moderately altered zones. Calculations are based on 32 oxygen atoms in the unit cell.

Cryptic antiperthite intergrowths within plagioclase phenocrysts were detected by microprobe analysis, as illustrated by backscatter image (Figure 4.16, analysis 2). These intergrowths show several distinct compositions: anorthoclase (Table 4.1, column 4) and microcline (Table 4.1, column 5). Anorthoclase occurs as fine to very fine intergrowths characterized by low SiO_2, high Al_2O_3, intermediate CaO, Na_2O and K_2O, and low BaO. Though the sampled anorthoclase intergrowth population is small, results show significant range of cation substitution within M and T sites based upon the unit formula MT_4O_8 defined by Smith and Brown (1988, pg. 4). M-site cation substitution ranges from 0.08 to 0.28 Ca, 2.54 to 3.11 Na, and 0.74 to 0.86 K atoms per unit cell. T-site cation substitution ranges from 11.07 to 11.87 Si and 4.35 to 5.25 Al atoms per unit cell. Aluminum, Ca, K and Ba values decrease while Si and Na increase from least to moderately altered varieties. The T-site substitution accounts for significant change in Al : Si proportions from 1 : 2.1 in least altered to 1 : 2.7 in moderately altered domains, indicative of a coupled ion exchange resulting from albitization of intergrowths.

Microcline intergrowths (Table 4.1, column 5) are coarser and have irregular shapes and non-uniform distribution within cores of albite phenocrysts. Moderate values of SiO_2, Al_2O_3, Na_2O, K_2O and BaO result from potassium feldspar stoichiometry. Phenocrysts of anorthoclase and microcline antiperthitic intergrowths suggest high temperature hypersolvus phases that exsolved on cooling.

Backscatter images of overgrowths on coarse grained plagioclase phenocrysts (Figure 4.16, analysis 4) show end member albite compositions. Average compositional values are detailed in column 3, Table 4.1. Compositional zonation toward albite demonstrated by the coarse grained plagioclase phenocrysts, coupled with end member albite overgrowths suggests albitization took place before the onset of K-metasomatism.

Potassium feldspar phenocrysts exhibit relatively homogenous compositions that plot at end member orthoclase (see Figure 4.12). The abundance of this species increases substantially between least to intensely altered zones of porphyry. Within least and moderately altered zones, potassium feldspar most commonly occurs as incipient marginal replacement of plagioclase phenocrysts or overgrowths. Figure 4.16 (analyses 3 and 5) well demonstrates the infiltration of incipient fine grained potassium feldspar which overprints albite overgrowths and phenocryst margins. Within intensely altered zones plagioclase phenocrysts are nearly completely replaced by potassium feldspar. Incipient potassium feldspar and completely replaced phenocrysts exhibit nearly uniform compositions of approximately Or_{98}. Backscatter images reveal very fine grained potassium feldspar and quartz form substantial coronas around potassium feldspar phenocrysts (Figure 4.18), showing similarly uniform compositions of approximately Or_{98}. Average compositional data for potassium feldspar phenocrysts and coronas are summarized in columns 6, 7, 8 and 9 of Table 4.2.

Fine grained potassium feldspar from the porphyry groundmass exhibits an insignificant compositional range from least, moderately and intensely altered zones. Groundmass compositions at approximately Or_{98} (Table 4.2, column 10) are comparable to those reported for potassium feldspar overgrowths. Potassium feldspar phenocrysts, coronas

Table 4.2 – Compositional details for plagioclase and alkali feldspar species.

	6	7	8	9	10
SiO_2	64.23	65.29	65.90	65.48	65.10
Al_2O_3	18.95	17.98	17.70	18.21	18.29
CaO	15.95	15.98	16.09	0.01	0.03
Na_2O	0.13	0.03	0.01	0.16	0.17
K_2O	0.23	0.29	0.12	15.57	16.23
BaO	0.75	0.31	0.21	0.43	0.20
TOTAL	100.23	99.88	100.03	99.86	100.02
Number of ions on the basis of 32 O					
Si	11.90	12.07	12.15	12.08	12.03
Al	4.13	3.92	3.85	3.96	3.98
Ca	0.03	0.01	0.00	0.00	0.01
Na	0.08	0.10	0.04	0.06	0.06
K	3.77	3.77	3.78	3.67	3.83
Ba	0.05	0.02	0.02	0.03	0.01
Z	15.99	15.97	15.98	16.00	15.97
X	3.97	3.96	3.86	3.80	3.94
Mole Percent					
An	0.66%	0.17%	0.06%	0.04%	0.17%
Ab	2.09%	2.69%	1.12%	1.51%	1.53%
Or	97.25%	97.14%	98.82%	98.46%	98.29%

6. *Potassium feldspar phenocryst compositions sampled from least altered porphyry (average composition, n = 5).*
7. *Potassium feldspar phenocryst compositions sampled from moderately altered porphyry (average composition, n = 9).*
8. *Potassium feldspar phenocryst compositions sampled from intensely altered porphyry (average composition, n = 6).*
9. *Composition of potassium feldspar overgrowths sampled from variably altered porphyry (average composition, n = 3).*
10. *Composition of very fine grained alkali feldspar sampled from porphyry groundmass (average composition, n = 34).*
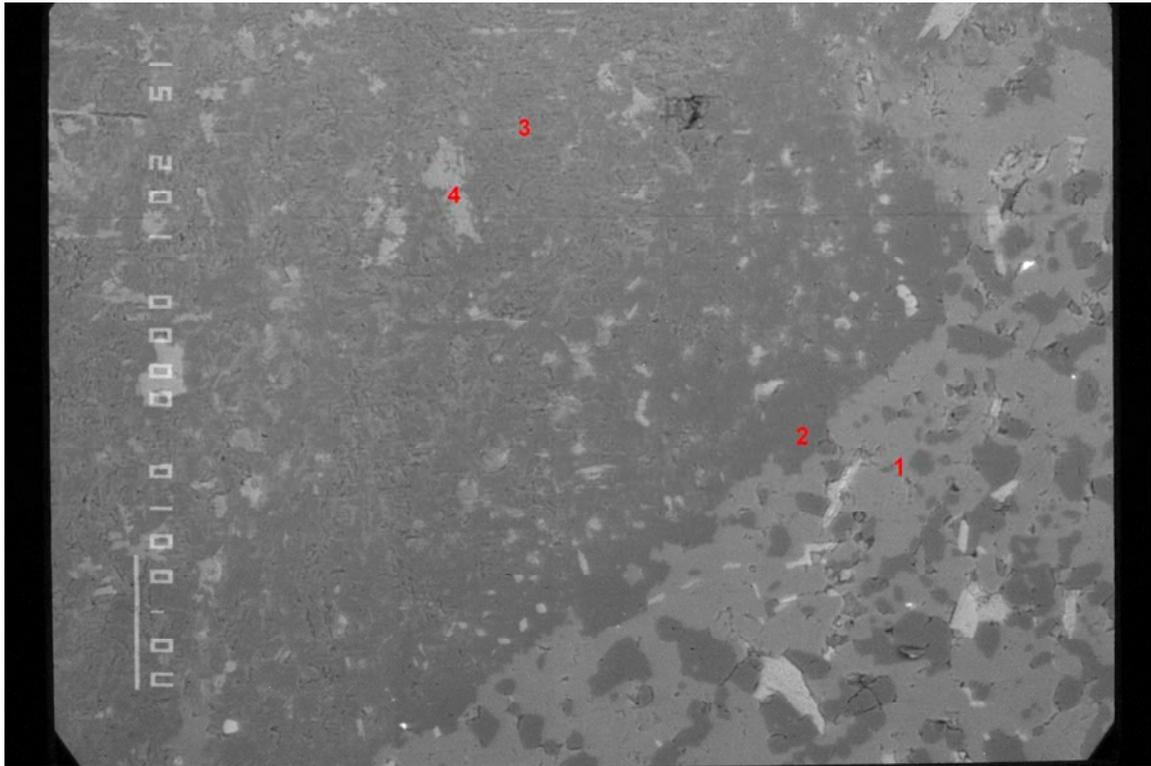
Figure 4.15 - Backscatter image of euhedral plagioclase phenocryst from least altered zone of feldspar porphyry. Individual microprobe analyses are identified in sequence on the image as follows: (1) very fine grained potassium feldspar groundmass [Or_{99}], (2) margin of plagioclase phenocryst [An_2Ab_{97}], (3) core of plagioclase phenocryst [$An_{11}Ab_{88}$], (4) epidote inclusion within plagioclase phenocryst. Image from sample GR-06-027W.
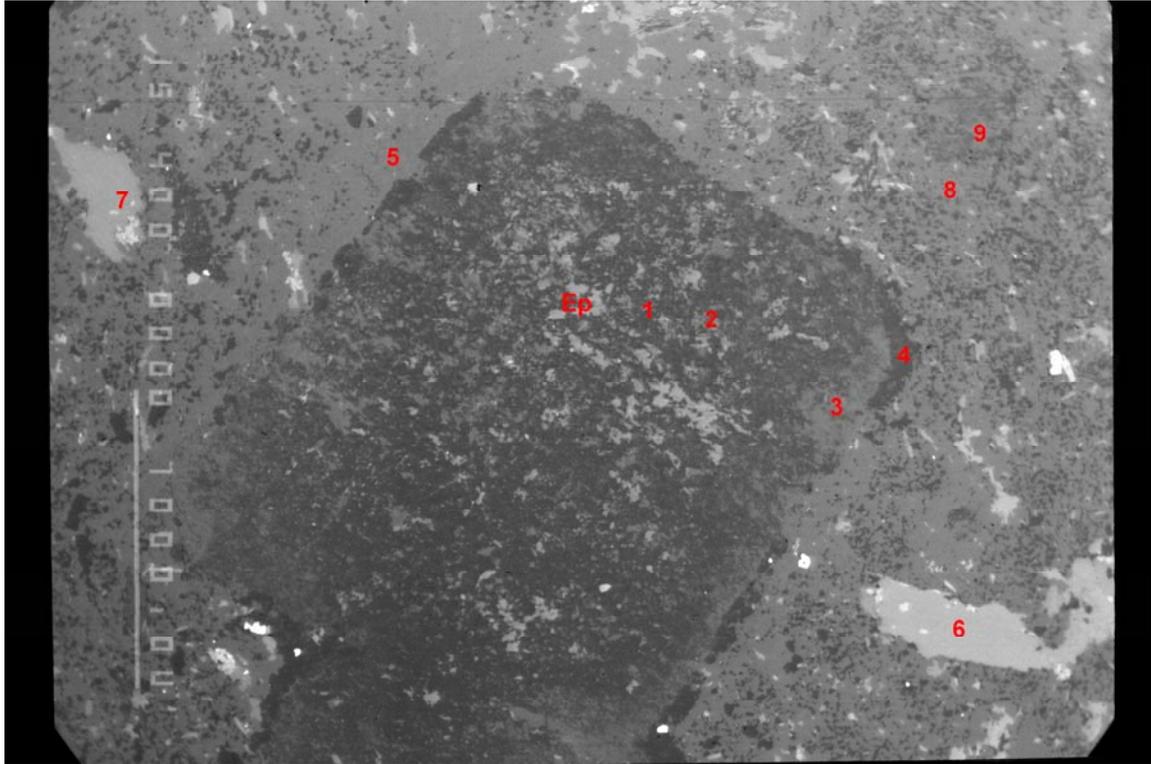
Figure 4.16 – Backscatter image of euhedral plagioclase phenocryst from a moderately altered zone of feldspar porphyry exhibiting enhanced porosity, albite overgrowth and incipient K-feldspar replacement along margins. Individual microprobe analyses are identified in sequence on the image as follows: (1) core of plagioclase phenocryst [An_1Ab_{98}], (2) microcline antiperthite intergrowth within plagioclase phenocryst [$An_2Ab_{21}Or_{77}$], (3) fine grained potassium feldspar incipient at phenocryst margin [Or_{98}], (4) albite overgrowth [An_2Ab_{97}], (5) very fine grained potassium feldspar groundmass [Or_{98}], (6,7) Fe-chlorite replacement of biotite, (8) very fine grained potassium feldspar groundmass [Or_{98}], (9) very fine grained potassium feldspar groundmass [Ab_7Or_{93}]. (Ep) Epidote inclusions (re: light grey) are concentrated within phenocryst cores indicative of saussuritization. The bright, fine grained inclusions within the overgrowth and porphyry groundmass are magnetite. Image from sample GR-06-005W2.
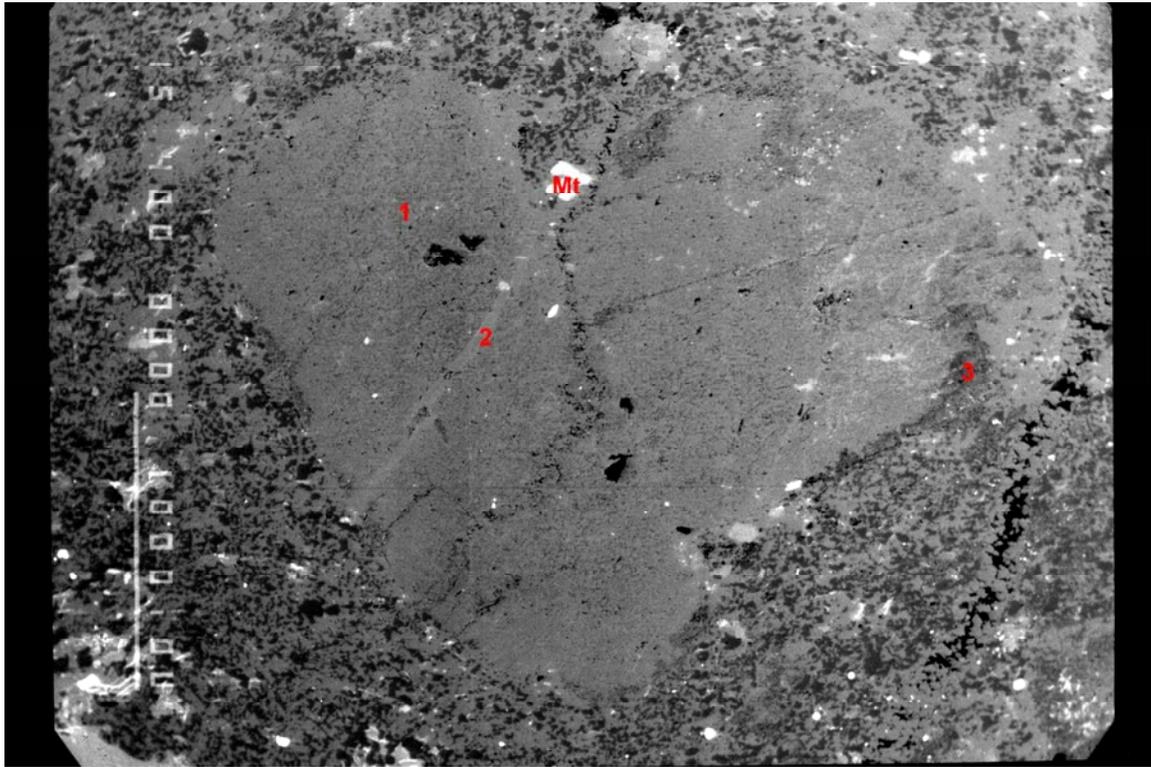
Figure 4.17 – Backscatter image of potassium feldspar cumulocryst from intensely altered of feldspar porphyry exhibiting nearly uniform feldspar composition, enhanced microporosity, crenulated margins and a substantial corona of fine grained potassium feldspar + quartz. Individual microprobe analyses are identified in sequence on the image as follows: (1) dominant darker grey potassium feldspar phenocryst core [Or_{100}], (2) lighter pink potassium feldspar band that transects phenocryst [Or_{97}], (3) very fine grained potassium feldspar within corona [Or_{99}], (Mt) magnetite inclusion within the corona. Image from sample GR-06-005E.

and groundmass collectively show limited cation substitution in M-sites with 0 to 0.03 Ca, 0.04 to 0.10 Na and 0.01 to 0.05 Ba atoms per unit cell. The end member orthoclase composition exhibited by potassium feldspar phenocrysts, overgrowths and groundmass is interpreted to be a product of K-metasomatism.

b) Other Metasomatic Feldspar Species

Pervasive textural destruction and mineralogical replacement by potassium feldspar is a characteristic effect of K-metasomatism at NICO. To quantitatively characterize this effect, samples of potassium feldspar metasomatite were selected from several locations exhibiting local and pervasive replacement of various lithologies. Feldspar compositions have been plotted on separate An:Ab:Or ternary diagrams.

End member albite and orthoclase species were identified from bands of potassium feldspar replacement within biotite amphibolite. These results are plotted in Figure 4.18, with orthoclase compositions summarized in column 11 of Table 4.3. A backscatter image of a portion of a replaced band (re: Figure 4.22) shows that ultra fine grained potassium feldspar with uniform compositions at Or_{99} comprises the dominant phase. Figure 4.19 shows compositionally similar feldspar populations exist within K-metasomatized subarenite (Table 4.3, column 12). Though mineralogically similar, replaced patches show minor variation between Or_{93} to Or_{100}. Chemical compositions of both sampled populations indicate limited cation substitution in M-sites of 0.06 to 0.11 Na and 0.02 Ba atoms per unit cell.

Islands of end member albite with uniform compositions at Ab_{96} were identified by microprobe analysis within K-metasomatized bands and patches (Figure 4.22, analyses 7 and
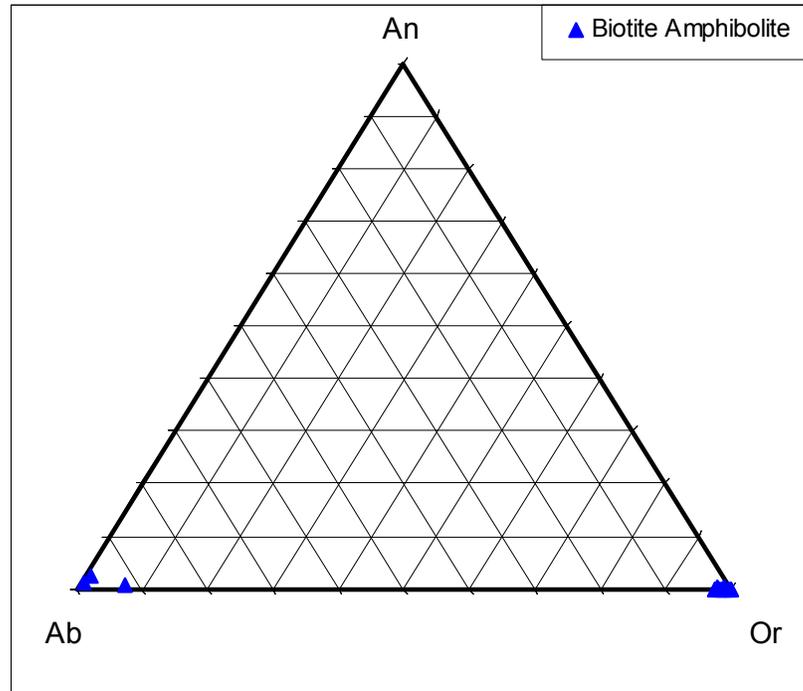
Figure 4.18 – Ternary diagram for compositions of banded potassium feldspar replacement sampled from biotite-amphibolite metasomatic rock plotted within the system An-Ab-Or.
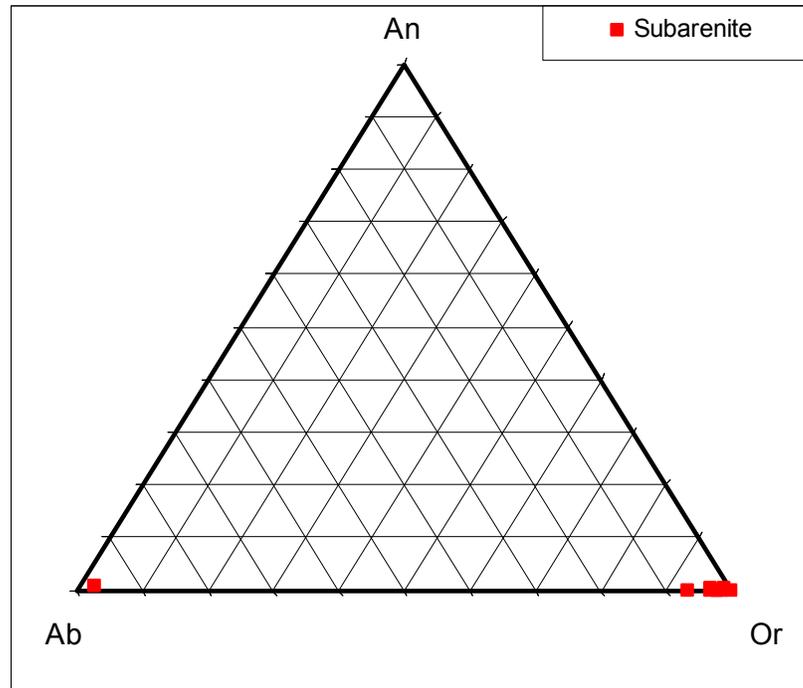
Figure 4.19 – Ternary diagram for compositions of patchy potassium feldspar replacement sampled from meta-arenite plotted within the system An-Ab-Or.
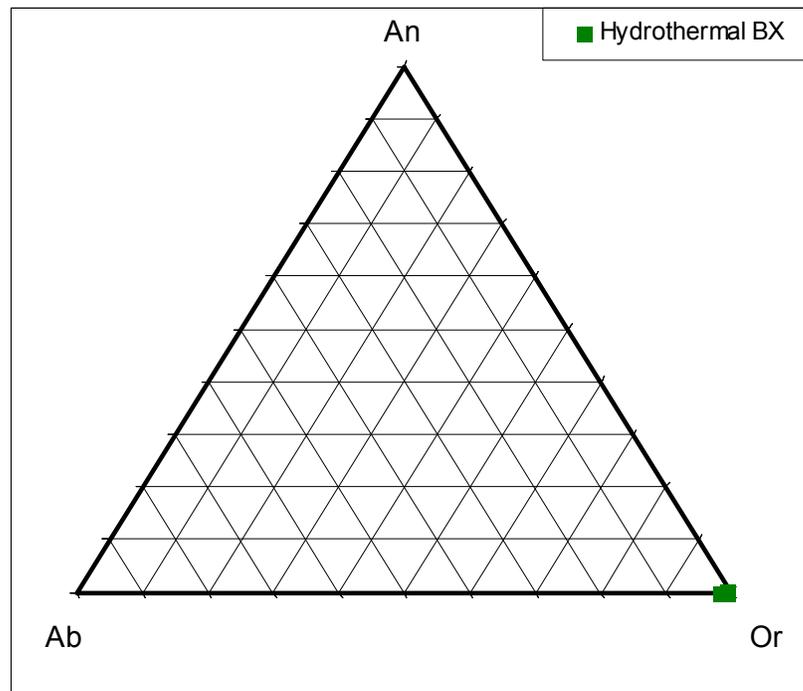
Figure 4.20 – Ternary diagram for compositions of potassium feldspar sampled from breccia fragments. Compositions are plotted within the system An-Ab-Or.
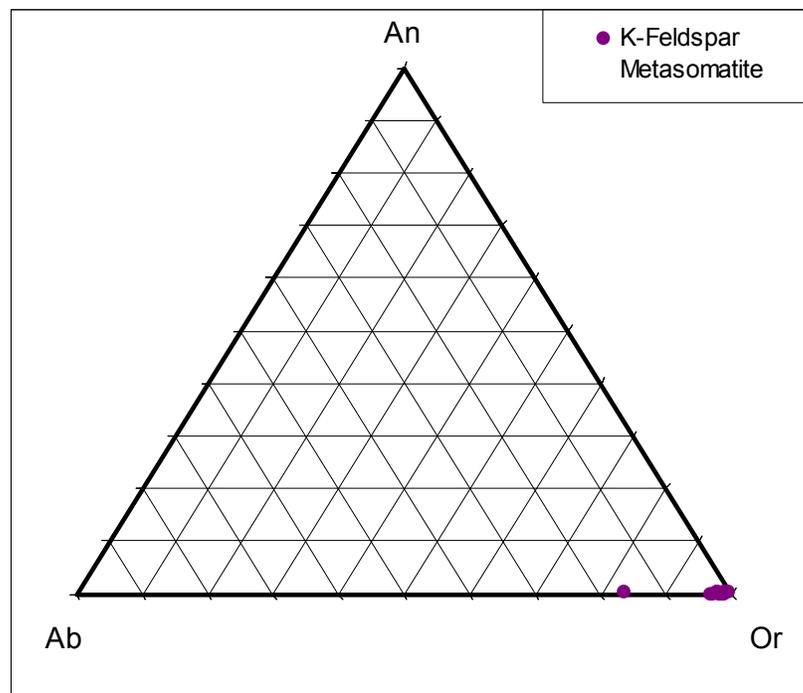
Figure 4.21 – Ternary diagram for compositions of potassium feldspar sampled from potassium feldspar metasomatite. Compositions are plotted within the system An-Ab-Or.

Table 4.3 – Compositional details for plagioclase and alkali feldspar species.

	11	12	13	14	15
SiO_2	63.79	64.04	66.73	63.87	65.12
Al_2O_3	17.18	17.98	20.33	18.60	18.30
CaO	0.01	0.01	0.30	0.00	0.02
Na_2O	0.16	0.30	11.90	0.12	0.30
K_2O	18.84	17.61	0.50	17.27	16.25
BaO	0.23	0.33	0.01	0.14	0.24
TOTAL	100.21	100.26	99.77	100.01	100.23
Number of ions on the basis of 32 O					
Si	11.99	11.95	11.76	11.89	12.02
Al	3.80	3.95	4.22	4.08	3.98
Ca	0.00	0.00	0.06	0.00	0.00
Na	0.06	0.11	4.07	0.04	0.11
K	4.52	4.19	0.11	4.10	3.83
Ba	0.02	0.02	0.00	0.01	0.02
Z	15.79	15.90	15.98	15.96	15.99
X	4.60	4.32	4.24	4.17	3.99
Mole Percent					
An	0.03%	0.05%	1.34%	0.02%	0.08%
Ab	1.29%	2.53%	96.01%	1.06%	2.75%
Or	98.68%	97.42%	2.65%	98.92%	97.17%

11. *Banded, ultra-fine grained potassium feldspar replacement sampled from biotite-amphibole metasomatic rock (average composition, n = 15).*
12. *Patchy potassium feldspar replacement sampled from subarenite (average composition, n = 8).*
13. *Plagioclase 'islands' sampled from local potassium feldspar replacement within metasedimentary rocks (average composition, n = 4).*
14. *Potassium feldspar metasomatite clasts sampled from breccia (average composition, n = 6).*
15. *Very fine grained potassium feldspar sampled from potassium feldspar metasomatite (average composition, n = 13).*
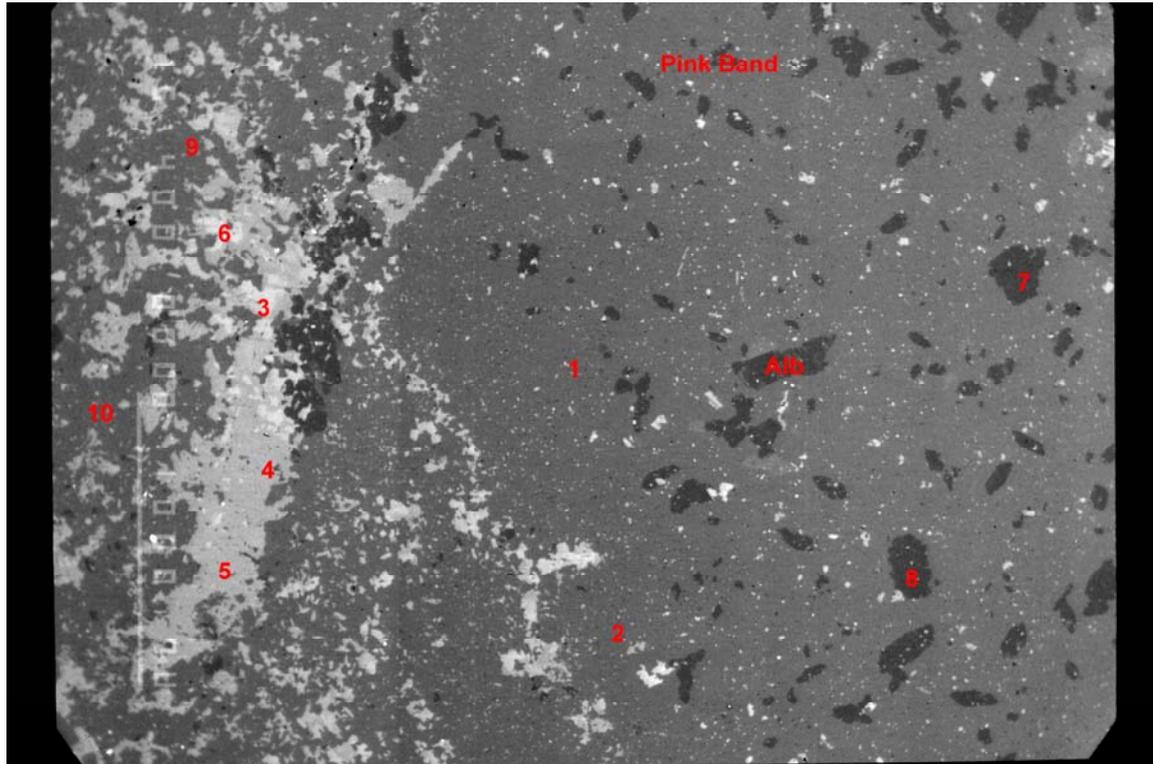
Figure 4.22 – Backscatter image of a portion of potassium feldspar band (right hemisphere of photo) within metasomatized sedimentary rock showing islands of albite composition (darker shade of grey) preserved within the band. Individual microprobe analyses are identified in sequence on the image as follows: (1,2) very fine grained potassium feldspar within pink band [Or$_{99}$], (3) lighter grey island of Fe-rich amphibole within adjacent band, (4,5) Fe,Mg-rich amphibole comprising the dominant phase within adjacent band, (6) another lighter grey island of Fe-rich amphibole within adjacent band, (7) albite island preserved within the potassium feldspar band [An$_1$Ab$_{98}$], (8) albite island preserved within the potassium feldspar band [An$_2$Ab$_{97}$], (9) albite composition matrix beyond band boundary [An$_2$Ab$_{97}$], (10) very fine grained potassium feldspar matrix beyond band boundary [Or$_{98}$]. The rare bright sparkles along the left hemisphere are occurrences of very fine grained thorium silicate that were too small to probe. Sample from GR-06-011W.
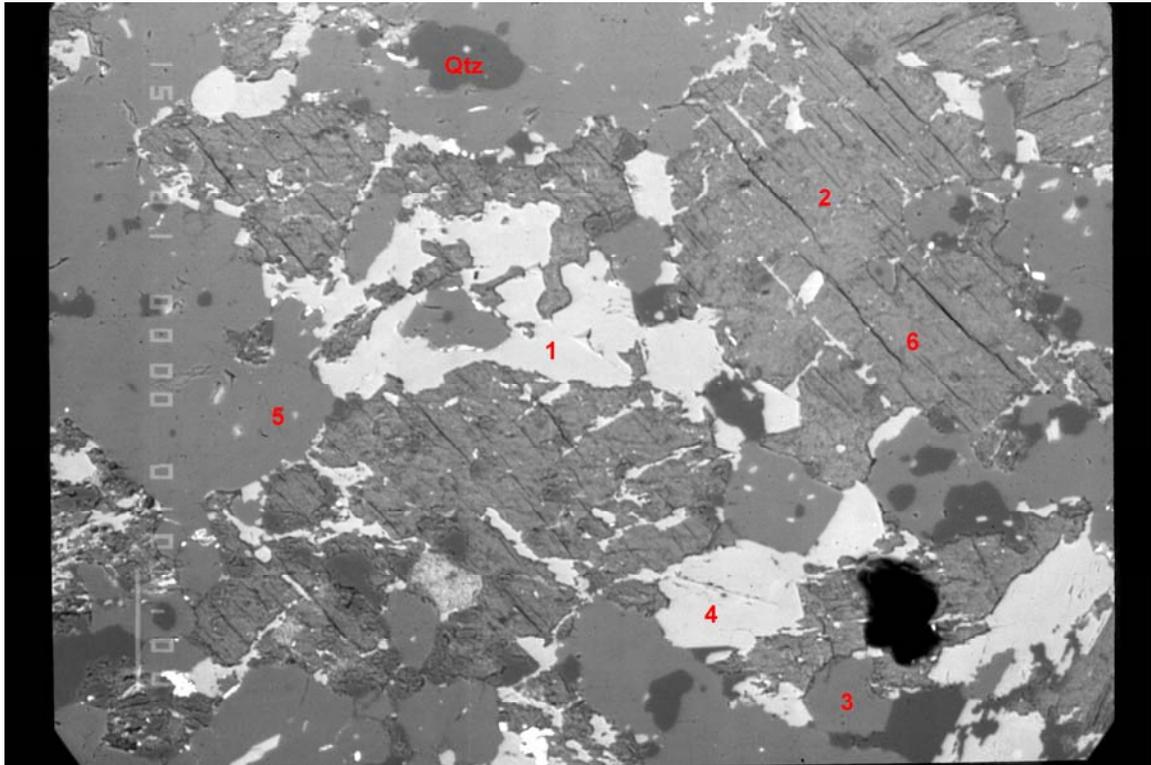
Figure 4.23 – Backscatter image of hydrothermal breccia sampled proximal to feldspar porphyry. Individual microprobe analyses are identified in sequence on the image as follows: (1) calc-amphibole breccia matrix, (2) Mg-Fe amphibole within fragment, (3) very fine grained potassium feldspar fragment [Or98], (4) calc-amphibole breccia matrix, (5) very fine grained potassium feldspar fragment [Or99], (6) Mg-Fe amphibole within fragment (Qtz) quartz fragment. Sample from GR-07-085C.
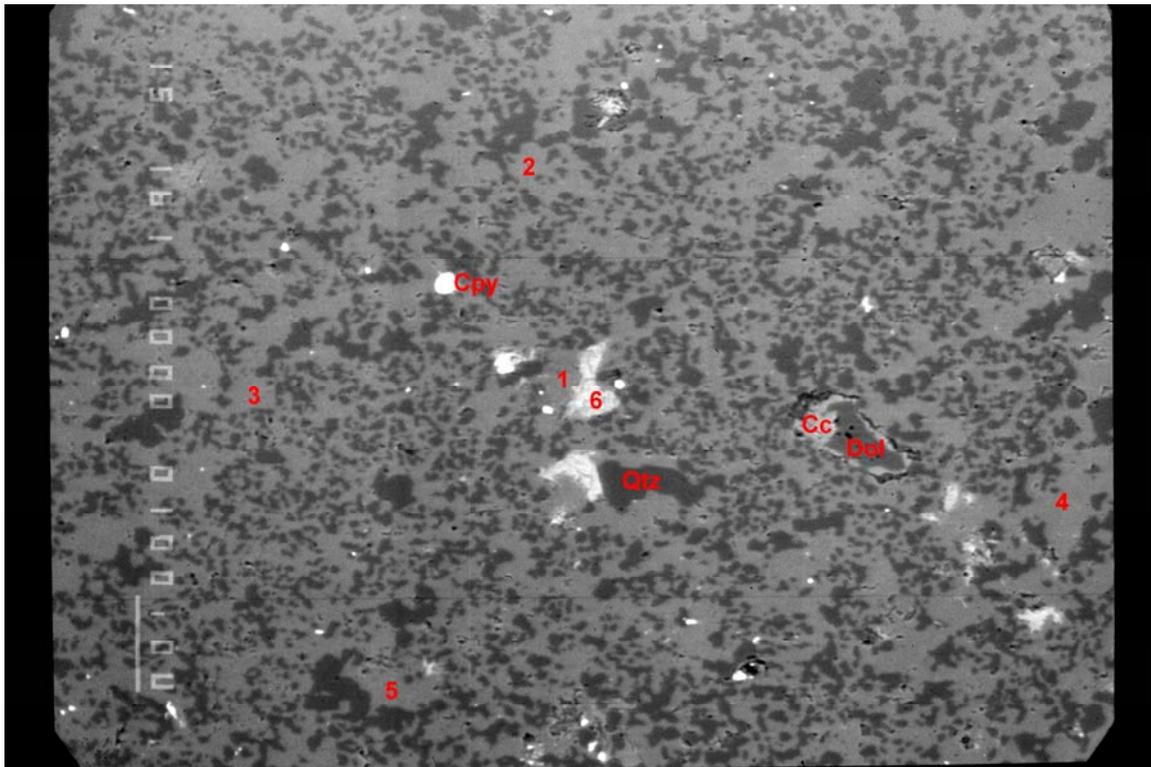
Figure 4.24 – Backscatter image of a portion of a nebulous relic preserved within the potassium feldspar metasomatite. Individual microprobe analyses are identified in sequence on the image as follows: (1,2) very fine grained potassium feldspar matrix [Or_{99}], (3) very fine grained potassium feldspar matrix [$Ab_{16}Or_{84}$], (4,5) very fine grained potassium feldspar matrix [Or_{98-99}], (6) fine grained inclusion of Fe-chlorite, (Cc) fine grained inclusion of calcite (darker grey), (Cpy) fine grained inclusions of chalcopyrite (bright spots), (Dol) fine grained inclusions of dolomite (darker grey), (Qtz) numerous inclusions of quartz within the metasomatite (medium grey). Sample from GR-07-087.

8). This species is characterized by high SiO_2 and Na_2O, moderate Al_2O_3, low CaO & K_2O. Compositions of this albitic phase are summarized in column 13 of Table 4.3. The Na-rich phase exhibits irregular morphologies with sutured boundaries. The compositional disequilibrium and overall texture is interpreted as the incomplete potassium feldspar replacement of an earlier phase that had equilibrated at Na-rich conditions.

Feldspar species from lobate clasts within hydrothermal breccia show uniform compositions at Or_{99}. Results are plotted in Figure 4.20, with compositional data detailed in Table 4.3, column 14. This species is characterized by high SiO_2 and K_2O, moderate Al_2O_3, low Na_2O and BaO. The textural and compositional evidence indicates brecciation occurred post potassium feldspar replacement.

Feldspar species analyzed from potassium feldspar metasomatite, though generally homogenous, demonstrate local compositional heterogeneity within patches where nebulous relics are preserved. Results are plotted as An:Ab:Or ratios in Figure 4.21 and summarized in column 15 of Table 4.3. Generally, the metasomatite is dominated by near end member orthoclase replacement (range from Or_{97} to Or_{99}). However, detection of a potassium feldspar phase with an $Ab_{16}Or_{84}$ composition (Figure 4.24, analysis 3) indicates a local disequilibrium and may result from several phases with grain size too small to probe. This is interpreted as evidence of incomplete replacement where ghosts exist within the metasomatite.

4.4.2 Amphibole Group Minerals

Amphibole group minerals are widely distributed throughout many lithologies of the NICO area. Species were probed from: a) biotite-amphibole-magnetite metasomatic rock,

where amphibole occurs as matrix bounding K-metasomatized bands; b) breccia, where amphibole comprises a primary constituent of both matrix and fragments; and c) potassium feldspar metasomatite, where amphibole occurs in preserved fragments. Amphiboles were classified on the basis of mineral chemistry according to the nomenclature scheme of Leake et al. (1997 & 2004) using the standard amphibole formula $AB_2{}^{VI}C_5{}^{IV}T_8O_{22}(OH)_2$. Formulas were solved with calculations based upon 22(O) making no assumption for water or halogen content to prevent not being able to satisfy the criteria specified by Leake et al. (1997). Specifically, calculations based upon 24(O,OH,F,Cl) or 23(O) with 1 or 2(OH,F,Cl) prevent solutions for T- and B-sites from meeting the established formula maxims for Si and Ca respectively. Iron is reported as FeO, and as indicated by Leake et al. (1997), an uncertainty arises in the determination of Fe^{2+} and Fe^{3+}. Ferrous and ferric cation content is calculated following the procedure of Rock & Leake (1984) primarily for the purpose of naming the amphibole.

Mg-Fe amphiboles were identified by backscatter image within breccia where they comprise the primary component of fragments (Figure 4.23, analyses 2 & 6). These clasts show generally complex morphologies characterized by irregular boundaries and embayments suggestive of corrosion (see Jebrak, 1997). Optically the weakly pleochroic brown amphibole clast component occurs as subhedral columnar aggregates. Figure 4.25A shows Mg-Fe amphibole compositions fall within the anthophyllite field. Chemical compositions show this species is enriched in silicon (7.7 to 7.8 atoms per formula unit), apparently at the expense of tetrahedral aluminum which show contents ranging from 0.15 to 0.28 atoms per formula unit with aluminum occupancy roughly divided between T- and C-sites. Apart from aluminum, these amphiboles are otherwise depleted in M-type cations, with C-site occupancy largely

filled by magnesium (3.9 to 4.1 atoms per formula unit). Calculations show moderate ferric iron enrichment with no ferrous content indicative of reducing conditions; occupancy is approximately split between C- (0.92 to 1.1 atoms) and B-sites (0.88 to 1.0 atoms). The anthophyllite compositions show limited alkali substitution in B-sites (0.04 to 0.10 Ca atoms and 0.06 to 0.07 Na atoms) and the A-site (0.02 to 0.06 K atoms). Aluminum:alkali ratios are relatively consistent between 1.9 to 2.2. Halide substitution is similarly limited, with trace chlorine (0 to 0.01 atoms) and weak fluorine (0.04 to 0.22 atoms) enrichment.

Calcic amphiboles were identified from all sampled lithologies, with compositions plotted in the appropriate classification diagram illustrated in Figures 4.25B, C and D. Generally the calcic amphiboles have limited sodium and potassium content, with results clustering in the ferrohornblende and ferro-actinolite fields of Figure 4.25B. Where sodium and potassium substitution within A-sites is greater than 0.50 atoms per formula unit, calcic amphiboles have been plotted within alternate schemes. Those with detected Al^{VI} content greater than or equal to calculated Fe^{3+} content plot within the ferropargasite field illustrated by Figure 4.25C. Those with calculated Fe^{3+} content greater than detected Al^{VI} content are plotted in Figure 4.25D, and show a compositional range between hastingsite to ferro-edenite. Sodium (up to 0.43 atoms per formula unit) and potassium enrichment (up to 0.48 atoms per formula unit) exhibited by the majority of those amphiboles plotted in Figures 4.25C and D indicates 'sodian' and 'potassian' modifiers are applicable.

Calcic amphiboles sampled from biotite-amphibole metasomatic rock and breccia matrix occur as fine grained anhedral and irregular green coloured grains showing light blue-green to grey-green pleochroism. They comprise the dominant phase of layers bounding K-metasomatized bands, as illustrated by backscatter image (Figure 4.22, left hemisphere),
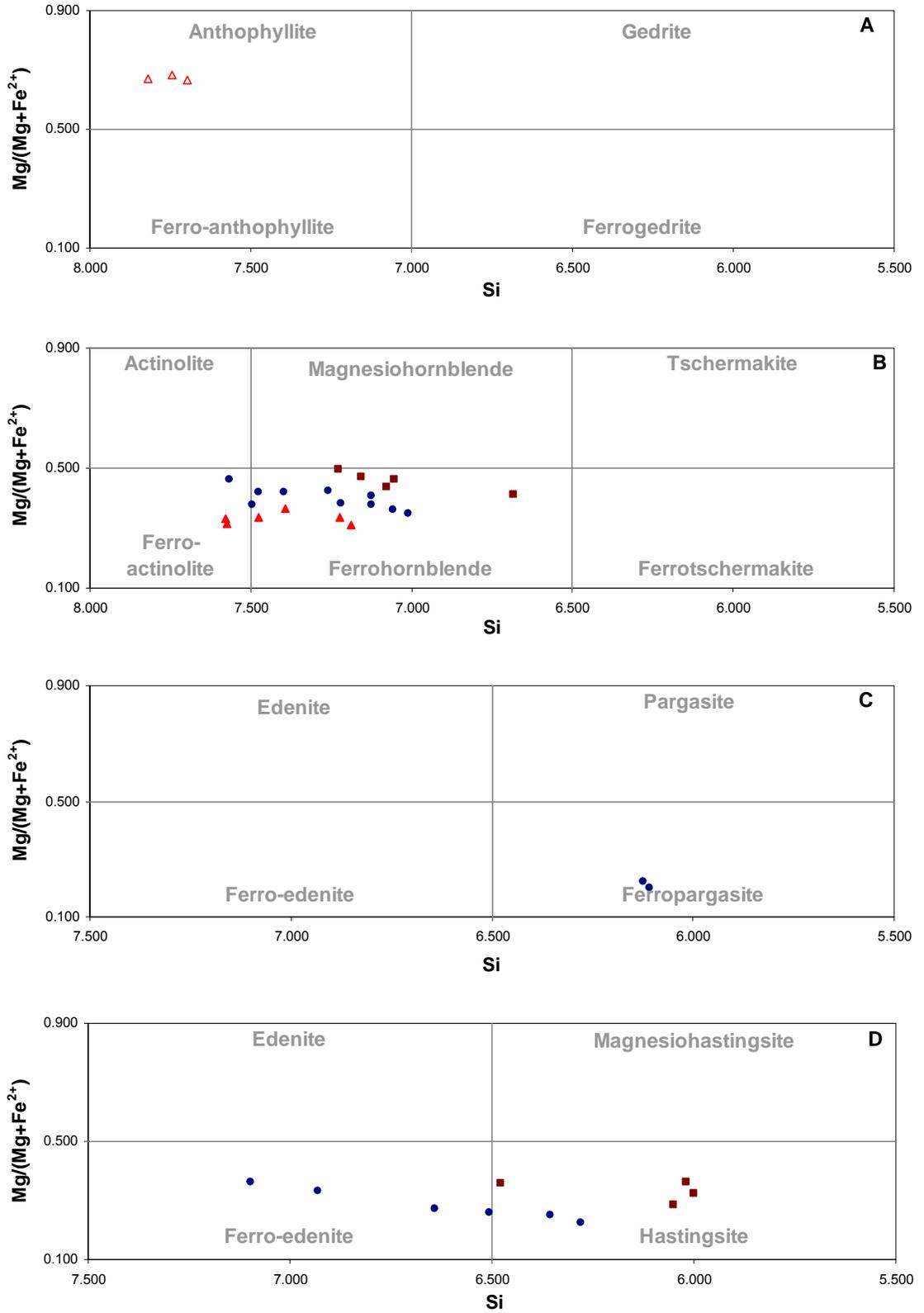
Legend: ●Biotite-amphibole ▲Breccia matrix △ Breccia fragments ■Metasomatite

Figure 4.25 – Amphibole composition classification diagrams (after Leake et al., 1997).
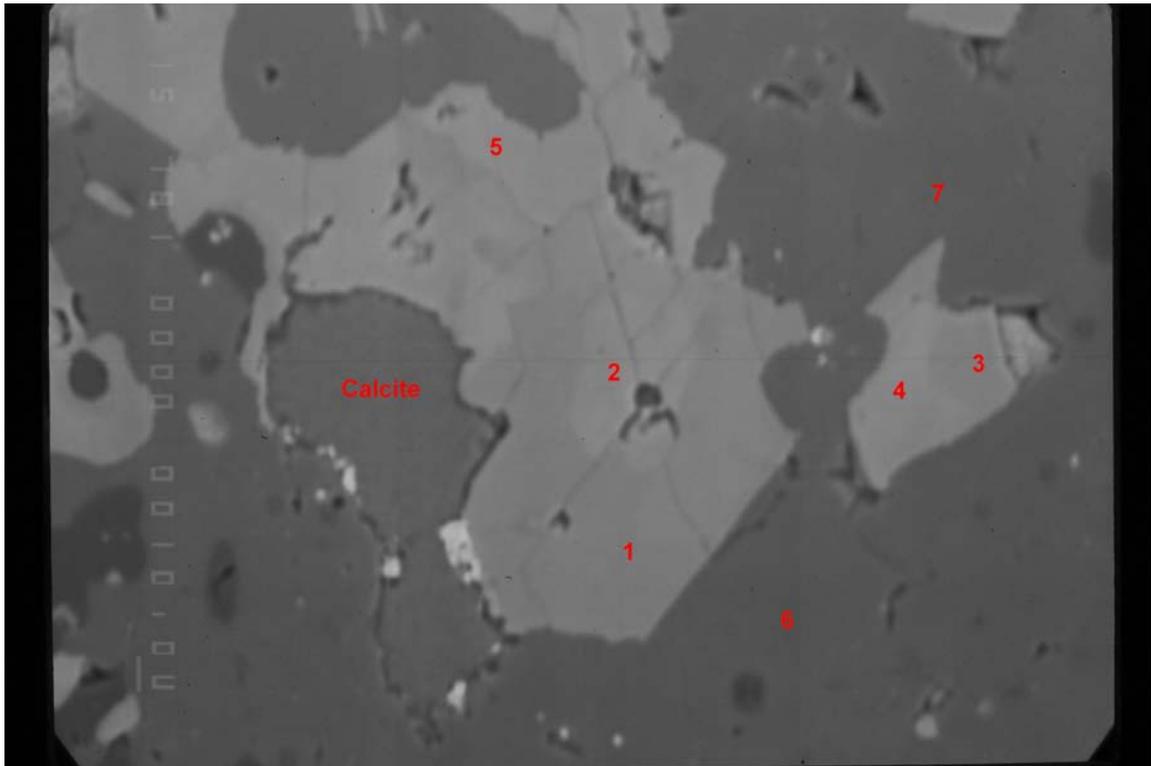
Figure 4.26 – Backscatter image showing compositional complexity of calcic amphiboles sampled from biotite-amphibole metasomatic rock. The two-phase assemblage is revealed as brighter and darker domains by backscatter. Individual microprobe analyses are identified in sequence on the image as follows: (1) darker domain of ferrohornblende composition, (2) domain of intermediate brightness characterized by hastingsite composition, (3) darker domain of ferro-edenite composition, (4) domain of intermediate brightness characterized by ferro-edenite composition, (5) brighter domain of ferro-edenite composition, (6 & 7) fine grained matrix of potassium feldspar [Or_{98}]. The darker domains within the potassium feldspar matrix are islands of near end member albite. Sample from GR-06-011W.
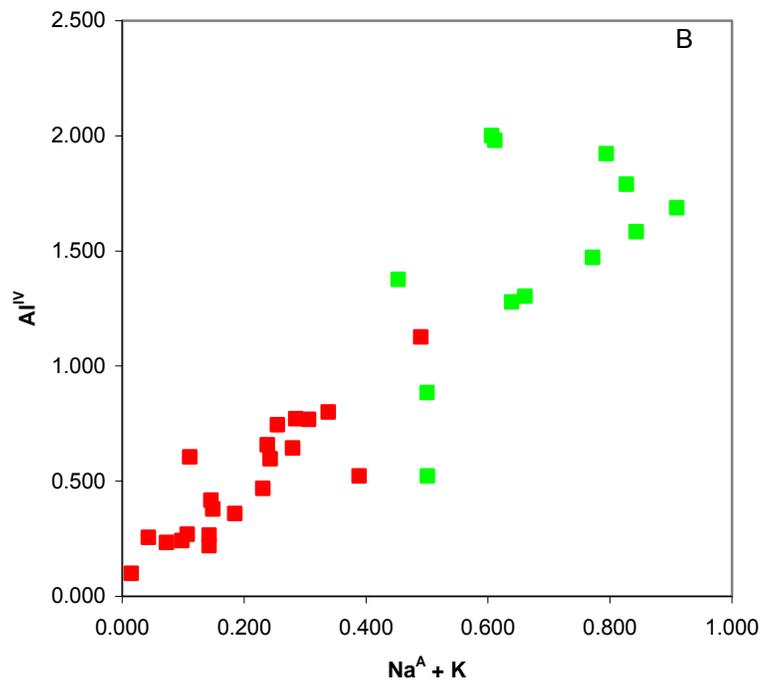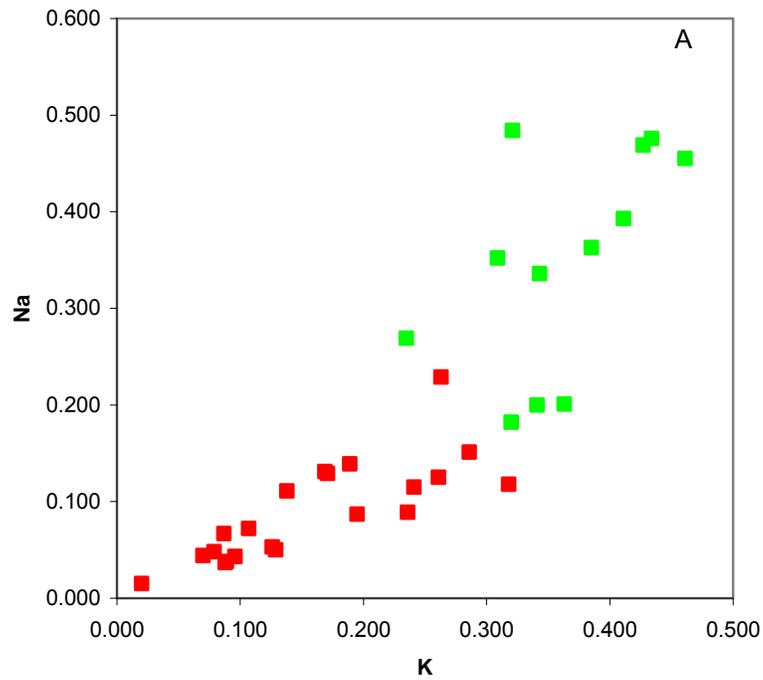
Figure 4.27 – Bivariate amphibole chemistry plots: A) Na vs. K, and B) Al^{IV} vs. Na^A+K

commonly occurring with quartz, albite, potassium feldspar, biotite, chlorite and calcite. They also comprise the primary component of the fine grained matrix hosting previously described fragments. Backscatter imaging show these amphiboles are compositionally complex, exhibiting a two-phase assemblage undetected optically (see Figure 4.26). The alkali-depleted phase shows a compositional variation ranging from ferrohornblende to ferro-actinolite. Based upon calculated ferric iron content, the alkali-enriched phase shows a compositional range from hastingsite to ferro-edenite. Locally these alkali-enriched domains are identified as ferropargasite based on the nomenclature criteria previously discussed. Chemical compositions show that the ferrohornblende to ferro-actinolite phase is enriched in silicon (7.1 to 7.6 atoms per formula unit) with respect to the hastingsite to ferro-edenite phase (6.1 to 7.1 atoms).

As observed with the Mg-Fe amphiboles previously discussed, this silicon enrichment apparently occurs at the expense of tetrahedral aluminum which ranges from 0.24 to 0.80 atoms and 0.52 to 1.8 atoms respectively. However, both silicon and aluminum content are accommodated in T-sites. Calculations show limited ferric iron substitution within C-sites exhibited by both phases (0 to 0.27 atoms per formula unit). C-sites are largely occupied by ferrous iron and magnesium, with trace chromium and manganese substitution. The alkali-depleted phase shows total iron to magnesium ratios range from 1.2 to 1.9. Comparatively the alkali-enriched phase shows greater substitution of magnesium by ferrous iron demonstrated by total iron to magnesium ratios that range from 1.8 to 4.0.

Chemical compositions indicate B-sites are largely taken by calcium, with occupancy ranging from 1.8 to 2.0 atoms for all species. Sodium substitution is divided between B-site

vacancies with the remainder sharing A-sites with potassium content. Alkali abundances for both phases of amphibole are illustrated in the bivariate sodium vs. potassium plot in Figure 4.27A showing a strong correlation between the two for mutual enrichment or depletion. A-site alkalis are plotted against tetrahedral aluminum in Figure 4.27B illustrating a similar correlation between aluminum and alkali content. Halide substitution shows limited fluorine substitution for both phases ranging from 0 to 0.18 atoms. The alkali-depleted phase shows similarly limited chlorine substitution of halogen ions ranging 0 to 0.11 atoms. The alkali-enriched phase shows weak but variable chlorine enrichment with substitution ranging from 0.02 to 0.45 atoms. The two phase assemblage is likely the result of initial high temperature equilibration of the alkali-poor phase post amphibole replacement of layering, followed by post-thermal peak equilibration with alkali-enriched feldspar phases.

Calcic amphiboles sampled from the potassium feldspar metasomatite show a similar two phase assemblage as those sampled from biotite-amphibole metasomatic rock, with compositions showing less variation and falling within the ferrohornblende and hastingsite fields for alkali-poor and alkali-enriched phases respectively (see Figures 4.33B and D). Chemical compositions show greater substitution of tetrahedral aluminum (alkali poor: 0.61 to 1.1 atoms; alkali-enriched: 1.4 to 2.0 atoms) within T-sites than similar phases observed in the biotite-amphibole metasomatic rock. Silicon content is correspondingly lower, showing 6.7 to 7.2 atoms per alkali-poor formula unit and 6.0 to 6.5 atoms per alkali-enriched formula unit.

M-type ion substitution within C-sites is very limited for the ferrohornblende phase, showing calculated ferric iron in several analyses up to 0.20 atoms. However, hastingsite compositions shows calculated ferric iron content ranges from 0.04 to 0.32 atoms, with

limited octahedral aluminum ranging from 0 to 0.10 atoms. C-site occupancies for both phases are largely filled by magnesium (1.9 to 2.2 atoms, and 1.2 to 1.5 atoms for ferrohornblende and hastingsite respectively) and ferrous iron (2.2 to 2.7 atoms, and 2.5 to 3.1 atoms for ferrohornblende and hastingsite respectively). Limited manganese substitutes within C-sites (0.01 to 0.03 atoms) as well.

The high calcium content exhibited by both phases (1.8 to 2.0 atoms) limits sodium substitution within B-sites. Sodium and potassium contents are plotted with results from biotite-amphibole metasomatic rock species in Figure 4.27A, showing a similarly strong correlation for mutual enrichment or depletion. Sodium to potassium ratios for the alkali-poor phase are very consistent between 1.15 to 1.36. Corresponding ratios for the alkali-enriched phase show considerable variation of 0.67 to 1.81. This variability is likely an effect resulting from the previously mentioned equilibration with sodic and potassic feldspar phases. The ferrohornblende species show limited fluorine substitution up to 0.37 atoms. Chlorine shows a narrow range of substitution for ferrohornblende (0.07 to 0.17 atoms), and substantial substitution for hastingsite (0.24 to 0.57 atoms). Chlorine enrichment of the hastingsite species likely reflects the composition of fluids with which these amphiboles last equilibrated.

4.4.3 Biotite

Biotite commonly occurs within porphyritic and metasedimentary rocks that exhibit effects of K-metasomatism. Compositions of biotite were determined from samples of porphyry demonstrating moderate to intense K-metasomatism, banded potassium feldspar replacement preserved within biotite-amphibole metasomatic rock, and patchy replacement

of meta-arenite. All species analysed from intrusive and metasedimentary rock classify as iron-rich annite when plotted on the "ideal biotite plane" of Guidotti (1984) in Figure 4.28. High titanium content similarly expressed by all species probed indicates they are Ti-annite. Figure 4.28 demonstrates reduced values of Al^{VI} between zones of least and moderately altered porphyry. The broad range of Al^{VI} values exhibited by species in least altered porphyry likely reflects hydrothermal overprinting. Biotites from metasedimentary rock show Al^{VI} : Mg(Mg+Fe) ratios comparable to those from least altered porphyry.

Backscatter images show depletion of titanium at the margins of biotite phenocrysts (Figure 4.29). An average of 2.74 weight percent TiO_2 was determined for phenocryst cores, compared to an average 1.97 TiO_2 for margins. Biotite grains from porphyry groundmass are further depleted with respect to titanium, showing an average of 1.54 weight percent TiO_2. This compares to an average content of 1.50 weight per cent TiO_2 for biotites in banded potassium feldspar replacement of metasedimentary rock, and 1.12 weight percent TiO_2 in biotites from patchy replacement of meta-arenite. Titanium substitution ranges from 0.28 to 0.36 per octahedral site for phenocryst cores, 0.21 to 0.26 for phenocryst margins, 0.17 to 0.19 for porphyry groundmass, 0.17 to 0.18 for banded potassium feldspar replacement, and 0.12 to 0.14 for patchy replacement, based on an anhydrous 22 oxygen unit cell. Figure 4.30A illustrates an inverse relationship between titanium and magnesium content for porphyritic species. A similar relationship was not indicated for metasedimentary varieties. Figure 4.31A shows depletion of titanium does not correlate with Al^{VI} content, suggesting secondary growth from hydrothermal fluid.

Biotite species from all sampled lithologies show high potassium and iron content, with moderate magnesium. The K_2O vs. FeO binary plot (Figure 4.30B) shows the

clustering of results by lithology. The biotite species sampled from pink potassium feldspar bands in metasedimentary rock have generally higher potassium than phenocryst varieties. Biotites from patchy replacement of arenite are comparatively enriched in iron. However, phenocrysts sampled from a zone of intense hematization shows the highest iron and the lowest potassium content of all species probed, demonstrating differential effects from K and Fe alteration.

Halide content is generally low for phenocryst species. Chlorine is also extremely low and fluorine nearly undetectable within metasedimentary biotites (Figure 4.32). Figure 4.31B suggests there is no obvious relationship between halide content and Al^{VI}. Fluorine substitution ranges from 0 to 0.189 and 0 to 0.005 atoms per unit cell for porphyritic and metasedimentary species respectively, and chlorine substitution ranges from 0 to 0.215 and 0 to 0.043 atoms per unit cell for phenocrysts and metasedimentary grains. Caution must be employed when considering fluorine as values approach the accuracy range for determination. Samples from moderately altered porphyry show chlorine depletion against least altered equivalents, and chlorine was not detected in species sampled from patchy replacement of subarenite.

Figure 4.33A demonstrates a general increase of fluorine with decreasing magnesium and iron, inconsistent with the preference of fluorine for magnesium suggested by Munoz and Ludington (1974). It is likely that these low fluorine contents are a result of the H_2O-HF composition and temperature of the fluid with which it last equilibrated. Chlorine content is low and generally consistent within phenocryst cores sampled from least altered porphyry (re: Figure 4.31B), with results falling within the range of those reported for igneous biotites by Parry and Jacobs (1975). Margins of biotite phenocrysts and those sampled from
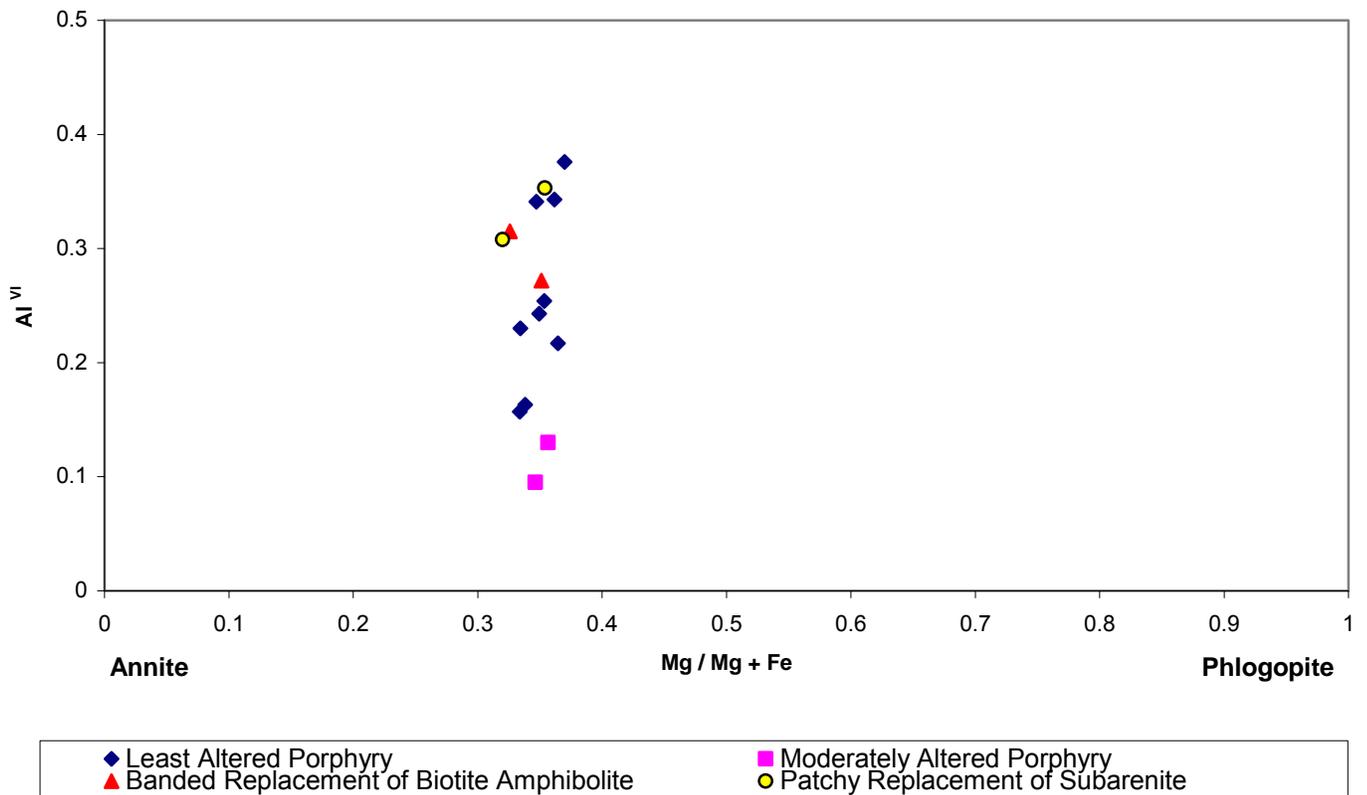
Figure 4.28 – Classification of all probed biotite species plotted as Al^{VI} vs. Mg/(Mg+Fe) after Guidotti (1984).
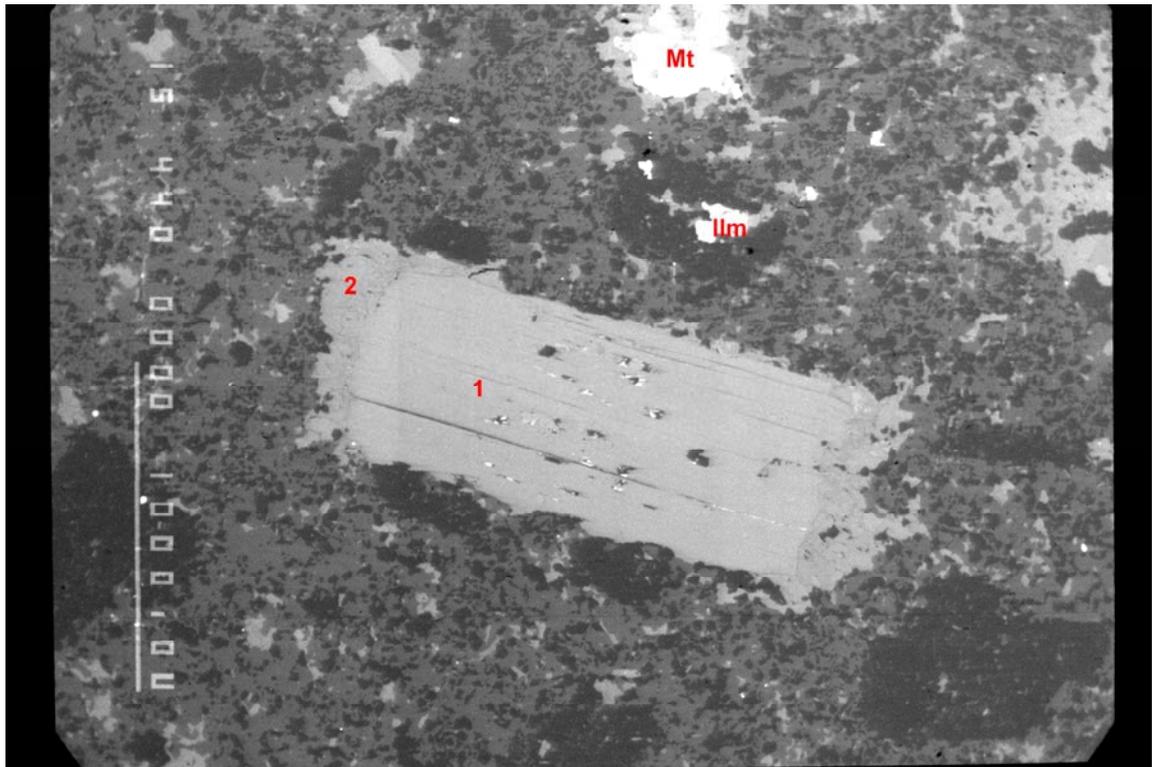
Figure 4.29 – Backscatter image of biotite phenocryst from least altered porphyry exhibiting marginal compositional variation. Individual microprobe analyses are identified in sequence on the image as follows: (1)Ti-annite phenocryst core, (2) Ti-annite margin, (Ilm) fine grained ilmenite occurring within quartz aggregates and as very fine grained inclusions along biotite cleavage planes, (Mt) fine grained magnetite. Sample from GR-06-027W.
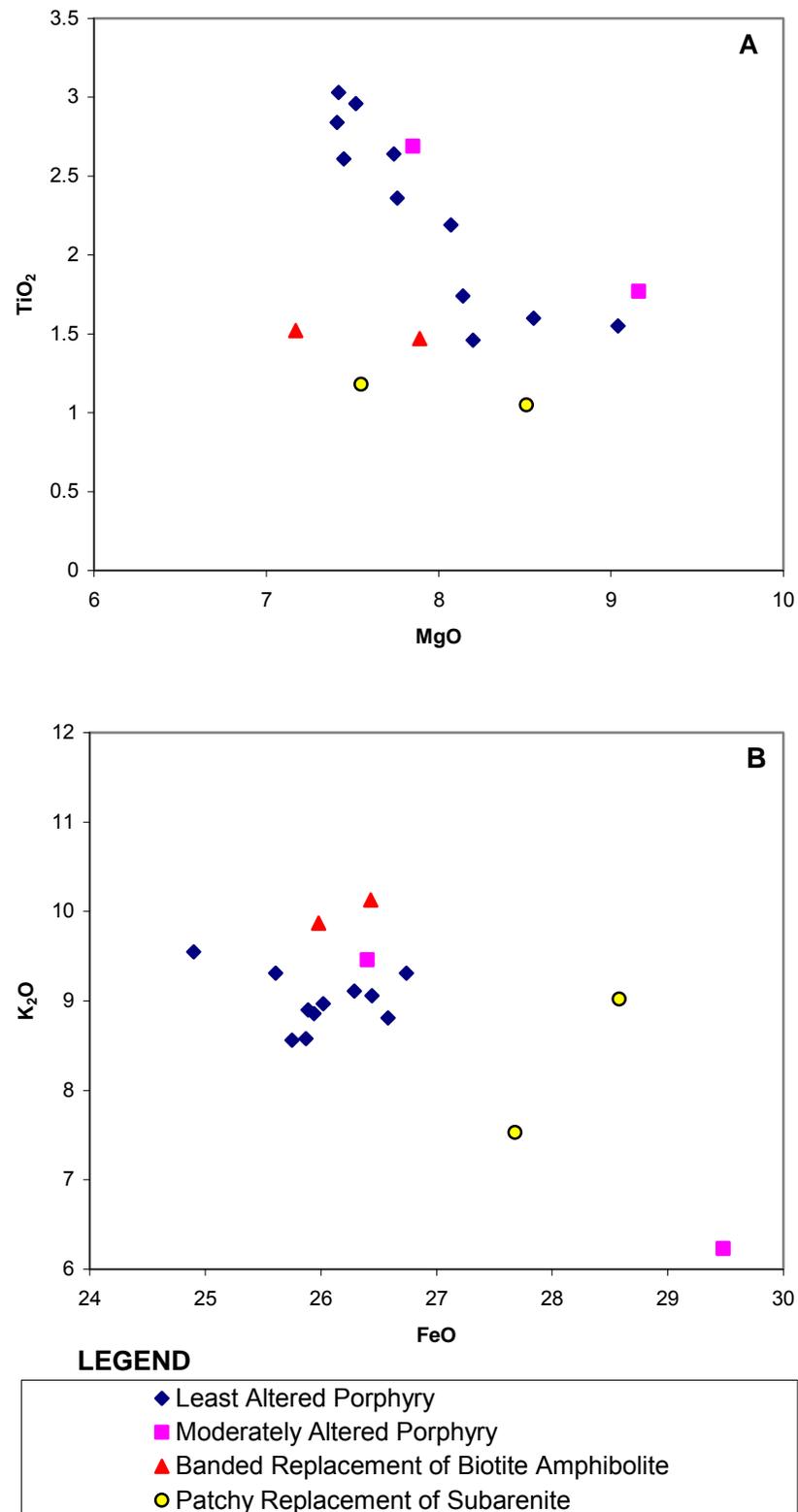
Figure 4.30 – Biotite composition oxide-oxide plots for: A) TiO₂ vs. MgO, B) K₂O vs. FeO

Figure 4.31 – Biotite composition ion-ion plots for: A) Ti vs. AL^{VI}, B) F+Cl vs. AL^{VI}
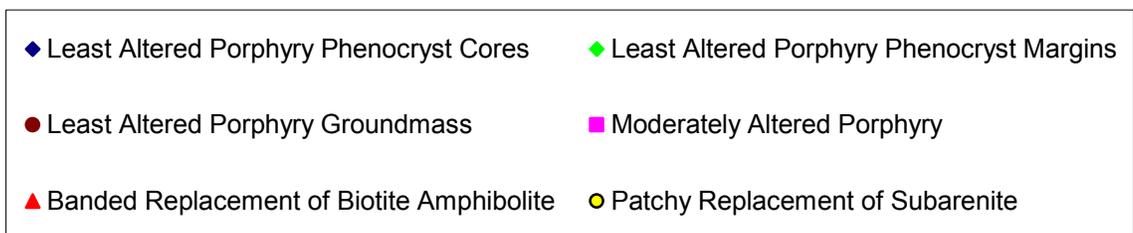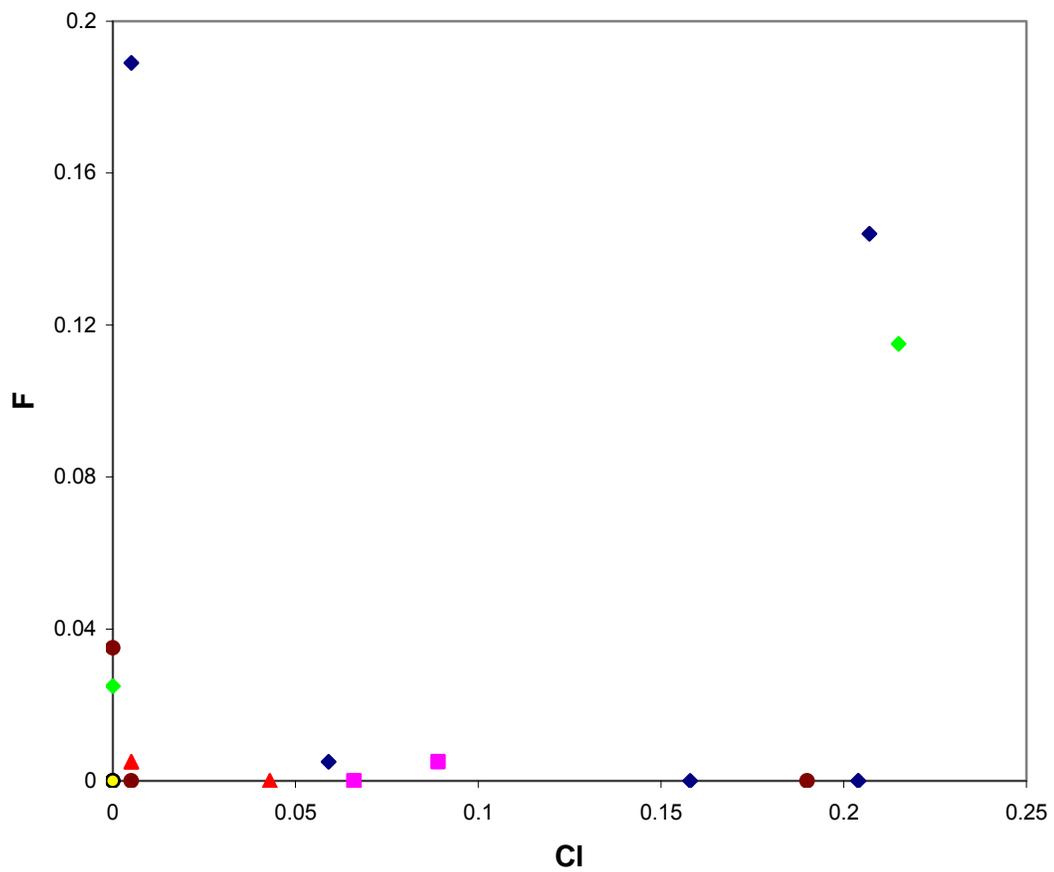
Figure 4.32 – Biotite composition halide plots for F vs. Cl.

156
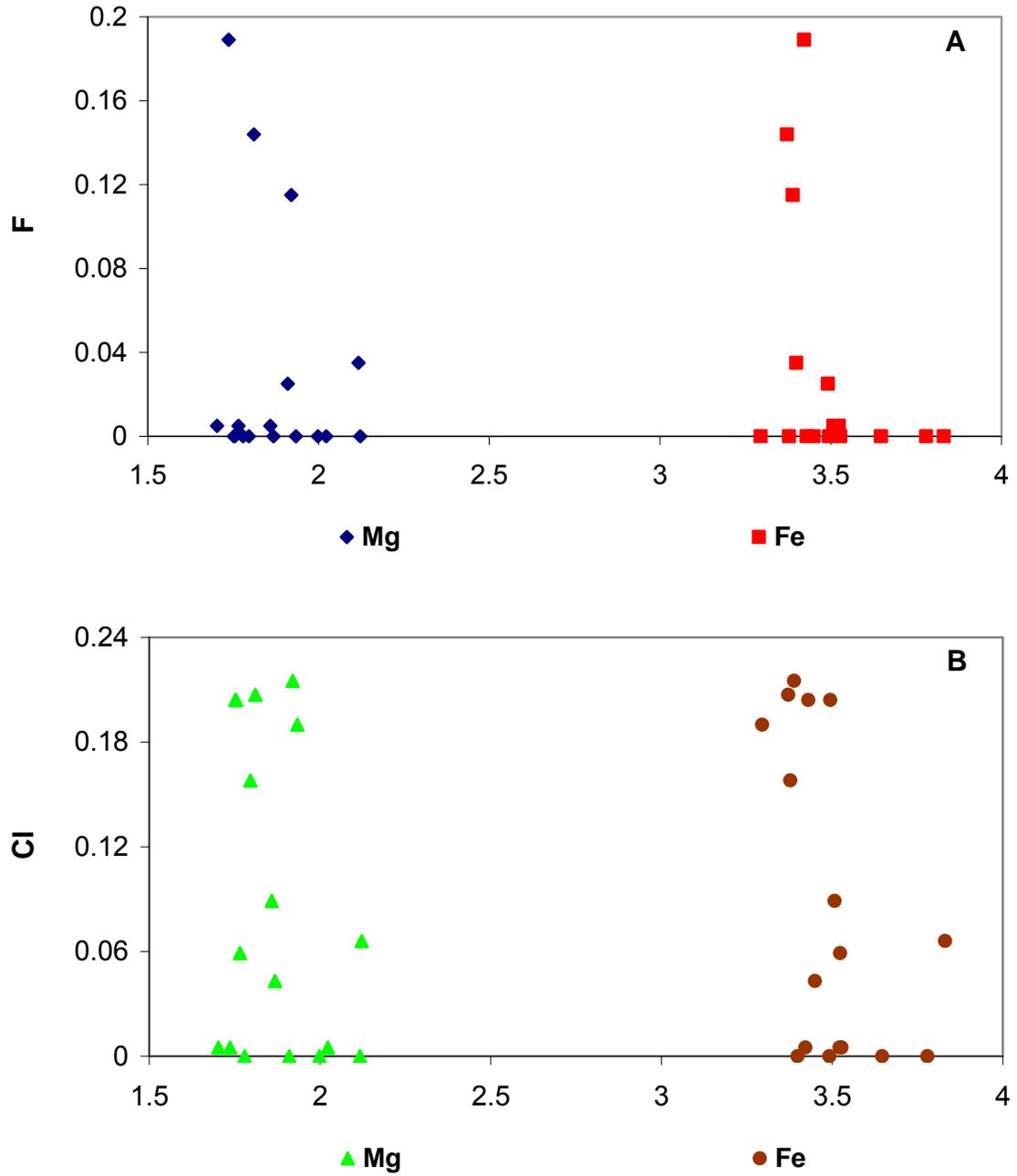
Figure 4.33 – Biotite composition halide-cation plots for: A) F vs. Mg and F vs. Fe, B) Cl vs. Mg and Cl vs. Fe. (Values are in atoms per formula unit).

porphyry groundmass show greater variation in chlorine content, and those probed from moderately altered porphyry show significant chlorine depletion. As Speer (1984) recognized, igneous biotites are readily metasomatically altered post-magmatic crystallization and thus are better indicators of late-stage fluids than of magmatic environments.

4.4.4 Chlorite Group Minerals

Chlorite species are ubiquitous within rocks exhibiting effects of K-metasomatism. Samples were analyzed to determine chlorite compositions from several lithologies, including feldspar porphyry dykes, local potassium feldspar replacement within subarenite, hydrothermal breccia and potassium feldspar metasomatite. Figure 4.42 illustrates all chlorite analyses on the classification diagram of Hey (1954) demonstrating compositions are predominantly within the brunsvigite field. Species analyzed from porphyy have been divided on the diagram to illustrate compositional differences among several populations, including: (1) pleochroic dark green to green-brown chlorite that occurs as the epitaxial replacement of biotite phenocrysts (Figure 4.16, analyses 6 & 7); and (2) pleochroic pale yellow-green to olive green, fine grained incipient chlorite that infiltrates the porphyry groundmass and commonly mantles other phenocrysts. The former generally has a higher silicon and magnesium and lower iron content than the latter. Chlorite species analyzed from subarenite and breccias occur as replacement of biotite, and thus have greater potassium and less magnesium content than the porphyritic varieties. Chlorite species analysed from the potassium feldspar metasomatite shows two populations falling in the brunsvigite and brunsvigite-pycnochlorite fields. The former have high iron and low magnesium content, and occur as fine grained inclusions within nebulous relics preserved within the metasomatite

(Figure 4.24). The latter have comparatively lower iron and higher magnesium content, and generally occur as mafic clots in assemblages with quartz and iron oxides within metasomatite (Figure 4.35).

Chlorite varieties from porphyry show highly variable tetrahedral aluminum substitution, ranging from 1.6 to 2.3 atoms per unit cell for species replacing biotite, and 2.0 to 2.7 for the incipient species. Tetrahedral aluminum substitution within varieties from other sampled lithologies collectively show less variation, ranging from 1.7 to 2.1. Figure 4.36A shows tetrahedral aluminum plotted against the ratio $Fe/(Fe+Mg)$ demonstrating the variable iron content within chlorites sampled from porphyry and potassium feldspar metasomatite. Chlorite species from subarenite and breccia show relatively high iron substitution relative to tetrahedral aluminum. The generally positive trend exhibited collectively by the species in porphyry suggests an increase in tetrahedral aluminum abundance with increasing $Fe/(Fe+Mg)$ ratios. Comparatively, the relatively neutral trend exhibited by the species probed from the metasomatite indicate a relatively constant tetrahedral aluminum content with an increasing $Fe/(Fe+Mg)$ ratio. Figure 4.36B provides an explanation for this relationship. The plot of magnesium vs. total iron shows that for chlorite species in porphyry, magnesium content remains relatively constant with increasing total iron. For those species sampled from the metasomatite, increasing iron content is coupled with a decrease in magnesium content.

Titanium substitution was low for all chlorite species, generally ranging from 0 to 0.05 atoms per unit cell for porphyry and metasomatite varieties, and from 0.09 to 0.19 for breccia and subarenite species. However, one chlorite species replacing biotite, classified as diabantite, showed a transitional composition anomalously high in titanium (0.47 atoms per
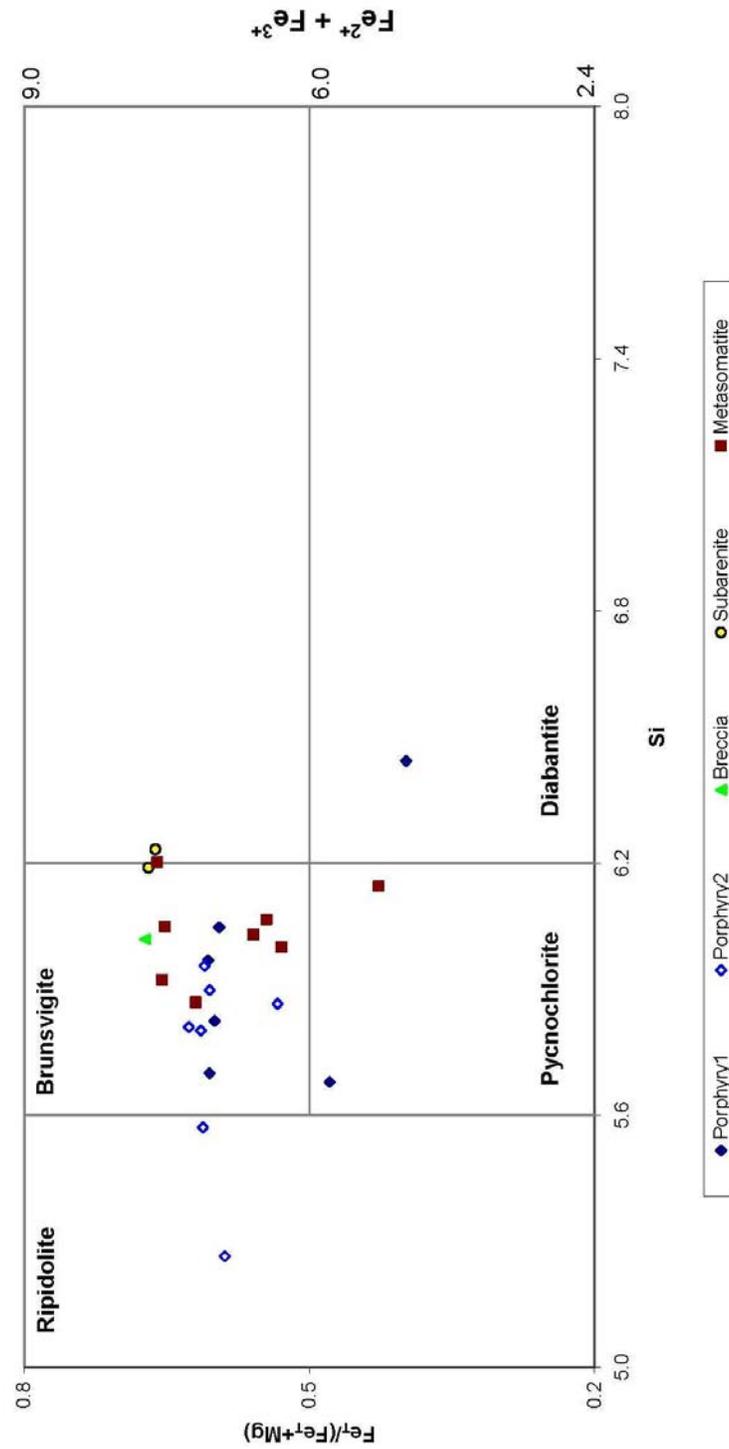
Figure 4.34 – Classification diagram for chlorite compositions (modified after Hey, 1954). Note: Porphyry[1] refers to chlorite occurring as the replacement of biotite, and Porphyry[2] refers to fine grained incipient chlorite.
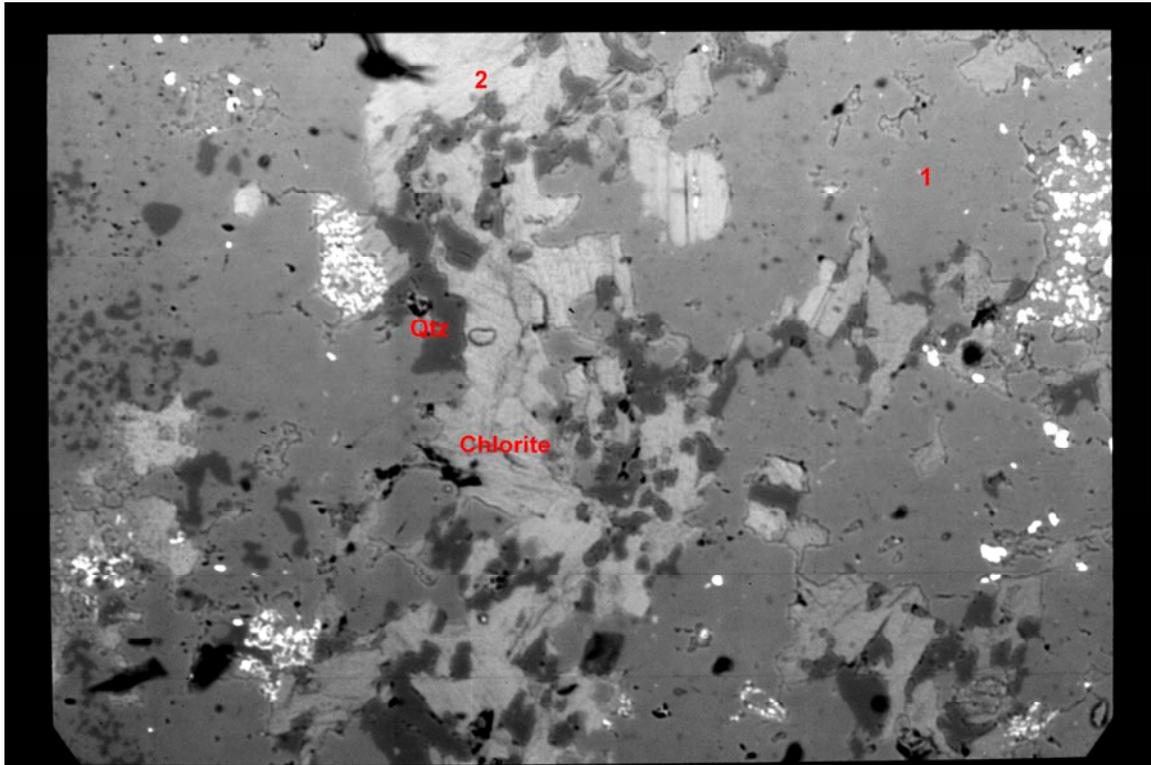
Figure 4.35 – Backscatter image of a mafic clot within the potassium feldspar metasomatite. These mafic clots are aggregates comprised of chlorite ±quartz ±Fe-oxide ±pyrite ±arsenopyrite ±chalcopyrite. Individual microprobe analyses are identified in sequence on the image as follows: (1)ultra-fine grained potassium feldspar [Or98], (2)fine grained Fe-chlorite aggregate, (Qtz) fine grained quartz. Sample GR-10-155.
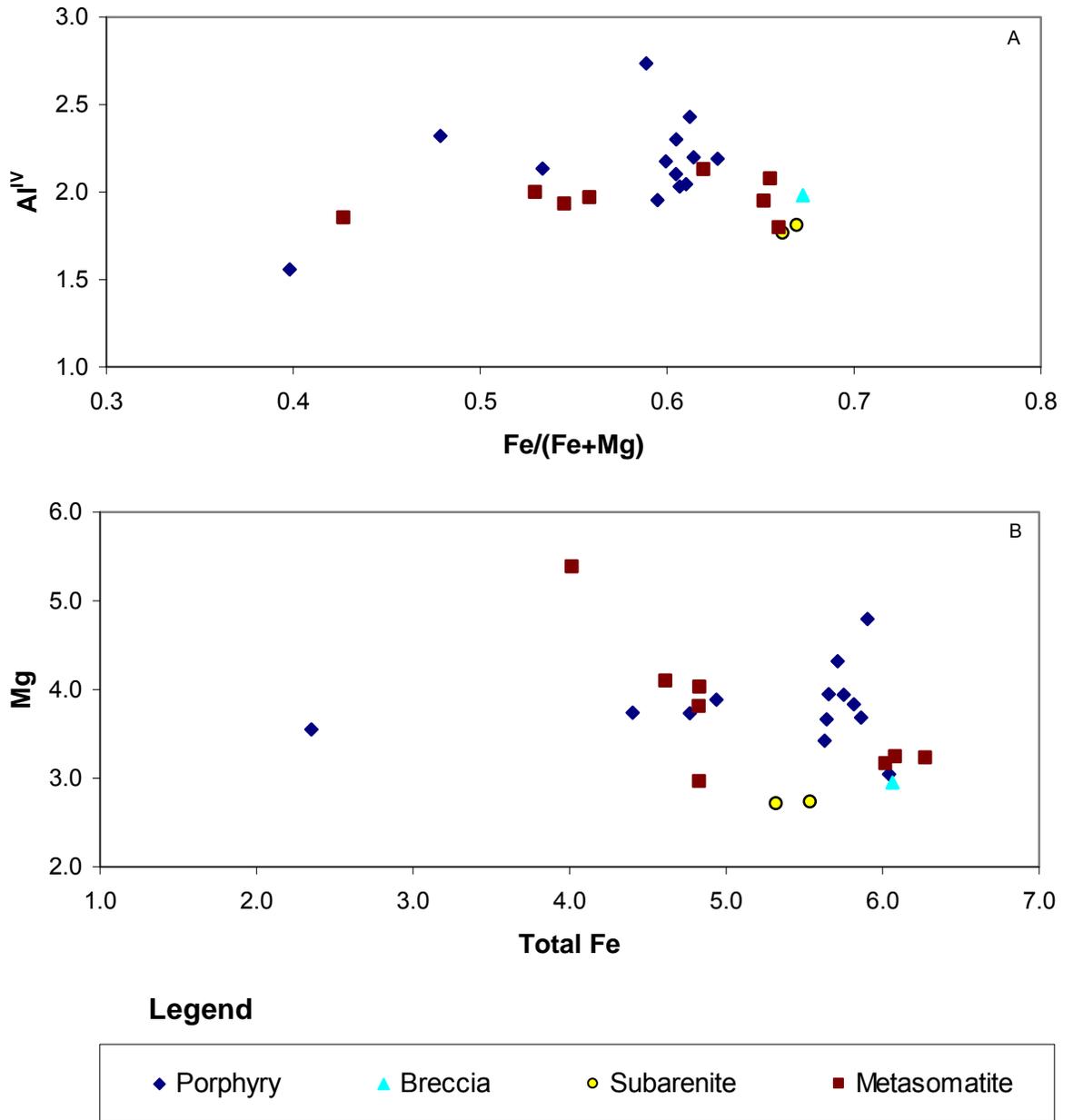
Figure 4.36 – Chlorite composition plots:
A) Al^{IV} vs. Fe/(Fe+Mg),   and B) Mg vs. Total Fe.
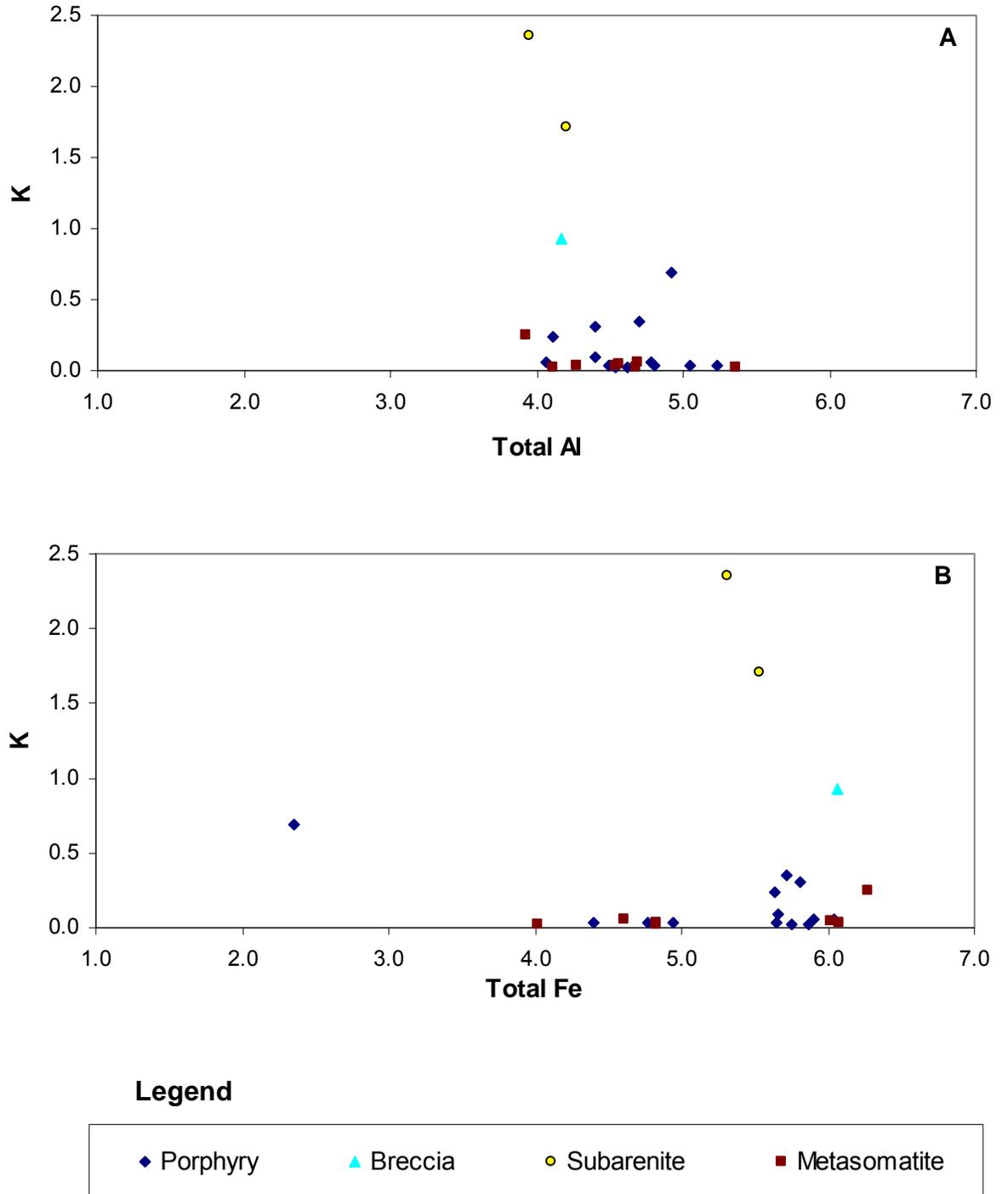
Figure 4.37 – Chlorite composition plots:
A) K vs. Total Al, and B) K vs. Total Fe.

unit cell) and correspondingly low in iron (2.35 atoms per unit cell) suggesting incomplete replacement of biotite.

Figure 4.37A illustrates the relationship between potassium and total aluminum for all lithologies. Species from both porphyry and metasomatite show limited potassium substitution (0.02 to 0.69 atoms, and 0.02 to 0.25 atoms respectively) over a large range of tetrahedral and octahedral aluminum content. The relationship suggests that increased aluminum is not coupled with potassium. Breccia and subarenite species demonstrate aluminum coupled with substantial potassium enrichment (0.93 atoms, and 1.7 to 2.4 atoms respectively). This potassium enrichment is apparently at the expense of magnesium, as evidenced in Figure 4.36B. The relationship between potassium and total iron is demonstrated in Figure 4.37B. Chlorite from porphyry and metasomatite exhibit limited potassium substitution over a large range of iron enrichment (4.1 to 6.1 atoms). An outlier within the population sampled from porphyry shows anomalously low iron (2.4 atoms) and comparatively high potassium (0.69 atoms) indicative of incomplete biotite replacement. High potassium and iron enrichment within breccia and arenite species demonstrate a relationship comparable to that expressed between potassium and aluminum.

4.4.5 Epidote Group Minerals

As illustrated by backscatter image (Figure 4.15 and 4.16), epidote species commonly occur as very fine grained inclusions within feldspar phenocrysts. Mineral chemistry indicates the epidote inclusions to be variably enriched in iron, though show significant compositional variation. The general formula for the epidote group has been defined by Deer et al. (1992, page 85) as $X_2Y_3Z_3(O,OH,F)_{13}$. The considerable substitution of Y cations,

particularly in the large M3 octahedral site, is demonstrated by the range of aluminum between 2.48 to 2.97 atoms per unit cell based upon 13 oxygens. Iron substitution for aluminum ranges from 0.39 atoms per unit cell for more aluminous varieties to 0.79 for those showing aluminum depletion. Trace substitution by titanium (0 to 0.021 atoms per unit cell), magnesium (0 to 0.013 atoms per unit cell) and potassium (0.005 to 0.017 atoms per unit cell) has also been detected. As potassium generally does not substitute within the epidote structure, this likely represents potassium within partially replaced feldspar grains that were too fine to probe. The occurrence of epidote as inclusions within plagioclase phenocrysts is interpreted to result from saussuritization of plagioclase common during hydrothermal alteration.

4.4.6 Apatite

Apatite species occur as accessory minerals of mafic clots preserved within pervasive domains of potassium feldspar metasomatite. Apatite is commonly associated with an assemblage of other minerals including chlorite, quartz, rutile, monazite, zircon and various iron oxides. Illustrated by backscatter image (Figure 4.38), the colourless apatite grains are distinguished by moderate relief and parallel extinction. Probed apatites are high in calcium (average of 56.76 mol per cent CaO) and phosphorous (average of 41.24 mol per cent P_2O_5). Substitution of calcium is highly variable, with limited replacement by iron (up to 0.31 mol per cent FeO), sodium (up to 0.10 mol per cent Na_2O), and rare earth elements such as yttrium (up to 0.15 mol per cent Y_2O_3), lanthanum (up to 0.37 mol per cent La_2O_3), neodymium (up to 0.06 mol per cent Nd_2O_3), praseodymium (up to 0.05 mol per cent Pr_2O_3), samarium (up to 0.04 mol per cent Sm_2O_3), and thorium (up to 0.06 mol per cent ThO_2). Chemical compositions show substitution of hydroxyl ions by chlorine (up to 0.25 mol per cent Cl),
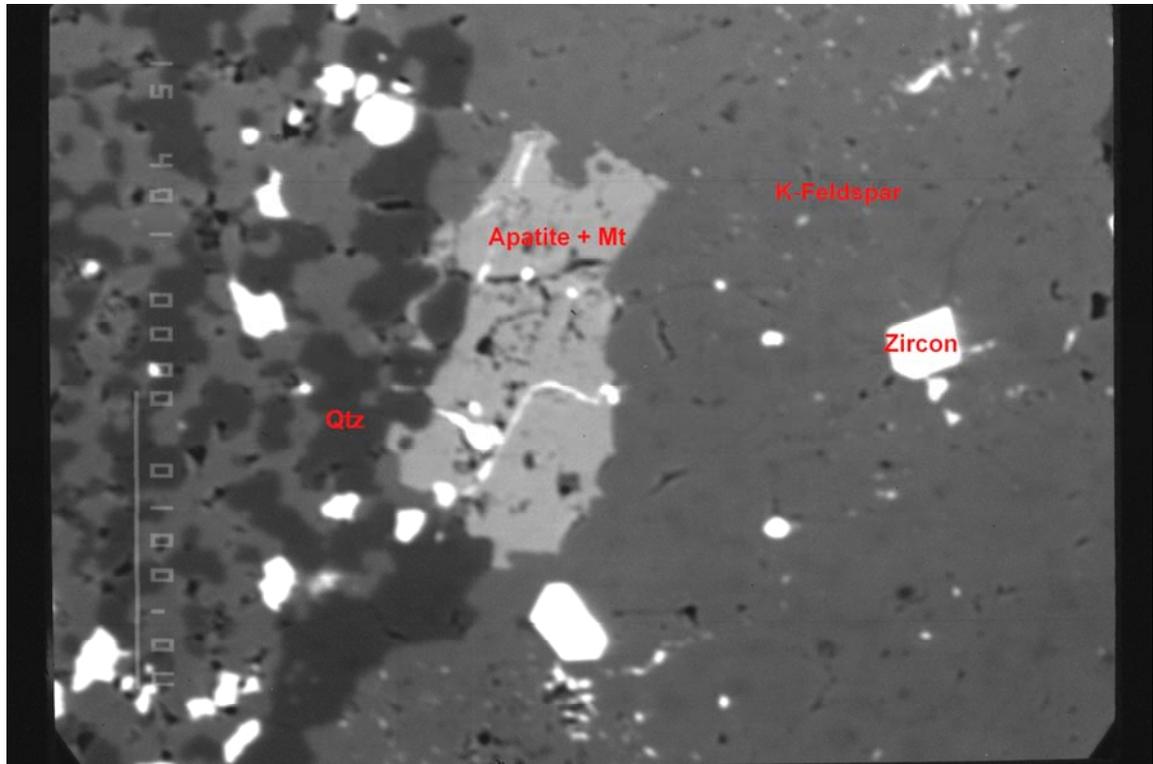
Figure 4.38 – Backscatter image of accessory minerals within a mafic clot (left hemisphere) sampled from pervasive potassium feldspar metasomatite (right hemisphere). These mafic clots are characterized by very fine grained aggregates of quartz, magnetite, apatite, rutile, zircon and other iron oxides. Sample from GR-10-139A.

with no detectable fluorine. The absence of fluorine coupled with the concentration of apatite within mafic clots of pervasively replaced rock suggests a hydrothermal origin.

4.4.7 Rutile

Rutile commonly occurs as an accessory component of mafic clots and grain aggregates preserved within otherwise pervasively potassium feldspar replaced rock. Rutile grains are optically distinguished from other accessories by a reddish brown colouration and elongate forms with square cross-sections. As illustrated in backscatter (Figure 4.39), images show rutile generally occurs intergrown with Ti-magnetite, and less commonly with Th-silicate inclusions. Rutile domains show significant titanium content (98.6 to 99.0 mol per cent TiO_2) with limited cation substitution by chromium (0 to 0.12 mol per cent Cr_2O_3), iron (0.86 to 1.37 mol per cent FeO), magnesium (0 to 0.60 MgO) and niobium (0.07 to 0.70 mol per cent Nb_2O_5). Ti-magnetite margins and domains show significant iron (77.5 to 92.0 FeO) with variable titanium content (3.66 to 12.1 mol per cent TiO_2). The transitional margins exhibit limited cation substitution by aluminum (0.1 to 0.6 mol per cent Al_2O_3), chromium (0.07 to 0.08 mol per cent Cr_2O_3), magnesium (0 to 1.35 mol per cent MgO), and zinc (0.16 mol per cent ZnO).

4.5 Whole Rock ^{18}O Isotope Geochemistry

Oxygen isotopes were determined for seven samples at The University of Western Ontario's Geology Isotope Laboratory. Whole rock separates were chosen to characterize the fluid source for pervasive potassium feldspar replacement. Samples were selected from a broad range of lithologies exhibiting effects of K-metasomatism including Treasure Lake
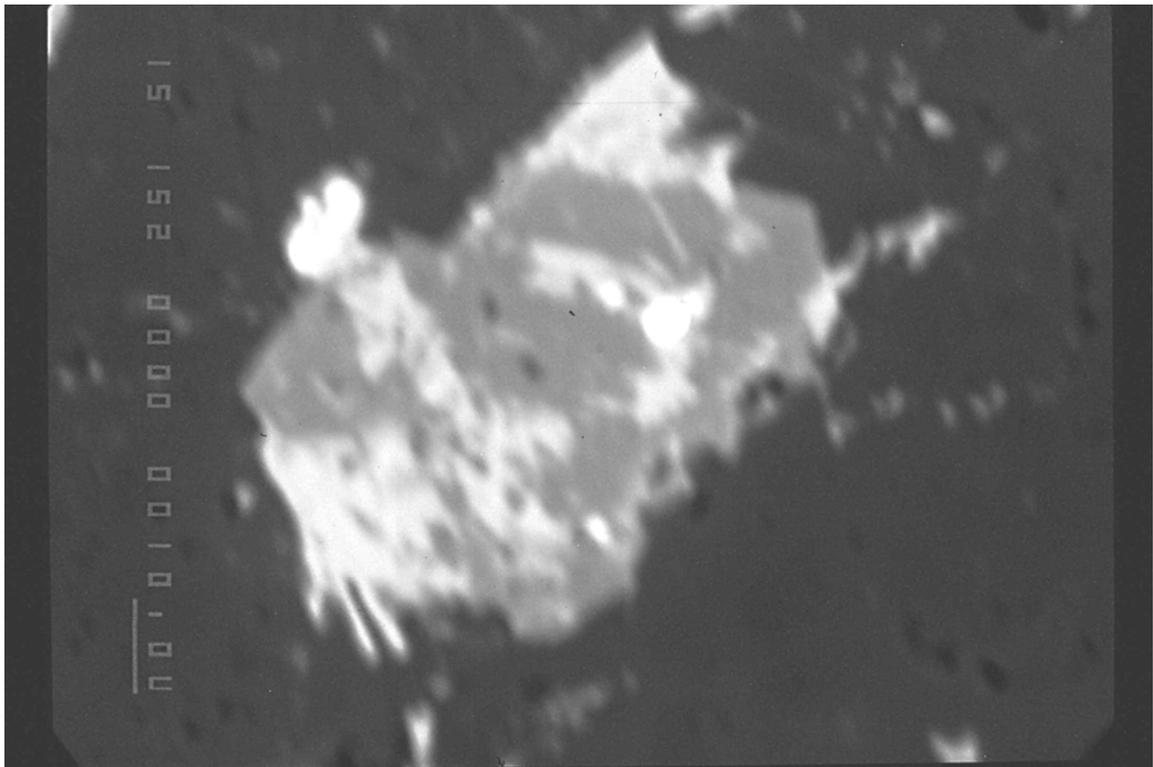
Figure 4.39 – Backscatter image of a rutile grain (darker grey) intergrown with Ti-magnetite (pale grey). The bright circular inclusion is Th-silicate. Sample GR-10-155.

Group meta-arenite, Lou Lake assemblage volcanic rocks, feldspar-phyric dykes, massive potassium feldspar metasomatite and K-feldspar matrix breccia. Results (relative to Standard Mean Ocean Water) presented in Table 4.1 show $\delta^{18}O$ values fall both within the top of the range typical for granitoids, and within the center of the range typical of metamorphic rocks (Rollinson, 1993). $\delta^{18}O$ enrichments are tightly constrained between 10.58 ‰ and 12.72 ‰, demonstrating a high degree of equilibrium was attained. Values exhibited a relatively high correlation (R = 0.71) with Na_2O and a weak positive correlation with Al_2O_3 (R = 0.22). Otherwise, values show low negative correlation with remaining oxides.

Table 4.4 - Oxygen Isotope Ratios for Select Altered Lithologies

Sample ID	Lithology	^{18}O (VSMOW)	SiO_2	K_2O
003E	Potassium Feldspar Metasomatite	11.92	73.40	10.60
014E	Feldspar Porphyry	11.21	67.33	11.22
015E	Feldspar Porphyry Endo-contact zone	10.84	75.26	10.28
008W	K-Metasomatized Meta-arenite	10.58	71.11	9.78
012W	K-Metasomatized Breccia	11.53	73.60	10.36
020W	Weakly K-Metasomatized Meta-arenite	11.35	80.42	4.14
031	K-Metasomatized Volcanics	12.72	73.17	6.72

CHAPTER 5 – ANALYSIS OF MASS EXCHANGE

5.1 Introduction

Several methods exist for estimating mass changes that result from metasomatic alteration, all of which require identification of immobile elements (Gresens, 1967; Grant, 1986; MacLean and Barrett, 1993; Stanley and Madeisky, 1996). Gresens' (1967) approach offers a mathematically complex technique that fails to provide an efficient, readily adaptable method. The isocon method of Grant (1986) simplifies Gresen's approach, but fails to account for primary compositional variation or provide a procedure for selecting unaltered precursors (Huston, 1993; Gifkins et al., 2005). MacLean and Barrett (1993) and Stanley and Madeisky (1996) offer techniques that overcome these limitations, however, the former provides calculations that are easier to utilize. For these reasons, the MacLean and Barrett (1993) method was used in this study to determine elemental gains and losses for a feldspar porphyry dyke which shows alteration effects leading to metasomatite. Results of these mass change calculations are presented in Section 5.2.

5.2 Mass Balance Analysis

Mass transfer of mobile components was determined for a feldspar porphyry dyke using the single precursor method of MacLean and Barrett (1993). This porphyry provides an optimal opportunity to estimate mass change as all samples were collected from a single coherent unit, alteration within the porphyry varies from weak to pervasive, and where replacement is nearly complete, the geological evidence for a porphyry precursor is irrefutable. MacLean and Barrett (1993) recommend the procedure be applied to chemically

homogenous rock whereas a porphyritic texture may be locally affected by crystal sorting. To accommodate this concern, an average composition (n = 3) was used as the least-altered precursor composition to account for chemical heterogeneities that may exist. It is assumed that utilization of an average least-altered precursor removes initial compositional variation. A second concern is that even the least-altered samples may show effects of hydrothermal alteration, and the method utilized does not provide a way to determine the composition of an unaltered protolith. As the least altered samples show limited alteration effects, it is assumed that any change to bulk composition was minimal.

Immobility was tested by calculating the correlation coefficient (R) for element pairs. Highly correlated linear trends (R > 0.90) indicate immobile element pairs which ideally produce regression lines that pass through bulk composition and origin when plotted on bivariate diagrams (MacLean and Kranidiotis, 1987). The regression line represents an alteration line where net elemental gains plot nearer to the origin; with net loss plotting further away. Coefficient values were determined using the Pearson product-moment coefficient of linear correlation procedure provided by Rollinson (1993). To summarize, a matrix of correlation coefficient values was populated utilizing the following equations provided by Rollinson:

$$R = CSCP / \sqrt{(CSSX \cdot CSSY)}$$

where:

CSCP (corrected sum of cross products) $= \sum (xy) - \sum (x) \cdot \sum (y)/n$

CSSX (corrected sum of squares for x) $= \sum (x^2) - \sum (x) \cdot \sum (x)/n$

CSSY (corrected sum of squares for y) $= \sum (y^2) - \sum (y) \cdot \sum (y)/n$

An abbreviated matrix of select elements is provided in Table 5.1, with a complete listing included in Appendix 4. Elements where incomplete data sets are available due to analytical results falling below detection limits were excluded from the matrix.

Barrett and MacLean (1994) recommend excluding volatile values and recalculating major element composition data to total 100%, however, this was not done for several reasons. Recalculating major oxides to total 100% overlooks the combined compositional contribution of trace elements which may produce positive distortions (Gifkins et al., 2005). Even small adjustments to compositional data may result in large magnitude distortion of mass change estimates due to closure. Also, Barton et al. (1991) have demonstrated volatile components to be an integral ingredient of metasomatic processes within a system. Their arbitrary removal and subsequent bulk recalculation may result in further distortion of mass change estimates. Although MacLean and Barrett (1993) recommend removing outlier assays that do not conform to a linear trend, in this case these values may represent heterogeneity within the porphyry and were therefore included.

Results of the immobility test show that a number of element pairs from the sampled porphyry are potentially immobile, including Ti-Sc, Ti-Zr, Sc-Y, and Sc-Zr. Bivariate plots of these element pairs have been provided in Figure 5.1 and 5.2. Titanium was chosen as the immobile monitor because it has multiple correlation coefficients greater than 0.90. Absolute mass changes of individual elements are calculated using the following equation (after Gifkins et al., 2005):

$$\text{Mass Change} = [Z^o/Z^a \cdot C^a] - C^o$$

where:

Z^o = quantity of immobile element in precursor rock

Z^a = quantity of immobile element in altered rock

C^o = quantity of mobile component in precursor rock

C^a = quantity of mobile component in altered rock

Absolute values of mass change are reported as g/100g where C^o and C^a values are expressed in wt %, and ppm/100g where C^o and C^a are expressed in ppm. Figure 5.3 illustrates calculated absolute mass change for all major elements; select trace elements are illustrated in Figure 5.5. Loss on ignition is included as a loosely defined analog for volatile components. A complete listing of calculated mass change is included in Table 5.2. As K-metasomatism is generally characterized by the replacement of Na and Ca by K phases, samples are ordered on the basis of absolute mass change of K_2O, with ordering consistently maintained for each graph and table to allow efficient comparison. Here, pale coloured bars are employed to represent samples that petrographically show weak to strong alteration effects, including variable preservation of porphyry texture. Intermediate colour is used to indicate pervasive replacement with poor preservation of primary texture. The darkest colour is used to indicate a sample obtained from the porphyry boundary showing intense textural destruction and pervasive potassium feldspar replacement. Samples were not further differentiated by alteration facies on the assumption that K-metasomatism was the most significant alteration process.

Mass change calculations postulate that altered samples share a precursor of similar composition to the least altered, therefore results reasonably quantify the magnitude of mass gain or loss of individual components with respect to the immobile monitor (re: TiO_2). How

Table 5.1 Correlation coefficient matrix calculated from all feldspar porphyry samples from Lou Lake (n=13). R values > 0.90 are in bold.

	TiO_2	Al_2O_3	Sc	Y	Zr	Nb	La	Ce	Nd	Sm	Tb	Ho
TiO_2	-											
Al_2O_3	0.8371	-										
Sc	**0.9559**	0.8067	-									
Y	0.7926	0.6189	0.8953	-								
Zr	**0.9058**	0.7493	0.8601	0.7351	-							
Nb	0.8234	0.8787	0.8117	0.7789	0.7047	-						
La	0.8059	0.6436	0.8605	0.7911	0.7309	0.7031	-					
Ce	0.7994	0.6270	0.8648	0.8100	0.7106	0.7015	**0.9975**	-				
Nd	0.8096	0.6545	0.8844	0.8346	0.7197	0.7439	**0.9888**	**0.9934**	-			
Sm	0.7587	0.5533	0.8516	0.8409	0.6807	0.7002	**0.9619**	**0.9725**	**0.9848**	-		
Tb	0.7406	0.5160	0.8524	**0.9028**	0.6786	0.7088	**0.9124**	**0.9286**	**0.9506**	**0.9825**	-	
Ho	0.8542	0.6483	**0.9428**	**0.9868**	0.7678	0.7786	0.8410	0.8585	0.8788	0.8802	**0.9238**	-
Hf	0.8509	0.7771	0.8136	0.7035	**0.9083**	0.7601	0.6942	0.6774	0.7094	0.6752	0.6738	0.7283

this calculated addition or removal compares to effects on bulk composition is also of considerable interest. These effects can be demonstrated in several ways including as a percent of the least-altered component, or as a net change to the least-altered composition. Both are included as they illustrate gains and losses differently, and provide alternate perceptions that allow an improved understanding of the alteration process. Percent changes from a least altered bulk composition are illustrated in Figure 5.4 for major elements with select trace elements illustrated in Figure 5.6. Net enrichment/depletion values are detailed in Table 5.3. Complete percent change details are included in Appendix 5. Calculations were determined as follows:

$$\% \text{ Change to Bulk Composition} = [C^a - C^o] / C^o \cdot 100$$

$$\text{Net Enrichment or Depletion} = C^a - C^o$$

All major elements show mobility relative to titanium. Mass change results and behaviour during K-metasomatism are discussed individually for select major and trace components below:

Silica

Mass change calculations show silica is highly mobile under hydrothermal conditions. Transfers are mixed (-19.8 to +758.3 g/100g) suggesting silica is locally removed or added to the porphyry. Mass balance values compare with a net depletion or enrichment (from a least-altered bulk composition) of -9.75 to +11.25 wt %. Mass change diagrams reveal that at low levels of potassium addition, silica is largely removed from the system. However, this relationship reverses under increasing intensity of potassium addition as greater transfers of
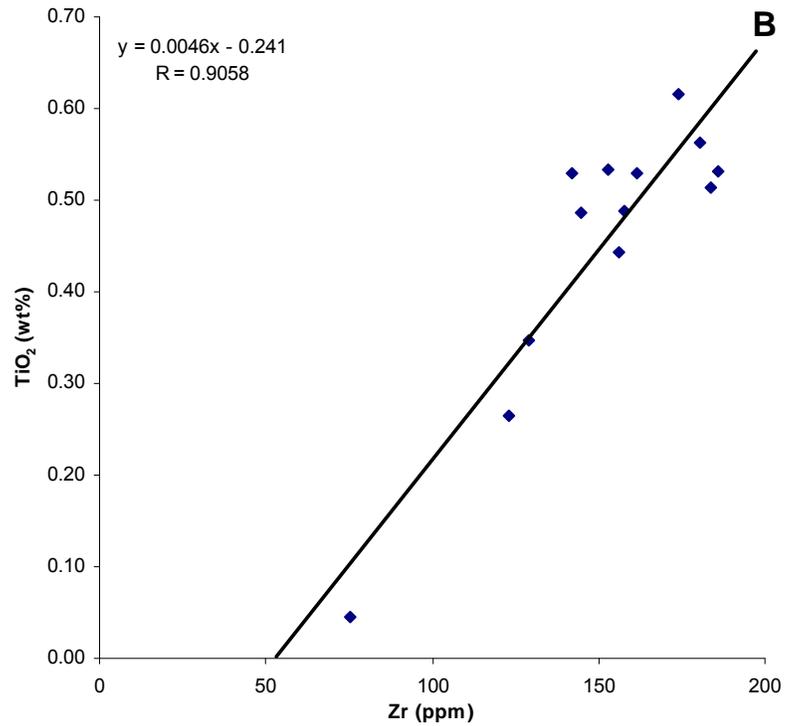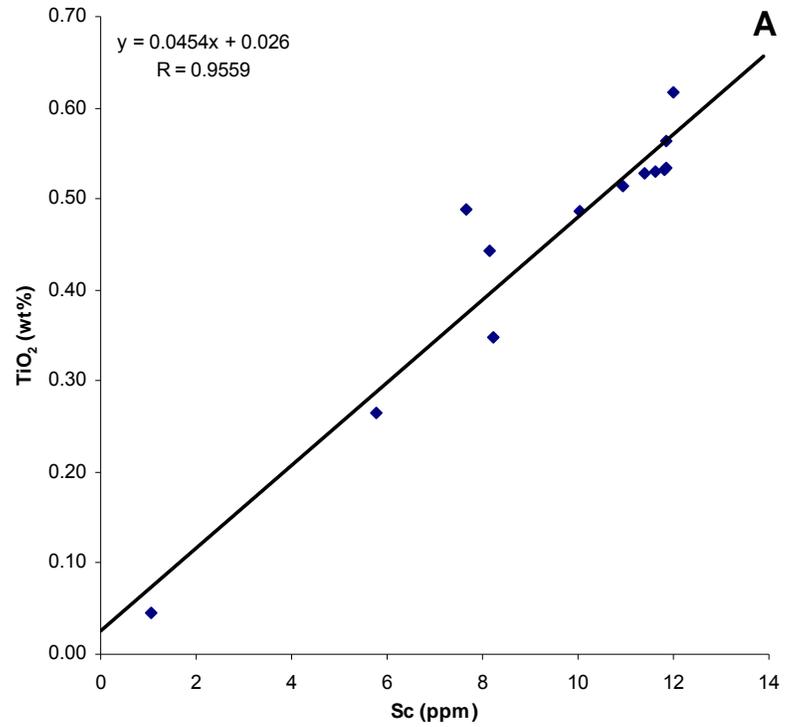
Figure 5.1 – Bivariate plots: a) TiO₂ vs. Sc, and b) TiO₂ vs. Zr. R values and equations of alteration lines are included in the upper left corner on each diagram.
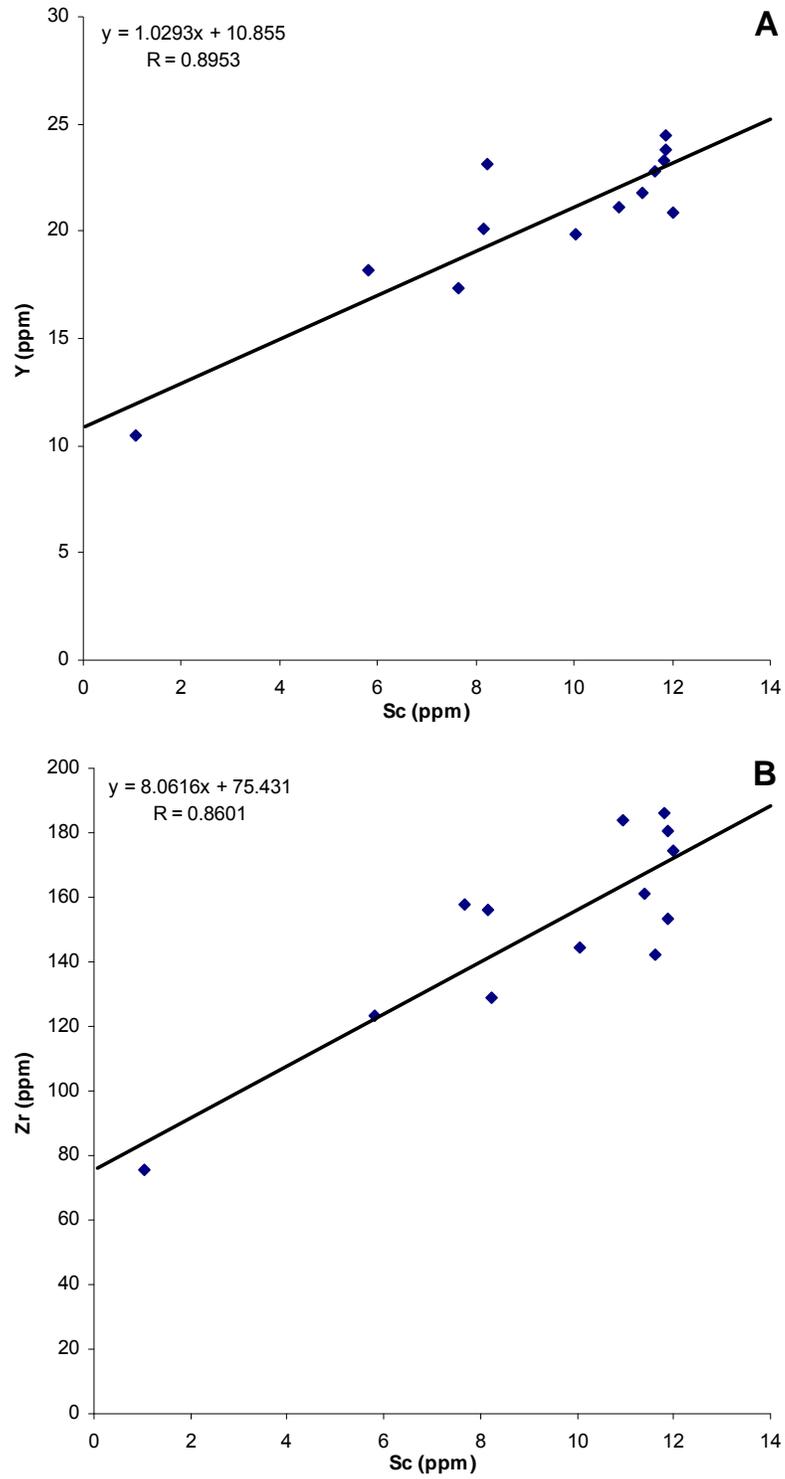
Figure 5.2 – Bivariate plots: a) Y vs. Sc, and b) Zr vs. Sc. R values and equations of alteration lines are included in the upper left corner on each diagram.

Table 5.2 – Calculated absolute mass change values relative to titanium for altered samples of feldspar porphyry.

Sample ID	024W	002E	026W	025W	005W	004E	006E	010W	014E	015E
(results in g/100g)										
SiO_2	-7.14	-3.85	-3.92	-2.16	-4.61	1.89	-19.79	28.94	63.76	758.32
Al_2O_3	-1.55	-0.64	-0.85	-0.32	-0.92	0.13	-0.71	4.74	11.42	114.99
Fe_2O_3T	-1.58	-0.55	1.71	-0.15	-0.91	0.22	0.69	0.79	-0.05	4.44
MnO	0.02	-0.01	0.03	-0.01	-0.00	0.03	-0.01	0.00	0.03	0.06
MgO	-0.35	-0.07	3.79	-0.07	-0.10	0.14	0.25	0.01	-0.01	-0.24
CaO	-0.15	-0.05	0.30	-0.09	0.02	-0.56	-0.88	-0.52	0.94	1.65
Na_2O	-1.14	-0.34	-2.74	-1.11	-1.22	-2.03	-2.87	-1.98	-2.44	-0.86
K_2O	1.00	1.03	1.45	1.53	2.23	2.62	4.23	8.93	14.65	105.72
P_2O_5	-0.01	-0.01	-0.01	-0.01	-0.01	-0.01	-0.03	-0.01	0.01	-
LOI	0.40	-0.05	3.12	0.03	0.09	0.52	0.88	0.15	1.93	2.45
Net	-10.49	-4.54	2.89	-2.35	-5.45	2.97	-18.25	41.06	90.23	986.55
(results in ppm/100g)										
Sc	0.03	0.27	-2.65	0.14	0.61	-0.17	-0.76	1.37	0.45	1.04
V	-5.21	1.79	-7.68	2.56	-1.50	11.87	-26.06	-3.87	-3.78	-
Cr	-15.72	-23.35	-20.78	-19.11	-20.98	1.96	-25.23	-22.84	-15.98	-
Cu	3.14	-29.83	45.70	-2.57	-3.31	-16.61	-28.79	-31.03	-22.34	668.52
Zn	-1.15	2.63	45.90	-2.72	1.27	21.31	7.73	4.58	2.80	94.28
Rb	-46.48	52.51	-40.01	47.86	43.60	6.27	-61.58	155.24	184.51	1940.45
Sr	-56.46	-19.18	-90.67	-11.46	-37.29	-49.22	-70.87	-59.23	-77.72	75.07
Y	-0.43	-1.53	-4.31	-1.56	-0.21	-1.69	-5.24	11.24	12.37	91.79
Zr	10.66	2.69	12.03	29.14	25.16	-1.18	-8.47	36.25	83.49	674.21
Nb	-1.58	-1.52	-1.66	-1.49	-0.99	-0.06	-0.95	3.84	6.07	58.28
Cs	-8.13	8.59	-4.74	-0.36	3.58	-3.71	-4.90	12.21	-4.28	3.67
Ba	12.49	-78.78	234.94	130.86	97.17	469.56	140.80	830.95	1574.52	12178.82
La	-2.56	-2.75	-25.39	-4.93	-7.87	-10.12	-18.21	-13.82	-23.26	-1.76
Ce	-7.72	-5.92	-52.55	-10.52	-18.17	-19.64	-39.36	-23.06	-44.55	-15.94
Pr	-1.13	-0.65	-5.68	-1.08	-1.71	-1.52	-3.99	-1.84	-4.51	-1.50
Nd	-3.20	-1.61	-18.82	-3.05	-4.92	-4.19	-12.22	-4.15	-14.33	-4.60
Sm	-0.56	-0.37	-2.37	-0.44	-0.38	-0.25	-2.01	-0.12	-1.51	1.21
Eu	-0.09	-0.07	-0.66	-0.13	-0.16	-0.21	-0.54	-0.26	-0.54	-0.24
Gd	-0.34	-0.13	-1.60	-0.26	-0.23	-0.28	-1.70	0.56	-0.47	5.28
Tb	-0.04	-0.06	-0.23	-0.04	-0.01	-0.00	-0.22	0.14	0.01	1.08
Dy	-0.15	-0.20	-1.00	-0.31	-0.09	-0.05	-0.95	1.46	0.93	12.21
Ho	-0.02	-0.04	-0.11	-0.04	-0.02	-0.02	-0.16	0.30	0.35	3.11
Er	0.05	-0.19	-0.03	-0.11	0.06	0.04	-0.29	1.16	1.63	11.17
Tm	0.02	-0.02	0.04	-0.00	-0.01	0.05	-0.01	0.21	0.34	2.03
Yb	-0.03	-0.04	0.33	-0.11	0.03	0.25	-0.01	1.54	2.55	14.98
Lu	0.01	0.00	0.12	0.00	0.00	0.05	-0.03	0.26	0.46	3.17
Hf	0.03	0.27	0.06	0.26	0.18	0.45	-0.30	1.33	2.97	24.56
Ta	-0.31	-0.23	-0.28	-0.25	-0.25	-0.05	0.06	1.20	2.68	25.24
Th	-2.24	-1.68	-1.93	-1.73	-1.34	1.62	-5.54	9.50	23.68	247.65
U	-1.18	-0.88	-2.04	-0.88	-0.63	0.08	-1.86	5.47	11.02	127.14
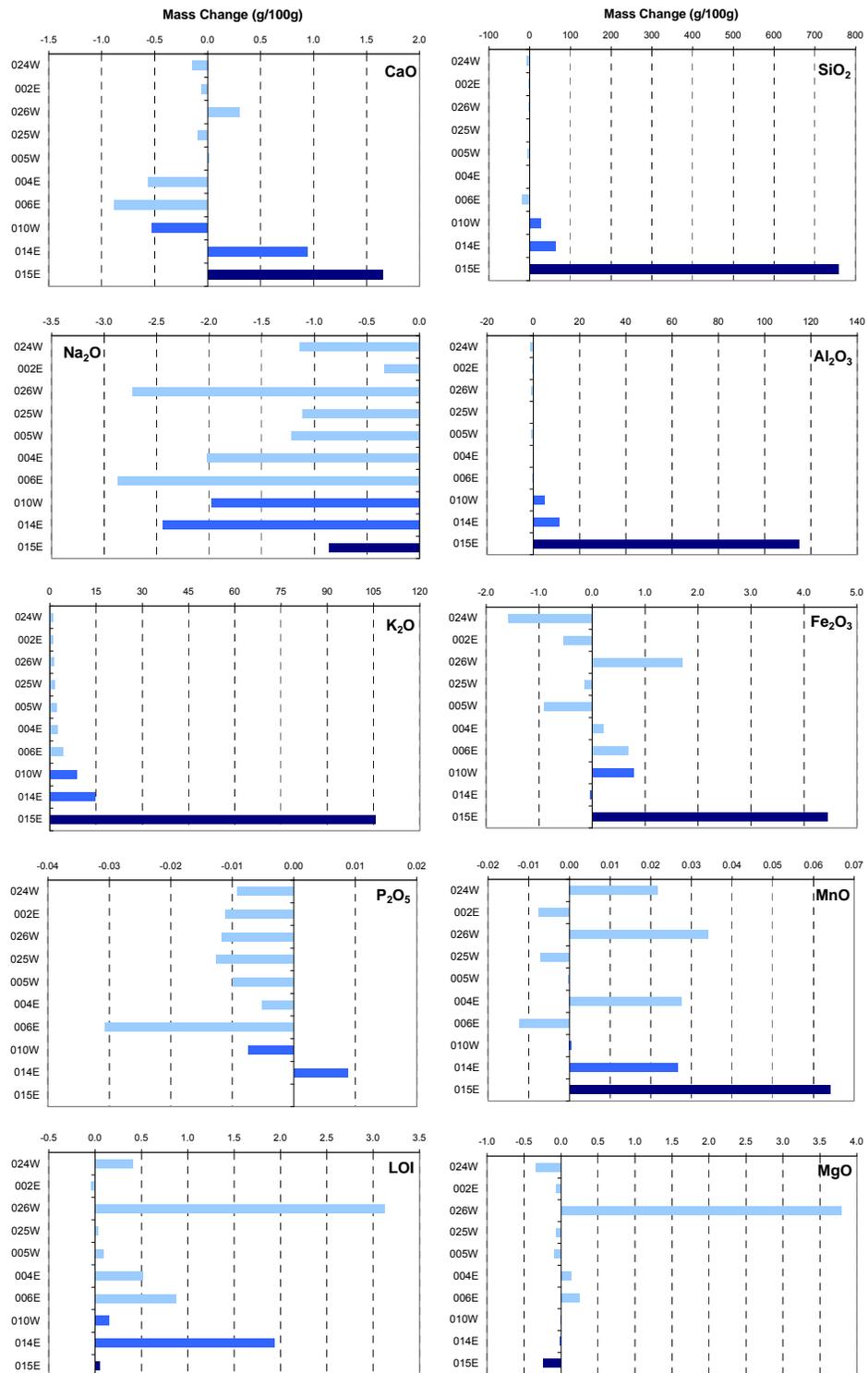
Figure 5.3 – Absolute mass gains or losses of major elements for altered feldspar porphyry samples. (pale blue – least to intermediate alteration effects; medium blue – strong alteration effects; dark blue – intense alteration effects).
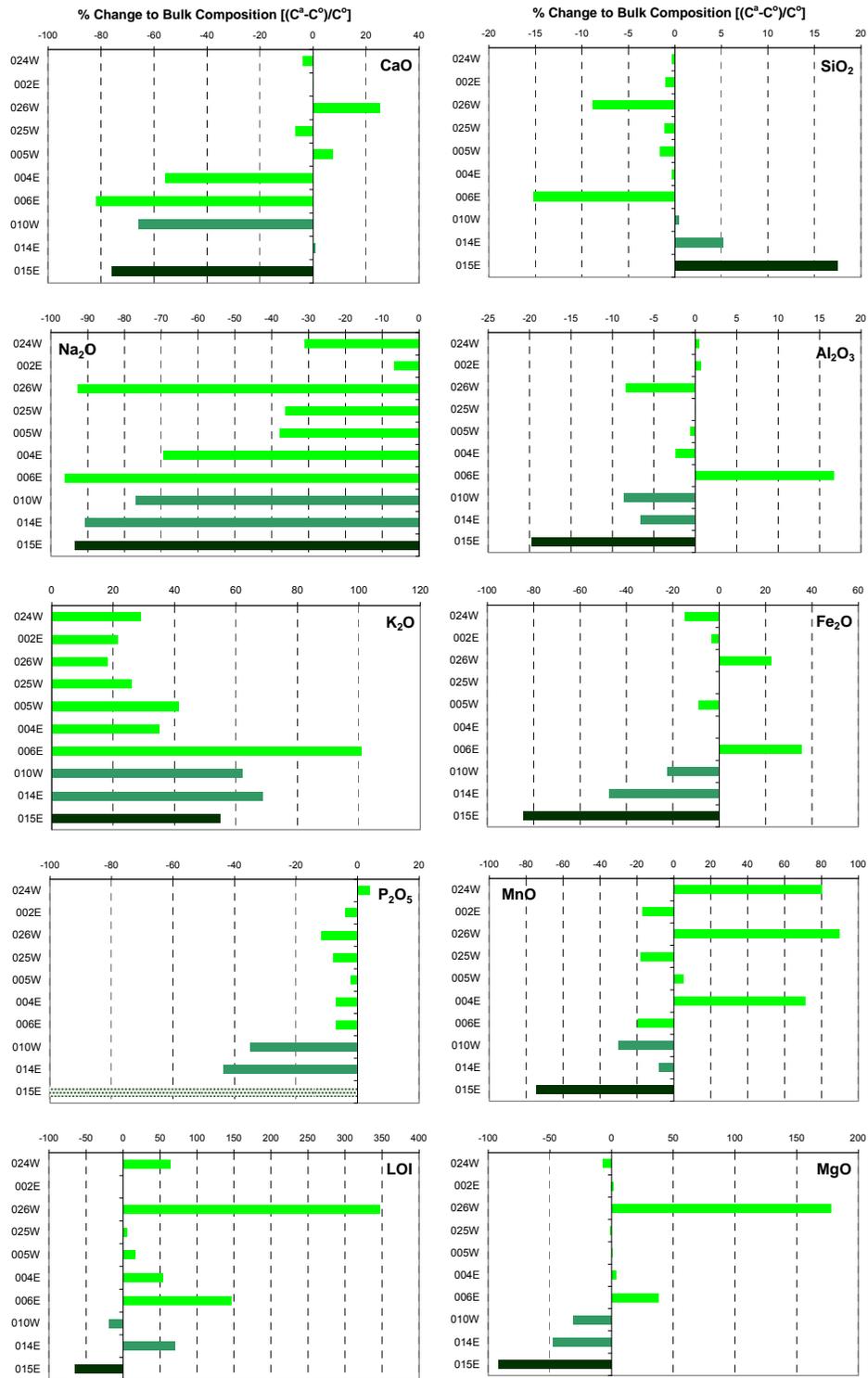
Figure 5.4 – % Change to bulk composition of altered feldspar porphyry samples from a least altered precursor. (pale green – least to intermediate alteration effects; medium green – strong alteration effects; dark green – intense alteration effects; stippled – estimated change).
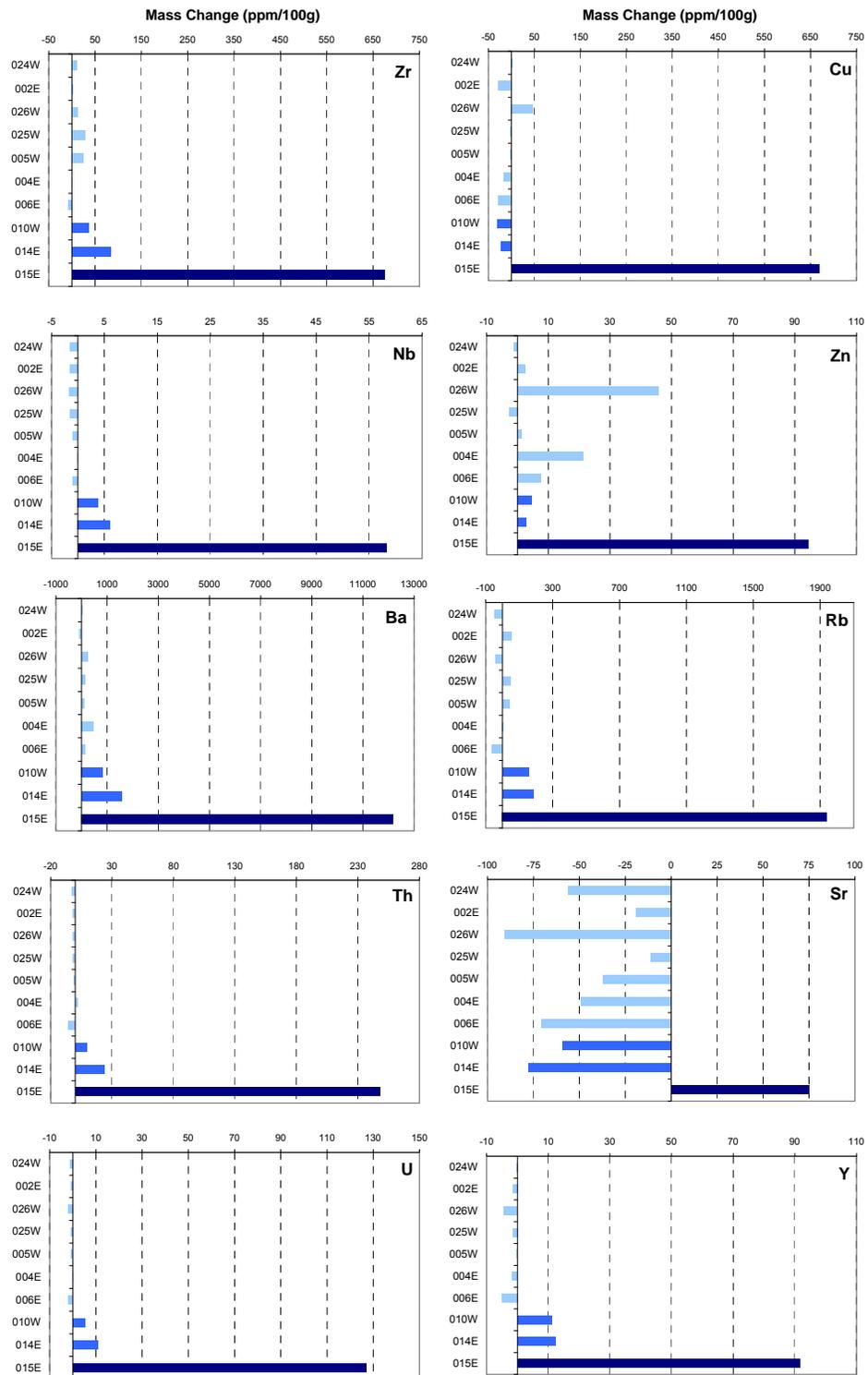
Figure 5.5 – Absolute mass gains or losses of trace elements for altered feldspar porphyry samples. (pale blue – least to intermediate alteration effects; medium blue – strong alteration effects; dark blue – intense alteration effects).
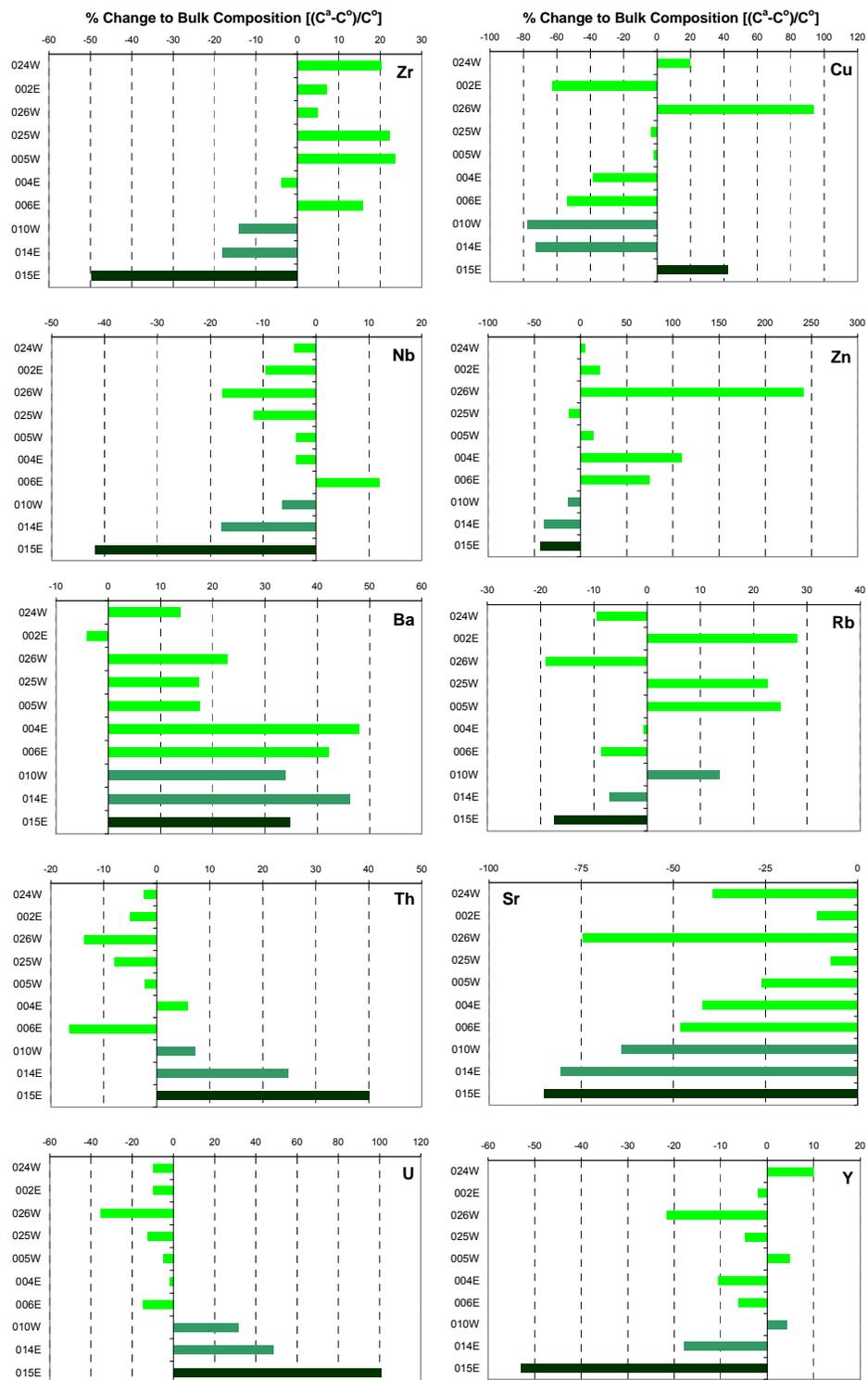
Figure 5.6 – % Changes in bulk composition for altered feldspar porphyry samples from a least altered precursor. (pale green – least to intermediate alteration effects; medium green – strong alteration effects; dark green – intense alteration effect).

Table 5.3 – Net element enrichment / depletion for altered samples of feldspar porphyry relative to an average least-altered bulk composition (n = 3).

Sample ID	024W	002E	026W	025W	005W	004E	006E	010W	014E	015E
(in wt%)										
SiO_2	-0.22	-0.67	-5.66	-0.74	-1.08	-0.24	-9.75	0.28	3.31	11.25
Al_2O_3	0.07	0.11	-1.25	0.01	-0.10	-0.35	2.49	-1.29	-0.99	-2.93
Fe_2O_3T	-0.97	-0.23	1.47	-0.00	-0.58	0.00	2.34	-1.48	-3.14	-5.57
MnO	0.03	-0.01	0.03	-0.01	0.00	0.03	-0.01	-0.01	-0.00	-0.03
MgO	-0.14	0.04	3.62	-0.02	0.02	0.07	0.77	-0.62	-0.97	-1.87
CaO	-0.04	-0.00	0.26	-0.07	0.08	-0.57	-0.84	-0.68	0.01	-0.78
Na_2O	-0.92	-0.20	-2.74	-1.07	-1.12	-2.06	-2.85	-2.28	-2.69	-2.77
K_2O	1.93	1.43	1.22	1.72	2.75	2.32	6.70	4.13	4.57	3.64
P_2O_5	0.01	-0.01	-0.02	-0.01	-0.00	-0.01	-0.01	-0.04	-0.06	-0.13
LOI	0.56	-0.01	3.01	0.05	0.15	0.48	1.27	-0.16	0.61	-0.56
(in ppm)										
Sc	1.32	0.85	-2.88	0.39	1.28	-0.50	1.46	-2.30	-4.75	-9.48
V	2.87	5.67	-9.53	4.27	2.67	9.17	-15.73	-24.73	-35.83	-71.53
Cr	-11.37	-21.87	-21.67	-18.37	-19.17	0.23	-19.27	-31.67	-32.77	-51.47
Cu	9.13	-28.97	43.03	-1.57	-0.77	-17.57	-24.87	-35.67	-33.57	19.33
Zn	0.93	3.73	44.03	-2.37	2.43	20.03	13.63	-2.47	-7.17	-7.97
Rb	-22.71	68.08	-45.87	54.52	60.59	-1.75	-20.64	32.80	-17.18	-42.08
Sr	-48.40	-13.70	-91.60	-8.90	-32.20	-51.60	-59.10	-78.80	-99.00	-104.60
Y	2.23	-0.43	-4.83	-1.09	1.10	-2.35	-1.38	0.93	-3.99	-11.78
Zr	30.27	10.79	7.31	33.28	35.62	-6.01	23.79	-21.32	-27.19	-74.98
Nb	-0.46	-1.03	-1.93	-1.28	-0.41	-0.41	1.30	-0.70	-1.94	-4.53
Cs	-7.95	9.56	-4.88	-0.15	4.37	-3.90	-3.83	5.49	-6.79	-8.38
Ba	121.97	-36.03	202.37	154.27	155.77	425.67	374.27	301.17	409.97	308.77
La	2.27	-0.66	-25.88	-4.07	-5.83	-11.16	-12.76	-22.59	-32.24	-38.54
Ce	1.83	-1.68	-53.52	-8.78	-14.12	-21.79	-28.74	-42.51	-64.23	-79.72
Pr	-0.14	-0.20	-5.78	-0.90	-1.26	-1.76	-2.80	-4.12	-6.74	-8.52
Nd	0.08	-0.10	-19.15	-2.43	-3.41	-5.03	-8.16	-12.16	-21.80	-27.79
Sm	-0.14	-0.18	-2.42	-0.36	-0.16	-0.37	-1.56	-1.32	-2.69	-3.53
Eu	0.02	-0.03	-0.67	-0.11	-0.11	-0.24	-0.44	-0.48	-0.74	-0.89
Gd	0.01	0.04	-1.65	-0.19	-0.05	-0.37	-1.34	-0.62	-1.80	-2.49
Tb	0.02	-0.03	-0.23	-0.03	0.01	-0.02	-0.16	-0.06	-0.24	-0.37
Dy	0.27	-0.03	-1.07	-0.23	0.12	-0.16	-0.35	-0.10	-1.21	-2.14
Ho	0.07	-0.00	-0.13	-0.03	0.02	-0.04	-0.04	-0.01	-0.15	-0.35
Er	0.29	-0.10	-0.08	-0.07	0.18	-0.03	0.08	0.21	-0.05	-0.73
Tm	0.06	-0.01	0.03	0.00	0.01	0.04	0.07	0.05	0.03	-0.10
Yb	0.23	0.07	0.26	-0.07	0.16	0.18	0.46	0.42	0.36	-0.52
Lu	0.05	0.02	0.11	0.01	0.02	0.04	0.03	0.08	0.09	-0.01
Hf	0.50	0.48	-0.05	0.35	0.41	0.31	0.50	-0.26	-0.24	-1.22
Ta	-0.18	-0.17	-0.32	-0.23	-0.18	-0.09	0.39	0.41	0.76	1.06
Th	-0.40	-0.85	-2.38	-1.37	-0.39	1.01	-2.86	1.23	4.28	6.93
U	-0.58	-0.61	-2.16	-0.76	-0.30	-0.12	-0.90	1.91	2.93	6.12

silica occur for samples that petrographically show the most intense potassium feldspar replacement. These transfers appear to be balanced by similarly high gains in aluminum and potassium. Several samples (026W and 006E) demonstrate significant silica depletion. Net change diagrams show this depletion is coupled with anomalous enrichment of total iron and magnesium. Petrographically, these two samples exhibit strong hematization and chloritization effects.

Aluminum

Though aluminum exhibits similar mass change patterns to silica, enrichment patterns are markedly different. Mass transfer calculations indicate a potential for very high mobility during alteration, with values ranging from -1.6 to +115.0 g/100g. Though net depletion-enrichment values vary between -2.9 and +2.5 wt %, aluminum content within the porphyry remains largely unchanged. These inconsistent changes suggest aluminum may be relatively immobile at low alteration intensity. Samples 026W and 006E (as discussed above for silica) show an inconsistent behaviour marked by changes to aluminum and calcium content that are inversely related. Mass change calculations also reveal that samples petrographically exhibiting the strongest alteration effects (010W, 014E, 015E) show both the greatest gains in aluminum but a net aluminum depletion This is interpreted to indicate equilibration of the porphyry at a bulk composition that approaches mineralogical potassium feldspar where alteration is most intense. It is likely that both net enrichment and depletion of aluminum results from mass balancing with silica and potassium. This suggestion is supported by equivalent mass change ratios of ~7 for SiO_2/Al_2O_3 and SiO_2/K_2O at peak intensity.

Total Iron

Iron shows low absolute mass change values that range from -1.6 to +4.4 g/100g which suggests its mobility may be limited during hydrothermal alteration. Net depletion and enrichment values range from -5.6 to +2.3 wt %. Though mass change diagrams imply iron and potassium share a mixed relationship, net change diagrams indicate iron is generally depleted from the porphyry. These diagrams imply the magnitude of iron depletion and potassium transfers are linked, suggesting dilution of the former less mobile element by highly mobile phases. Iron enrichment is restricted to those samples (026W and 006E) previously identified as showing intensification of hematite.

Manganese

Manganese exhibits moderate mobility and mixed behaviour to potassium enrichment. Mass transfer ranges from -0.012 to +0.064 g/100g. Although net depletion-enrichment values are low (-0.027 to +0.032 wt %) they represent changes to bulk composition of -74.4 to +89.8 %. Though a link between net changes to manganese to potassium is unclear, it is generally depleted when rates of potassium transfer are high. This relationship implies manganese depletion occurs through dilution of the system by more mobile phases, as suggested for total iron.

Magnesium

Magnesium generally shows limited mobility and subsequently low mass transfer. Absolute mass change ranges from -0.35 to +3.8 g/100g, with net depletion-enrichment values ranging between -1.9 and +3.6 wt %. Samples show mixed behaviour where net potassium

enrichment is low, although magnesium depletion is common where potassium transfer is high. Samples of porphyry exhibiting effects of hematite and chlorite alteration (026W and 006E) show enriched magnesium content. This enrichment corresponds with gains of iron and calcium, and loss of silica, suggesting the porphyry underwent Mg-metasomatism at a local scale.

Calcium

Calcium shows moderate mobility and a mixed behaviour to potassium. Though absolute mass changes range between -0.9 and +1.6 g/100g, predominantly negative transfers indicate calcium is generally removed from the system. Changes from a least-altered bulk composition vary between -82.0 and +25.3 %. Contrasting patterns between mass transfer and net change diagrams demonstrate the relative mobility and bulk composition are not necessarily linked.

Calcium occurs as a component of several major and trace minerals in the porphyry including plagioclase and apatite, as well as the secondary minerals calcite and epidote. Variable but low magnitude changes in calcium content exhibited by samples showing lesser effects of alteration likely indicate calcium was liberated from calcic plagioclase via diffusive processes. This interpretation is supported by evidence that epidote aggregates occur most commonly within cores of saussuritized feldspars. However, samples showing the greatest mass gains demonstrate significant depletion which suggests a different process was active. Perhaps the large-scale reduction of soluble components occurs as the porphyry is impregnated more fully by hydrothermal fluids. This is evidenced texturally at the outcrop and hand sample scale by patchy grain coarsening. Sample 014E marks a curious exception where net change

to bulk composition is negligible, apparently mass balanced by large positive transfers.

Sodium

Highly mobile sodium exhibits a behaviour that is consistently the inverse of potassium. Sodium is ubiquitously removed from the porphyry, indicated by mass losses (-0.3 to -2.9 g/100g) and consistent depletion from bulk composition of -6.7 to -96.2 %. Net change diagrams show the greatest sodium depletion is coincident with extreme potassium or magnesium enrichment. Relationship with the former suggests a primary coupled exchange of K for Na. The latter implies a secondary exchange process may have been active where the most probable arrangement has Na exchanged for Ca, and Ca exchanged for Mg (and possibly Fe).

Potassium

Mass change calculations show potassium is highly mobile and consistently added to the porphyry system. Results show additions range between 1.0 and 105.7 g/100g, with net changes to bulk compositions from 18.3 to 100.8 %. Mass change and enrichment patterns are markedly different revealing net enrichment is not solely a product of potassium transfer. Rather, peak potassium enrichment coincides with peak aluminum enrichment as suggested by sample 026W, apparently at the expense of silica. The extreme potassium mobility exhibited at the porphyry boundary (sample 015E) appears to be balanced by similarly extreme mobility of silica and aluminum, as discussed above with aluminum.

Phosphorous

Phosphorous generally shows negative transfers except at peak alteration intensity.

Absolute mass change is limited, ranging between -0.031 and +0.009 g/100g, suggesting phosphorous mobility is also low. As phosphorous content fell below detection limits for the sample obtained at the porphyry boundary (015E), mobility under intense alteration conditions remains undefined. Net depletion-enrichment diagrams shows the porphyry bulk composition is commonly depleted in phosphorous (-43.6 to +4.0 %), with observed depletion inversely related to potassium transfer. Extrapolation of known quantities suggests depletion of this relatively immobile species approaches 100% under extreme mobility, most likely a result of dilution by highly mobile components.

Copper

Absolute mass changes for copper range from -31.0 to +668.5 ppm/100g, with net changes varying between -77.4 and +93.4 %. Both mass transfer and enrichment-depletion diagrams show similar patterns which suggest changes to bulk composition is linked to copper mobility. However, these measurements show magnitudinal inconsistencies, and significant copper mobility is spatially limited to the porphyry boundary where intense alteration occurred (see sample 015E) which implies changes may also be a product of gross dilution. A mixed relationship to potassium is revealed by variable gains or losses of copper that are inconsistent with changes to potassium. Correlation coefficients of element pairs involving copper were largely negative, hinting copper may play an independent role during hydrothermal alteration.

Zinc

Absolute mass change diagrams show zinc is moderately mobile. Though mobility is inconsistent with potassium enrichment, it is greatest near the porphyry boundary where alteration is most intense. Zinc shares a high correlation coefficient with MgO (R = 0.9038),

which helps to explain similar patterns as illustrated by respective net change diagrams. Mass transfers range between -2.7 and +94.3 ppm/100g, which compare with net depletion or enrichment that varies between -43.6 and +241.1 %. Significant zinc enrichment occurs in those samples that petrographically show strong chloritization effects. Zinc also demonstrates a moderate correlation to Fe_2O_{3T} (R = 0.5803). This results in moderate enrichment in those samples showing the greatest effects of hematization (samples 004E and 006E).

Rubidium

Rubidium is an alkali that has demonstrated limited substitution for potassium (or sodium). It occupies M-sites within the feldspar structure (Smith, 1983). As microprobe analysis of feldspars does not typically analyze for rubidium, it is assumed here that measured content most likely occur as a trace component of the potassium feldspar species. Rubidium behaviour is inconsistent, showing mixed gains and losses where potassium addition is limited and large transfers where potassium addition is greater. Possibly the former results from a reorganization of elements on a local scale, while the extreme gains during intense alteration (evidenced by sample 015E) indicate high mobility and likely removal from the system during peak hydrothermal conditions. Though mass gains and losses show considerable range (-61.6 to +1940 ppm/100g), net change to bulk composition are more restricted (-45.9 to +68.1 ppm). Interestingly, low magnitude gains and losses exhibited by lesser-altered samples show the greatest net enrichment or depletion of rubidium from the porphyry, evidence that supports the above interpretation.

Strontium

Strontium is an alkaline earth element that demonstrates limited substitution within M-

sites of the feldspar structure. As with rubidium, strontium content is assumed to occur as a trace component of Ca-plagioclase species. Mass balance calculations show strontium is mostly removed from the system during alteration, with moderate addition only at peak intensity. Mass transfers range from -90.7 to +75.1 ppm/100g, and net change to bulk composition varies between -7.2 and -85.2 %. Depletion patterns for strontium mirror that of sodium, showing consistent loss during potassium enrichment. Though Steele and Smith (1982) have shown sodium and strontium to be highly correlated from magmatic suites, calculated coefficients (R = 0.6532) show the two are only fairly correlated for the sampled porphyry.

Yttrium

Calculated mass change for yttrium ranges from -5.2 to +91.8 ppm/100g, with yttrium showing limited losses where alteration intensity is low, but significant gains where alteration intensity is high. This suggests yttrium immobility is relative, with immobility largely compromised during more extreme hydrothermal conditions. Mass balance and net change diagrams show different patterns, though the latter indicates the porphyry is generally depleted in yttrium as a result of K-metasomatism.

Zirconium

Zirconium shows a strong correlation with titanium (R = 0.9058) and fair correlation with scandium (R = 0.8601). However, a bivariate plot of TiO_2 vs. Zr resulted in a linear trend that diverged from the origin suggesting some measure of mobility (see Figure 4.11B). Mass balance calculations show zirconium is mostly added where the porphyry is altered, showing gains up to +674 ppm/100g where alteration is most intense. Different patterns demonstrated

by mass balance and net change diagrams indicate low level gains result in low to moderate enrichment, however the greatest zirconium gains are coupled with net depletion.

Niobium

Mass change calculations show that niobium is commonly removed from the porphyry during low intensity K-metasomatism, and added where potassium addition is more intense. Though absolute gains and losses range between -1.7 to +58.3 ppm/100g, the porphyry shows a net depletion of niobium with alteration is typical. Niobium and aluminum are reasonably correlated (R = 0.8787) which explains their comparable behaviour.

Barium

Barium is another alkaline earth element that, like strontium, demonstrates limited substitution within M-sites of the feldspar structure. Microprobe analysis reported earlier in Chapter 4 show barium occurs as a trace component of potassium feldspar species. Barium shows a fair correlation with potassium (R = 0.7609) explaining similarities between mass transfer and enrichment diagrams. Mass calculations indicate barium is highly mobile during alteration, with transfer values ranging from -78.8 to +12200 ppm/100g. That net barium enrichment of the porphyry is limited (-4.1 to +48.1 % change to bulk composition) suggests barium is largely removed from the system at peak alteration intensity. This is evidenced by simple and complex barite veins that commonly cross-cut altered porphyry.

Rare Earth Elements

Behaviour patterns for the rare earth elements (REE) are most clearly observed by plotting per cent changes relative to the least altered precursor composition (Figure 5.7).

Patterns for light REE's show consistent depletion with magnitude of change largely corresponding to degrees of potassium enrichment. This relationship most likely results from relatively strong correlations between the light REE's and sodium (see complete correlation coefficient matrix for feldspar porphyry in Appendix 4). Sample 026W is distinguished by significant light REE depletion concurrent with low potassium but high magnesium enrichment. Though absolute mass change results are variable element-by-element, negative values illustrate how the light REE's are largely removed from the porphyry during potassium metasomatism (Table 5.2).

The heavy REE's exhibit a behaviour that generally contrasts that of the light REE's. Absolute mass change values show limited removal where effects of potassium metasomatism are less but moderate addition where effects are stronger. Greater variation demonstrated by patterns of per cent change to bulk composition correspond strongly to atomic radii (Figure 5.7). Elements with greater atomic radii (Tb, Dy, Ho) express magnitudes of depletion that more closely resemble those observed for the light REE's. Gradually lower depletion marked by decreasing radius is most strongly expressed by the heaviest REE's (Er, Tm, Yb, Lu) which exhibit variable low level enrichment or minimal change coincident with increasing potassium enrichment. With the exception of Lu, the heavy REE's show a strong correlation to Sc, with Lu moderately correlated to both Tm and Yb. The three heaviest REE's (Tm, Yb, Lu) exhibit moderate enrichment in sample 026W, suggesting a link with calcium and magnesium which show similar enrichment.

Thorium

Mass balance calculations indicate a mixed behaviour and moderate mobility for

thorium. Where alteration effects are less, thorium is generally lost from the system, and where alteration effects are more severe, thorium is gained. Mass transfers range from -5.5 to +247.6 ppm/100g. Net change patterns are consistent with mass balancing, showing a net depletion or enrichment of the porphyry between -16.5 and +40.0 %.

Uranium

Uranium exhibits behaviour very similar to thorium, showing similar mass transfer and net change patterns and moderate mobility. Absolute mass changes range from -2.0 to +127.1 ppm/100g. The losses or additions result in net changes to uranium content that varies between -35.5 to +100.8 % from the least-altered bulk composition.
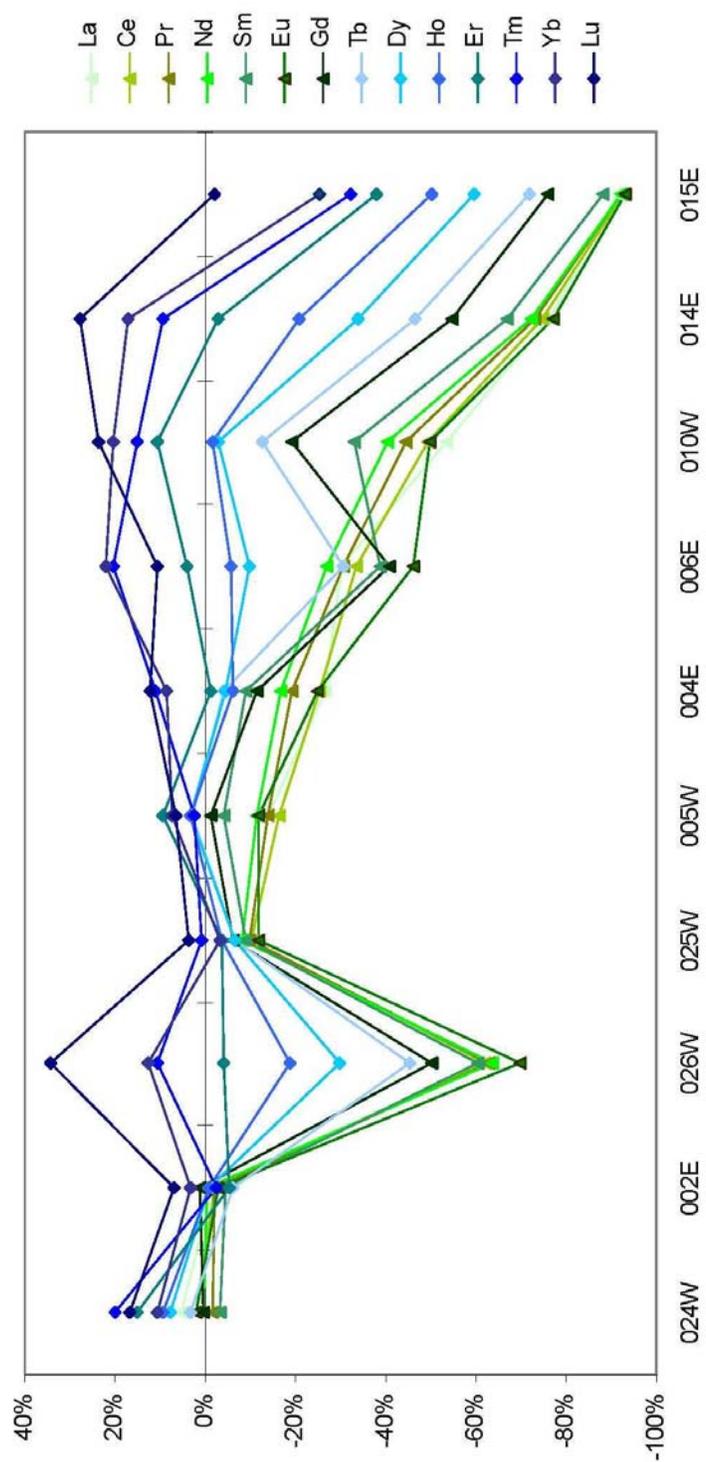
Figure 5.7 – Linear plot of % change to bulk composition for altered feldspar porphyry samples relative to a least altered precursor. (Green triangles – light REE's; Blue rhombs – heavy REE's; REE's are listed in order of decreasing atomic radii from top to bottom).

CHAPTER 6 – DISCUSSION

6.1   Introduction

At the NICO deposit, both Paleoproterozoic metasedimentary and volcanic rocks are overprinted by extreme K-metasomatism. The effects of K-metasomatism have been described in terms of petrography, bulk rock and mineral chemistry, oxygen isotopes and mass transfer estimates as a part of this investigation. K-metasomatism has pervasively affected rocks across the metasedimentary-volcanic transition. As this boundary condition is the focus for K-metasomatism, defining its specific character is important for understanding the development of K-metasomatism at NICO. The regional tectonic setting and its geochronological development are reviewed in Section 6.2. The nature of the metasedimentary-volcanic boundary and significance of the associated brecciation are discussed in Section 6.3. In Section 6.4, cross-cutting relationships and petrographic evidence are used to constrain the relative timing of K-metasomatism. Additional constraints on tectonic conditions and fluid sources that were active during K-metasomatism are outlined in Section 6.5.

6.2   Regional Tectonic Setting

Lou Lake occurs at the southern extent of the Great Bear Magmatic Zone, a magmatic arc that developed in the core of the Wopmay Orogen. The immediate study area covers the boundary between regionally metamorphosed Treasure Lake Group metasedimentary rocks and well preserved non-metamorphosed Lou Lake volcanic rocks.

The Treasure Lake Group comprises an upward-coarsening platform succession comprised of basal metasiltstone, lower carbonate, middle meta-arenite and upper

metasiltstone. Gandhi and van Breeman (2005) assert deposition of Treasure Lake Group occurred within the Hottah arc terrane. They distinguish this sequence from Snare Group metasedimentary rocks deposited on Slave basement east of the Wopmay Fault Zone on the basis of stratiform disseminated magnetite within basal metasiltstone. Detrital zircons sourced from meta-arenite indicate a provenance as young as 1886 Ma, providing a maximum age of deposition. Deformation and regional upper greenschist to amphibolite-facies metamorphism of metasedimentary rocks occurred coeval with accretion of the Hottah terrane along the western margin of the Slave craton during the Calderian Orogeny ca. 1883 Ma.

Gandhi et al. (2001) documented post-collisional development of the southern GBMZ from early arc and associated volcanism, and later anorogenic magmatism. This magmatism evolved from early sodic, to medial calc alkaline, to late potassic. Overlapping geochronology indicate that the calc alkaline volcanism was the extrusive equivalent of regional batholiths emplaced ca. 1867 Ma. Constrained by U-Pb zircon dates of 1867 Ma obtained from cross-cutting quartz monzonite plutons, deposition of Lou Lake volcanism occurred early in this time interval. The Lou Lake volcanic succession is broadly defined by massive to flow-banded tuffs and subporphyritic to porphyritic flows.

The Marion River Batholith and the later Faber Lake granitic suite dominated the magmatic development of the southern GBMZ. The former is exposed as coarse-grained plutonic rocks immediately north and east of Lou Lake. U-Pb zircon dates reported by Gandhi et al. (2001) for granodiorite and gneissic equivalents demonstrate syntectonic emplacement of the Marion River Batholith at 1866 Ma. These same authors' note foliations parallel to metasedimentary boundaries and lit-par-lit magmatic injections into metasedimentary layering. This style of deformation is consistent with fabrics that result from large temperature contrasts

during emplacement between intrusive and intruded rocks (Thorpe and Brown, 1985). Development of cordierite knots and local garnet spots in Treasure Lake Group metasiltstone bordering the Marion River granodiorite between Dianne and Peanut Lakes are indicative of a regional amphibolite-facies metamorphic overprint.

Post-kinematic emplacement of the potassic Faber Lake Granite ca. 1856 Ma post-dated emplacement of the Marion River Batholith, and marked a tectonic change to post-orogenic. The Faber Lake intrusive suite comprises coarse-grained rapakivi-textured granitic and finer aplitic rocks forming a 20 kilometer circular pluton north of Lou Lake. D'Oria (1998) documented rapakivi textures with albitic plagioclase rinds developed on alkali feldspar and andesine phenocrysts. Close agreement between Faber Lake geochronology and U-Pb zircon dating ca. 1851 Ma obtained from potassium feldspar metasomatic rocks at Summit Lake suggest a link between late potassic magmatic activity and K-metasomatism.

6.3   The Metasedimentary-Volcanic Boundary

Substantial evidence collected at NICO indicates permeability enhancement played a significant role in promoting K-metasomatism. Secondary permeability resulted from processes occurring at the metasedimentary-volcanic interface. Previous investigators have regarded this boundary as either an unconformity or a detachment fault. Both interpretations offer a mechanism for juxtaposing high-level, relatively young rocks onto deep-level comparatively older ones. Though the nature of this boundary was not a primary focus of this investigation, its apparent control on K-metasomatism requires some clarification.

Primary field evidence used to support an unconformity at Lou Lake arises from contacts observed at surface between metasedimentary rocks and potassium feldspar

metasomatic rocks commonly misinterpreted as rhyolite. As demonstrated by Plate 6.1, sharp metasedimentary-metasomatite contacts demonstrate a truncation of tilted, older metasedimentary sequence against younger rocks, a relationship further demonstrated in cross sections (Figure 3.2 – back pocket). Closer scrutiny of these contacts reveal infiltration of potassium feldspar from overlying rocks penetrating metasedimentary structures, indicative of their metasomatic origin. Sensu stricto, an angular unconformity is defined as a surface of erosion or non-deposition separating younger strata from older rocks (Billings, 1972). Though an unconformity-like relationship clearly exists, there are genetic implications to their classification. They result from a sequence of uplift or rotation, followed by erosion or a period of non-deposition, and subsequent renewal of deposition (Hatcher, 1995). The discordant potassium feldspar replacement as evidenced by these bounding relationships is unconformable in a descriptive sense. However the metasomatic origin of these discordant surfaces distinguishes them in a genetic sense from those resulting from classic unconformity processes.

Contact relationships between metasedimentary and volcanic rocks revealed through drilling activities are equally ambiguous. These show fresh volcanic rocks juxtaposed against metasedimentary rocks. Geochronological evidence shows volcanic deposition pre-dated magmatic emplacement, but magmatic emplacement was syn-tectonic as revealed by the development of gneissic domains. The lack of metamorphic overprints on high-level volcanic rocks suggests this boundary against deep-level metasedimentary rocks post-dated emplacement of the Marion River Batholith.

Respective orientations of metasedimentary and volcanic stratigraphy provide further clues to the nature of this boundary. Treasure Lake Group rocks are moderately dipping from

40° to nearly vertical. They are overlain by Lou Lake volcanic rocks dipping moderately between 20° and 40° along a similar strike direction. Orientations for the metasedimentary-potassium feldspar metasomatite transition as revealed in cross section are markedly horizontal to shallowly dipping, suggesting this surface records the metasomatic event.

The complex styles of brecciation developed at the boundary between metasedimentary rocks and potassium feldspar metasomatite are best interpreted as an intermingling of breccia derived through multiple processes. Though these breccias are typically matrix supported with randomly distributed clast populations chiefly derived from metasedimentary basement and potassium feldspar metasomatic rocks, they show significant variation in clast morphology, abundance, and matrix compositions. Clast shapes indicative of brittle deformation show variable preservation suggestive of corrosive hydrothermal infiltration. Drill core intersections show disaggregation developed over thicknesses up to 10's of meters at the metasedimentary-metasomatite interface, indicating significant displacement (Figure 3.5). As evidenced by the abundance of metasomatite clasts, pervasive fine grained K-feldspar breccia matrix and assimilation textures demonstrating interactions between potassium feldspar metasomatic rocks and brecciation (Plate 6.2a–d), this expansion occurred syn- to post-K-metasomatism. Rebrecciation textures further suggest expansion was episodic. As reviewed by Jébrak (1997), this style of brecciation is most consistent with hydrothermal percolation during fault dilation. Volume expansion accounts for numerous unique breccia bodies locally occurring south of Summit Lake.

The breccia characteristics at the metasedimentary-volcanic transition are most consistent with fault displacement. Emplacement of porphyry dykes during crustal extension provides a reasonable explanation for their origin. Crustal extension could give rise to

anorogenic magmatism. Davis and Hardy (1981) described how tectonic denudation during post-collisional extension results in lateral thinning of brittle crustal rocks by low angle listric-normal fault-block rotation. Low angle faulting during extension might be initiated by nonuniform stress conditions caused by magmatism (Parsons and Thompson, 1993). Resultant low angle fault zones provide suitable conduits accommodating hydrothermal regimes and associated disaggregation.

6.4   Relative Timing of K-Metasomatism

Lithostratigraphic relationships at Lou Lake provide a context for the relative timing of K-metasomatism. K-metasomatism has affected rocks across the entire supracrustal succession. However, effects of pervasive K-metasomatism are focused within basal volcanic ash and crystal ash tuff of the Lou Lake volcanics and the immediately underlying metasedimentary units. Porphyritic intrusives exhibit a strong spatial relationship to the potassic overprint as evidenced by intensification of potassium developed at immediate boundaries.

The onset of K-metasomatism clearly post-dated deposition of volcanic rocks at Lou Lake. In general, this volcanic succession is very well preserved, showing only typical deuteric effects from post-depositional consolidation. Preferential metasomatic K-feldspar replacement of basal ash tuff and crystal ash tuff suggests these beds provided favourable conduits for potassic alteration. Extensive brecciation generally obscures the metasedimentary-volcanic interface at surface. Various interpretations include basal agglomerate-lithic tuff to the Lou Lake volcanic sequence, laharic breccia or a fault breccia. However, this breccia body hosts common clasts of pink potassium feldspar metasomatite,

Plate 6.1

The metasedimentary-metasomatite boundary (left hemisphere) demonstrates a truncation of tilted, older metasedimentary sequence against younger rocks. The discordant potassium feldspar replacement as evidenced by these bounding relationships is unconformable in a descriptive sense, however infiltration of potassium feldspar from overlying rocks penetrating metasedimentary structures are indicative of a metasomatic origin. Photo taken south of the Bowl Zone.

Plate 6.2

Selection of core photos taken from DDH NICO-10-325 demonstrating diverse brecciation processes associated with K-metasomatism at the metasedimentary-metasomatite boundary. Plate 6.2a demonstrates brittle disaggregation of metasomatite (purple-red fragments) within an ultra-fine matrix of reddish-orange K-feldspar (39.8 – 40.0 m interval). In Plate 6.2b, metasomatite (purple-red) and amphibolite (pale green) fragments are overprinted by a front of reddish-orange K-feldspar. Post-K-metasomatism veins of amphibole, chlorite and quartz cross-cut the interval (55.0 – 55.2 m interval). Plate 6.2c demonstrates the assimilation of metasedimentary clasts by infiltrating red-orange K-feldspar (58.5 – 58.7 m interval). Heterolithic brecciation exhibited in Plate 6.2d shows angular fragments of metasomatite and metasedimentary rock within a matrix of rock flour (60.8 – 61.0 m interval). Core photos are oriented so the top corresponds with the up-hole direction.

10cm

5cm
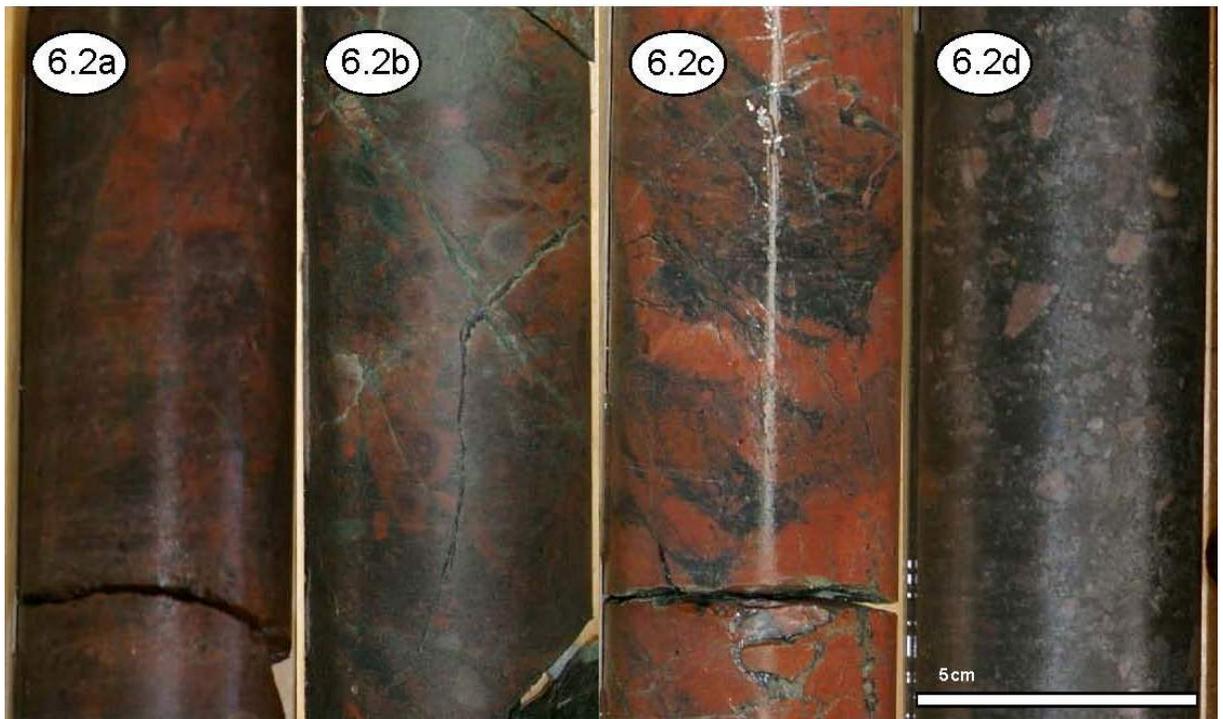
demonstrating that processes leading to K-metasomatism were active prior to brecciation. It's impossible for clasts of potassium feldspar metasomatite to be incorporated into a basal volcanic unit, when overlying units clearly post-date their formation. Though the relationship of this breccia body to the fault breccia described in Section 6.3 is unclear, on the basis of fragment shape, composition, and comparable stratigraphic position, a reasonable assertion is that they share a similar origin.

Cross sections show sills of early plagioclase-phyric porphyry were emplaced both concordant with and discordant to metasedimentary bedding. 'Pinkification' of concordant sill boundaries is due to interactions leading to K-metasomatic replacement. However, permeation textures showing amphibole overprinting K-feldspar at immediate sill boundaries conclusively demonstrate amphibole growth post-dates K-metasomatism. A temporal relationship between plagioclase-phyric porphyry and K-metasomatism is most clearly established by enclaves of porphyry hosted by potassium feldspar metasomatic rocks, which demonstrate porphyritic emplacement prior to the onset of peak K-metasomatism. Rare breccia-hosted porphyritic fragments suggest emplacement of discordant sills most likely coincided with the onset of tectonic displacement. Faulting provides a mechanism for truncating metasedimentary layering, and the created space would accommodate the magmatic influx. The relationship between plagioclase-phyric porphyry to regional magmatic events in the Lou Lake area is uncertain. Emplacement of the plagioclase-phyric porphyry likely coincides with regional anorogenic magmatism; however, geochronology has not been done on this unit so timing constraints are relative.

Quartz- and feldspar-phyric porphyritic dykes cross-cut metasedimentary stratigraphy and intrude into potassium feldspar metasomatic rocks. Their high potassium content and

strong spatial and temporal relationship to K-metasomatism suggest they were emplaced coeval with the main potassic hydrothermal event. This relationship to K-metasomatism is spatially evidenced by the development of intense K-feldspar zoning at porphyry boundaries. Similarly intense metasomatic aureoles that transition into brecciation suggest emplacement of dykes was coeval with or post-onset of brecciation. Brittle fracturing and disaggregation of potassic aureoles demonstrate ongoing hydrothermal activity post-dating K-metasomatism within breccia conduits. Though relationships between these porphyries and regional magmatism have not been conclusively defined, their temporal link to K-metasomatism suggests they are most likely coeval with Faber Lake magmatism.

U-Pb zircon dating of potassium feldspar metasomatic rocks at Summit identified an upper intercept of 1851 +18/-16 Ma (Gandhi et al., 2001). The high discordance of these results is indicative of an open metasomatic system (Faure, 1986). Analysis of mass balance on feldspar porphyry demonstrated zirconium mobility relative to titanium. The immobility of titanium was demonstrated petrographically by concentrations of sphene within potassicly altered selvages. Zirconium mobility relative to titanium showed the greatest gains where alteration intensity from K-metasomatism was also greatest; suggesting the zoning within the zircon population that was dated relates to the potassic hydrothermal event.

6.5   Additional Constraints on Conditions during K-Metasomatism

K-metasomatism affects rocks across the supracrustal succession at NICO. The most intense and pervasive replacement is focused at the metasedimentary-volcanic boundary. Though this replacement is generally marked by K-feldspar with turbid hematite, contemporaneous development of both hematite and magnetite-associated K-feldspar

assemblages at different stratigraphic levels is apparent. Fragments of coarse grained quartz and K-feldspar poikiloblastically enclosed by K-feldspar metacrysts in calc-silicate rocks indicate replacement was episodic. Local heterogeneities within the potassium feldspar metasomatite identified by grain size are often associated with alternate redox regimes. Early replacement assemblages are characteristically ultra-fine grained and occur either with fine disseminations of magnetite or variable hematite dusting. They represent neocrystallization processes that result from chemical changes associated with their development (O'Hara et al., 1997).

Crystallinities an order of magnitude larger are indicative of recrystallization processes. Chemical modification of K-feldspar during coarsening was negligible, as evidenced by mineral chemistries showing ultra fine and coarse varieties sharing identical K-feldspar compositions between Or_{97-99}. As both neocrystallized and recrystallized varieties occur as magnetite and hematite bearing assemblages, mutual development of both processes under reducing and oxidizing conditions are indicated.

Quantitative electron microprobe analysis and corresponding petrographic evidence of pink K-metasomatized layering from basal metasiltstone suggest potassium addition was commonly accommodated by replacement of albite by K-feldspar. This K-Na cation exchange reaction can be represented by the following equation:

$$NaAlSi_3O_8 + K^+ \Leftrightarrow KAlSi_3O_8 + Na^+$$

However, mass transfer estimates on feldspar porphyry demonstrated most elements were highly mobile relative to titanium during the neocrystallization phase. The consistent addition of Si, K, and Ba and loss of Na and Sr are primarily accommodated by dissolution of

plagioclase and precipitation of potassium feldspar and quartz. This is evidenced by modal changes to >95% K-feldspar within porphyry endocontact zones. Mass change calculations showed an inconsistent behaviour for Al where increased alteration intensity resulted in both the greatest gains but also a net Al depletion. This most likely indicates equilibration of the porphyry occurred at a bulk composition approaching mineralogical potassium feldspar. Equivalent mass change ratios of ~7 for SiO_2/Al_2O_3 and SiO_2/K_2O calculated at peak intensity supports this assertion. Excess Si is accommodated by ubiquitous quartz vugs within the potassium feldspar metasomatite. The inconsistent behaviour of calcium is partly accommodated by replacement of Ca-plagioclase by epidote. Liberation of Ca from Ca-plagioclase also resulted in the precipitation of secondary ankerite. These modal changes suggest peak K-metasomatism was promoted primarily via dissolution-precipitation reactions, as represented by the following unbalanced equation:

$$Ca\text{-plagioclase} + albite + K+ + Si^{4+} \Leftrightarrow K\text{-feldspar} + quartz + Ca^{2+} + Na^+$$
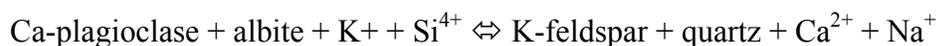
Barium demonstrates a moderate correlation with K (R = 0.7609) suggesting some accommodation within the potassium feldspar structure. As M-site substitution of K by Ba is likely, isochemical behaviour is expected. However, quantitative measurements of Ba content of K-feldspar were low indicating Ba not flushed from the system syn-K-metasomatism was likely remobilized post-K-metasomatism. The latter is evidenced by the cross-cutting relationships of barite veins. Strontium demonstrates a moderate correlation to Na (R = 0.6532), and is comparatively assumed to occupy M-site vacancies within the Ca-plagioclase structure. Depletion patterns similar to Na indicate that Sr mobility coincided with dissolution of plagioclase species.

The ubiquitous presence of an iron oxide component within K-feldspar replacement assemblages suggests redox conditions played a role during K-metasomatism. Further analysis, however, indicate this relationship is not likely. Magnetite and hematite provide a proxy for oxygen fugacity; the former suggests a comparatively reduced regime, the latter a comparatively oxidized one. Petrographic examinations during this investigation revealed finely disseminated magnetite is a common occurrence within many of the rocks across the supracrustal succession. They occur as stratiform concentrations within the basal units of the Treasure Lake Group, they are a constituent within mafic aggregates of crystal ash tuff, and are a matrix component within local porphyries. The presence of similar disseminations within K-metasomatized equivalents indicates that magnetite was sourced locally. This indicates that the relatively reduced conditions implied by the presence of inherited magnetite were internally governed by protolith mineral assemblages (Frost, 1991). As neocrystallization assemblages occur with either magnetite or hematite, K-metasomatism at NICO apparently occurred independent of oxygen fugacity.

Mass change analysis revealed an inconsistent relationship between K addition and Fe mobility that confirms this assertion. Though Fe is generally depleted, there is an apparent relationship to the degree of hematization where addition was greatest. Domains of enrichment within feldspar porphyry show progressive replacement of feldspar phenocrysts to brick-red spots, textures which suggest that hematization post-dates K-metasomatism. Very low correlations between potassium and iron (R = -0.13) indicate precipitation via separate processes; the former by concentration gradients and the latter by redox conditions. Petrographic analysis identified hematite intensification at boundaries of mafic aggregates. Similar intensification haloes around chlorite suggest iron mobility post-dated retrograde

chlorite. Taylor (1977) asserted brick-red albite as textural evidence of infiltration by lower temperature crustal fluids. Intense hematite flooding and brecciation of metasedimentary layering supports this claim. Therefore, the imposition of oxidizing conditions by the influx of crustal fluids almost certainly occurred independent of K-metasomatism at NICO.

Thermal conditions active during peak K-metasomatic activity are best constrained by the temporal link to dyke emplacement, and microstructural relationships revealed under petrographic analysis. The intense potassic exocontact zones developed at immediate porphyry boundaries indicate peak K-metasomatism was coeval to dyke emplacement. The extreme effects of wall rock dissolution is evidenced by immobile residue concentrated within selvages bordering veins that cross-cut the potassic halo and infiltrate feldspar porphyry. These clinopyroxene ± epidote ± chlorite veins bordered by K-feldspar selvages record a mineralogical paragenesis that implicates amphibolite-facies conditions prevailed post K-metasomatism.

Petrographic examination of hydrothermal breccia identified metasediment and potassium feldspar metasomatite fragments within a matrix of Mg-Fe amphibole. Anthophyllite compositions within metasedimentary clasts identify an early pre-fragmental Mg-Fe amphibole phase. Anthophyllite generally appears in lower amphibolite-facies regional metamorphism (Chinner and Fox, 1974). Their presence indicates regional metamorphic conditions following the Hottah-Slave collision reached lower amphibolite-facies. The amphibole-rich breccia matrix shows a compositional range between ferro-actinolite to ferrohornblende that clearly post-dates the K-feldspar fragments. When in coexistence, these amphibole assemblages may relate to prograde metamorphism at uppermost greenschist to amphibolite facies (Deer et al., 1992). These textural relationships and temporal links to Faber

Lake magmatism indicate emplacement of dykes and K-metasomatism occurred coeval to peak prograde thermal metamorphic conditions. Peak contact metamorphism post-dating pervasive K-feldspar replacement achieved the greenschist-amphibolite transition. This evolution was marked by Mg-Fe amphibole ± clinopyroxene assemblages indicating a thermal peak between 400 and 500°C.

6.5.1 K-Metasomatism during Retrograde Conditions

Secondary biotite and iron oxide assemblages overprint metasedimentary rocks, marking a later stage of K-metasomatism. This stage was documented by Sidor (2000) as the effects of "black rock" Ca-K-Fe alteration, and is briefly discussed here to demonstrate the retrograde effects of K-metasomatism. Disseminated green and brownish green biotite occurs as a ubiquitous matrix component that is, in general, pervasively disseminated within metasiltstone, amphibole metasomatic rock, calc-silicate rocks and meta-arenite. In amphibole metasomatic rocks and calc-silicate rocks, secondary biotite, magnetite and Fe-chlorite assemblages typically occur overprinting aggregates of ferro-actinolite, ferrohornblende and clinopyroxene. Biotite and hematite assemblages are observed in quartz and feldspar-phyric porphyries and in metasedimentary rocks proximal to porphyritic intrusions. In porphyry dykes, tan to dark brown Ti-annite and amphibole phenocrysts typically show partial to complete replacement by brownish green, lower Ti-annite and Mg-Fe chlorite. Intensification of hematite at grain boundaries is ubiquitous. Biotite infiltration into metasedimentary rocks is characteristically dark green to green-brown and marked by strong hematite dusting.

Quantitative analysis demonstrates retrograde potassium and iron enrichment is largely accommodated by secondary biotite. Differential effects observed suggest potassium and iron

enrichment occurred under dissimilar processes. Specifically, biotite species from K-metasomatized layering in metasedimentary rock show the greatest potassium enrichment. In comparison, biotite phenocrysts from feldspar porphyry samples showed intense hematization coincident with pronounced iron enrichment. Secondary biotite typically replaces amphibole which might best be represented by the following equation after Ferry (1976):

$$\text{calcic amphibole} + \text{microcline} + H_2O + CO_2 \Leftrightarrow \text{biotite} + \text{calcite} + \text{quartz}$$

Ar-Ar dating of annite separates obtained from samples of biotite-amphibole-magnetite metasomatic rock and quartz feldspar porphyry dyke gave ages of 1832 Ma and 1831 ± 11Ma (Gandhi et al., 2001). As argon escapes by diffusion, its retention decreases rapidly once a critical temperature is exceeded (Dodson, 1973). Berger and York (1981) demonstrated closure temperatures for biotite range from 352 to 394°C. Close agreement of these dates most likely relate to the timing of secondary biotite replacement at NICO. This indicates a prolonged cooling history that post-dates peak thermal conditions coeval with K-metasomatism by 20 Ma.

6.5.2 Isotopic Constraints on Fluid Sources

Tightly constrained oxygen isotope values between 10.6 and 12.7 ‰ from rocks representing different crustal sources demonstrate a marked resetting of ratios. Close agreement between values suggests isotopic equilibration was approached between dissimilar rock types; however, interval sampling across contacts was not completed to verify this. These results show δ18O values fall both within the top of the range typical for granitoids, and within the center of the range typical of metamorphic rocks (Rollinson, 1993). They suggest re-equilibration of crustal fluids to prevailing higher temperature conditions, with the isotopic

signature internally controlled by rock composition.

Moderate correlation between oxygen isotopes and Na_2O (R = 0.71) suggest isotope and sodium exchange resulted from the same process (Labotka et al., 2004). However, strong antipathy between Na_2O and K_2O (R = -0.79), and a low negative oxygen isotope-K_2O correlation (R = -0.32) implies a different process led to K-feldspar precipitation. These relationships collectively demonstrate that K-feldspar replacement occurred as a combination of separate processes; the dissolution of precursor minerals, and the subsequent precipitation of K-feldspar.

CHAPTER 7 – CONCLUSIONS

7.1 Introduction

The iron oxide copper-gold (IOCG) class of deposits have a tremendous diversity in terms of age, styles of alteration, mineralization potential and structural setting (Hitzman et al., 1992; Hitzman, 2000). IOCG systems exhibit intense and extensive regional- to deposit- scale sodic, calcic, potassic and iron alteration with strong structural and stratigraphic control. The broad diversity of mineralization can be characterized by polymetallic metal associations that include REE's, U, P, Co and Bi. IOCG deposits are predominantly associated with abundant hydrothermal and/or structural breccia. They are largely regarded to occur within districts where regional scale hydrothermal systems correlate with large-scale crustal features, such as the many well studied examples in the Cloncurry district (Williams and Skirrow, 2000). The prospective potential for an IOCG district within the Great Bear Magmatic Zone has recently been better defined in large part due to mapping regional-scale alteration by federal and local government agencies (Corriveau and Mumin, 2009).

The NICO deposit has been profiled as one of several IOCG deposits within the Great Bear Magmatic Zone (Goad et al., 2000). However, the low abundance of iron oxide and copper are uncharacteristic of IOCG's as defined by Williams et al. (2005). Williams (2009) has more recently asserted that NICO is an IOCG-affiliated deposit that falls under a Co-As $\pm$ iron oxide $\pm$ Au $\pm$ Ag $\pm$ U (low Cu) sub-classification. The deposit has demonstrated economic concentrations of cobalt, gold and bismuth hosted within amphibole-magnetite-biotite metasomatic rock immediately underlying potassium feldspar metasomatite. This study examined the extensive potassium feldspar metasomatic rocks exposed east of Lou Lake, and

only the role played by K-metasomatism in their development will be addressed here. Potassium feldspar metasomatite exhibits an intimate spatial and temporal relationship to porphyry dykes. The porphyry dykes and K-metasomatism are likely coeval with Faber Lake magmatism, and their emplacement coincided with peak thermal metamorphic conditions.

The boundary between younger, overlying non-metamorphosed volcanic rocks juxtaposed against older regionally metamorphosed metasedimentary basement is the structural control for the development of K-metasomatism. Brecciation styles developed at this interface support significant displacement. This boundary is interpreted as a low angle decollement that resulted from post-collisional crustal extension that coincided with regional anorogenic magmatism. The combined potassium input from crustal and magmatic sources by fluidization of the displacement interface provides a mechanism that accounts for heterogeneities observed in the potassium feldspar metasomatic rocks. A model for the development of K-metasomatism is proposed in Section 7.2. The role of potassic alteration on mineralization, and the metallogenic potential of K-metasomatism are explored in Section 7.3. The results of this study have been summarized in Section 7.4. Finally, recommendations for future research are listed in Section 7.5.

7.2   A Model for K-Metasomatism at NICO

Development of the GBMZ resulted from rapid onset of voluminous syn- to post-tectonic granitic magmatism and associated volcanism following the Hottah-Slave collision. Arc magmatism occurred when subducted Hottah arc rocks descended beneath an overlying Slave margin due to subduction reversal. Hildebrand and Bowring (1984) argued convincingly that the volume and composition of arc magmatism and volcanism generated

during this event could only result from recycling of continental crust. Anorogenic magmatism is generally attributed to a rift environment (Best, 2003). In the southern GBMZ, post-collisional extension is indicated by rotated ash flow tuff fields. Post-orogenic crustal extension provides a mechanism to accommodate magmatic ascension. Brecciation at the metasedimentary-volcanic boundary supports a decollement and significant fluid interaction occurred at this interface (Figure 7.1).

At NICO, the fluid flux along this interface accounts for the voluminous K-metasomatism. Mass transfer estimates for feldspar porphyry show extreme elemental mobility when massive addition of potassium occurred at dyke contacts against intruded metasedimentary rocks. Several sources of potassium were likely, including the downward percolation of crustal fluids and upward migration of magmatically-derived fluids. Descension of crustal fluids implicates the volcanic succession as a source of potassium. Downward migration would have been promoted along fault structures created during tectonic extension. Descension to depths up to five to eight kilometers would account for the metamorphic conditions in footwall metasediments and porphyritic textures and crystallinity developed in dykes. With the upper plate volcanic succession accounting for up to three kilometers of thickness, and dyke emplacement within the lower plate as deep as eight kilometers, up to five kilometers of crustal displacement is indicated.

Upward migrating magmatically-derived fluids could provide a second potassium source. Post-tectonic emplacement of the Faber Lake magmatic suite coincided with the emplacement of local dykes and K-metasomatism at NICO. This temporal link to regional potassic magmatism strongly suggests a direct relationship. Though A-type magmas typically have low water content, identification of biotites within Faber Lake granite by D'Oria (1998)
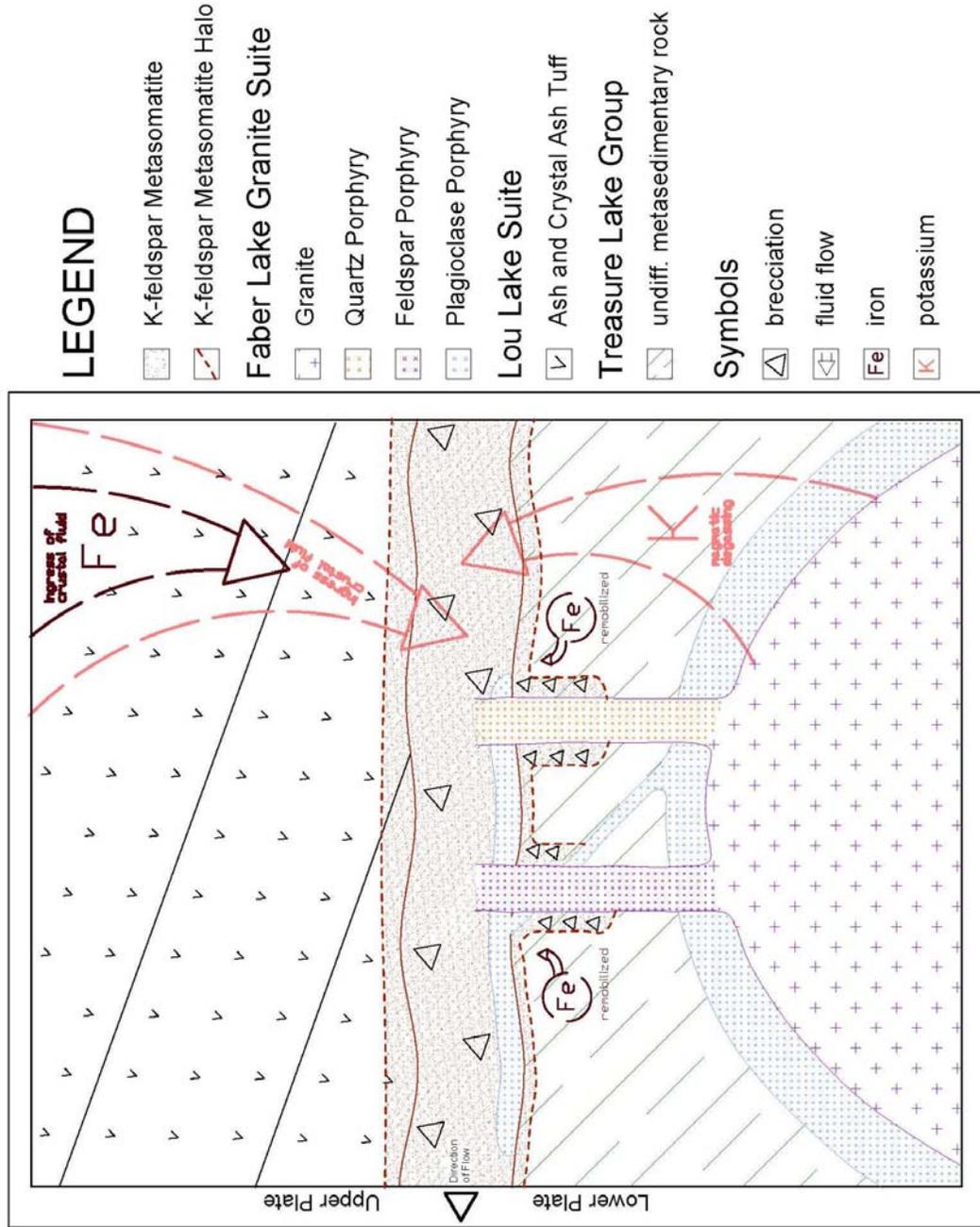
Figure 7.1 – A model for K-metasomatism at the metasedimentary-volcanic boundary.

suggests water contents of up to 1.5% (Wyllie et al., 1976).

Petrographic evidence collected at porphyry boundaries clearly demonstrates high temperature fluid rock interactions. The lack of significant thermal contrast between melt and wall rock accounts for the lack of chill margins. Pyroxene-hornblende calc-silicate veins that cross-cut potassium feldspar metasomatite attest to amphibolite-facies thermal conditions post-dyke emplacement. Heating of migrating fluids to prevailing amphibolite-facies metamorphic conditions accounts for the internal buffering of δ18O values and the pervasive reactivity demonstrated by the potassium feldspar metasomatite.

7.3   The Metallogenic Significance of K-Metasomatism at NICO

The potential of hydrothermal fluids to mobilize, transport and subsequently precipitate concentrations of economically important elements is universally recognized. The alteration haloes that develop as a result of such systems are typically orders of magnitude larger than the prospective mineralization bodies they may host. Thus alteration zones provide efficient vectors for exploration, and the mineralization potential of a specific style of alteration is therefore of particular interest.

Several occurrences of copper mineralization have been documented within potassium feldspar metasomatic rocks southeast of Lou Lake. Although this style of mineralization is developed within domains of brecciation, the spatial relationship to K-metasomatized rocks implies a direct association. Estimates of mass change relative to titanium show that copper was readily removed from porphyry overprinted by K-metasomatism. The obvious implication is that processes that led to K-metasomatism liberated copper. As copper exhibits no direct correlation to Na_2O (R = 0.00) and weak antipathy with K_2O (R = -0.40), mobility,

transport and re-precipitation were independent. Copper mobility at NICO is undoubtedly linked to alkaline fluid compositions which would account for the alkaline metasomatic replacement. Copper precipitation is largely dependant upon the availability of sulphur within mineralized breccias, as copper occurrences are commonly hosted within potassium feldspar metasomatite breccia zones. Brittle deformation and subsequent mineralization undoubtedly post-dates K-metasomatism. Copper mineralization (chalcopyrite ± bornite) typically occurs within chlorite-cemented breccia. Therefore development of conditions favourable to copper concentration coincided with retrograde chloritization. High temperature K-metasomatism as documented at NICO provides the conditions for substantial metal liberation, though copper concentration occurs independently during retrograde cooling. Post-potassium feldspar replacement fluid evolution provides a mechanism for copper transport and subsequent precipitation.

Rare earth element behaviour shows consistent depletion of light REE's, the magnitude of change largely corresponding to degrees of potassium enrichment. Strong correlations to Na_2O indicate that mobilization of these elements occurred during dissolution, which allowed for transportation and reprecipitation. Mobilization of light REE's corresponded with high temperature K-metasomatism at NICO, therefore the potential exists for their deposition and concentration elsewhere. The behaviour of heavy REE's contrasts that of the light REE's. The depletion of HREE's corresponds strongly to atomic radii. Elements with greater atomic radii (Tb, Dy, Ho) express magnitudes of depletion that more closely resemble those observed for the light REE's. The heaviest REE's (Er, Tm, Yb, Lu) exhibit variable low level enrichment or minimal change with respect to increasing potassium enrichment. Strong correlations with TiO_2 and scandium clearly demonstrate these HREE's are relatively

immobile. This suggests processes active during high temperature K-metasomatism at NICO were not conducive to the liberation of HREE's.

The magnitude of potassic alteration at Lou Lake was initially recognized by a multi-parameter spectrometric survey which demonstrated low eTh/K ratios neighboring elevated eU/eTh ratios (Charbonneau et al., 1994). Low eTh/K ratios are useful geophysical indicators of potassic alteration as potassium enrichment is not typically accompanied by thorium (Galbraith and Saunders, 1983). Thorium insolubility results from its single valency state. Its reduced abundance relative to potassium and uranium are therefore a consequence of potassium and uranium enrichment respectively. Local occurrences of pitchblende peripheral to the immediate K-metasomatism at NICO as documented by Gandhi and Lentz (1990) correspond to the uranium enrichment halo detected by geophysical means. Shives and others (1997) attributed their occurrence to lateral transportation of uranium away from a hydrothermal center. The mobility of uranium identified by analysis of mass exchange in this study supports this assertion. Strong sympathy with SiO_2 ($R_U = 0.86$) suggests subsequent reprecipitation accompanies retrograde silicification and quartz veining post-K metasomatism.

7.4 Summary

This study supports the following conclusions:

1. Regional prograde metamorphism of the Treasure Lake Group reached the upper greenschist-amphibolite facies transition, and coincided with emplacement of the Marion River Batholith.

2. Post-collisional tectonic extension created space for anorogenic Faber Lake magmatism, and emplacement coincided with peak thermal conditions.

3. Detachment faulting accommodated the strain above a still-buried intrusion, resulting in shallow volcanic rocks being juxtaposed against deeper metamorphic basement. Porphyry dykes injecting metamorphic basement are coeval with emplacement of post-kinematic Faber Lake intrusive suite, and this dyking coincided with peak-K-metasomatism.

4. Descending lower temperature crustal fluids transported potassium remobilized from overlying volcanic rocks. These fluids comingled with contemporaneously ascending potassium-rich melt along this structural conduit.

5. High temperature conditions promoted pervasive K-metasomatism. Internal buffering resulted in isotopic homogenization at high temperature conditions. Remobilization of ferric iron from crustal sources imposed comparatively oxidized conditions onto potassium feldspar metasomatite post-K-metasomatism.

6. K-metasomatism provided conditions favourable for the liberation of elements of economic interest. The magnitude of potassic alteration zones therefore provides a strong indication of mineralization potential.

7. Brittle deformation of K-metasomatized rocks provided a favourable setting for the precipitation of copper-bearing minerals.

8. Pervasive retrograde biotite replacement of amphibole-calcsilicate assemblages occurred as a result of a prolonged cooling history. The economic concentration of Au-Co-Bi occurred during the retrograde hydrothermal overprint.

7.5   Recommendations

The present study has characterized the effects of K-metasomatism and demonstrated the

relationship between metasomatic processes, the development of associated breccia, and the mineralization at Lou Lake. Additional research that could further elucidate these relationships include:

1.   A detailed geochronological study of the local intrusives at Lou Lake should be conducted to document their link to the anorogenic Faber Lake suite.

2.   A detailed investigation of brecciation should be conducted to classify the breccia bodies and clarify their temporal and spatial relationship to the episodic hydrothermal history. Of most interest is the specific development of extensive brecciation at the interface between Treasure Lake Group metasedimentary basement and overlying Lou Lake volcanic rocks.

REFERENCES

Badham, J.P. N. 1973. *Calc-alkaline volcanism and plutonism from the Great Bear batholith, N.W.T.* Canadian Journal of Earth Sciences, Vol. 10, p. 1319-1328.

Barrett, T.J. and MacLean, W.H. 1994. *Chemostratigraphy and hydrothermal alteration in exploration for VHMS deposits in greenstones and younger volcanic rocks.* In: Alteration and alteration processes associated with ore forming processes, Edited by D.R. Lentz, Geological Society Short Course Notes, Vol. 11, p. 433-467.

Barton, M.D., Ilchik, R.P. and Marikos, M.A. 1991. *Metasomatism.* In: Contact Metamorphism, Edited by D.M. Kerrick, Mineralogical Society of America, Reviews in Mineralogy, Vol. 26, p. 321-350.

Bevins, R.E., Kokelaar, B.P. and Dunkley, P.N. 1984. *Petrology and geochemistry of lower to middle Ordovician igneous rocks in Wales: a volcanic arc to marginal basin transition.* Proceedings of the Geological Association, Vol. 95, p. 337-347.

Best, M.G. 2003. Igneous and Metamorphic Petrology, 2nd Edition, Blackwell Publishing, Malden, MA, 729 pp.

Billings, M.P. 1972. Structural Geology. Prentice-Hall, Inc., New Jersey. 606 pp.

Boone, G. M. 1969. *Origin of clouded re feldspars: petrologic contrasts in a granitic porphyry intrusion.* American Journal of Science, Vol. 267, p. 633-668.

Bowring, S.A. 1984. *U-Pb zircon geochronology of early Proterozoic Wopmay Orogen, N.W.T., Canada: an example of rapid crustal evolution.* PhD thesis, University of Kansas. 148 pp.

Bowring, S.A. and Grotzinger, J.P. 1992. *Implications of new chronostratigraphy for tectonic evolution of Wopmay orogen, northwest Canadian Shield.* American Journal of Science, Vol. 292, p. 1-20.

Bryan, D. 1981. *Geological report, GAR 1-3 claims (Jan-Nov, 1980), Lou Lake area, District of Mackenzie (85-N-10).* Department of Indian and Northern Affairs, Document

081154, 12 pp.

Bryan, D. 1982. *Geological report, GAR 1-5, 7, and 9 claims (Jan-Dec 1981), Lou Lake area, District of Mackenzie (85-N-10).* Department of Indian and Northern Affairs, Document 081422, 16pp.

Byrne, N.W. 1968. *Details of diamond drilling, mineral claim CAB #1, Lou Lake, Marian River area, N.W.T.* Department of Indian and Northern Affairs, Document 018845, 14 pp.

Camier, J. 2002. *The Sue Dianne Proterozoic Fe-oxide Cu-Ag-Au breccia complex, Southern Great Bear Magmatic Zone, Northwest Territories, Canada.* MSc Thesis, The University of Western Ontario, 208 pages.

Chapin, C.E. and Lindley, J.I. 1986. *Potassium metasomatism of igneous and sedimentary rocks in detachment terranes and other sedimentary basins: Economic implications.* Arizona Geological Society Digest, Vol. 16, p. 118-126.

Charbonneau, B.W., Ghandhi, S.S., Hetu, R.J., Holman, P.B., Prasad, N. 1994. *Multiparameter airborne geophysical survey of the Mazenod Lake area and its metallogenic implications (NTS 85 N/10 and parts of 85 N/11, 14, 15).* Exploration Overview 1994, Northwest Territories, compiled by R. Kusick and S.P. Goff. Department of Indian Affairs and Northern Development, Yellowknife, p. 26-27. (Abstract for oral and poster presentation at Geoscience Forum, Yellowknife, November 1994.)

Chinner, G.A. and Fox, J.S. 1974. *The origin of cordierite-anthophyllite rocks in the Land's End aureole.* Geology Magazine, Vol. 111, p. 397-408.

Climie, J.A. 1976. *Geological, geophysical and drill investigations of the Dianne/Sue Groups, District of Mackenzie, Canada.* Department of Indian and Northern Affairs, document No. 080524.

Coles, R.L., Haines, G.V. and Hannaford, W. 1976. *Large scale magnetic anomalies over western Canada and the Arctic: a discussion.* Canadian Journal of Earth Science, Vol.

13, p. 790-802.

Corriveau, L. and Mumin, H. 2009. *Exploring for Iron Oxide Copper-Gold (Ag-Bi-Co-U) deposits: Case examples, classification and exploration vectors.* In: Exploring For Iron Oxide Copper-Gold Deposits: Canada and Global Analogues, Edited by L. Corriveau and H. Mumin, Geological Association of Canada Short Course Notes 20, p. 1-11.

Corriveau, L., Williams, P.J. and Mumin, H. 2009. Alteration vectors to IOCG mineralization – from uncharted terranes to deposits. In: Exploring For Iron Oxide Copper-Gold Deposits: Canada and Global Analogues, Edited by L. Corriveau and H. Mumin, Geological Association of Canada Short Course Notes 20, p. 89-110.

Davis, G.H. and Hardy, J.J., Jr. 1981. The Eagle Pass detachment, southeastern Arizona: Product of mid-Miocene listric(?) normal faulting in the southern Basin and Range. Geological Society of America Bulletin, Part 1, Vol. 92, p. 749-762.

Deer, W.A., Howie, R.A. and Zussman, J. 1992. An Introduction to the Rock-Forming Minerals 2nd Edition. Prentice Hall, Harlow, England. 696 pp.

Dodson, M.H. 1973. *Kinetic processes and the thermal history of slowly cooling rocks.* Nature, Vol. 259, p. 551-553.

D'Oria, R.M. 1998. *An investigation of the comagmatic signature of the intrusive/extrusive phases of the Faber Lake Rapakivi Suits, Great Bear Magmatic Zone, NWT.* BSc Thesis, University of Western Ontario, 105 pp.

Duke, N.A. 1996. Follow up Report, NICO Claims, Bear Province, NWT, Private Report of Fortune Minerals Limited, 47 pp.

Duke, N.A. 1998. Field Report, Lou Lake Geology, Update. Private Report of Fortune Minerals Limited.

Duke, N.A., Sidor, M., and Mulligan, D.L. 1998a. *Postcollisional rift setting of Olympic Dam-type iron oxide deposits in the southern Bear Province, Northwest Territories.* Program with Abstracts, Geological Association of Canada – Mineralogical Association of Canada, p. 33.

Duke, N.A., Shepley, M., and Mulligan, D.L. 1998b. *The significance of detachment fault breccias occurring at the southern end of the Great Bear Magmatic Zone, Wopmay Orogen, N.W.T.* Program with Abstracts of Talks and Posters. 26th Yellowknife Geoscience Forum, 25-27 November 1998, p. 35-36.

Easton, R.M. 1981. Stratigraphy of the Akaitcho Group and the development of an early Proterozoic continental margin, Wopmay Orogen, Northwest Territories. In: Proterozoic Basins of Canada. Edited by F.H.A. Campbell. Geological Survey of Canada Paper 81-10, p. 79-96.

Faure, G. 1986. Principles of Isotope Geology, 2nd Edition, John Wiley & Sons, Columbus, Ohio, 589 pp.

Ferry, J.M. 1976. *P, T, fCO$_2$, and fH$_2$O during metamorphism of calcareous sediments in the Waterville area, South-Central Maine*. Contributions to Mineralogy and Petrology, Vol. 57, p. 119-143.

Fortune Minerals Limited, 1995. News Release, October 1995.

Fortune Minerals Limited, 1996a. News Release, April 1996.

Fortune Minerals Limited, 1996b. News Release, May 1996.

Fortune Minerals Limited, 2007. Annual Report.

Fortune Minerals Limited, 2009. Annual Report.

Fraser, J.A., Hoffman, P.F., Irvine, T.N., and Mursky, G. 1972. The Bear Province. In: Variations in tectonic styles in Canada. Edited by R.A. Price and R.J.W. Douglas. Geological Association of Canada, Special Paper 11, p. 453-503.

Frost, B.R. 1991. *Introduction to oxygen fugacity and its petrologic significance*. In: Oxide Minerals: Petrologic and Magnetic Significance, ed. D.H. Lindsley, Reviews in Mineralogy, Vol. 25, p. 1-8.

Galbraith, J.H. and Saunders, D.F. 1983. *Rock classification by characteristics of aerial gamma ray measurements*. Journal of Geochemical Exploration, V. 18, p. 49-73.

Gandhi, S.S. 1989. *Rhyodacite ignimbrites and breccias of the Sue-Dianne and Mar Cu-Fe-U deposits, southern Great Bear magmatic zone, Northwest Territories.* In: Current Research, Part C, Geological Society of Canada, Paper 89-1C, p. 263-273.

Gandhi, S.S. 1992a. *Magnetite deposits in metasiltstones of the Snare Group at Hump Lake, Northwest Territories.* In: Current Research, Part A; Geological Society of Canada Paper 92-1A, p. 225-235.

Gandhi, S.S. 1992b. *Polymetallic deposits of the southern Great Bear Magmatic Zone. I*n: Project Summaries: Canada-Northwest Territories. Mineral Development Subsidiary Agreement 1987-1991: Geological Survey of Canada, Open File 2484, p. 135-139.

Gandhi, S.S. (1994) Geological setting and genetic aspects of mineral occurrences in the southern Great Bear magmatic zone, Northwest Territories. In: Studies of Rare Metal Deposits in the Northwest Territories, ed. W.D. Sinclair and D.G. Richardson; Geological Survey of Canada, Bulletin 475, p. 63-96.

Gandhi, S.S. and Lentz, D.R. 1990. *Bi-Co-Cu-Au-As and U occurrences in metasediments of the Snare Group and felsic volcanics of the southern Great Bear magmatic zone, Lou Lake, Northwest Territories.* In: Current Research, Part C, Geological Survey of Canada, Paper 90-1C, p. 239-253.

Gandhi, S.S., Mortensen, J.K., Prasad, N., van Breeman, O. 2001. *Magmatic evolution of the southern Great Bear continental arc, northwestern Canadian Shield: geochronological constraints.* Canadian Journal of Earth Sciences, Vol. 38, p. 767-785.

Gandhi, S.S., Prasad, N., and Charbonneau, B.W. 1996. *Geological and geophysical signatures of a large polymetallic exploration target at Lou Lake, southern Great Bear magmatic zone, Northwest Territories.* In: Current Research, Part E, Geological Survey of Canada, p. 147-158.

Gandhi, S.S. and van Breeman, O. 2005. *SHRIMP U-Pb geochronology of detrital zircons from the Treasure Lake Group – new evidence for Paleoproterozoic collisional tectonics in the southern Hottah terrane, northwestern Canadian Shield.* Canadian Journal of Earth Science, Vol. 42, p. 833-845.

Goad, R.E., Mumin, A.H., Duke, N.A., Neale, K.L., Mulligan, D.L. 2000. *Geology of the Proterozoic iron oxide-hosted, NICO cobalt-gold-bismuth, and Sue-Dianne copper-silver deposits, southern Great Bear magmatic zone, Northwest Territories, Canada.* In: Hydrothermal iron oxide copper-gold and related deposits; a global perspective; Vol. 1, Edited by T.M. Porter. Australian Mineral Foundation, Glenside, South Australia, Australia, p. 249-267.

Goad, R.E., Mumin, A.M., Duke, N.A., Neale, K.L., Mulligan, D.L., Camier, J. 2001. *The NICO and Sue-Dianne Proterozoic, Iron oxide hosted, polymetallic deposits, Northwest Territories: Applications of the Olympic Dam model in exploration.* Canadian Institute of Mining, Metallogeny and Petroleum, Vol. 9, No. 2, p. 123-140.

Goldschmidt, V.M. 1922. *On the metasomatic processes in silicate rocks.* Economic Geology, Vol. 17, p. 105-123.

Guidotti, C.V. 1984. *Micas in metamorphic rocks.* In: Micas, Reviews in Mineralogy, Vol. 13, p. 357-468.

Hall, B. 1969. *Diamond drill hole logs, holes 69-5 to 69-21, CAB claim group, Lou Lake area, N.W.T.* Department of Indian and Northern Affairs, Document 060406.

Hatcher, R.D. Jr. 1995. Structural Geology: Principles, Concepts, and Problems 2nd Edition. Prentice Hall, New Jersey. 525 pp.

Hennessey, B.T., Puritch, E., Ward, I.R., Konigsmann, K.V., Hayden, A.D., Bocking, K.A. and Rougier, M. 2007. Technical report on the bankable feasibility study for NICO cobalt-gold-bismuth deposit, Mazenod Lake Area, Northwest Territories, Canada. Micon International Limited. Internal document, Fortune Minerals Limited, 137 pp.

Hey, M.H. 1954. *A new review of the chlorites.* Mineralogical Magazine, Vol. 30, p. 277-292.

Hildebrand, R. S. 1981. Early Proterozoic LaBine Group of Wopmay orogen: Remnant of a continental volcanic arc developed during oblique convergence. In: Proterozoic Basins of Canada. Edited by F.H.A. Campbell. Geological Society of Canada Paper 81-10, p.

133-156.

Hildebrand, R.S. 1982. An early Proterozoic continental volcanic arc at Great Bear Lake, Northwest Territories. Ph.D. thesis, Memorial University of Newfoundland, St. John's, 237 pp. (unpublished).

Hildebrand, R.S. 1984. *Folded cauldrons of the early Proterozoic LaBine Group, northwestern Canadian Shield*. Journal of Geophysical Research, Vol. 89, p. 8429-8440.

Hildebrand, R.S. 1986. *Kiruna-type deposits: Their origin and relationship to intermediate subvolcanic plutons in the Great Bear magmatic zone, Northwest Canada*. Economic Geology, Vol. 81, No. 3, p. 640-659.

Hildebrand, R.S., Annesley, I.R., Bardoux, M.V., Davis, W.J., Heon, D., Reichenback, I.G. and Van Nostrand, T. 1984. *Geology of the early Proterozoic rocks of the Leith Peninsula map area, District of Mackenzie*. In: Current Research, Part A: Geological Survey of Canada Paper 84-1A, p. 217-221.

Hildebrand, R.S. and Bowring, S.A. 1984. *Continental intra-arc depressions: A nonextensional model for their origin, with a Proterozoic example from Wopmay Orogen*. Geology, Vol. 12, p. 73-77.

Hildebrand, R.S., Bowring, S.A. and Housh, T. 1990. *The medial zone of the Wopmay orogen, District of MacKenzie*. In: Current Research: Geological Survey of Canada, Paper 90-1C, p. 167-176.

Hildebrand, R.S., Bowring, S.A., Steer, M.E., and Van Schmus, W.R. 1983. *Geology and U-Pb geochronology of parts of the Leith Peninsula and Riviere Grandin map areas, District of Mackenzie*. In: Current Research, Part A: Geological Survey of Canada Paper 83-1A, p. 329-342.

Hildebrand, R.S., Hoffman, P.F., Bowring, S.A. 1987. *Tectono-magmatic evolution of the 1.9 Ga Great Bear magmatic zone, Wopmay orogen, northwestern Canada*. Journal of Volcanology and Geothermal Research, Vol. 32, p. 99-118.

Hildebrand, R.S., Hoffman, P.F., Bowring, S.A. 2010. *The Calderian orogeny in Wopmay orogen (1.9 Ga), northwestern Canadian Shield.* Geological Society of America Bulletin, Vol.122 , p 794-814.

Hildebrand, R.S., Paul, D., Pietikainen, P., Hoffman, P.F., Bowring, S.A., and Housh, T. 1991. *New geological developments in the internal zone of Wopmay orogen, District of Mackenzie.* In: Current Research, Part C: Geological Society of Canada Paper 91-1C, p. 157-164.

Hitzman, M.W. 2000. *Iron oxide-Cu-Au deposits: what, where, when, and why?* In: Hydrothermal iron oxide copper-gold and related deposits; a global perspective; Vol. 1, Edited by T.M. Porter. Australian Mineral Foundation, Glenside, South Australia, Australia, p. 9-25.

Hitzman, M.W., Oreskes, N. and Einaudi, M.T. 1992. *Geological characteristics and tectonic settings of Proterozoic iron oxide (Cu-U-Au-REE) deposits.* Precambrian Research, Vol. 58, p. 241-287.

Hoefer, T.W. 1989. *Exploration potential of the NICO Claims, Lou Lake, Marian River area, District of Mackenzie, NWT.* Unpublished, 14 pp.

Hoffman, P.F. 1973. *Evolution of an early Proterozoic continental margin: The Coronation geosyncline and associated aulacogens of the northwestern Canadian Shield.* Royal Society of London Philosophical Transactions, Vol. 273, Ser. A, p. 547-581.

Hoffman, P.F. 1980. Wopmay Orogen: A Wilson Cycle of Early Proterozoic age in the Northwest of the Canadian Shield. In: Continental Crust and its Mineral Deposits. Edited by D.W. Strangway. Geological Association of Canada, Special Paper 20, p. 523-549.

Hoffman, P.F. 1984. Geology of the northern internides of Wopmay orogen, District of Mackenzie, Northwest Territories. Geological Survey of Canada Map 1576A, scale 1:250,000.

Hoffman, P.F. 1988. *United plates of America, the birth of a craton: Early Proterozoic*

assembly and growth of Laurentia. Annual Review of Earth and Planetary Science, Vol. 16, p. 543-603.

Hoffman, P.F. and Bowring, S.A.   1984.   *Short-lived 1.9Ga continental margin and its destruction, Wopmay orogen, northwest Canada.* Geology, Vol. 12, p. 68-72.

Hoffman, P.F. and Pelletier, K.S. 1982. *Cloos nappe in Wopmay orogen: Significance for stratigraphy of the Akaitcho Group, and implications for opening and closing of an early Proterozoic continental margin.* In: Current Research, Part A: Geological Association of Canada Paper 82-1A, p. 109-115.

Housh, T., Bowring, S.A. and Villeneuve, M. 1989. *Lead isotopic study of early Proterozoic Wopmay orogen, NW Canada: Role of continental crust in arc magmatism.* The Journal of Geology, Vol. 97, p. 735-747.

Hughes, C.J. 1973. *Spilites, keratophyres and the igneous spectrum.* Geological Magazine, Vol. 109, p. 513-527.

Jébrak, M. 1997. *Hydrothermal breccias in vein-type ore deposits: A review of mechanisms, morphology and size distribution.* Ore Geology Reviews, Vol. 12, p. 111-134.

Joesten, R.L.   1991.   *Kinetics of coarsening and diffusion-controlled mineral growth.* In: Contact Metamorphism, Edited by D.M. Kerrick, Mineralogical Society of America, Reviews in Mineralogy, Vol. 26, p. 507-582.

Kidd, D.F.   1932.   *A pitchblende-silver deposit, Great Bear Lake, Canada.* Economic Geology, Vol. 27, p. 145.

Kidd, D.F. 1936. *Rae to Great Bear Lake, Mackenzie District, N.W.T.* Geological Survey of Canada, Memoir 187, 44 pp.

King, J.E.   1986.   *The metamorphic internal zone of Wopmay orogen (early Proterozoic), Canada: 30 km of structural relief in a composite section based on plunge projection.* Tectonics, Vol. 5, p. 973-994.

Lang, A.H., Griffith, J.W. and Steacy, H.R.   1962.   *Canadian Deposits of Uranium and*

Thorium. Geological Survey of Canada, Economic Geology Series, No. 16, 2nd Edition.

Laznicka, P. 1988. Breccias and Coarse Fragmentites: Petrology, Environments, Associations, Ores. Developments in Economic Geology, 25. Elsevier, Amsterdam, 832 pp.

Laznicka, P. 1989. *Breccias and ores. Part 1: history, organization and petrography of breccias*. Ore Geology Reviews, Vol. 4, p. 315-344.

Leake, B.E., Woolley, A.R., Arps, C.E.S., Birch, W.D., Gilbert, M.C., Grice, J.D., Hawthorne, Kato F.C., A., Kisch, H.J., Krivovichev, V.G., Linthout, K., Laird, J., Mandarino, J.A., Maresch, W.V., Nickel, E.H., Rock, N.M.S., Schumacher, J.C., Smith, D.C., Stephenson, N.C.N., Ungaretti, L., Whittaker, E.J.W., and Youzhi, G. 1997. *Nomenclature of amphiboles: Report of the Subcommittee on Amphiboles of the International Mineralogical Association, Commission on New Minerals and Mineral Names*. American Mineralogist, Vol. 82, p. 1019-1037.

Leake, B.E., Woolley, A.R., Birch, W.D., Burke, E.A.J., Ferraris, G., Grice, J.D., Hawthorne, F.C., Kisch, H.J., Krivovichev, V.G., Schumacher, J.C., Stephenson, N.C.N. and Whittaker, E.J.W. 2004. *Nomenclature of amphiboles: Additions and revisions to the International Mineralogical Association's amphibole nomenclature*. American Mineralogist, Vol. 89, p. 883-887.

Labotka, T.C., Cole, D.R., Fayek, M., Riciputi, L.R. and Stadermann, F.J. 2004. *Coupled cation and oxygen-isotope exchange between alkali feldspar and aqueous chloride solution*. American Mineralogist, Vol. 89, p. 1822-1825.

Le Bas, M.J., Le Maitre, R.W., Streckeisen, A., and Zanettin, B. 1986. *A chemical classification of volcanic rocks based on the total alkali-silica diagram*. Journal of Petrology, Vol. 27, p. 745-750.

Lord, C.S. 1942. Geological Map, Snare River, District of Mackenzie, Northwest Territories. Geological Survey of Canada, Map 690, scale 1 : 253,440.

MacLean, W.H. and Barrett, T.J. 1993. *Lithogeochemical techniques using immobile*

elements. Lournal of Geochemical Exploration, Vol. 48, p. 109-133.

Mathieu, G.I. 1966. *Investigation of a gold-cobalt-bismuth ore from the Marion River area for Precambrian Mining Services Limited, Yellowknife, N.W.T., Canada.* Department of Energy, Mines and Resources, Mines Branch Investigation Report, TR 66-83, 13 pp.

McGlynn, J.C. 1979*. Geology of the Precambrian rocks of the Riviere Grandin and in part of the Marian River map areas, District of Mackenzie.* In: Current Research, Part A, Geological Survey of Canada, Paper 79-1A, p. 127-131.

Mulligan, D.L. 1995. *Proterozoic iron oxide and As-Co-Bi-Cu vein mineralization at the NICO property, NWT.* BSc Thesis, University of Western Ontario, 77 pp.

Mumin, A.H. 2000. *Proterozoic Fe-oxide hosted polymetallic mineralization associated with the Marion River Batholith, southern Great Bear Magmatic Zone, Northwest Territories.* Abstract for oral presentation at Millennium Geoscience Summit, Calgary, 2000.

Munoz, J.L. and Ludington, S.D. 1974. *Flouride-hydroxyl exchange in biotite.* American Journal of Science, Vol. 274, p. 396-413.

Nockolds, S.R., Knox, R.W.O'B., and Chinner, G.A. 1978. Petrology, Cambridge University Press, London, UK, 435 pp.

OèHara, K.D., Sharp, Z.D., Moecher, D.P. and Jenkin, G.R.T. 1997. *The effect of deformation on oxygen isotope exchange in quartz and feldspar and the significance of isotopic temperatures in mylonites.* The Journal of Geology, Vol. 105, p. 193-204.

Park, J.K., Buchan, K.L. and Gandhi, S.S. 1995. *Paleomagmatism of 779 Ma Hottah gabbro sheets of the Wopmay Orogen, Northwest Territories.* In: Current Research, Part C. Geological Survey of Canada, Paper 87-2, p. 3-7.

Parry, W.T. and Jacobs, D.C. 1975. *Fluorine and chlorine in biotite from Basin and Range plutons.* Economic Geology, Vol. 70, p. 554-558.

Parsons, T. and Thompson, G.A. 1993. *Does magmatism influence low-angle normal faulting?* Geology, Vol. 21, p. 247-250.

Pearce, J.A. 1982. *Trace element characteristics of lavas from destructive plate boundaries*. In: Andesites; Edited by R.S. Thorpe. Wiley, Chichester, pp. 525-548.

Pearce, J.A. 1983. *Role of the sub-continental lithosphere in magma genesis at active continental margins*. In: Continental basalts and mantle xenoliths; Edited by C.J. Hawkesworth and M.J. Norry. Shiva, Nantwich, pp. 230-249.

Pollard, P.J. 2000. *Evidence of a magmatic-fluid and metal source for Fe-oxide Cu-Au mineralization*. In: Hydrothermal iron oxide copper-gold and related deposits; a global perspective; Vol. 1, Edited by T.M. Porter. Australian Mineral Foundation, Glenside, South Australia, Australia, p. 27-41.

Putnis, A., Hinrichs, R., Putnis, C.V., Golla-Schindler, U. and Collins, L.G. 2007. *Hematite in porous red-clouded feldspars: Evidence of large-scale crustal fluid-rock interaction*. Lithos, Vol. 95, p. 10-18.

Putnis. C.V., Tsukamoto, K. and Nishimura, Y. 2005. *Direct observations of pseudomorphism: compositional and textural evolution at a fluid-solid interface*. American Mineralogist, Vol. 90, p. 1909-1912.

Rock, N.M.S. 1987. *The need for standardization of normalized multi-element diagrams in geochemistry: a comment*. Geochmistry Journal, Vol. 21, p. 75-84.

Rock, N.M.S. and Leake, B.E. 1984. *The International Mineralogical Association amphibole nomenclature scheme: computerization and its consequences*. Mineralogical Magazine, Vol. 48, p. 211-227.

Rollinson, H.R. 1993. Using Geochemical Data: Evaluation, Presentation, Interpretation. Pearson Education Limited, Edinburgh Gate, UK. 352 pp.

Sachs, L. 1984. Applied Statistics: A Handbook of Techniques, 2nd Edition. Springer-Verlag, New York.

Shepley, M. 1999. *The evidence for detachment fault breccias in the Southern Great Bear Magmatic Zone, NWT*. BSc, Thesis, University of Western Ontario, 42 pp.

Shives, R.B. K., Charbonneau, B.W. and Ford, K.L. 1997. *The detection of potassic alteration by gamma ray spectrometry – recognition of alteration related to mineralization*. In: Geophysics and Geochemistry at the Millenium, Proceedings of the Fourth Decennial International Conference on Mineral Exploration (Exploration 97). 17 pp.

Sibson, R. 1977. *Fault rocks and fault mechanisms*. Journal of the Geological Society, London. Vol. 133, p. 191-213.

Sidor, M. 2000. *The origin of the black rock alteration overprinting iron-rich sediments and its genetic relationship to disseminated polymetallic sulphide ores, Lou Lake, Northwest Territories, Canada*. MSc. Thesis, The University of Western Ontario, 243 pp.

Sillitoe, R. 1985 *Ore-related breccias in volcanoplutonic arcs*. Economic Geology, Vol. 80, p. 1467-1514.

Smith, J.V. 1983. *Some chemical properties of feldspars*. In: Reviews in Mineralogy, Vol. 2, Edited by P.H. Ribbe. Mineralogical Society of America. P.

Smith, J.V. and Brown, W.L. 1988. Feldspar Minerals: Crystal Structures, Physical, Chemical, and Microtextural Properties, 2nd Revised and Extended Edition. Springer-Verlag, Berlin, Germany, 828 pp.

Speer, J.A. 1984. *Micas in igneous rocks*. In: Micas, Reviews in Mineralogy, Vol. 13, Edited by S.W. Bailey. Mineralogical Society of America. p. 299-356.

Steele, I.M. and Smith, J.V. 1982. *Ion probe analysis of plagioclase in three howardites and three eucrites*. Geochimica Cosmochimica Acta, Vol. 42, p. 959-971.

Stockwell, C.H., McGlynn, J.C., Emslie, R.F., Sanford, B.V., Norris, A.W., Donaldson, J.A., Fahrig, W.F., Currie, K.L. 1970. Geology of the Canadian Shield. In: Geology and Economic Minerals of Canada. Edited by R.J.W. Douglas. Geological Survey of Canada, Economic Geology Report No. 1, p. 44-54.

St-Onge, M.R. and King, J.E. 1987. *Evolution of regional metamorphism during back-arc stretching and subsequent crustal shortening in the 1.9 Ga Wopmay Orogen, Canada*.

Royal Society of London Philosophical Transactions, Vol. 321, Ser. A, p. 199-218.

Taylor Jr., H.P. 1977. *Water/rock interactions and the origin of H$_2$O in granitic batholiths*. Journal of the Geological Society (London), Vol. 133, p. 509-558.

Thalenhorst, H. and Farquharson, G. 2002. *Updated review, NICO Cobalt-Gold-Bismuth Project, Mazenod Lake District, Northwest Territories, Canada, for Fortune Minerals Limited*. Technical Report for Fortune Minerals Limited, Strathcona Mineral Services Limited, 132 pp., plus appendices.

Thomas, M. and Olson, R.A. 1978. *Exploration – 1977 and 1978; LOO, BW and C mineral claims, Lou Lake, Mackenzie Mining District, N.W.T*. Department of Indian and Northern Affairs, Document 080960, 6 pp.

Thompson, J.B. 1959. *Local equilibrium in metasomatic processes*. In: Researches in Geochemistry, Volume 1, Edited P.H. Abelson. Wiley, New York, p. 427-457.

Thorpe, R. and Brown, G. 1985. The Field Description of Igneous Rocks, John Wiley & Sons Ltd., England, 154 pp.

Vernon, R.H. and Clarke, G.L. 2008. Principles of Metamorphic Petrology, Cambridge University Press, Cambridge, 446 pp.

Williams, P.J. 2009. *Classifying IOCG deposits*. In: Exploring For Iron Oxide Copper-Gold Deposits: Canada and Global Analogues, Edited by L. Corriveau and H. Mumin, Geological Association of Canada Short Course Notes 20, p. 13-21.

Williams, P.J., Barton, M.D., Johnson, D.A., Fontbote, L., de Haller, A., Mark, G., Oliver, N.H.S. and Marschik, R. 2005. *Iron-oxide copper-gold deposits: geology, space-time distribution, and possible modes of origin*. Economic Geology 100th Anniversary Volume, p. 371-405.

Williams, P.J. and Skirrow, R.G. 2000. *Overview of iron oxide-copper-gold deposits in the Curnamona Province and Cloncurry district (Eastern Mount Isa Block), Australia*. In: Hydrothermal iron oxide copper-gold and related deposits; a global perspective; Vol. 1, Edited by T.M. Porter. Australian Mineral Foundation, Glenside, South Australia,

Australia, p. 105-122.

Wilson, J.T. 1949. *Some major structures of the Canadian Shield*. Canadian Institute of Mining and Metals Bulletin, Vol. 42, No. 450, p. 543-554.

Woodcock, N.H. and Mort, K. 2008. *Classification of fault breccias and related rocks*. Geology Magazine, Vol. 145 (3), p. 435-440.

Wyllie, P.J., Huang, W.L., Stern, C.R. and Maaloe, S. 1976. *Granitic magmas: possible and impossible sources, water contents, and crystallization sequences*. Canadian Journal of Earth Science, Vol. 13, p. 1007-1019.

Zharikov, V., Pertsev, N., Rusinov, V., Callegari, E. and Fettes, D. (2007) *Metasomatism and Metasomatic Rocks*. In: Metamorphic Rocks: A Classification and Glossary of Terms, Edited by D Fettes and J. Desmons, Recommendations of the International Union of Geological Sciences Subcommission on the Systematics of Metamorphic Rocks, Cambridge University Press, p. 58-68.

APPENDICES

Appendix 1A - Decline Sample Location and Description

Sample ID	UTM Co-ordinates (NAD83)		Description
	X	Y	
GR-06-001E	513031	7046395	Massive maroon to reddish-brown potassium feldspar metasomatite. The metasomatite is locally altered by patchy earthy hematite.
GR-06-001W	513024	7046398	Boundary between polymict hydrothermal breccia and quartz wacke exhibiting variable effects of potassium metasomatism. The boundary is defined by brecciation of the greywacke, with angular to sub-angular greywacke fragments exhibiting sharp clast margins, and cryptocrystalline potassium feldspar moderately pervasive alteration of wacke matrix.
GR-06-002E	513021	7046385	Feldspar porphyry exhibiting preferential alteration effects of potassium metasomatism including pervasive (though cryptic) alteration of groundmass and selective alteration of feldspar phenocrysts. Porphyry locally host to exogenous inclusions of metasedimentary rock.
GR-06-002W	513014	7046386	Fine to medium grained quartz wacke, with very fine banding defined by alternating very fine-to-fine and fine-to-medium grain size.
GR-06-003E	513029	7046393	Massive maroon to reddish-brown potassium feldspar metasomatite. The metasomatite is locally altered by patchy earthy hematite.
GR-06-003W	512995	7046363	Fine to medium grained quartz wacke with incipient quartz+potassium feldspar alteration front.
GR-06-004E	513010	7046373	Feldspar porphyry exhibiting preferential alteration effects of potassium metasomatism including pervasive (though cryptic) alteration of groundmass and selective alteration of feldspar phenocrysts. Porphyry locally host to exogenous inclusions of metasedimentary rock.
GR-06-004W	512986	7046358	Massive maroon to reddish-brown potassium feldspar metasomatite endocontact zone of feldspar porphyry.
GR-06-005E	513009	7046371	Feldspar porphyry endocontact zone characterized by moderate to strong pervasive potassium metasomatism and earthy hematite alteration of porphyry groundmass and phenocryst population. Leaching along brittle fractures of the porphyry has resulted in a bleached selvage between 1-3 cm in thickness from the fracture.
GR-06-005W	512898	7046371	Feldspar porphyry exhibiting variable alteration effects of potassium metasomatism including weak to moderate pervasive alteration of groundmass and selective potassium feldspar replacement of feldspar phenocrysts.
GR-06-006E	513008	7046370	High phenocryst density domain within the feldspar porphyry characterized by strong to intense patches of pervasive potassium feldspar and hematite alteration of groundmass and feldspar phenocrysts and bleached domains similar to the leached selvage in GR-06-005E.
GR-06-006W	512975	7046356	Pervasive amphibole and moderately pervasive to patchy magnetite alteration of the greywacke.
GR-06-007E	513006	7046398	Interface between the pervasive potassium feldspar + hematite altered domain and bleached domain of GR-06-006E, which can be characterized as a razor sharp front.
GR-06-007W	512977	7046356	Massive maroon to reddish-brown potassium feldspar metasomatite endocontact zone of feldspar porphyry.

	UTM Co-ordinates (NAD83)		
Sample ID	***X***	***Y***	**Description**
GR-06-008E	513004	7046365	Apparently monomict hydrothermal breccia characterized by a fine to medium grained matrix of amphibole+biotite, and variably mottled to nebulous fragments of potassium feldspar metasomatite exhibiting varying degrees of marginal dissolution.
GR-06-008Wa	512981	7046357	Fine to medium grained quartz wacke with gradational weak to moderate pervasive potassium metasomatism of the matrix.
GR-06-008Wb	512981	7046357	Monomict hydrothermal breccia characterized by a fine grained matrix of amphibole and biotite. Fragments are matrix-supported, and represent less then 10% of the unit. The reddish brown potassium feldspar fragment composition is conspicuous.
GR-06-009E	512992	7046355	Massive reddish brown potassium feldspar metasomatite characteristic of the feldspar porphyry endocontact zone.
GR-06-009W	512979	7046356	Sharp contact between potassium feldspar metasomatite and feldspar porphyry. Clasts of potassium feldspar metasomatite are hosted within the porphyry proximal to the boundary. The clasts of metasomatite exhibit incompletely replaced phenocrysts of feldspar, comparable to the endocontact zone typical of the feldspar porphyry.
GR-06-010E	512975	7046351	Brecciated boundary between the polymict hydrothermal breccia and greywacke. Fragments are mottled to nebulous, matrix supported, and apparently of potassium feldspar metasomatite composition.
GR-06-010W	513000	7046368	Pervasive potassium metasomatism effects on feldspar porphyry characterized by groundmass and selective feldspar phenocryst replacement, with streaks and clots of fine grained shreddy biotite. Incipient amphibole alteration results in a brecciated appearance.
GR-06-011E	512960	7046353	Feldspar porphyry exhibiting preferential alteration effects of potassium metasomatism including pervasive (though cryptic) alteration of groundmass and selective alteration of feldspar phenocrysts.
GR-06-011W	512927	7046365	Thickly laminated to medium bedded greywacke, metasiltstone and stratabound potassium feldspar metasomatite.
GR-06-012E	512945	7046356	Oriented, strong amphibole alteration front incipient to strongly pervasive through the calc silicate matrix.
GR-06-012W	512924	7046365	Hybrid potassium feldspar metasomatite-matrix pseudobreccia characterized by leucocratic domains and mottled cryptocrystalline matrix with complex textures.
GR-06-013E	512897	7046365	Contact between the variably biotite-amphibole+/-magnetite altered calc silicate rock and a domain of massive potassium feldspar metasomatite. The metasomatite is characteristic of the exocontact zone of the feldspar porphyry.
GR-06-013W	512920	7046367	Boundary between potassium feldspar metasomatite and quartz wacke. The boundary is defined by crackle brecciation of the greywacke, cemented by incipient fine grained biotite-amphibole. The biotite-amphibole matrix hosts mottled clasts of potassium feldspar metasomatite composition. The metasomatite clasts exhibit moderate to severe evidence of dissolution.
GR-06-014E	512887	7046367	Pervasive potassium metasomatism effects on feldspar porphyry characterized by groundmass and feldspar phenocryst replacement, with streaks and clots of fine grained shreddy biotite. Incipient amphibole appears to brecciate the porphyry locally.

Sample ID	UTM Co-ordinates (NAD83)		Description
	X	Y	
GR-06-014W	512920	7046367	Boundary between potassium feldspar metasomatite and quartz wacke exhibiting variable effects of potassium metasomatism. The boundary is defined by brecciation of the greywacke, with angular to sub-angular greywacke fragments exhibiting sharp clast margins hosted within the cryptocrystalline potassium feldspar metasomatite matrix.
GR-06-015E	512888	7046367	Massive reddish brown potassium feldspar metasomatite. Exocontact zone of the feldspar porphyry effects on the greywacke, and endocontact effects on the feldspar porphyry are nearly identical.
GR-06-016E	512854	7046370	Massive reddish brown potassium feldspar metasomatite characteristic of the feldspar porphyry endocontact zone.
GR-06-017E	512777	7046375	Pervasive potassium metasomatism effects on feldspar porphyry characterized by groundmass and selective feldspar phenocryst replacement, with streaks and clots of fine grained shreddy biotite. Incipient amphibole alteration results in a brecciated appearance.
GR-06-018E	513005	7046366	Carbonate (calcite) breccia cementing a brittle fracture within the potassium feldspar metasomatite. Fragments are angular clasts of potassium feldspar metasomatite. Pyrite disseminated throughout the calcite matrix as isolated grains or concentrated patches of fine grains.
GR-06-019E	512897	7046365	Variably subtle to moderate biotite-amphibole+magnetite alteration of fine grained calc silicate rock.
GR-06-019W	512868	7046375	Pervasive potassium metasomatism effects on feldspar porphyry characterized by groundmass and selective feldspar phenocryst replacement, with streaks and clots of fine grained shreddy biotite. Incipient amphibole alteration results in a brecciated appearance.
GR-06-020E	512763	7046376	Exogenous inclusion of greywacke within the potassium feldspar metasomatite. Inclusion is characterized by medium grained quartz and biotite, and fine grained amphibole with disseminated to blebby arsenopyrite and pyrite.
GR-06-020W	512998	7046367	Fine to medium grained quartz wacke.
GR-06-021E	512693	7046381	Apparently least-altered feldspar porphyry with purple brown very fine grained groundmass, with phenocrysts of feldspar, biotite, quartz and biotite-after-amphibole.
GR-06-021W	512912	7046367	Fine to medium grained, banded metasomatic amphibolitic ironstone characteristic of the pervasive amphibole+magnetite replacement of the greywacke.
GR-06-022W	512911	7046367	Massive maroon to reddish-brown potassium feldspar metasomatite endocontact zone of feldspar porphyry. The metasomatite is locally altered by patchy earthy hematite.
GR-06-023W	512909	7046367	Massive maroon to reddish-brown potassium feldspar metasomatite endocontact zone of feldspar porphyry.
GR-06-024W	512895	7046371	Pervasive potassium metasomatism effects on feldspar porphyry characterized by groundmass and selective feldspar phenocryst replacement, with streaks and clots of fine grained shreddy biotite.
GR-06-025W	512881	7046374	Feldspar porphyry exhibiting variable alteration effects of potassium metasomatism including weak to moderate pervasive alteration of groundmass and selective potassium feldspar replacement of feldspar phenocrysts.

Sample ID	UTM Co-ordinates (NAD83)		Description
	X	*Y*	
GR-06-026W	512871	7046375	Pervasive potassium metasomatism effects on feldspar porphyry characterized by groundmass and selective feldspar phenocryst replacement, with streaks and clots of fine grained shreddy biotite.
GR-06-027W	512841	7046377	Feldspar porphyry with purple-black groundmass and a locally increased abundance of biotite.
GR-06-030W	512904	7046369	Gradational maroon to reddish brown to brown pink endocontact zone of the feldspar porphyry. Sample marks the interface between endocontact zone and exocontact zone of the feldspar porphyry with the metasedimentary rock.
GR-07-084	512951	7046355	Horizon of greywacke hosting front of potassium metasomatism.
GR-07-085A	512860	7046362	Apparently monomict hydrothermal breccia characterized by a cryptocrystalline matrix of potassium feldspar + earthy hematite, with variably mottled to nebulous fragments of amphibolitized greywacke and metasiltstone exhibiting varying degrees of marginal dissolution.
GR-07-085B	512861	7046362	Apparently monomict hydrothermal breccia characterized by a cryptocrystalline matrix of potassium feldspar + earthy hematite, with variably mottled to nebulous fragments of amphibolitized greywacke and metasiltstone exhibiting varying degrees of marginal dissolution.
GR-07-085C	512860	7046362	Apparently monomict hydrothermal breccia characterized by a cryptocrystalline matrix of potassium feldspar + earthy hematite, with variably mottled to nebulous fragments of amphibolitized greywacke and metasiltstone exhibiting varying degrees of marginal dissolution.
GR-07-086	512790	7046375	Feldspar porphyry with pervasive (though cryptic) potassium feldspar replacement of groundmass and selective potassium alteration effects on phenocrysts. Amphibole-clinopyroxene conjugate veining discordant to the porphyry with a general trend of $270/75^o$ and $120/85^o$. Potassium feldspar replacement of groundmass within the 1 to 3 cm thick altered selvage expressed by the amphibole-clinopyroxene vein.
GR-07-087	512916	7046366	Exocontact zone of porphyry characterized by inclusions of fine to medium grained greywacke with disseminated to blebby arsenopyrite, and inclusions of medium to coarse gained biotite-altered metasedimentary rock.

Appendix 1B - Surface Sample Location and Description

Sample ID	UTM Co-ordinates (NAD 83)		Description
	X	Y	
GR-06-061	511741	7047700	Cordierite-bearing upper siltstone.
GR-06-062B	511747	7047694	Massive potassium feldspar metasomatite.
GR-06-076	512968	7046143	Quartz feldspar porphyry.
GR-06-077	513824	7045836	Massive potassium feldspar metasomatite.
GR-06-080	513837	7045815	Bedded subarenite.
GR-06-082	513830	7045810	Biotite amphibolite.
GR-06-083	513026	7046128	Biotite amphibolite.
GR-10-101	512170	7045441	Reactivation and quartz cementation of brittle fracture system post-magnetite infiltration of potassium feldspar metasomatite.
GR-10-102	512212	7045437	Biotite matrix microbrecciation of potassium feldspar metasomatite.
GR-10-103	512466	7045802	Discordant relationship exposed at contact between potassium feldspar metasomatite and metasedimentary rock.
GR-l0-103B	512466	7045802	Sharp contact relationship between quartz-feldspar porphyry and potassium feldspar metasomatite.
GR-10-104	512418	7046083	Relic of biotitic siltstone within potassium feldspar metasomatite, potassium alteration invading siltstone at margins.
GR-10-104B	512418	7046083	Dilational microbrecciation hosting potassium metasomatized fragments.
GR-10-105	512465	7048051	Patchy potassium metasomatism of feldspar-amphibole±quartz porphyry.
GR-10-106	512461	7046027	Fragment-supported magnetite-cemented brecciation of banded, potassium-altered metasedimentary rock.
GR-10-107	512410	7046018	Stratabound potassium metasomatism of cherty metasediments. Cherty bands exhibit moderate to strong magnetism.
GR-10-108	512430	7045928	Discordant potassium metasomatism cross-cutting bands of cherty iron (magnetite) metasiltstone.
GR-10-108A	512421	7045921	Hematitic potassium feldspar metasomatite cemented brecciation of banded cherty iron (magnetite) metasedimentary rock with stratabound potassium feldspar metasomatite.
GR-10-108B	512421	7045921	Pseudotachylitic biotite-amphibole matrix breccia injecting into the banded cherty iron metasedimentary rock; cross-cutting brecciation of 108a.
GR-10-109	512369	7045877	Discordant replationship between potassium feldspar metasomatite and banded iron metasedimentary rock. (Note - metasedimentary rock grades into massive greywacke over several meters North of this station).
GR-10-110	512365	7045843	Accidental inclusion of metasedimentary rock (country rock) within the endocontact zone of quartz feldspar porphyry.
GR-10-111	512365	7045843	Silicification of metasedimentary rock at the quartz-feldspar porphyry boundary. Note that the quartz-feldspar porphyry cross-cuts the banded metasedimentary rock sharply and without intensificsation of potassium at the interface.
GR-10-112	512351	7046061	Sharp contact relationship between potassium metasomatized endocontact zone of feldspar porphyry and stratiform potassium metasomatized magnetite-rich metasedimentary rock.
GR-10-113	511682	7047528	Mottled pseudobrecciated appearance resulting from irregular mafic remnants (remnant components oxidized to magnetite) within otherwise massive potassium feldspar metasomatite.
GR-10-114	511613	7047498	Leucocratic bleaching within massive potassium feldspar metasomatite.
GR-10-115	511528	7047444	Matrix supported heterolithic breccia exhibiting clast imbrication, zoned clasts, and clast compositions including potassium feldspar metasomatite and quartz feldspar poprhyry.
GR-10-116	511273	7047403	Banded potassium feldspar metasomatite.
GR-10-116B	511273	7047403	Banded potassium feldspar metasomatite.
GR-10-117	511273	7047403	Chalcopyrite-cemented potassium feldspar metasomatite breccia.

| Sample ID | UTM Co-ordinates (NAD 83) | | Description |
	X	Y	
GR-10-118	511211	7047290	Diatreme breccia.
GR-10-119	511296	7047190	Strong incipient earthy hematite alteration of potassium feldspar metasomatite, resulting in a maroon coloration and weak to moderate magnetitzation.
GR-10-119A	511296	7047169	Quartz feldspar porphyry endocontact zone characterized by strong potassium feldspar metasomatization of groundmass and feldspar phenocrysts.
GR-10-120	511325	7046993	Glomeroporphyritic feldspar porphyry with saussuritized plagioclase grains.
GR-10-121	511371	7046959	Polymict breccia with potassium feldspar alteration haloes around sub-round magnetite and magnetite-rich fragments.
GR-10-122	511270	7047038	Moderately magnetitc crypocrystalline quartz (jasperite) microbreccia.
GR-10-123A	514098	7045745	Silicate iron formation (ferroactinilite, amphibole, weakly magnetic) hosted in pink arenite.
GR-10-123B	514339	7045735	Silicate iron formation (ferroactinilite, amphibole, weakly magnetic) hosted in pink arenite. Striking 285/35°N.
GR-10-124	514447	7045802	Sharp contact between pink arenite and massive potassium feldspar metasomatite.
GR-10-125	514471	7045838	Hornblende dyke discordant to potassium feldspar metasomatite and psammite. Dyke contact is microbrecciated by a magnitite-rich matrix.
GR-10-125B	514471	7045838	Razor sharp contact between pink arenite and massive potassium feldspar metasomatite. Patchy potassium metasomatism of the arenite.
GR-10-126	514496	7045882	Polyphase metasomatic overprints producing a pseudobrecciated appearance within an exposure of mafic greywacke.
GR-10-127	514667	7045922	Cordierite schist.
GR-10-127A	514667	7045922	Intrusion of quartz porphyry cross-cutting the cordierite schist. Nature of the contact is sharp, and the porphyry exhibits strong potassium metasomatism effects.
GR-10-127B	514667	7045922	Matrix of the cordierite schist has been altered by incipient potassium metasomatism proximal to discordant quartz-phyric porphyry.
GR-10-128	510519	7048611	Banded potassium feldspar metasomatite striking 295/32°N. Sample location on north shore of Lou Lake directly across the lake from the Lou Lake float base.
GR-10-129	510466	7048624	Patchy potassium-metasomatized and pervasively hematite-altered coherent porphyryitic felsic volcanics (potential feeder to Lou Lake voclanism?)
GR-10-130	510423	7048675	Agglomerate breccia with subround to angular porphyritic blocks (10 to 15 cm) and rounded hematite altered blocks (up to 50 cm diameter).
GR-10-130B	510423	7048675	Patchy potassium metasomatism and hematite alteration of streaky banded porphyritic felsic volcanics.
GR-10-130C	510423	7048675	Weak patchy hematite alteration and incipient jasper alteration of ash tuff groundmass. Coarser ash grains have been selectively replaced by jasper.
GR-10-130D	510421	7048673	12 cm bomb hosted in massive buff greyish-green ash tuff.
GR-10-130E	510421	7048673	Sharp contact between ash lapilli tuff and overlying banded to locally massive ash tuff.
GR-10-130E-F	510426	7048646	Flat Iron - specular hematite cementation along low angle fracture surface of ash tuff.
GR-10-130F	510427	7048636	Stratabound earthy hematite alteration of banded ash tuff. Lenticular specular hematite is conspicuous within the hematite altered bands, and exhibit an intensification of earthy hematite at lenticular boundaries.

Sample ID	UTM Co-ordinates (NAD 83)		Description
	X	*Y*	
GR-10-131A	510423	7048715	Porphyritic felsic volcanics with abundant angular to sub-round cognate blocks of buff grey-green earthy hematite-altered volcanics and massive potassium feldspar metasomatite. The groundmass of the porphyritic felsic volcanics are altered by patchy domains of earthy hematite.
GR-10-131B	510423	7048715	Sub-round buff grey cognate fragments within the porphyritic felsic volcanics.
GR-10-131C	510423	7048715	Porphyritic felsic volcanics have been locally pervasively altered to potassium feldspar. The metasomatite has been microbrecciated and cemented by specularite-quartz.
GR-10-132	510397	7048575	Cordierite-bearing argilaceous metasiltstone showing stringers and pods of epidote parallel to bedding (285°/50S)
GR-10-136	511361	7077996	Non-graded lapilli ash tuff with imbrication of clasts striking 315/88°N.
GR-10-136B	511361	7077996	Discordant open space filling quartz-tourmaline vein with 5mm altered selvage.
GR-10-137	511447	7048053	Stratabound siltstone and greywacke Treasure Lake metasedimentary rocks, marked by alternating bands of chert (2-3 cm thick).
GR-10-137A	511447	7048053	Exposure of Treasure Lake metasedimentary rock forms an anticline with south limb striking 204/40° and north limb striking 244/29°N, and fold axis dipping slightly to the west.
GR-10-137B	511447	7048053	Subtle hints of crossbeds preserved in the greywacke. Ambiguous due to the diffuse nature of the laminations.
GR-10-137C	511447	7048053	Pervasive potassium feldspar brecciation and replacement of stratabound chert.
GR-10-137D	511447	7048053	Vein of magnetite infiltrates along bedding contacts.
GR-10-138	511623	7048199	Thin bedded ash tuff and ash lapilli tuff interbedded on a 1-2 cm to 4-5 cm sacle. Sequence is locally altered by patches of potassium metasomatism.
GR-10-138B	511623	7048199	sequence of GR-10-138. Sub-unit is cross-cut by significant quartz veining.
GR-10-139	512179	7048120	"Blotting paper" potassium feldspar metasomatite exhibiting amoeboid domains rich with magnetite "spots".
GR-10-140	512635	7048211	The "LP showing" of disseminated to blebby chalcopyrite hosted within potassium feldspar metasomatite. Localized malachite staining at surface.
GR-10-141	512243	7047857	Succession of very thick bedded medium grained greywacke overlain by thin to medium bedded coarse grained greywacke.
GR-10-141A	512243	7047857	Up direction of greywacke bedding indicated by bomb depression in bed.
GR-10-141B	512243	7047857	Stratabound matrix-supported brecciated units interbedded within the greywacke succession. Fragments of potassium feldspar metasomatite composition exhibit sharp distinct outlines.
GR-10-141C	512243	7047857	Stratabound pervasive potassium metasomatism infiltrates along preferential layers of the greywacke sequence. Terminal tongue of potassium metasomatism causes stratabound brecciation and partially completely replaces the infiltrated horizon.
GR-10-142	512905	7046339	Magnetite-cemented brecciation at contact between biotite-amphibole-magnetite metasomatic rocks and potassium feldspar metasomatite.
GR-10-143	512942	7046210	Brecciated spotted relicts within potassium feldspar metasomatite.
GR-10-144	513024	7046285	Magnetite veins infiltrating brecciated domain of potassium feldspar metasomatite.
GR-10-145A	513022	7046610	Hydrothermal breccia, angular to sub-round fragments, monolithic appearance (potassium feldspar metasomatite clasts).
GR-10-145E	512991	7046211	Hydrothermal breccia, angular to sub-round fragments, monolithic appearance (potassium feldspar metasomatite clasts).

Appendix 1C - Core Sample Location and Description

Sample ID	Drill Hole	Interval (m)	Description
GR-06-031	NW-00-01	6.01 - 7.24	Crystal ash tuff exhibiting appearance of pervasive alteration to potassium feldspar.
GR-06-032	NW-00-01	8.23 - 9.63	Crystal ash tuff exhibiting appearance of variable alteration to potassium feldspar.
GR-06-033	NW-00-01	96.48 - 97.48	Vitric-rich crystal ash tuff exhbiting appearance of variable alteration to potassium feldspar.
GR-06-034	NW-00-01	170.18 - 171.55	Crystal ash tuff showing absent from effects of K-metasomatism.
GR-06-035	NICO-06-287	0.06 - 0.97	Massive potassium feldspar metasomatite
GR-06-036	NICO-97-100	151.71 - 158.11	Basal Metasiltstone
GR-06-037	NICO-98-140	24.10 - 25.09	Cordierite-bearing Upper Metasiltstone
GR-10-146	NICO-10-313	7.26 - 7.52	Crackle- to mosaic-brecciated potassium metasomatite.
GR-10-147	NICO-10-313	9.62 - 10.00	Spotted relic within potassium feldspar metasomatite.
GR-10-148	NICO-10-313	24.71 - 24.88	Spotted relic within potassium feldspar metasomatite.
GR-10-149	NICO-10-313	46.61 - 46.67	Contact between the potassium metasomatite and quartz-feldspar porphyry.
GR-10-150	NICO-10-313	57.41 - 57.76	Relics within pink potassium feldspar metasomatite.
GR-10-151	NICO-10-317	12.38 - 12.61	Feldspar-phyric fine grained porphyry.
GR-10-152	NICO-10-317	108.86 - 109.00	Pervasive K-feldspar altered feldspar-phyric fine grained porphyry.
GR-10-153	NICO-10-317	120.70 - 121.00	Feldspar-phyric fine grained porphyry.
GR-10-154	NICO-10-314	15.96 - 16.80	Bleached domains within potassium feldspar metasomatite.
GR-10-155	NICO-10-317	27.05 - 27.67	Relics within pink potassium feldspar metasomatite.

Appendix 2A - Bulk Rock Geochemistry - Major Oxides

Sample No.	SiO_2 wt %	TiO_2 wt %	Al_2O_3 wt %	Fe_2O_3T wt %	MnO wt %	MgO wt %	CaO wt %	Na_2O wt %	K_2O wt %	P_2O_5 wt %	LOI wt %	Total wt %
001E	74.28	0.04	12.12	1.16	0.03	0.51	0.77	0.45	9.92	< 0.066	0.83	100.27
002E	63.35	0.53	14.92	6.35	0.03	2.07	1.03	2.76	8.08	0.12	0.86	100.28
003E	73.40	0.09	12.38	2.10	0.02	0.48	0.19	0.11	10.60	< 0.051	0.54	100.12
004E	63.78	0.49	14.45	6.59	0.06	2.10	0.46	0.91	8.97	0.12	1.34	99.47
006E	54.27	0.62	17.29	8.92	0.03	2.80	0.19	0.11	13.35	0.12	2.14	100.09
009E	73.83	0.05	12.72	1.14	0.02	0.30	0.50	0.46	10.60	< 0.043	0.52	100.34
009Ed	73.74	0.05	12.64	1.21	0.02	0.29	0.50	0.45	10.33	< 0.054	0.52	99.96
011E	65.54	0.44	14.85	5.36	0.05	1.97	1.63	3.10	5.86	0.13	1.00	100.15
012E	49.58	0.24	5.45	23.21	0.25	8.70	9.79	0.50	2.40	0.06	0.52	100.75
013E	43.44	0.37	7.27	27.70	0.23	4.75	11.44	0.68	2.40	0.07	0.29	98.71
014E	67.33	0.26	13.82	3.44	0.03	1.06	1.04	0.28	11.22	0.07	1.47	100.23
015E	75.26	0.05	11.88	1.01	0.01	0.16	0.25	0.19	10.28	< 0.043	0.30	99.58
019E	42.59	0.35	7.74	30.75	0.18	5.70	7.32	0.44	3.90	0.07	0.54	99.65
003W	78.82	0.25	5.23	7.97	0.04	1.95	0.22	0.04	3.28	0.06	0.97	98.98
004W	71.29	0.04	14.15	0.78	0.02	0.17	0.52	0.81	11.18	< 0.052	0.50	99.65
005W	62.94	0.53	14.71	6.00	0.04	2.05	1.11	1.84	9.40	0.12	1.02	99.97
008W	71.11	0.12	11.91	4.85	0.03	0.84	0.27	0.44	9.78	< 0.055	0.63	100.27
010W	64.29	0.35	13.52	5.10	0.03	1.41	0.35	0.68	10.78	0.08	0.70	97.48
011W	63.20	0.56	12.49	7.71	0.06	2.45	2.68	0.47	9.92	0.09	0.56	100.44
012W	73.60	0.04	11.85	1.98	0.02	0.50	0.73	0.16	10.36	< 0.036	0.88	100.25
014W	71.35	0.09	12.04	3.23	0.03	1.03	0.95	0.16	10.15	< 0.045	0.81	99.99
020W	80.42	0.24	5.91	6.33	0.03	1.66	0.31	0.08	4.14	0.05	0.83	100.10
024W	63.80	0.56	14.87	5.61	0.06	1.89	0.99	2.04	8.58	0.13	1.42	100.17
025W	63.28	0.51	14.82	6.58	0.03	2.01	0.96	1.89	8.37	0.12	0.92	99.69
026W	58.35	0.49	13.55	8.05	0.07	5.65	1.29	0.22	7.87	0.11	3.87	99.88
027W	62.97	0.53	14.75	7.16	0.03	2.06	0.73	2.90	7.12	0.12	0.80	99.35
027Wd	63.53	0.53	14.81	7.22	0.03	2.07	0.73	2.89	6.97	0.13	0.80	99.90
031	73.17	0.09	13.54	1.46	0.02	0.40	0.31	2.31	6.72	< 0.05	0.65	98.88
032	72.28	0.10	13.29	2.82	0.02	0.29	0.34	1.22	8.25	0.04	0.59	99.45
033	73.72	0.10	13.31	2.57	0.02	0.20	0.32	0.70	8.44	0.04	0.89	100.59
034	74.14	0.10	12.88	2.43	0.04	0.62	1.35	2.08	3.96	< 0.037	1.17	98.92
035	73.82	0.05	12.57	0.99	0.02	0.27	0.50	1.00	9.66	< 0.061	0.58	99.62
036	62.97	0.67	16.13	5.13	0.01	2.49	1.28	4.65	5.30	0.11	0.47	99.37
037	58.93	0.55	16.08	11.72	0.02	2.86	0.29	1.60	5.71	0.11	1.98	99.94
061	63.46	0.09	19.11	4.32	0.02	2.05	0.15	2.21	5.90	< 0.056	2.28	99.66
062B	71.98	0.06	13.09	2.85	0.01	0.13	0.15	1.03	9.67	< 0.051	0.12	99.37
076	70.44	0.12	13.62	2.67	0.04	0.65	0.38	1.57	8.61	0.06	0.79	99.13
077	74.26	0.04	11.60	2.85	0.02	0.75	0.04	0.19	9.52	< 0.046	0.49	99.93
080	82.32	0.12	3.98	7.71	0.02	1.23	0.04	0.04	2.44	< 0.046	1.06	100.61
081	54.08	0.86	16.88	9.73	0.10	4.03	5.89	2.10	4.75	0.16	1.32	100.10
082	35.12	0.40	8.53	36.97	0.14	9.07	2.03	0.12	5.09	0.09	1.05	98.66
083	42.46	0.35	7.94	31.86	0.16	4.91	6.80	0.46	4.34	0.07	0.21	99.67
116	68.35	0.05	14.11	2.90	0.02	0.33	0.11	0.30	11.67	0.03	0.56	98.40
128	76.30	0.05	12.79	1.64	0.02	0.13	0.33	1.32	7.81	0.03	0.54	101.00
129	73.71	0.06	13.44	2.43	0.01	0.27	0.40	1.11	7.61	0.04	0.75	99.84
130E	74.41	0.43	12.88	2.63	0.07	1.32	0.18	0.06	5.35	0.12	2.01	99.47
139	71.82	0.06	12.88	3.58	0.02	0.34	0.06	0.65	9.56	0.04	0.46	99.47
143	72.34	0.05	12.54	2.78	0.01	0.21	0.06	0.50	9.87	0.02	0.24	98.61
147	72.08	0.06	14.01	1.23	0.01	0.29	0.18	1.77	9.37	0.02	0.33	99.35
151	68.57	0.18	15.16	2.78	0.02	0.44	0.50	3.04	8.13	0.08	0.46	99.36
152	72.46	0.17	14.03	0.84	0.01	0.23	0.67	3.66	6.13	0.05	0.45	98.72
153	67.53	0.18	14.53	2.37	0.03	0.50	1.18	3.30	7.55	0.06	0.92	98.13
154	71.90	0.05	13.57	1.51	0.01	0.43	0.07	0.17	11.41	0.02	0.22	99.36

Appendix 2B - Bulk Rock Geochemistry - Trace Elements

Sample No.	Sc	V	Cr	Co	Cu	Ni	Zn	As	Rb	Sr	Y	Zr
	ppm	ppm	ppm	ppm	ppm	ppm	ppm	ppm	ppm	ppm	ppm	ppm
001E	< 0.66	< 26.5	< 26.5	< 26.5	19.20	< 66.3	< 8	< 159	155.57	15.90	5.64	87.81
002E	11.39	77.20	29.60	< 14.3	17.10	58.00	22.00	< 85.5	309.88	109.00	21.78	161.25
003E	1.61	22.10	< 20.5	< 20.5	15.20	< 51.3	52.30	< 123.2	183.20	31.90	12.24	77.12
004E	10.04	80.70	51.70	< 19.5	28.50	< 48.9	38.30	< 117.2	240.05	71.10	19.86	144.45
006E	12.00	55.80	32.20	17.30	21.20	< 37.4	31.90	< 89.6	221.16	63.60	20.83	174.24
009E	0.79	< 17.1	< 17.1	< 17.1	24.80	< 42.8	32.80	< 102.7	184.17	32.90	7.32	91.42
009Ed	0.96	< 21.5	< 21.5	< 21.5	22.90	< 53.6	10.90	< 128.7	183.49	32.90	7.96	98.79
011E	8.14	60.40	64.50	< 14.2	28.00	< 35.4	21.30	< 85	224.58	244.30	20.08	156.10
012E	3.92	31.00	27.40	< 18.1	36.10	< 45.4	29.70	< 108.9	151.10	10.20	25.35	121.63
013E	7.01	46.20	38.70	< 18.3	79.50	< 45.7	42.10	< 109.6	62.98	14.50	43.70	209.89
014E	5.79	35.70	18.70	< 18.7	12.50	< 46.7	11.10	< 112.2	224.63	23.70	18.22	123.27
015E	1.06	< 17.1	< 17.1	< 17.1	65.40	< 42.8	10.30	< 102.6	199.72	18.10	10.43	75.47
019E	8.21	49.10	63.90	< 18.2	107.20	< 45.4	46.30	< 109	417.96	13.50	21.25	89.74
003W	8.61	36.40	29.00	< 19.9	< 10	< 49.8	13.70	< 119.5	169.29	8.80	6.90	204.55
004W	0.84	< 20.7	< 20.7	< 20.7	16.70	< 51.9	< 6.2	< 124.5	185.28	29.80	8.40	98.31
005W	11.82	74.20	32.30	< 14.8	45.30	< 37	20.70	< 88.7	302.40	90.50	23.31	186.07
008W	2.20	33.90	< 21.9	< 21.9	54.10	< 54.8	14.90	< 110.8	215.81	41.80	8.46	112.44
010W	8.24	46.80	19.80	< 15.1	10.40	< 37.7	15.80	< 90.6	274.60	43.90	23.14	129.13
011W	11.85	57.30	66.00	< 14.5	27.30	< 36.2	7.00	< 86.9	391.51	34.80	22.59	167.66
012W	1.94	< 14.3	< 14.3	< 14.3	9.40	< 35.7	< 4.3	< 85.7	230.96	16.60	18.88	72.05
014W	4.59	< 18.1	< 18.1	< 18.1	64.70	< 45.4	11.70	< 108.8	234.47	25.30	16.50	89.10
020W	1.75	23.50	29.30	< 17.5	64.40	< 43.8	20.40	< 105.2	182.01	12.90	6.16	222.74
024W	11.86	74.40	40.10	< 22.4	55.20	< 56	19.20	< 134.3	219.09	74.30	24.43	180.73
025W	10.93	75.80	33.10	< 18.1	44.50	< 45.3	15.90	< 108.7	296.33	113.80	21.12	183.73
026W	7.66	62.00	29.80	46.90	89.10	71.00	62.30	< 133.8	195.93	31.10	17.38	157.77
027W	11.63	76.10	33.10	< 18.5	50.50	48.40	20.30	< 111.2	263.55	61.50	22.78	142.20
027Wd	11.86	78.10	56.80	< 19.3	59.70	< 48.2	13.20	< 115.8	237.28	62.30	23.77	153.08
031	2.79	< 19.9	< 19.9	< 19.9	22.00	< 49.9	6.20	< 119.7	227.89	53.70	18.14	131.46
032	3.61	< 14.7	< 14.7	< 14.7	27.10	40.10	14.60	< 88.2	330.67	49.70	22.34	98.21
033	2.78	< 14.6	< 14.6	< 14.6	9.70	37.30	6.50	< 87.9	359.57	33.50	20.39	99.90
034	3.97	< 14.9	29.90	< 14.9	172.90	46.50	21.90	< 89.6	226.33	55.00	29.34	125.90
035	< 0.61	< 24.4	< 24.4	< 24.4	26.00	< 61.1	8.30	< 123.4	147.53	16.60	8.33	93.35
036	17.09	88.80	81.70	< 14.1	22.70	< 35.3	5.50	< 84.6	240.35	81.20	32.03	171.35
037	20.85	102.80	62.20	< 14.5	46.30	47.40	5.60	< 87.2	285.92	23.40	21.58	127.56
061	11.53	< 22.3	< 22.3	< 22.3	34.00	< 55.6	8.30	< 133.5	259.61	11.40	41.57	177.36
062B	19.90	< 20.5	< 20.5	< 20.5	41.90	< 51.3	9.50	< 123.2	170.86	36.00	60.51	121.64
076	3.25	< 22.4	< 22.4	< 22.4	15.00	< 56.1	21.40	< 134.5	120.45	24.50	11.23	98.55
077	1.33	< 18.3	< 18.3	21.60	9.20	< 45.7	7.70	< 109.7	158.13	15.40	7.09	87.13
080	1.48	< 18.3	< 18.3	179.20	89.70	< 45.7	7.10	13014.70	137.15	7.40	20.00	90.45
081	25.36	174.90	51.20	31.60	33.20	< 54	33.90	< 129.5	176.75	246.20	30.87	127.73
082	8.81	52.70	25.30	< 15.4	8.60	< 38.5	17.30	< 92.3	502.83	8.10	18.65	109.19
083	8.45	47.70	54.20	< 17.4	108.70	< 43.5	38.00	< 150	329.56	15.10	27.26	92.38
116	4.00	< 5	< 20	2.00	20.00	< 20	< 30	6.00	238.00	58.00	16.00	112.00
128	4.00	< 5	< 20	< 1	< 10	< 20	< 30	< 5	231.00	44.00	16.00	97.00
129	8.00	< 5	< 20	< 1	< 10	< 20	< 30	< 5	271.00	39.00	15.00	126.00
130E	8.00	50.00	< 20	15.00	< 10	< 20	240.00	< 5	293.00	11.00	24.00	176.00
139	6.00	< 5	< 20	3.00	< 10	< 20	< 30	< 5	198.00	32.00	23.00	92.00
143	1.00	6.00	< 20	< 1	< 10	< 20	< 30	< 5	186.00	32.00	4.00	93.00
147	1.00	7.00	< 20	7.00	< 10	< 20	< 30	10.00	166.00	22.00	6.00	112.00
151	4.00	6.00	< 20	14.00	< 10	< 20	< 30	19.00	186.00	32.00	28.00	192.00
152	1.00	5.00	< 20	< 1	< 10	< 20	< 30	< 5	98.00	20.00	25.00	179.00
153	4.00	8.00	< 20	< 1	< 10	< 20	< 30	15.00	174.00	24.00	16.00	195.00
154	2.00	< 5	< 20	5.00	60.00	< 20	< 30	24.00	210.00	15.00	7.00	99.00

Sample No.	Nb	Mo	Ag	Sn	Sb	Cs	Ba	La	Ce	Pr	Nd	Sm
	ppm	ppm	ppm	ppm	ppm	ppm	ppm	ppm	ppm	ppm	ppm	ppm
001E	7.40	< 132.5	< 6	6.04	< 70	< 0.06	1106.80	10.75	20.69	2.04	6.41	0.77
002E	9.84	< 71.3	< 3	4.33	< 40	19.14	851.00	41.58	84.47	9.02	30.03	3.83
003E	8.47	< 102.7	< 4	4.64	< 50	0.31	1280.20	12.97	23.89	2.35	7.41	1.03
004E	10.45	< 97.7	< 4	9.44	< 50	5.69	1312.70	31.08	64.36	7.46	25.09	3.64
006E	12.17	< 74.7	< 3	7.67	< 40	5.76	1261.30	29.49	57.41	6.42	21.97	2.45
009E	2.21	< 85.6	< 7	< 7	< 90	2.28	1352.50	116.29	214.60	21.07	62.06	6.11
009Ed	2.50	< 107.3	< 9	< 9	< 200	< 0.05	1351.90	119.66	231.19	22.26	64.92	6.59
011E	11.37	< 70.8	< 3	< 3	< 40	9.04	967.60	40.92	80.71	8.80	28.55	3.77
012E	5.44	< 90.7	< 4	11.35	< 50	9.62	103.50	36.80	71.94	8.35	28.49	4.55
013E	9.26	< 91.4	< 4	24.25	< 50	0.80	73.20	11.18	30.31	4.60	20.24	4.56
014E	8.92	< 93.5	< 4	< 4	< 50	2.80	1297.00	10.00	21.92	2.49	8.33	1.32
015E	6.33	< 85.5	< 4	< 4	< 50	1.21	1195.80	3.70	6.43	0.71	2.34	0.48
019E	7.95	< 90.9	< 4	11.96	< 50	36.61	120.20	6.66	13.67	1.78	7.51	1.58
003W	7.35	< 99.6	< 4	5.98	< 50	14.28	228.60	24.13	46.82	5.16	17.69	2.41
004W	4.11	< 103.7	< 4	4.43	< 50	< 0.05	1264.20	68.85	125.16	12.69	38.11	4.07
005W	10.46	< 73.9	< 3	5.20	< 40	13.96	1042.80	36.41	72.03	7.96	26.71	3.85
008W	6.82	< 109.7	< 5	6.29	< 60	8.34	1481.50	8.55	16.72	1.83	5.97	0.80
010W	10.17	< 75.5	< 3	3.15	< 40	15.08	1188.20	19.65	43.64	5.10	17.97	2.69
011W	10.57	< 72.4	< 3	6.34	< 40	16.68	1437.60	53.88	106.01	11.58	39.02	4.93
012W	9.25	< 71.4	< 3	< 3	< 40	2.37	949.90	20.44	42.88	4.79	16.16	2.67
014W	9.30	< 90.7	< 4	< 4	< 50	1.37	994.00	22.84	44.41	4.99	16.56	2.61
020W	4.51	< 87.7	< 4	< 4	< 50	12.16	389.70	17.76	36.73	4.10	13.68	1.78
024W	10.41	< 111.9	< 5	< 5	< 60	1.64	1009.00	44.52	87.98	9.08	30.20	3.87
025W	9.58	< 90.6	< 4	< 4	< 50	9.44	1041.30	38.17	77.37	8.33	27.70	3.65
026W	8.93	< 111.5	< 5	14.10	< 60	4.71	1089.40	16.36	32.63	3.44	10.98	1.59
027W	10.44	< 92.7	< 4	11.41	< 50	11.09	848.20	43.14	89.55	9.31	30.72	4.02
027Wd	10.78	< 96.5	< 4	< 4	< 50	8.64	845.30	42.66	88.19	9.56	31.11	4.23
031	10.49	< 99.7	< 4	6.03	< 50	7.48	1455.00	40.37	82.43	8.55	28.51	3.45
032	9.65	< 73.5	< 3	4.71	< 40	11.53	1330.90	27.18	57.87	6.16	20.86	2.80
033	10.49	< 73.2	< 3	3.04	< 40	11.39	1764.80	31.17	63.55	6.85	22.49	2.94
034	10.89	< 74.7	< 3	187.44	< 40	22.92	555.10	28.56	58.34	6.20	20.68	2.95
035	9.46	< 122.2	< 5	5.05	< 60	< 0.05	1035.70	31.91	57.12	5.80	17.13	1.84
036	13.57	< 70.5	< 3	< 3	< 40	22.52	712.20	42.57	87.99	10.29	36.41	5.03
037	9.31	< 72.7	< 3	8.83	< 40	47.36	264.00	28.10	59.77	6.69	23.20	3.19
061	20.07	< 111.3	< 5	14.32	< 60	14.63	177.20	63.51	137.82	14.48	50.16	6.49
062B	13.96	< 102.7	< 20	< 20	< 300	< 0.04	1579.10	316.90	693.56	76.02	250.45	31.66
076	11.66	< 112.1	< 5	6.95	< 60	< 0.05	1168.00	34.30	68.85	7.38	23.98	3.17
077	8.30	< 91.4	< 4	< 4	< 50	1.74	1071.00	11.41	24.91	2.58	7.94	1.09
080	2.63	< 91.3	< 4	7.95	< 50	10.25	166.90	27.71	56.22	6.35	21.26	3.01
081	9.38	< 107.9	< 5	< 5	< 60	7.06	847.60	27.40	61.11	7.37	27.67	4.46
082	7.63	< 76.9	< 4	11.53	< 40	37.89	86.70	12.09	24.57	2.93	10.48	1.92
083	8.63	< 87	< 4	14.49	< 50	22.23	125.80	4.03	9.27	1.18	4.93	1.33
116	11.00	< 2	< 0.5	1.00	1.00	1.20	1645.00	6.90	13.10	1.31	4.60	1.10
128	10.00	< 2	< 0.5	4.00	5.80	1.90	763.00	27.50	51.60	5.53	18.60	3.40
129	12.00	< 2	< 0.5	5.00	2.60	3.00	787.00	21.50	42.90	4.82	17.20	3.00
130E	12.00	< 2	0.80	7.00	1.40	4.60	327.00	48.10	93.50	10.60	35.90	6.80
139	12.00	< 2	< 0.5	2.00	1.60	0.70	1094.00	57.80	108.00	11.90	42.10	7.40
143	3.00	< 2	< 0.5	< 1	1.10	0.70	1149.00	9.20	17.10	1.66	5.50	0.80
147	7.00	8.00	< 0.5	< 1	1.9	1.30	888.00	15.00	26.60	2.65	8.20	1.2
151	10.00	< 2	< 0.5	1	0.8	2.00	1045.00	48.60	92.80	9.92	31.70	5.5
152	8.00	3.00	7.3	< 1	5.2	< 0.5	779.00	19.20	37.60	4.02	14.70	2.9
153	10.00	< 2	2.8	1	7.8	2.20	994.00	49.30	91.90	9.72	33.60	5.6
154	4.00	< 2	< 0.5	< 1	2.3	1.20	1073.00	39.70	66.40	6.59	20.00	2.8

Sample No.	Eu	Gd	Tb	Dy	Ho	Er	Tm	Yb	Lu	Hf	Ta	W
	ppm	ppm	ppm	ppm	ppm	ppm	ppm	ppm	ppm	ppm	ppm	ppm
001E	< 0.06	0.50	0.09	0.75	0.15	0.73	0.12	1.04	0.19	2.82	1.35	< 132.5
002E	0.93	3.32	0.48	3.56	0.70	1.83	0.31	2.16	0.35	4.30	1.21	< 71.3
003E	0.09	1.02	0.20	1.75	0.36	1.30	0.25	1.80	0.38	2.93	2.64	< 102.7
004E	0.72	2.90	0.49	3.42	0.66	1.90	0.35	2.26	0.37	4.13	1.29	< 97.7
006E	0.51	1.94	0.36	3.23	0.66	2.01	0.38	2.55	0.36	4.31	1.76	< 74.7
009E	0.96	2.87	0.33	1.35	0.22	0.72	0.14	1.18	0.22	2.79	0.47	< 85.6
009Ed	1.14	3.21	0.33	1.59	0.26	0.77	0.14	1.15	0.23	2.96	0.50	< 107.3
011E	0.97	2.98	0.48	3.27	0.62	1.71	0.30	1.96	0.31	4.08	1.70	< 70.8
012E	1.33	4.09	0.65	4.04	0.79	2.16	0.35	2.36	0.37	2.96	0.38	< 90.7
013E	2.76	5.52	0.89	6.76	1.35	3.96	0.62	4.08	0.69	4.81	1.05	< 91.4
014E	0.22	1.48	0.27	2.38	0.56	1.87	0.35	2.44	0.42	3.58	2.14	< 93.5
015E	0.07	0.78	0.15	1.45	0.35	1.20	0.21	1.56	0.32	2.60	2.44	< 85.5
019E	0.82	2.18	0.36	3.04	0.67	2.02	0.33	2.33	0.42	2.12	0.66	< 90.9
003W	0.36	1.57	0.22	1.27	0.25	0.73	0.12	0.94	0.16	5.25	0.82	< 99.6
004W	0.61	2.00	0.26	1.37	0.24	0.87	0.16	1.35	0.27	3.03	1.31	< 103.7
005W	0.84	3.23	0.53	3.70	0.73	2.11	0.32	2.24	0.35	4.23	1.19	< 73.9
008W	0.09	0.80	0.12	1.05	0.27	0.92	0.17	1.32	0.24	3.35	1.28	< 109.7
010W	0.48	2.65	0.45	3.49	0.69	2.14	0.36	2.51	0.40	3.56	1.78	< 75.5
011W	1.62	3.58	0.55	3.80	0.69	2.00	0.35	2.35	0.37	4.01	0.98	< 72.4
012W	0.45	2.28	0.41	3.04	0.58	1.73	0.32	2.38	0.39	2.70	3.00	< 71.4
014W	0.39	2.24	0.37	2.61	0.57	1.73	0.28	2.19	0.41	3.05	3.17	< 90.7
020W	0.32	1.38	0.19	1.09	0.21	0.69	0.13	0.86	0.16	4.93	0.46	< 87.7
024W	0.98	3.29	0.53	3.86	0.77	2.22	0.38	2.31	0.38	4.31	1.20	< 111.9
025W	0.84	3.08	0.48	3.35	0.68	1.86	0.32	2.02	0.34	4.17	1.15	< 90.6
026W	0.29	1.63	0.28	2.51	0.57	1.85	0.35	2.35	0.44	3.76	1.06	< 111.5
027W	0.91	3.38	0.51	3.72	0.74	1.98	0.32	2.10	0.33	3.36	1.22	< 92.7
027Wd	0.99	3.47	0.55	3.77	0.75	2.09	0.33	2.20	0.34	4.01	1.21	< 96.5
031	0.50	2.80	0.45	2.96	0.58	1.70	0.28	2.04	0.30	3.62	2.11	< 99.7
032	0.43	2.78	0.49	3.54	0.69	1.90	0.34	2.16	0.33	2.64	2.06	< 73.5
033	0.46	2.89	0.48	3.41	0.68	1.96	0.34	2.15	0.35	2.87	2.14	< 73.2
034	0.41	3.17	0.60	4.56	0.92	2.55	0.43	2.76	0.43	3.01	2.02	< 74.7
035	0.27	1.27	0.19	1.37	0.30	0.99	0.19	1.49	0.24	3.00	1.49	< 122.2
036	1.18	4.53	0.75	5.36	1.08	3.02	0.50	3.30	0.46	4.21	1.31	< 70.5
037	0.78	2.97	0.48	3.70	0.77	2.13	0.35	2.38	0.37	3.34	0.96	< 72.7
061	1.29	5.66	0.95	6.77	1.36	3.70	0.64	4.17	0.62	5.14	2.24	< 111.3
062B	5.76	17.02	2.28	12.20	1.87	4.72	0.75	4.36	0.62	3.68	1.40	< 102.7
076	0.49	2.01	0.27	2.09	0.37	1.04	0.20	1.44	0.23	2.88	2.03	< 112.1
077	0.14	0.71	0.11	0.90	0.21	0.74	0.16	1.19	0.21	2.57	1.41	< 91.4
080	0.38	2.39	0.43	3.34	0.71	2.08	0.31	1.88	0.24	2.42	0.23	< 91.3
081	1.20	4.17	0.67	4.83	0.96	2.70	0.45	2.90	0.41	3.21	0.75	< 107.9
082	0.73	2.00	0.35	2.80	0.57	1.59	0.27	2.04	0.36	2.63	0.62	< 76.9
083	0.96	2.21	0.42	3.68	0.86	2.55	0.43	2.93	0.49	2.27	0.67	< 87
116	0.28	1.90	0.30	2.40	0.50	1.60	0.28	2.30	0.41	3.30	1.80	7.00
128	0.41	3.30	0.40	2.60	0.50	1.60	0.27	2.10	0.37	3.00	1.70	7.00
129	0.41	3.10	0.40	2.60	0.50	1.80	0.32	2.50	0.43	4.10	1.50	3.00
130E	0.92	6.60	0.80	4.40	0.80	2.30	0.36	2.70	0.43	5.00	1.40	3.00
139	1.03	6.70	0.90	4.70	0.90	2.40	0.37	2.60	0.44	3.00	1.50	10.00
143	0.13	0.70	< 0.1	0.60	0.10	0.40	0.09	0.90	0.19	2.70	1.00	< 1
147	0.21	1.2	0.2	0.8	0.2	0.7	0.14	1.3	0.25	3.2	1.3	< 1
151	0.75	4.9	0.8	5.1	1.1	3.2	0.49	3.3	0.55	5.1	1.2	4.00
152	0.4	3.1	0.6	3.9	0.8	2.4	0.38	2.6	0.45	4.5	1.3	1.00
153	0.74	3.9	0.6	2.9	0.6	1.8	0.3	2.2	0.39	5	1.4	< 1
154	0.36	2.1	0.2	1.1	0.2	0.7	0.15	1.3	0.27	2.9	1	1.00

Sample No.	Pb	Bi	Th	U
	ppm	ppm	ppm	ppm
001E	< 40	2.96	20.84	8.18
002E	< 20	< 2	16.46	5.46
003E	< 30	9.24	23.53	14.91
004E	< 30	3.27	18.33	5.95
006E	< 20	< 2	14.46	5.17
009E	< 30	< 4	20.65	14.14
009Ed	< 30	< 5	19.30	13.96
011E	< 20	< 2	18.76	7.33
012E	< 30	2.86	5.37	20.71
013E	< 30	< 2	5.92	16.57
014E	< 30	< 2	21.60	9.00
015E	< 30	< 2	24.25	12.19
019E	< 30	< 2	5.44	7.95
003W	< 30	< 2	5.68	2.56
004W	< 30	2.29	22.50	10.23
005W	< 20	< 2	16.93	5.77
008W	< 30	2.86	17.25	9.27
010W	< 20	< 2	18.55	7.98
011W	< 20	< 2	11.07	3.38
012W	< 20	< 2	25.01	15.71
014W	< 30	< 2	24.45	16.14
020W	< 30	< 2	4.70	1.41
024W	< 30	< 3	16.91	5.49
025W	< 30	< 2	15.95	5.31
026W	< 30	8.97	14.94	3.91
027W	< 30	5.46	16.37	5.46
027Wd	< 30	< 2	16.82	5.42
031	< 30	< 2	18.80	10.11
032	20.02	< 2	17.00	11.71
033	< 20	< 2	17.69	10.47
034	44.04	196.75	17.41	12.59
035	< 30	2.44	22.70	7.14
036	< 20	< 2	12.96	3.04
037	< 20	< 2	11.35	3.58
061	< 30	3.64	25.36	6.29
062B	< 30	< 10	18.98	5.38
076	< 30	< 3	16.10	7.08
077	< 30	2.29	18.60	6.63
080	< 30	30.02	3.25	3.29
081	< 30	< 3	7.82	2.11
082	< 20	< 2	6.87	1.78
083	< 30	< 2	6.15	18.15
116	6.00	1.00	22.00	6.90
128	11.00	< 0.4	20.30	8.10
129	6.00	< 0.4	24.50	6.80
130E	6.00	1.10	21.70	16.20
139	< 5	< 0.4	20.90	4.30
143	10.00	< 0.4	25.90	10.10
147	14	< 0.4	27.6	11.4
151	12	1.5	24.9	8.4
152	6	< 0.4	22.3	7.5
153	13	< 0.4	23.1	7.2
154	< 5	1	27.3	8.6

Appendix 3A - Feldspar Mineral Chemical Analysis
Oxide Weight Percent

No.	MIN	DESCRIPTION	SiO2	Al2O3	CaO	Na2O	K2O	BaO	TOTAL
1	FEL	******27W PIC 307 SPOT 4 FG ORTHO	64.85	18.45	0.03	0.09	16.73	0.06	100.21
2	FEL	27W PIC 307 SPOT 4 FG ORTHO	66.98	17.7	0	0.22	15.48	0.1	100.48
3	FEL	27W PIC 307 SPOT 5 FG ORTHO INT W QTZ+BT	65.72	17.85	0	0.11	15.71	0.09	99.48
4	FEL	27W PIC 310 SPOT 1 FG ORTH ADJ TO PHENO	64.24	18.7	0	0.08	16.43	0.1	99.55
5	FEL	27W PIC 310 SPOT 2 RIND OF CG PHENO	66.81	19.4	0.48	12.3	0.15	0	99.14
6	FEL	27W PIC 310 ANOTHER PART OF RIND	67.31	19.88	0.36	12.37	0.14	0	100.06
7	FEL	27W PIC 310 SPOT 3 ALB RIND W ORTH DOMAI	66.19	18.78	0.02	0.12	14.86	0.2	100.17
8	FEL	27W AGAIN PIC 310 SPOT 3 AGAIN W BA	65.8	17.93	0	0.12	15.76	0.54	100.15
9	FEL	27W PIC 313 SPOT 2	64.18	18.8	0	0.13	16.24	0.55	99.9
10	FEL	27W AGAIN PIC 313 SPOT 2 AGAIN W BA	64.39	18.47	0	0.3	16.54	0.66	100.36
11	FEL	27W PIC 314 SPOT 1 CG PHENO	63.78	19.38	0.53	0.22	15.69	0.6	100.2
12	FEL	27W PIC 314 ANOTHER DOMAIN OF KSPAR	64.21	19.7	0.06	0.24	15.14	0.98	100.33
13	FEL	27W PIC 314 "K-FELD+PLAG DOMAIN" LABEL O	62.38	25.09	1.49	7.38	3.8	0.11	100.25
14	FEL	27W PIC 314 SPOT 2 ANOTHER PLAG	64.05	21.95	3.32	9.73	0.19	0	99.24
15	FEL	27W PIC 315 SPOT 3 FG KSPAR	64.85	18.52	0	0.15	16.17	0.13	99.82
16	FEL	27W PIC 317 SPOT 1 FG KSPAR GMASS	64.55	18.73	0.04	0.1	15.75	0.08	99.25
17	FEL	27W PIC 317 SPOT 2 MARGIN OF PHENO	65.66	19.97	0.49	12.74	0.22	0	99.08
18	FEL	27W PIC 317 SPOT 3 INTERIOR OF CG PHENO	63.54	21.25	2.2	10.08	0.17	0.06	97.3
19	FEL	27W AGAIN GMASS ORTHO WITH BA	64.98	18.13	0	0.05	16.46	0.12	99.74
20	FEL	27W AGAIN RANDOM GMASS KSPAR	64.93	18.46	0	0.24	16.79	0.06	100.48
21	FEL	27W AGAIN RANDOM GMASS KSPAR	64.88	18.4	0.05	0.23	15.28	0.2	99.04
22	FEL	27W AGAIN RANDOM GMASS KSPAR	66.12	18.52	0	0.26	15.9	0	100.8
23	FEL	27W AGAIN RANDOM GMASS KSPAR	65.27	18.41	0	0.19	16.24	0.1	100.21
24	FEL	27W ANOTHER COARSE GRAINED PHENO KSPAR D	64.6	18.38	0.05	0.24	16.14	0.95	100.36
25	FEL	27W PLAG DOMAIN IN SAME COARSE GRAINED P	66.02	21.21	1.82	10.74	0.26	0.2	100.25
26	FEL	******04E PIC 319 SPOT 1 PINK ORTH DOMA	64.31	19.33	0.04	0.1	16.02	0.25	100.05
27	FEL	04E PIC 319 ANOTHER ORTHO	65.53	17.89	0	0.14	15.9	0.25	99.71
28	FEL	04E PIC 319 SPOT 2 DARK DOMAIN	68.95	17.41	0.79	11.81	0.21	0	99.17
29	FEL	04E PIC 319 SPOT 3	65.38	17.36	0.02	0.26	17.11	0.08	100.21
30	FEL	04E PIC 319 SPOT 4	65.16	17.61	0.05	0.75	16.06	0.11	99.74
31	FEL	04E PIC 319 SPOT 5 ALB MARGIN	68.92	18.11	0.15	12.78	0.12	0	100.08
32	FEL	04E PIC 321 SPOT 1 ORTHO+EPIDOTE CORE	64.63	17.95	0	0.32	16.28	0.13	99.31
33	FEL	04E PIC 321 SPOT 2 ALB RIND	69.31	17.02	0.87	11.9	0.14	0	99.24

No.	MIN	DESCRIPTION	SiO2	Al2O3	CaO	Na2O	K2O	BaO	TOTAL
34	FEL	04E PIC 323 SPOT 3 GMASS KFELD	64.88	17.41	0	0.06	16.84	0.17	99.36
35	FEL	04E PIC 323 SPOT 4 GMASS KFELD	65.89	16.67	0	0.38	17.06	0.4	100.4
36	FEL	04E PIC 323 SPOT 5 GMASS KFELD	65.85	17.14	0	0.26	16.37	0.32	99.94
37	FEL	04E PIC 324 ORTHO SPOT 1	65.26	17.06	0.02	0.3	16.47	1.55	100.66
38	FEL	04E PIC 324 SPOT 2 PLAG DARKER DOMAIN	69.33	18.86	0.71	10.79	0.77	0	100.46
39	FEL	04E FG RANDOM GMASS ORTHO	64.94	17.51	0	0.17	16.62	0.16	99.4
40	FEL	04E FG RANDOM GMASS ORTHO	65.2	17.5	0	0.25	16.92	0.88	100.75
41	FEL	******05E PIC 325 SPOT 1 PHENO ORTH	64.57	18.25	0.07	0.19	16.14	0.15	99.37
42	FEL	05E PIC 325 SPOT 2 PHENO ORTH MARGIN	64.44	17.93	0	0.23	16.1	0.56	99.26
43	FEL	05E SPOT A ON MAP	63.52	19.5	0	0.09	16.69	0.12	99.92
44	FEL	05E SPOT A ON MAP ANOTHER	63.29	20.75	0.09	0.14	15.74	0.11	100.12
45	FEL	05E SPOT B ON MAP IN QTZ	64.73	19.66	0.08	0.19	15.55	0.4	100.61
46	FEL	05E SPOT C ON MAP	64.72	19.06	0	0.05	15.51	0.13	99.47
47	FEL	05E PIC 327 SPOT 1 PHENO ORTH	66.37	18.03	0	0.03	15.47	0.07	99.97
48	FEL	05E PIC 327 SPOT 2 PHENO ORTH BRIGHT BAN	65.79	18.31	0	0.29	15.58	0.67	100.64
49	FEL	05E PIC 327 SPOT 3 ORTHO INT W QTZ	65.54	17.81	0	0.11	16.43	0.27	100.16
50	FEL	05E PIC 328 & 329 SPOT D ON MAP BRIGHT A	65.49	19.36	0.01	0.08	14.68	0	99.62
51	FEL	05E SPOT E ON MAP	62.78	20.15	0	0.18	16.12	0	99.23
52	FEL	05E PIC 330 SPOT 1 ORTHO	65.24	17.85	0	0	17.67	0.01	100.77
53	FEL	05E PIC 331 SPOT 1 ORTHO	67.87	15.96	0	0.1	15.24	0.08	99.25
54	FEL	05E PIC 331 SPOT 4 GMASS ORTHO	65.84	17.99	0	0.05	16.63	0.26	100.77
55	FEL	05E PIC 331 SPOT 5 GMASS ORTHO	65.63	18.94	0	0.13	14.74	0.48	99.92
56	FEL	05E PIC 333 SPOT 2 GMASS FELD	65.4	17.94	0.02	0.11	16.53	0	100
57	FEL	05E PIC 333 SPOT 3 GMASS FELD	64.57	17.76	0	0.13	16.86	0.56	99.88
58	FEL	05E PIC 333 SPOT 4 GMASS FELD	64.81	17.23	0.01	0.04	17.65	0.18	99.92
59	FEL	******05W AREA "A" ON THIN SECTION - SLIDE 1 SPOT 2	66.61	18.42	0.13	0.33	13.90	0	99.53
60	FEL	05W AREA "A" ON THIN SECTION - SLIDE 1 SPOT 2	65.49	20.67	0.41	9.00	3.27	0	99.45
61	FEL	******05W2 GMASS ORTHO	65.78	17.51	0.04	0.18	16.74	0.3	100.55
62	FEL	05W2 PIC 334 SPOT 1 ALB	67.67	20.16	0.27	11.3	0.22	0	99.62
63	FEL	05W2 PIC 334 SPOT 2 ORTHO	65.18	18.75	0.41	2.19	12.54	0.45	99.52
64	FEL	05W2 PIC 334 SPOT 3 ORTHO	64.91	18.72	0	0.24	15.32	0.11	99.3
65	FEL	05W2 PIC 334 SPOT 4 ALB RIND	67.58	20.27	0.36	11.48	0.14	0.06	99.89
66	FEL	05W2 PIC 334 SPOT 5	65.82	17.73	0	0.19	16.47	0.01	100.22
67	FEL	05W2 PIC 334 SPOT 8	65.26	17.19	0.07	0.15	17.46	0.12	100.25
68	FEL	05W2 PIC 334 SPOT 9	65.39	18.21	0.04	0.7	15.18	0.92	100.44
69	FEL	05W2 PIC 335 SPOT 2 FG GMASS ORTHO	65.03	18.46	0	0.17	16.97	0	100.63

No.	MIN	DESCRIPTION	SiO2	Al2O3	CaO	Na2O	K2O	BaO	TOTAL
70	FEL	05W2 PIC 335 SPOT 3 FG GMASS ORTHO	65.73	17.22	0.71	0.2	15.57	0.39	99.82
71	FEL	05W2 RANDOM FG GMASS ORTHO	65.66	18.28	0.01	0.13	16.3	0	100.38
72	FEL	05W2 RANDOM FG GMASS ORTHO	65.76	18.24	0	0.09	16.52	0.11	100.72
73	FEL	******11W PIC 337 SPOT 1 IN PINK BAND	62.39	18.34	0	0.14	18.09	0.43	99.39
74	FEL	11W PIC 337 SPOT 2 IN PINK BAND	62.11	17.81	0	0.15	19.52	0.39	99.98
75	FEL	11W PIC 337 SPOT 7 DARK INSIDE VEIN	66.66	20.65	0.26	12.27	0.13	0	99.97
76	FEL	11W PIC 337 SPOT 8 DARK INSIDE VEIN	66.32	20.88	0.56	12.08	0.15	0	99.99
77	FEL	11W PIC 337 SPOT 9 GMASS OUT OF VEIN	65.96	20.4	0.19	11.22	1.26	0.05	99.08
78	FEL	11W PIC 337 SPOT 10 GMASS OUT OF VEIN	64.04	19.05	0	0.27	16.98	0.42	100.76
79	FEL	11W PIC 338 SPOT 2 KSPAR ADJ TO AMP	64.57	12.64	0.03	0.34	22.97	0	100.55
80	FEL	11W PIC 338 SPOT 3 KSPAR ADJ TO AMP	63.66	12.33	0.04	0.17	23.4	0.3	99.9
81	FEL	11W PIC 338 SPOT 6 KSPAR	63.95	17.46	0	0.17	18.51	0.29	100.38
82	FEL	11W PIC 338 SPOT 7 KSPAR	63.56	17.3	0	0.32	18.12	0.62	99.92
83	FEL	11W PIC 338 SPOT 8 KSPAR	63.4	17.65	0	0.15	18.61	0.41	100.22
84	FEL	11W RANDOM KSPAR	63.47	17.87	0	0.03	18.58	0.22	100.17
85	FEL	11W PIC 339 SPOT 6 KSPAR	64.21	17.61	0.02	0.15	18.61	0.05	100.65
86	FEL	11W PIC 339 SPOT 7 KSPAR	63.76	18.69	0	0.21	18.02	0.18	100.86
87	FEL	******085C PIC 340 SPOT 1 KFELD PHE	63.21	18.58	0	0.13	17.8	0	99.72
88	FEL	085C PIC 340 SPOT 2 KFELD	64.61	18.31	0	0.1	16.74	0.21	99.97
89	FEL	085C PIC 340 SPOT 3 KFELD	63.19	19.22	0	0.12	16.91	0.27	99.71
90	FEL	085C SPOT A OM MAP - RANDOM KSPAR	63.99	18.92	0	0.07	16.11	0.33	99.42
91	FEL	085C PIC 341 SPOT 3	63.51	19.23	0	0.21	17.54	0.02	100.51
92	FEL	085C PIC 341 SPOT 5 KFELD	64.7	17.36	0.02	0.1	18.53	0.01	100.72
93	FEL	******088 PIC 345 SPOT 3 KSPAR	64.04	17.48	0	0.22	17.7	0	99.44
94	FEL	088 PIC 346 SPOT 1 KSPAR	64.37	17.59	0	0.05	18.05	0.02	100.08
95	FEL	088 PIC 346 SPOT 2 KSPAR	64.25	17.83	0	0.02	18.2	0.07	100.37
96	FEL	088 PIC 346 SPOT 3 KSPAR	65.06	18.09	0	0.04	17.23	0	100.42
97	FEL	******08W PIC 347 SPOT 1 KFELD	64.48	17.24	0	0.24	17.74	0.63	100.33
98	FEL	08W PIC 347 SPOT 2 KFELD	64.26	17.93	0	0.8	17.03	0.78	100.8
99	FEL	08W PIC 347 SPOT 3 KFELD	63.8	17.47	0	0.28	18	0.35	99.9
100	FEL	08W PIC 347 SPOT 4 KFELD	64.06	17.42	0.05	0.13	18.16	0.35	100.17
101	FEL	08W PIC 347 SPOT 5 KFELD	64.28	17.74	0	0.39	17.38	0.18	99.97
102	FEL	08W PIC 347 SPOT 6 KFELD	63.56	19.02	0.03	0.38	17.43	0.23	100.65
103	FEL	08W PIC 347 SPOT 7 KFELD	63.31	18.6	0	0.17	18.06	0.03	100.17
104	FEL	08W PIC 348 SPOT 1 ALBITE	67.98	19.38	0.19	12.03	0.46	0	100.04
105	FEL	08W PIC 348 SPOT 2 KSPAR	64.56	18.39	0	0.02	17.05	0.1	100.12

No.	MIN	DESCRIPTION	SiO2	Al2O3	CaO	Na2O	K2O	BaO	TOTAL
106	FEL	******087 RANDOM KSPAR FG	64.99	18.58	0	0.33	16.18	0	100.08
107	FEL	087 PIC 349 SPOT 1 KSPAR ADJ TO CHL	64.59	18.03	0.06	0.04	17.22	0.13	100.07
108	FEL	087 PIC 349 SPOT 2 KSPAR	64.19	18.89	0	0.15	16.41	0.15	99.79
109	FEL	087 PIC 349 SPOT 3 KSPAR	65.04	18.88	0.03	1.76	13.71	0.31	99.73
110	FEL	087 PIC 349 SPOT 4 KSPAR	64.57	18.42	0.05	0.22	16.96	0.29	100.51
111	FEL	087 PIC 349 SPOT 5 KSPAR	64.27	19.27	0.01	0.09	16.75	0.2	100.59
112	FEL	******03E KSPAR IN CIRCLED AREA	64.47	18.04	0.02	0.13	17.15	0.59	100.4
113	FEL	03E KSPAR IN CIRCLED AREA	65.06	18.35	0	0.21	16.72	0.44	100.78
114	FEL	03E KSPAR IN CIRCLED AREA	65.06	17.49	0.03	0.22	16.87	0.59	100.26
115	FEL	03E KSPAR OUTSIDE CIRCLE	65	18.11	0	0.13	16.47	0.27	99.98
116	FEL	03E KSPAR IN VEIN AREA	65.41	18	0	0.33	16.33	0.18	100.25
117	FEL	******155 AREA A' SLIDE 2 SPOT 1 - DARK MELANO	66.41	18.56	0.00	0.17	15.48	0	100.68
118	FEL	155 AREA A'' - LIGHT LEUCOSOMAL	67.49	17.23	0.00	0.16	15.01	0	99.96

Appendix 3A - Feldspar Mineral Chemical Analysis
Atomic Proportions

No.	DESCRIPTION	Si	Al	Ca	Na	K	Ba	O	Z	X
1	******27W PIC 307 SPOT 4 FG ORTHO	11.985	4.019	0.006	0.032	3.944	0.004	32.000	16.000	3.990
2	27W PIC 307 SPOT 4 FG ORTHO	12.221	3.805	0.000	0.078	3.602	0.007	32.000	16.000	3.713
3	27W PIC 307 SPOT 5 FG ORTHO INT W QTZ+BT	12.144	3.887	0.000	0.039	3.703	0.007	32.000	16.000	3.780
4	27W PIC 310 SPOT 1 FG ORTH ADJ TO PHENO	11.941	4.097	0.000	0.029	3.895	0.007	32.000	16.000	3.969
5	27W PIC 310 SPOT 2 RIND OF CG PHENO	11.847	4.054	0.091	4.229	0.034	0.000	32.000	15.901	4.354
6	27W PIC 310 ANOTHER PART OF RIND	11.819	4.113	0.068	4.211	0.031	0.000	32.000	15.933	4.310
7	27W PIC 310 SPOT 3 ALB RIND W ORTH DOMAI	12.084	4.040	0.004	0.042	3.460	0.014	32.000	16.000	3.644
8	27W AGAIN PIC 310 SPOT 3 AGAIN W BA	12.123	3.892	0.000	0.043	3.703	0.039	32.000	16.000	3.801
9	27W PIC 313 SPOT 2	11.919	4.114	0.000	0.047	3.847	0.040	32.000	16.000	3.967
10	27W AGAIN PIC 313 SPOT 2 AGAIN W BA	11.942	4.036	0.000	0.108	3.913	0.048	32.000	15.978	4.068
11	27W PIC 314 SPOT 1 CG PHENO	11.807	4.228	0.105	0.079	3.705	0.044	32.000	16.000	3.967
12	27W PIC 314 ANOTHER DOMAIN OF KSPAR	11.836	4.279	0.012	0.086	3.560	0.071	32.000	16.000	3.843
13	27W PIC 314 "K-FELD+PLAG DOMAIN" LABEL O	11.069	5.246	0.283	2.539	0.860	0.008	32.000	16.000	4.005
14	27W PIC 314 SPOT 2 ANOTHER PLAG	11.385	4.598	0.632	3.353	0.043	0.000	32.000	15.983	4.029
15	27W PIC 315 SPOT 3 FG KSPAR	11.998	4.038	0.000	0.054	3.816	0.009	32.000	16.000	3.915
16	27W PIC 317 SPOT 1 FG KSPAR GMASS	11.979	4.095	0.008	0.036	3.728	0.006	32.000	16.000	3.852
17	27W PIC 317 SPOT 2 MARGIN OF PHENO	11.696	4.192	0.094	4.400	0.050	0.000	32.000	15.888	4.543
18	27W PIC 317 SPOT 3 INTERIOR OF CG PHENO	11.493	4.529	0.426	3.535	0.039	0.004	32.000	16.000	4.027
19	27W AGAIN GMASS ORTHO WITH BA	12.046	3.961	0.000	0.018	3.892	0.009	32.000	16.000	3.925
20	27W AGAIN RANDOM GMASS KSPAR	11.978	4.013	0.000	0.086	3.950	0.004	32.000	15.990	4.041
21	27W AGAIN RANDOM GMASS KSPAR	12.043	4.024	0.010	0.083	3.617	0.015	32.000	16.000	3.792
22	27W AGAIN RANDOM GMASS KSPAR	12.064	3.982	0.000	0.092	3.700	0.000	32.000	16.000	3.838
23	27W AGAIN RANDOM GMASS KSPAR	12.026	3.997	0.000	0.068	3.816	0.007	32.000	16.000	3.914
24	27W ANOTHER COARSE GRAINED PHENO KSPAR D	11.973	4.014	0.010	0.086	3.815	0.069	32.000	15.987	3.981
25	27W PLAG DOMAIN IN SAME COARSE GRAINED P	11.598	4.391	0.343	3.658	0.058	0.014	32.000	15.989	4.073
26	******04E PIC 319 SPOT 1 PINK ORTH ORTH DOMA	11.878	4.207	0.008	0.036	3.774	0.018	32.000	16.000	3.920
27	04E PIC 319 ANOTHER ORTHO	12.116	3.898	0.000	0.050	3.750	0.018	32.000	16.000	3.832
28	04E PIC 319 SPOT 2 DARK DOMAIN	12.182	3.625	0.150	4.046	0.047	0.000	32.000	15.807	4.243
29	04E PIC 319 SPOT 3	12.116	3.791	0.004	0.093	4.044	0.006	32.000	15.907	4.147
30	04E PIC 319 SPOT 4	12.086	3.849	0.010	0.270	3.799	0.008	32.000	15.934	4.087
31	04E PIC 319 SPOT 5 ALB MARGIN	12.085	3.742	0.028	4.345	0.027	0.000	32.000	15.828	4.400
32	04E PIC 321 SPOT 1 ORTHO+EPIDOTE CORE	12.042	3.941	0.000	0.116	3.869	0.009	32.000	15.983	3.994
33	04E PIC 321 SPOT 2 ALB RIND	12.235	3.540	0.165	4.073	0.032	0.000	32.000	15.776	4.269

No.	DESCRIPTION	Si	Al	Ca	Na	K	Ba	O	Z	X
34	04E PIC 323 SPOT 3 GMASS KFELD	12.112	3.830	0.000	0.022	4.010	0.012	32.000	15.942	4.044
35	04E PIC 323 SPOT 4 GMASS KFELD	12.211	3.640	0.000	0.137	4.033	0.029	32.000	15.852	4.198
36	04E PIC 323 SPOT 5 GMASS KFELD	12.192	3.740	0.000	0.093	3.866	0.023	32.000	15.932	3.982
37	04E PIC 324 ORTHO SPOT 1	12.133	3.738	0.004	0.108	3.906	0.113	32.000	15.871	4.131
38	04E PIC 324 SPOT 2 PLAG DARKER DOMAIN	12.076	3.871	0.132	3.644	0.171	0.000	32.000	15.947	3.947
39	04E FG RANDOM GMASS ORTHO	12.105	3.846	0.000	0.061	3.951	0.012	32.000	15.951	4.024
40	04E FG RANDOM GMASS ORTHO	12.079	3.820	0.000	0.090	3.998	0.064	32.000	15.899	4.152
41	*******05E PIC 325 SPOT 1 PHENO ORTH	12.011	4.000	0.014	0.069	3.829	0.011	32.000	16.000	3.934
42	05E PIC 325 SPOT 2 PHENO ORTH MARGIN	12.038	3.947	0.000	0.083	3.836	0.041	32.000	15.985	3.960
43	05E SPOT A ON MAP	11.797	4.267	0.000	0.032	3.954	0.009	32.000	16.000	4.059
44	05E SPOT A ON MAP ANOTHER	11.667	4.507	0.018	0.050	3.701	0.008	32.000	16.000	3.951
45	05E SPOT B ON MAP IN QTZ	11.865	4.247	0.016	0.068	3.636	0.029	32.000	16.000	3.859
46	05E SPOT C ON MAP	11.962	4.151	0.000	0.018	3.656	0.009	32.000	16.000	3.796
47	05E PIC 327 SPOT 1 PHENO ORTH	12.168	3.895	0.000	0.011	3.617	0.005	32.000	16.000	3.696
48	05E PIC 327 SPOT 2 PHENO ORTH BRIGHT BAN	12.069	3.958	0.000	0.103	3.645	0.048	32.000	16.000	3.823
49	05E PIC 327 SPOT 3 ORTHO INT W QTZ	12.104	3.876	0.000	0.039	3.870	0.020	32.000	15.980	3.929
50	05E PIC 328 & 329 SPOT D ON MAP BRIGHT A	11.998	4.180	0.002	0.028	3.430	0.000	32.000	16.000	3.638
51	05E SPOT E ON MAP	11.704	4.426	0.000	0.065	3.833	0.000	32.000	16.000	4.028
52	05E PIC 330 SPOT 1 ORTHO	12.045	3.883	0.000	0.000	4.161	0.001	32.000	15.928	4.162
53	05E PIC 331 SPOT 1 ORTHO	12.495	3.462	0.000	0.036	3.579	0.006	32.000	15.958	3.620
54	05E PIC 331 SPOT 4 GMASS ORTHO	12.091	3.893	0.000	0.018	3.895	0.019	32.000	15.984	3.932
55	05E PIC 331 SPOT 5 GMASS ORTHO	12.037	4.094	0.000	0.046	3.448	0.034	32.000	16.000	3.660
56	05E PIC 333 SPOT 2 GMASS FELD	12.083	3.906	0.004	0.039	3.895	0.000	32.000	15.989	3.939
57	05E PIC 333 SPOT 3 GMASS FELD	12.038	3.902	0.000	0.047	4.009	0.041	32.000	15.939	4.097
58	05E PIC 333 SPOT 4 GMASS FELD	12.095	3.789	0.002	0.014	4.201	0.013	32.000	15.884	4.231
59	*******05W AREA "A" ON THIN SECTION - SLIDE 1 SPOT 2	12.164	3.964	0.025	0.117	3.238	0.000	32.000	16.127	3.683
60	05W AREA "A" ON THIN SECTION - SLIDE 1 SPOT 2	11.869	4.347	0.078	3.114	0.744	0.000	32.000	16.036	4.188
61	*******05W2 GMASS ORTHO	12.130	3.805	0.008	0.064	3.937	0.022	32.000	15.934	4.031
62	05W2 PIC 334 SPOT 1 ALB	11.874	4.168	0.051	3.844	0.049	0.000	32.000	16.000	3.987
63	05W2 PIC 334 SPOT 2 ORTHO	11.970	4.057	0.081	0.780	2.937	0.032	32.000	16.000	3.857
64	05W2 PIC 334 SPOT 3 ORTHO	12.008	4.081	0.000	0.086	3.615	0.008	32.000	16.000	3.798
65	05W2 PIC 334 SPOT 4 ALB RIND	11.841	4.186	0.068	3.900	0.031	0.004	32.000	16.000	4.030
66	05W2 PIC 334 SPOT 5	12.127	3.849	0.000	0.068	3.870	0.001	32.000	15.976	3.939
67	05W2 PIC 334 SPOT 8	12.118	3.761	0.014	0.054	4.135	0.009	32.000	15.880	4.212
68	05W2 PIC 334 SPOT 9	12.043	3.952	0.008	0.250	3.566	0.066	32.000	15.995	3.890
69	05W2 PIC 335 SPOT 2 FG GMASS ORTHO	11.981	4.008	0.000	0.061	3.988	0.000	32.000	15.988	4.048

No.	DESCRIPTION	Si	Al	Ca	Na	K	Ba	O	Z	X
70	05W2 PIC 335 SPOT 3 FG GMASS ORTHO	12.162	3.754	0.141	0.072	3.674	0.028	32.000	15.916	3.915
71	05W2 RANDOM FG GMASS ORTHO	12.063	3.957	0.002	0.046	3.820	0.000	32.000	16.000	3.888
72	05W2 RANDOM FG GMASS ORTHO	12.063	3.943	0.000	0.032	3.865	0.008	32.000	16.000	3.911
73	******11W PIC 337 SPOT 1 IN PINK BAND	11.809	4.091	0.000	0.051	4.367	0.032	32.000	15.900	4.451
74	11W PIC 337 SPOT 2 IN PINK BAND	11.798	3.986	0.000	0.055	4.729	0.029	32.000	15.784	4.813
75	11W PIC 337 SPOT 7 DARK INSIDE VEIN	11.715	4.276	0.079	4.181	0.029	0.000	32.000	15.991	4.259
76	11W PIC 337 SPOT 8 DARK INSIDE VEIN	11.663	4.327	0.106	4.119	0.034	0.000	32.000	15.990	4.258
77	11W PIC 337 SPOT 9 GMASS OUT OF VEIN	11.733	4.276	0.036	3.870	0.286	0.003	32.000	16.000	4.204
78	11W PIC 337 SPOT 10 GMASS OUT OF VEIN	11.844	4.152	0.000	0.097	4.005	0.030	32.000	15.995	4.133
79	11W PIC 338 SPOT 2 KSPAR ADJ TO AMP	12.409	2.862	0.006	0.127	5.630	0.000	32.000	15.272	5.763
80	11W PIC 338 SPOT 3 KSPAR ADJ TO AMP	12.393	2.828	0.008	0.064	5.810	0.023	32.000	15.221	5.906
81	11W PIC 338 SPOT 6 KSPAR	11.977	3.853	0.000	0.062	4.422	0.021	32.000	15.830	4.505
82	11W PIC 338 SPOT 7 KSPAR	11.976	3.841	0.000	0.117	4.355	0.046	32.000	15.818	4.518
83	11W PIC 338 SPOT 8 KSPAR	11.921	3.911	0.000	0.055	4.463	0.030	32.000	15.831	4.548
84	11W RANDOM KSPAR	11.912	3.952	0.000	0.011	4.448	0.016	32.000	15.863	4.475
85	11W PIC 339 SPOT 6 KSPAR	11.972	3.869	0.004	0.054	4.426	0.004	32.000	15.842	4.488
86	11W PIC 339 SPOT 7 KSPAR	11.839	4.089	0.000	0.076	4.268	0.013	32.000	15.928	4.356
87	******085C PIC 340 SPOT 1 KFELD PHE	11.846	4.103	0.000	0.047	4.255	0.000	32.000	15.948	4.302
88	085C PIC 340 SPOT 2 KFELD	11.989	4.003	0.000	0.036	3.962	0.015	32.000	15.992	4.013
89	085C PIC 340 SPOT 3 KFELD	11.799	4.229	0.000	0.043	4.027	0.020	32.000	16.000	4.118
90	085C SPOT A OM MAP - RANDOM KSPAR	11.911	4.150	0.000	0.025	3.825	0.024	32.000	16.000	3.935
91	085C PIC 341 SPOT 3	11.787	4.205	0.000	0.076	4.152	0.001	32.000	15.992	4.229
92	085C PIC 341 SPOT 5 KFELD	12.034	3.805	0.004	0.036	4.396	0.001	32.000	15.839	4.437
93	******088 PIC 345 SPOT 3 KSPAR	12.019	3.866	0.000	0.080	4.237	0.000	32.000	15.885	4.317
94	088 PIC 346 SPOT 1 KSPAR	12.016	3.869	0.000	0.018	4.298	0.001	32.000	15.886	4.317
95	088 PIC 346 SPOT 2 KSPAR	11.975	3.916	0.000	0.007	4.327	0.005	32.000	15.891	4.339
96	088 PIC 346 SPOT 3 KSPAR	12.024	3.940	0.000	0.014	4.062	0.000	32.000	15.964	4.076
97	******08W PIC 347 SPOT 1 KFELD	12.049	3.796	0.000	0.087	4.228	0.046	32.000	15.845	4.361
98	08W PIC 347 SPOT 2 KFELD	11.943	3.927	0.000	0.288	4.037	0.057	32.000	15.870	4.382
99	08W PIC 347 SPOT 3 KFELD	11.982	3.866	0.000	0.102	4.312	0.026	32.000	15.848	4.440
100	08W PIC 347 SPOT 4 KFELD	12.000	3.845	0.010	0.047	4.339	0.026	32.000	15.845	4.422
101	08W PIC 347 SPOT 5 KFELD	11.996	3.901	0.000	0.141	4.137	0.013	32.000	15.897	4.291
102	08W PIC 347 SPOT 6 KFELD	11.800	4.161	0.006	0.137	4.127	0.017	32.000	15.961	4.287
103	08W PIC 347 SPOT 7 KFELD	11.833	4.097	0.000	0.062	4.305	0.002	32.000	15.929	4.369
104	08W PIC 348 SPOT 1 ALBITE	11.927	4.007	0.036	4.092	0.103	0.000	32.000	15.934	4.231
105	08W PIC 348 SPOT 2 KSPAR	11.971	4.018	0.000	0.007	4.032	0.007	32.000	15.989	4.047

No.	DESCRIPTION	Si	Al	Ca	Na	K	Ba	O	Z	X
106	*******087 RANDOM KSPAR FG	11.988	4.039	0.000	0.118	3.807	0.000	32.000	16.000	3.952
107	087 PIC 349 SPOT 1 KSPAR ADJ TO CHL	12.003	3.948	0.012	0.014	4.081	0.009	32.000	15.951	4.117
108	087 PIC 349 SPOT 2 KSPAR	11.911	4.130	0.000	0.054	3.884	0.011	32.000	16.000	3.990
109	087 PIC 349 SPOT 3 KSPAR	11.956	4.090	0.006	0.627	3.215	0.022	32.000	16.000	3.916
110	087 PIC 349 SPOT 4 KSPAR	11.950	4.017	0.010	0.079	4.003	0.021	32.000	15.966	4.113
111	087 PIC 349 SPOT 5 KSPAR	11.855	4.189	0.002	0.032	3.941	0.014	32.000	16.000	4.033
112	*******03E KSPAR IN CIRCLED AREA	11.983	3.951	0.004	0.047	4.066	0.043	32.000	15.934	4.160
113	03E KSPAR IN CIRCLED AREA	11.992	3.986	0.000	0.075	3.931	0.032	32.000	15.977	4.038
114	03E KSPAR IN CIRCLED AREA	12.084	3.828	0.006	0.079	3.997	0.043	32.000	15.912	4.125
115	03E KSPAR OUTSIDE CIRCLE	12.040	3.953	0.000	0.047	3.891	0.020	32.000	15.992	3.957
116	03E KSPAR IN VEIN AREA	12.067	3.913	0.000	0.118	3.842	0.013	32.000	15.980	3.974
117	*******155 AREA A' SLIDE 2 SPOT 1 - DARK MELANO	12.093	3.983	0.000	0.060	3.595	0.000	32.000	16.076	3.824
118	155 AREA A'' - LIGHT LEUCOSOMAL	12.324	3.708	0.000	0.057	3.496	0.000	32.000	16.032	3.636

Appendix 3B - Amphibole Mineral Chemical Analysis
Oxide Weight Percent

No.	DESCRIPTION	SiO2	TiO2	Al2O3	Fe2O3*	FeO	MnO	MgO	CaO	Na2O	K2O	Cr2O3	F	Cl	H2O*	-0= F+Cl	TOTAL
1	*****11W PIC 337 SPOT 3 BRIGHT OUTSIDE	40.23	0.68	9.41	0.00	25.73	0.10	4.13	12.92	1.47	2.45	0.01	0.21	1.75	1.24	100.33	0.48	99.85
2	11W PIC 337 SPOT 4 ADJ DARK OUTSIDE VEIN	51.06	0.14	1.42	0.00	22.53	0.04	9.24	12.78	0.25	0.24	0.05	0.13	0.02	1.83	99.73	0.06	99.67
3	11W PIC 337 SPOT 5 ADJ DARK OUTSIDE VEIN	49.07	0.08	2.41	1.30	23.17	0.11	8.12	12.48	0.44	0.28	0.00	0.39	0.06	1.67	99.57	0.18	99.40
4	11W PIC 337 SPOT 6	40.23	0.66	10.00	0.00	27.09	0.05	3.81	11.87	1.45	2.42	0.03	0.26	1.54	1.27	100.68	0.46	100.23
5	11W PIC 338 SPOT 1 AMPH ADJ TO Th-Si	48.17	0.11	3.01	0.00	24.22	0.11	7.75	12.66	1.12	0.97	0.00	0.00	0.34	1.78	100.24	0.08	100.16
6	11W PIC 338 SPOT 4 AMP	48.74	0.15	3.74	0.00	23.45	0.00	7.99	12.09	0.92	0.67	0.00	0.00	0.45	1.76	99.96	0.10	99.86
7	11W PIC 338 SPOT 5 AMP BRIGHTER	41.21	0.37	8.82	1.39	26.60	0.08	4.34	11.80	1.56	2.34	0.00	0.02	0.56	1.65	100.74	0.13	100.61
8	11W PIC 338 SPOT 9 AMP	47.51	0.04	4.60	0.31	24.01	0.00	7.28	12.02	1.00	0.80	0.06	0.05	0.26	1.77	99.71	0.08	99.63
9	11W PIC 339 SPOT 1 DARK AMP	48.14	0.18	2.69	3.41	21.69	0.07	8.47	12.29	0.68	0.46	0.02	0.00	0.32	1.79	100.22	0.07	100.15
10	11W PIC 339 SPOT 2 BRIGHT AMP	41.41	0.53	8.14	0.32	26.01	0.14	4.90	11.97	1.38	2.01	0.01	0.06	0.52	1.63	99.03	0.14	98.89
11	11W PIC 339 SPOT 3 DARK AMP	46.44	0.24	5.03	0.00	23.96	0.08	6.70	12.25	1.18	1.05	0.02	0.02	0.20	1.78	98.95	0.05	98.90
12	11W PIC 339 SPOT 4 BRIGHT AMP	42.97	0.64	7.30	0.36	26.04	0.07	5.18	11.79	1.31	1.88	0.00	0.00	0.69	1.63	99.87	0.16	99.71
13	11W PIC 339 SPOT 5 BRIGHT AMP	43.92	0.48	7.18	0.00	25.02	0.05	5.29	12.10	1.17	1.74	0.07	0.02	0.06	1.79	98.89	0.02	98.87
14	*****088 PIC 345 SPOT 1 AMP	53.55	0.04	1.53	0.00	20.72	0.15	9.94	12.11	0.35	0.24	0.11	0.00	0.00	1.95	100.69	0.00	100.69
15	088 PIC 345 SPOT 2 AMP	49.86	0.02	2.21	1.85	21.79	0.15	9.12	12.63	0.38	0.39	0.05	0.01	0.13	1.86	100.45	0.03	100.42
16	088 PIC 346 SPOT 4 AMP CLAST	51.36	0.00	1.28	0.00	23.44	0.11	7.93	12.91	0.31	0.20	0.00	0.00	0.00	1.88	99.42	0.00	99.42
17	088 PIC 346 SPOT 5 AMP CLAST	48.21	0.09	4.47	1.77	23.22	0.20	7.34	11.79	1.12	0.63	0.00	0.02	0.06	1.86	100.78	0.02	100.76
18	088 PIC 346 SPOT 6 AMP IN VEIN	52.26	0.00	1.60	0.00	22.13	0.00	9.06	12.92	0.32	0.21	0.03	0.01	0.10	1.89	100.53	0.03	100.50
19	*****085C PIC 340 SPOT 5 AMP W INCL	51.02	0.00	2.10	0.00	23.90	0.07	7.76	12.92	0.46	0.27	0.02	0.00	0.00	1.90	100.42	0.00	100.42
20	085C PIC 341 SPOT 1 - AMP	51.63	0.00	0.57	0.00	25.95	0.17	6.65	12.34	0.07	0.08	0.00	0.35	0.05	1.69	99.55	0.16	99.39
21	085C PIC 341 SPOT 4 AMP	51.38	0.00	1.55	0.00	24.74	0.18	7.08	12.76	0.31	0.36	0.00	0.00	0.10	1.86	100.32	0.02	100.30
22	085C SPOT B ON MAP - AMP	48.37	0.09	3.41	0.00	25.70	0.05	6.43	12.05	0.82	0.47	0.05	0.00	0.00	1.85	99.29	0.00	99.29
23	085C SPOT C ON MAP	52.14	0.08	1.36	0.00	24.40	0.01	6.86	12.50	0.28	0.26	0.00	0.04	0.06	1.86	99.85	0.03	99.82
24	085C SPOT D ON MAP	48.78	0.05	2.99	0.00	24.22	0.04	6.88	12.81	0.84	0.61	0.02	0.02	0.10	1.82	99.18	0.03	99.15
25	*****085C PIC 341 SPOT 2 - AMP	57.05	0.11	1.74	0.00	17.32	0.00	19.53	0.72	0.24	0.36	0.00	0.52	0.05	1.77	99.41	0.23	99.18
26	085C PIC 341 SPOT 2 - AMP	58.33	0.03	0.98	0.00	17.57	0.04	20.14	0.26	0.23	0.13	0.01	0.21	0.03	1.94	99.90	0.10	99.80
27	085C PIC 341 SPOT 6	58.20	0.02	1.58	0.00	16.84	0.07	20.53	0.67	0.26	0.38	0.00	0.09	0.00	2.02	100.66	0.04	100.62
28	*****087 PIC 351 SPOT 1 AMP DARK DOM	50.71	0.04	3.60	2.62	18.44	0.24	10.26	12.02	0.50	0.61	0.03	0.00	0.25	1.88	101.20	0.06	101.14
29	087 PIC 351 SPOT 2 AMP BRIGHT DOMAIN	48.55	0.08	4.34	0.00	21.01	0.10	9.18	12.34	0.67	0.75	0.04	0.00	0.42	1.77	99.21	0.09	99.12
30	087 PIC 351 SPOT 3 AMP BRIGHT DOMAIN	39.83	0.27	10.74	0.49	23.70	0.08	5.38	12.22	1.09	2.50	0.04	0.00	2.08	1.26	99.68	0.47	99.21
31	087 PIC 355 SPOT 1 AMP	48.69	0.18	4.50	0.00	19.92	0.13	9.65	12.93	0.61	0.70	0.00	0.00	0.29	1.82	99.42	0.07	99.36
32	087 PIC 355 SPOT 2 AMP BRIGHT	43.89	0.33	7.91	1.30	22.02	0.18	7.01	12.32	0.82	1.43	0.00	0.79	0.93	1.23	100.16	0.54	99.62
33	087 PIC 355 SPOT 3 AMP BRIGHT	45.80	0.19	6.55	0.65	21.66	0.05	8.55	12.78	0.93	1.23	0.00	0.00	0.70	1.70	100.79	0.16	100.63
34	087 PIC 355 SPOT 4 AMP DARK	50.13	0.14	3.91	0.00	20.09	0.12	10.01	12.67	0.61	0.72	0.04	0.00	0.28	1.85	100.57	0.06	100.51
35	087 PIC 356 SPOT 2 MAIN AMP	40.39	0.57	11.87	3.87	19.78	0.12	6.42	12.21	1.07	1.85	0.02	0.00	1.25	1.54	100.96	0.28	100.68
36	087 PIC 356 SPOT 3 ATTENUATED AMP	40.07	0.26	11.56	1.89	21.59	0.06	5.96	12.73	1.25	1.05	0.00	0.25	2.24	1.13	100.04	0.61	99.43

Appendix 3B - Amphibole Mineral Chemical Analysis
Atomic Proportions

No.	DESCRIPTION	Si	Al IV	Al VI	Ti	Cr	Fe 3+	Fe 2+	Mn	Mg	Ca	Na	K	F	Cl	OH	Total	O
1	*******11W PIC 337 SPOT 3 BRIGHT OUTSIDE	6.765	1.235	0.630	0.086	0.001	0.000	3.618	0.014	1.035	2.328	0.479	0.526	0.112	0.499	1.390	18.718	24.000
2	11W PIC 337 SPOT 4 ADJ DARK OUTSIDE VEIN	8.081	0.000	0.265	0.017	0.006	0.000	2.982	0.005	2.180	2.167	0.077	0.048	0.065	0.005	1.930	17.829	24.000
3	11W PIC 337 SPOT 5 ADJ DARK OUTSIDE VEIN	7.884	0.116	0.341	0.010	0.000	0.134	3.121	0.015	1.945	2.148	0.137	0.057	0.198	0.016	1.785	17.908	24.000
4	11W PIC 337 SPOT 6	6.742	1.258	0.717	0.083	0.004	0.000	3.797	0.007	0.952	2.131	0.471	0.517	0.138	0.437	1.425	18.680	24.000
5	11W PIC 338 SPOT 1 AMPH ADJ TO Th-Si	7.759	0.241	0.331	0.013	0.000	0.000	3.263	0.015	1.861	2.185	0.350	0.199	0.000	0.093	1.907	18.216	24.000
6	11W PIC 338 SPOT 4 AMP	7.793	0.207	0.497	0.018	0.000	0.000	3.135	0.000	1.904	2.071	0.285	0.137	0.000	0.122	1.878	18.048	24.000
7	11W PIC 338 SPOT 5 AMP BRIGHTER	6.850	1.150	0.578	0.046	0.000	0.148	3.707	0.011	1.075	2.101	0.503	0.496	0.011	0.158	1.832	18.666	24.000
8	11W PIC 338 SPOT 9 AMP	7.659	0.341	0.532	0.005	0.008	0.032	3.239	0.000	1.749	2.076	0.313	0.165	0.025	0.071	1.903	18.118	24.000
9	11W PIC 339 SPOT 1 DARK AMP	7.718	0.282	0.226	0.022	0.003	0.352	2.929	0.010	2.024	2.111	0.211	0.094	0.000	0.087	1.913	17.982	24.000
10	11W PIC 339 SPOT 2 BRIGHT AMP	6.952	1.048	0.562	0.067	0.001	0.035	3.654	0.020	1.226	2.153	0.449	0.430	0.032	0.148	1.820	18.598	24.000
11	11W PIC 339 SPOT 3 DARK AMP	7.572	0.428	0.539	0.029	0.003	0.000	3.267	0.011	1.629	2.140	0.373	0.218	0.010	0.055	1.934	18.209	24.000
12	11W PIC 339 SPOT 4 BRIGHT AMP	7.121	0.879	0.546	0.080	0.009	0.038	3.611	0.010	1.280	2.093	0.421	0.397	0.000	0.194	1.806	18.477	24.000
13	11W PIC 339 SPOT 5 BRIGHT AMP	7.250	0.750	0.646	0.060	0.009	0.000	3.454	0.007	1.302	2.140	0.374	0.366	0.010	0.017	1.973	18.358	24.000
14	******088 PIC 345 SPOT 1 AMP	8.252	0.000	0.278	0.005	0.013	0.000	2.670	0.020	2.284	2.000	0.105	0.047	0.000	0.000	2.000	17.673	24.000
15	088 PIC 345 SPOT 2 AMP	7.890	0.110	0.302	0.002	0.006	0.188	2.895	0.020	2.151	2.141	0.117	0.079	0.005	0.035	1.960	17.902	24.000
16	088 PIC 346 SPOT 4 AMP CLAST	8.176	0.000	0.240	0.000	0.000	0.000	3.121	0.015	1.882	2.202	0.096	0.041	0.000	0.000	2.000	17.772	24.000
17	088 PIC 346 SPOT 5 AMP CLAST	7.669	0.331	0.507	0.011	0.000	0.181	3.100	0.027	1.741	2.009	0.345	0.128	0.010	0.016	1.974	18.048	24.000
18	088 PIC 346 SPOT 6 AMP IN VEIN	8.161	0.000	0.294	0.000	0.004	0.000	2.890	0.000	2.109	2.162	0.097	0.042	0.005	0.026	1.969	17.759	24.000
19	******085C PIC 340 SPOT 5 AMP W INCL	8.064	0.000	0.391	0.000	0.002	0.000	3.159	0.009	1.828	2.188	0.141	0.054	0.000	0.000	2.000	17.837	24.000
20	085C PIC 341 SPOT 1 - AMP	8.296	0.000	0.108	0.000	0.000	0.000	3.487	0.023	1.593	2.124	0.022	0.016	0.178	0.014	1.809	17.669	24.000
21	085C PIC 341 SPOT 4 AMP	8.161	0.000	0.290	0.000	0.000	0.000	3.286	0.024	1.676	2.171	0.095	0.073	0.000	0.027	1.973	17.778	24.000
22	085C SPOT B ON MAP - AMP	7.839	0.161	0.490	0.011	0.006	0.000	3.483	0.007	1.553	2.092	0.258	0.097	0.000	0.000	2.000	17.999	24.000
23	085C SPOT C ON MAP	8.272	0.000	0.254	0.010	0.000	0.000	3.237	0.001	1.622	2.125	0.086	0.053	0.020	0.016	1.964	17.661	24.000
24	085C SPOT D ON MAP	7.888	0.112	0.458	0.006	0.003	0.000	3.275	0.005	1.659	2.219	0.263	0.126	0.010	0.027	1.962	18.014	24.000
25	******085C PIC 341 SPOT 2 - AMP	8.443	0.000	0.303	0.012	0.000	0.000	2.144	0.000	4.309	0.114	0.069	0.068	0.243	0.013	1.744	17.462	24.000
26	085C PIC 341 SPOT 2 - AMP	8.547	0.000	0.169	0.003	0.001	0.000	2.153	0.005	4.400	0.041	0.065	0.024	0.097	0.007	1.895	17.409	24.000
27	085C PIC 341 SPOT 6	8.456	0.000	0.271	0.002	0.000	0.000	2.046	0.009	4.447	0.104	0.073	0.070	0.041	0.000	1.959	17.478	24.000
28	******087 PIC 351 SPOT 1 AMP DARK DOM	7.843	0.157	0.499	0.005	0.004	0.261	2.400	0.031	2.366	1.992	0.150	0.120	0.000	0.066	1.934	17.827	24.000
29	087 PIC 351 SPOT 2 AMP BRIGHT DOMAIN	7.738	0.262	0.553	0.010	0.000	0.000	2.800	0.013	2.181	2.107	0.207	0.152	0.000	0.113	1.887	18.025	24.000
30	087 PIC 351 SPOT 3 AMP BRIGHT DOMAIN	6.674	1.326	0.794	0.034	0.005	0.052	3.324	0.011	1.344	2.194	0.354	0.534	0.000	0.591	1.409	18.647	24.000
31	087 PIC 355 SPOT 1 AMP	7.706	0.294	0.545	0.021	0.000	0.000	2.636	0.017	2.277	2.192	0.187	0.141	0.000	0.078	1.922	18.018	24.000
32	087 PIC 355 SPOT 2 AMP BRIGHT	7.142	0.858	0.659	0.040	0.000	0.136	3.004	0.025	1.701	2.148	0.259	0.297	0.407	0.256	1.337	18.269	24.000
33	087 PIC 355 SPOT 3 AMP BRIGHT	7.309	0.691	0.541	0.023	0.000	0.066	2.895	0.007	2.034	2.185	0.288	0.250	0.000	0.189	1.811	18.288	24.000
34	087 PIC 355 SPOT 4 AMP DARK	7.819	0.181	0.537	0.016	0.005	0.000	2.620	0.016	2.327	2.117	0.184	0.143	0.000	0.074	1.926	17.967	24.000
35	087 PIC 356 SPOT 2 MAIN AMP	6.548	1.452	0.816	0.070	0.003	0.404	2.706	0.016	1.552	2.121	0.336	0.383	0.000	0.343	1.657	18.405	24.000
36	087 PIC 356 SPOT 3 ATTENUATED AMP	6.615	1.385	0.865	0.032	0.000	0.201	2.993	0.008	1.467	2.252	0.400	0.221	0.131	0.627	1.243	18.438	24.000

Appendix 3C - Biotite Mineral Chemical Analysis
Oxide Weight Percent

No.	DESCRIPTION	SiO2	TiO2	Al2O3	Cr2O3	FeO	MnO	MgO	K2O	CaO	Na2O	F	Cl	BaO	TOTAL	-0= F+Cl	TOTAL
1	******27W PIC 307 SPOT 1 CORE TI-BT	35.86	3.03	13.29	0	25.89	0	7.42	8.9	0.02	0.02	0	0.76	0.02	95.21	0.17	95.04
2	27W PIC 307 SPOT 2 BRIGHTEST	36.39	2.36	13.79	0	25.75	0	7.76	8.56	0	0.07	0.29	0.78	0.06	95.81	0.3	95.51
3	27W PIC 307 SPOT 3 DARKEST	33.05	1.74	16.7	0.09	25.61	0	8.14	9.31	0.02	0.14	0.23	0.8	0	95.83	0.28	95.55
4	27W PIC 307 SPOT 5 FG BT INT W ORTH	35.15	1.46	15.09	0	24.9	0.04	8.2	9.55	0.02	0.02	0	0.71	0.1	95.24	0.16	95.08
5	27W PIC 313 SPOT 3 TI-BT	35.01	2.64	15.75	0	25.94	0	7.74	8.86	0	0.05	0	0.6	0.02	96.61	0.14	96.47
6	27W PIC 315 SPOT 1 CORE TI-BT	34.76	2.61	14.69	0.04	26.44	0.02	7.45	9.06	0	0.03	0	0.76	0.09	95.95	0.17	95.78
7	27W PIC 316 SPOT 1 TI-BT	35.22	2.96	14.04	0.03	26.74	0	7.52	9.31	0.04	0.05	0.01	0.22	0.15	96.29	0.05	96.24
8	27W PIC 316 SPOT 2 TI-BT MARGIN	34.48	2.19	14.84	0	26.29	0.03	8.07	9.11	0	0	0.05	0	0.22	95.28	0.02	95.26
9	27W AGAIN RANDOM FG GMASS BT	35.66	1.6	13.67	0.02	26.58	0.02	8.55	8.81	0	0.05	0	0.02	0.09	95.05	0	95.05
10	27W AGAIN RANDOM FG GMASS BT	35.96	1.55	14.15	0.01	25.87	0	9.04	8.58	0	0.03	0.07	0	0.05	95.32	0.03	95.29
11	27W AGAIN RANDOM CG BT PHENO	35.57	2.84	14.28	0	26.02	0	7.41	8.97	0.01	0.05	0.38	0.02	0.08	95.64	0.16	95.48
12	******04E PIC 322 SPOT 2 TIBT	35.36	1.77	14.39	0	29.48	0.09	9.16	6.23	0	0.08	0	0.25	0.24	97.05	0.06	96.99
13	04E PIC 323 SPOT 1 TIBT	35.46	2.69	13.14	0	26.4	0.01	7.85	9.46	0	0.08	0.01	0.33	0.16	95.59	0.08	95.51
14	******11W PINK BAND MICA	35.91	1.47	13.73	0.05	25.98	0.05	7.89	9.87	0.04	0.03	0	0.16	0.32	95.5	0.04	95.46
15	11W PINK BAND MICA	35.8	1.52	13.9	0.09	26.43	0.08	7.17	10.13	0.01	0.06	0.01	0.02	0.15	95.37	0.01	95.36
16	******08W PIC 347 SPOT 8 MICA	35.16	1.05	15.16	0.07	27.68	0.08	8.51	7.53	0	0	0	0	0.39	95.63	0	95.63
17	08W RANDOM MICA BRIGHT	35.08	1.18	14.82	0.03	28.58	0.03	7.55	9.02	0	0.02	0	0	0.02	96.33	0	96.33

Appendix 3C - Biotite Mineral Chemical Analysis
Atomic Proportions

No.	DESCRIPTION	Si	Al4	Al6	Ti	Cr	Fe	Mn	Mg	K	Ca	Ba	Na	F	Cl	O
1	******27W PIC 307 SPOT 1 CORE TI-BT	5.681	2.319	0.163	0.361	0	3.43	0	1.752	1.798	0.003	0.001	0.006	0	0.204	22
2	27W PIC 307 SPOT 2 BRIGHTEST	5.699	2.301	0.243	0.278	0	3.372	0	1.811	1.71	0	0.004	0.021	0.144	0.207	22
3	27W PIC 307 SPOT 3 DARKEST	5.229	2.771	0.343	0.207	0.011	3.389	0	1.92	1.879	0.003	0	0.043	0.115	0.215	22
4	27W PIC 307 SPOT 5 FG BT INT W ORTH	5.562	2.438	0.376	0.174	0	3.295	0.005	1.934	1.927	0.003	0.006	0.006	0	0.19	22
5	27W PIC 313 SPOT 3 TI-BT	5.451	2.549	0.341	0.309	0	3.378	0	1.796	1.76	0	0.001	0.015	0	0.158	22
6	27W PIC 315 SPOT 1 CORE TI-BT	5.494	2.506	0.23	0.31	0.005	3.495	0.003	1.755	1.826	0	0.006	0.009	0	0.204	22
7	27W PIC 316 SPOT 1 TI-BT	5.55	2.45	0.157	0.351	0.004	3.524	0	1.766	1.871	0.007	0.009	0.015	0.005	0.059	22
8	27W PIC 316 SPOT 2 TI-BT MARGIN	5.476	2.524	0.254	0.262	0	3.492	0.004	1.91	1.846	0	0.014	0	0.025	0	22
9	27W AGAIN RANDOM FG GMASS BT	5.66	2.34	0.217	0.191	0	3.528	0.003	2.023	1.784	0	0.006	0.015	0	0.005	22
10	27W AGAIN RANDOM FG GMASS BT	5.649	2.351	0.269	0.183	0.002	3.399	0	2.117	1.719	0	0.003	0.009	0.035	0	22
11	27W AGAIN RANDOM CG BT PHENO	5.593	2.407	0.239	0.336	0.001	3.422	0	1.737	1.799	0.002	0.005	0.015	0.189	0.005	22
12	******04E PIC 322 SPOT 2 TIBT	5.495	2.505	0.13	0.207	0	3.831	0.012	2.122	1.235	0	0.015	0.024	0	0.066	22
13	04E PIC 323 SPOT 1 TIBT	5.634	2.366	0.095	0.321	0	3.508	0.001	1.859	1.917	0	0.01	0.025	0.005	0.089	22
14	******11W PINK BAND MICA	5.703	2.297	0.272	0.176	0.006	3.45	0.007	1.868	1.999	0.007	0.02	0.009	0	0.043	22
15	11W PINK BAND MICA	5.705	2.295	0.315	0.182	0.011	3.522	0.011	1.703	2.059	0.002	0.009	0.019	0.005	0.005	22
16	******08W PIC 347 SPOT 8 MICA	5.539	2.461	0.353	0.124	0.009	3.647	0.011	1.998	1.513	0	0.024	0	0	0	22
17	08W RANDOM MICA BRIGHT	5.547	2.453	0.308	0.14	0.004	3.779	0.004	1.779	1.819	0	0.001	0.006	0	0	22

Appendix 3D - Chlorite Mineral Chemical Analysis
Oxide Weight Percent

No.	DESCRIPTION	SiO2	TiO2	Al2O3	FeO	MnO	MgO	CaO	Na2O	K2O	Cr2O3	TOTAL
1	******27W PIC 313 SPOT 4 TI-BT ALTERED	33.99	3.27	21.36	14.82	0.09	12.57	0.22	0.02	1.43	0.1	87.87
2	27W PIC 314 SPOT 3 CHL ON MARGIN OF BT	26.67	0.28	17.91	31.57	0.06	10.54	0.07	0	0.42	0.02	87.54
3	******04E PIC 319 SPOT 6 CHL	25.51	0.05	18.51	32.1	0.08	11.49	0	0.04	0.07	0	87.85
4	04E PIC 322 SPOT 1 TIBT ALTERED TO CHL	27.78	0.24	15.96	30.93	0.09	11.82	0	0	0.55	0.02	87.39
5	04E PIC 323 SPOT 2 CHL MARGIN	26.79	0.15	15.6	32.53	0.18	12.03	0.01	0	0.17	0.04	87.5
6	******05E PIC 331 SPOT 2 CHL IN ORTHO	27.65	0.15	17.87	27.83	0.11	13.66	0.02	0.07	0.64	0.02	88.02
7	05E PIC 331 SPOT 3 CHL IN ORTHO	24.32	0.1	20.44	30.66	0.11	12.21	0	0.01	0.04	0	87.89
8	05E PIC 333 SPOT 1 CHL BT	27.03	0.35	19.34	25.06	0.05	15.31	0.11	0	0.11	0.06	87.42
9	******05W AREA "A" SLIDE 1 SPOT 3	28.38	0.03	20.21	27.17	0.12	9.74	1.84	0.07	0.11	0.06	87.73
10	******05W2 PIC 334 SPOT 6 CHL	26.63	0	17.07	31.79	0.03	11.92	0	0	0.06	0.05	87.55
11	05W2 PIC 334 SPOT 7 CHL	27.99	0.03	17.46	31.71	0.08	11.53	0.08	0	0.06	0.03	88.97
12	05W2 PIC 335 SPOT 1 CHL WITH FG SPHENE	26.3	0.02	18.38	31.52	0.09	11.55	0.1	0.06	0.07	0.01	88.1
13	05W2 CHL VEINLET	26.7	0.01	17.68	32.26	0.04	11.37	0	0	0.05	0	88.11
14	******085C PIC 340 SPOT 4 CHL-BT IN	27.34	0.57	15.93	32.93	0.14	8.99	0.13	0.05	1.66	0.04	87.78
15	******08W PIC 347 SPOT 8 CHL DARK DOMAI	28.83	1.14	15.1	29.03	0.06	8.43	0.21	0.17	4.27	0.19	87.43
16	08W RANDOM MICA DARK = CHL	28.47	0.55	16.14	30.45	0.21	8.44	0	0.08	3.09	0.07	87.5
17	******087 PIC 349 SPOT 6 CHL	28.28	0.02	15.11	34.19	0.1	9.89	0	0.02	0.45	0.03	88.09
18	087 PIC 356 SPOT 1 CHL MARGIN	27.06	0.01	17.58	32.87	0.08	9.71	0.03	0.03	0.09	0	87.46
19	087 PIC 356 SPOT 4 CHL	27.56	0.09	16.42	33.12	0.07	9.93	0.03	0.06	0.07	0.02	87.37
20	******155 AREA A' SLIDE 2 SPOT 2	28.57	0.06	18.81	26.26	0.20	13.10	0.05	0.06	0.10	0.00	87.21
21	155 AREA "B" CHLORITE	29.94	0.02	16.93	23.38	0.02	17.61	0.09	0.00	0.05	0.03	88.07
22	******144 AREA "B" CHLORITE SLIDE 5 W INCL OF ILM - DARK DOMAIN	28.77	0.11	18.78	27.53	0.33	12.21	0.05	0.00	0.05	0.03	87.86
23	144 AREA "B" CHLORITE SLIDE 5 - BRIGHT DOMAINS	28.20	0.27	21.60	27.73	0.53	9.56	0.00	0.02	0.04	0.00	87.95
24	144 AREA "B" CHLORITE SLIDE 5 - ANOTHER DARK DOMAIN	28.89	0.03	18.22	27.50	0.13	12.88	0.03	0.00	0.07	0.00	87.75

Appendix 3D - Chlorite Mineral Chemical Analysis
Oxide Weight Percent

No.	DESCRIPTION	Si	Al 4	Al 6	Ti	Cr	Fe 3+	Fe 2+	Mn	Mg	Ca	Na	K	O
1	*****27W PIC 313 SPOT 4 TI-BT ALTERED	6.443	1.557	3.367	0.466	0.015	1.373	0.976	0.014	3.552	0.045	0.015	0.692	28
2	27W PIC 314 SPOT 3 CHL ON MARGIN OF BT	5.810	2.190	2.429	0.046	0.003	0.134	5.617	0.011	3.423	0.016	0.000	0.233	28
3	*****04E PIC 319 SPOT 6 CHL	5.571	2.429	2.346	0.008	0.000	0.000	5.903	0.015	3.741	0.000	0.034	0.039	28
4	04E PIC 322 SPOT 1 TIBT ALTERED TO CHL	6.046	1.954	2.159	0.039	0.003	0.094	5.537	0.017	3.835	0.000	0.000	0.305	28
5	04E PIC 323 SPOT 2 CHL MARGIN	5.898	2.102	1.957	0.025	0.007	0.000	6.041	0.034	3.948	0.002	0.000	0.095	28
6	*****05E PIC 331 SPOT 2 CHL IN ORTHO	5.865	2.135	2.355	0.024	0.003	0.062	4.876	0.020	4.320	0.005	0.058	0.346	28
7	05E PIC 331 SPOT 3 CHL IN ORTHO	5.264	2.736	2.498	0.016	0.000	0.000	5.642	0.020	3.940	0.000	0.008	0.022	28
8	05E PIC 333 SPOT 1 CHL BT	5.679	2.321	2.483	0.055	0.010	0.144	4.259	0.009	4.795	0.025	0.000	0.059	28
9	*****05W AREA "A" SLIDE 1 SPOT 3	5.955	2.045	3.006	0.005	0.010	0.518	4.251	0.021	3.047	0.414	0.057	0.059	28
10	*****05W2 PIC 334 SPOT 6 CHL	5.824	2.176	2.229	0.000	0.009	0.027	5.788	0.006	3.886	0.000	0.000	0.033	28
11	05W2 PIC 334 SPOT 7 CHL	5.968	2.032	2.373	0.005	0.005	0.191	5.464	0.014	3.665	0.018	0.000	0.033	28
12	05W2 PIC 335 SPOT 1 CHL WITH FG SPHENE	5.700	2.300	2.402	0.003	0.002	0.041	5.672	0.017	3.731	0.023	0.050	0.039	28
13	05W2 CHL VEINLET	5.801	2.199	2.336	0.002	0.000	0.072	5.790	0.007	3.683	0.000	0.000	0.028	28
14	*****085C PIC 340 SPOT 4 CHL-BT IN	6.019	1.981	2.190	0.094	0.007	0.011	6.052	0.026	2.950	0.031	0.043	0.932	28
15	*****08W PIC 347 SPOT 8 CHL DARK DOMAI	6.233	1.767	2.179	0.185	0.032	0.000	5.317	0.011	2.717	0.049	0.143	2.355	28
16	08W RANDOM MICA DARK= CHL	6.189	1.811	2.395	0.090	0.012	0.041	5.495	0.039	2.735	0.000	0.067	1.714	28
17	*****087 PIC 349 SPOT 6 CHL	6.202	1.798	2.126	0.003	0.005	0.132	6.139	0.019	3.233	0.000	0.017	0.252	28
18	087 PIC 356 SPOT 1 CHL MARGIN	5.923	2.077	2.478	0.002	0.000	0.208	5.809	0.015	3.168	0.007	0.025	0.050	28
19	087 PIC 356 SPOT 4 CHL	6.049	1.951	2.316	0.015	0.003	0.202	5.877	0.013	3.249	0.007	0.051	0.039	28
20	*****155 AREA A' SLIDE 2 SPOT 2	6.000	2.000	2.691	0.009	0.000	0.372	4.240	0.036	4.101	0.011	0.049	0.054	28
21	155 AREA "B" CHLORITE	6.145	1.855	2.259	0.003	0.005	0.227	3.787	0.003	5.388	0.020	0.000	0.026	28
22	*****144 AREA "B" CHLORITE SLIDE 5 W.INCL OF ILM-DARK DOM	6.030	1.970	2.707	0.017	0.005	0.426	4.400	0.059	3.815	0.011	0.000	0.027	28
23	144 AREA "B" CHLORITE SLIDE 5 - BRIGHT DOMAINS	5.869	2.131	3.232	0.042	0.000	0.647	4.180	0.093	2.966	0.000	0.016	0.021	28
24	144 AREA "B" CHLORITE SLIDE 5 - ANOTHER DARK DOMAIN	6.066	1.934	2.607	0.005	0.000	0.372	4.457	0.023	4.031	0.007	0.000	0.037	28

Appendix 3E - Epidote Mineral Chemical Analysis
Oxide Weight Percent

No.	DESCRIPTION	SiO2	TiO2	Al2O3	Cr2O3	FeO	MgO	MnO	K2O	CaO	Na2O	TOTAL
1	*******27W PIC 317 SPOT 4 EPIDOTE	37.01	0	30.79	0	5.71	0.01	0.11	0.16	23.79	0	97.58
2	******"05W AREA "A" SLIDE 1 SPOT 4 EPIDOTE	38.87	0.34	25.42	0.00	11.44	0.00	0.00	0.05	22.57	0.03	98.72

Appendix 3E - Epidote Mineral Chemical Analysis
Atomic Proportions

No.	DESCRIPTION	Si	Al 4	Al 6	Ti	Cr	Fe	Mn	Mg	Ca	K	Na	O	X	Y
1	*******27W PIC 317 SPOT 4 EPIDOTE	3.026	0.000	2.967	0.000	0.000	0.390	0.001	0.013	2.084	0.017	0.000	13.000	3.026	5.473
2	******"05W AREA "A" SLIDE 1 SPOT 4 EPIDOTE	3.218	0.000	2.480	0.021	0.000	0.792	0.000	0.000	2.002	0.005	0.005	13.000	3.218	5.306

Appendix 3F - Apatite Mineral Chemical Analysis
Atomic Proportions

No.	DESCRIPTION	F	Na2O	MgO	Al2O3	SiO2	P2O5	Cl	CaO	FeO	SrO	La2O3
1	139A GRAIN OF APATITE + MAGNETITE	0.00	0.10	0.00	0.01	0.04	40.95	0.25	56.68	0.31	0.00	0.37
2	139A ANOTHER RANDOM APATITE	0.00	0.06	0.00	0.00	0.01	41.52	0.16	56.83	0.21	0.00	0.16

		Ce2O3	Nd2O3	Sm2O3	Y2O3	Pr2O3	ThO2	TOTAL
1	139A GRAIN OF APATITE + MAGNETITE	0.00	0.04	0.04	0.15	0.05	0.06	99.05
2	139A ANOTHER RANDOM APATITE	0.00	0.06	0.00	0.04	0.01	0.01	99.07

Appendix 3G - Rutile Mineral Chemical Analysis
Atomic Proportions

No.	DESCRIPTION	SiO2	TiO2	Al2O3	Cr2O3	FeO	MnO	MgO	ZnO	NiO	Nb2O5	TOTAL
1	155 RUTILE IN MELANO DOMAIN - CENTER OF GRAIN	0.01	98.61	0.00	0.12	0.86	0.00	0.60	0.00	0.00	0.70	100.90
2	139A RUTILE INTERGROWN WITH TI-MT	0.11	99.02	0.00	0.00	1.37	0.05	0.00	0.00	0.01	0.07	100.63

Appendix 4 – Matrix of correlation coefficients determined for a feldspar porphyry (Part 1).

	SiO₂	TiO₂	Al₂O₃	Fe₂O₃T	MnO	MgO	CaO	Na₂O	K₂O	P₂O₅	LOI	Sc	V	Cr	Cu	Zn	Rb
SiO₂	-																
TiO₂	-0.8452	-															
Al₂O₃	-0.7899	0.8371	-														
Fe₂O₃T	-0.9433	**0.9106**	0.7630	-													
MnO	-0.3945	0.4538	0.1519	0.3999	-												
MgO	-0.7415	0.5504	0.2689	0.7395	0.6308	-											
CaO	-0.0598	0.2379	0.0170	0.0956	0.4989	0.3552	-										
Na₂O	0.0108	0.4509	0.2764	0.2161	0.0342	-0.0961	0.4851	-									
K₂O	-0.1286	-0.2317	0.1257	-0.1328	-0.3398	-0.2088	-0.6545	-0.7897	-								
P₂O₅	-0.1708	0.5071	0.3672	0.3530	0.2614	0.1925	0.2249	0.6111	-0.5521	-							
LOI	-0.6332	0.3149	0.1721	0.5193	0.6437	**0.8947**	0.2592	-0.4369	0.0983	0.0558	-						
Sc	-0.7231	**0.9559**	0.8067	0.8082	0.2830	0.3230	0.1296	0.5369	-0.1998	0.4531	-0.2147	-					
V	-0.0398	0.4384	0.1505	0.2999	0.1700	0.0933	0.0333	0.5714	-0.5519	0.8113	-0.1676	0.4798	-				
Cr	0.0841	0.2020	0.1692	0.1192	0.2945	-0.0083	0.2370	0.5242	-0.6043	0.6918	0.2963	0.1493	0.4914	-			
Cu	0.0452	-0.0150	-0.3321	0.0739	0.2673	0.4528	0.1661	0.0006	-0.3970	0.4273	0.3607	-0.1336	0.4154	0.2024	-		
Zn	-0.6008	0.3625	0.1288	0.5803	0.6857	**0.9038**	0.1734	-0.3122	-0.0741	0.1439	0.8602	0.1207	0.0865	0.0209	0.3829	-	
Rb	-0.1069	0.3389	0.2214	0.1783	-0.2897	-0.1815	0.0847	0.4585	-0.1188	0.0418	-0.5981	0.5129	0.3263	-0.2468	-0.4077	-0.3088	-
Sr	-0.0718	0.3273	0.3610	0.1517	0.2005	-0.0066	0.6019	0.6532	-0.5459	0.5120	-0.2109	0.2782	0.2076	0.6128	-0.2427	-0.0818	0.2435
Y	-0.5452	0.7926	0.6189	0.6004	0.2444	0.1449	0.1883	0.5709	-0.2228	0.2177	-0.1661	**0.8953**	0.2538	0.0687	-0.2693	-0.0926	0.5388
Zr	-0.7375	**0.9058**	0.7493	0.7432	0.4654	0.4860	0.4184	0.3914	-0.1856	0.4532	0.2320	**0.8601**	0.3505	0.1188	-0.0120	0.2688	0.4120
Nb	-0.7335	0.8234	**0.8787**	0.7419	0.2957	0.2643	0.1189	0.4026	-0.0730	0.3211	-0.0223	0.8117	0.1040	0.3271	-0.3836	0.1334	0.2285
Cs	-0.2094	0.3410	0.2108	0.2816	-0.2609	0.0079	0.1357	0.4996	-0.2272	0.0602	-0.3268	0.4542	0.2079	-0.1480	-0.4008	-0.1257	**0.8611**
Ba	0.0597	-0.4130	-0.1575	-0.2709	0.0412	-0.1215	-0.4502	-0.8849	0.7609	-0.5887	0.0353	-0.4602	-0.5561	-0.3087	-0.2890	0.1652	-0.3784
La	-0.3920	0.8059	0.6436	0.5672	0.2492	0.1130	0.3307	**0.8574**	-0.5598	0.7020	-0.2150	**0.8605**	0.6488	0.4759	-0.0529	-0.0844	0.4747
Ce	-0.3853	0.7994	0.6270	0.5684	0.2330	0.1018	0.3121	**0.8637**	-0.5661	0.6661	-0.2335	**0.8648**	0.6425	0.4587	-0.0724	-0.0980	0.4977
Pr	-0.3985	0.8045	0.6426	0.5799	0.2309	0.0934	0.2885	0.8473	-0.5427	0.6477	-0.2442	**0.8734**	0.6328	0.4738	-0.1185	-0.0930	0.5174
Nd	-0.4101	0.8096	0.6545	0.5837	0.2208	0.0819	0.2595	0.8292	-0.5088	0.6304	-0.2526	**0.8844**	0.6233	0.4485	-0.1475	-0.0987	0.5374
Sm	-0.3378	0.7587	0.5533	0.5283	0.2433	0.0534	0.2818	0.8350	-0.5560	0.5839	-0.2972	**0.8516**	0.6357	0.4598	-0.1393	-0.1122	0.5760
Eu	-0.2830	0.7317	0.5486	0.4723	0.2378	0.0335	0.3685	**0.8962**	-0.6161	0.6662	-0.3013	0.8082	0.6438	0.5169	-0.0856	-0.1555	0.5121
Gd	-0.2916	0.7158	0.4702	0.4782	0.2124	0.0286	0.2885	0.8379	-0.5625	0.5050	-0.3424	0.8308	0.6056	0.3626	-0.1444	-0.1561	0.6355
Tb	-0.3447	0.7406	0.5160	0.5079	0.2636	0.0385	0.2486	0.7673	-0.4856	0.4662	-0.3114	**0.8524**	0.5496	0.3744	-0.1847	-0.1297	0.5929
Dy	-0.5205	0.8309	0.6400	0.6301	0.2717	0.1360	0.1628	0.6604	-0.3275	0.3997	-0.2103	**0.9269**	0.4477	0.2321	-0.2369	-0.0462	0.5680
Ho	-0.5849	**0.8542**	0.6483	0.6710	0.2954	0.2094	0.1762	0.5938	-0.2725	0.3132	-0.1347	**0.9428**	0.3767	0.1168	-0.1932	-0.0112	0.5333
Er	-0.6383	0.7372	0.5638	0.6152	0.3645	0.2755	0.0811	0.2451	0.0140	0.0066	0.0334	0.8047	0.0560	-0.1077	-0.2019	0.0767	0.3333
Tm	-0.7627	0.6579	0.5956	0.6463	0.5313	0.4430	0.0069	-0.1263	0.2563	-0.1751	0.3490	0.6192	-0.2057	-0.1956	-0.2747	0.3578	0.0242
Yb	-0.7174	0.5018	0.4959	0.5541	0.3452	0.4037	-0.0676	-0.2732	0.4209	-0.4054	0.3217	0.4804	-0.4010	-0.3874	-0.3777	0.3245	0.0625
Lu	-0.3182	-0.0006	-0.1512	0.1417	0.4257	0.4723	0.0241	-0.5988	0.3587	-0.6331	0.4484	-0.0864	-0.5150	-0.5749	0.0248	0.4760	-0.2488
Hf	-0.6802	**0.8509**	0.7771	0.6768	0.4960	0.3711	0.3512	0.3537	-0.1165	0.3790	0.0927	0.8136	0.2887	0.2365	-0.2592	0.2396	0.3681
Ta	0.5771	-0.8245	-0.3967	-0.7412	-0.5435	-0.6079	-0.3861	-0.5181	0.5447	-0.5149	-0.4501	-0.7923	-0.6643	-0.1844	-0.3122	-0.4318	-0.4176
Th	**0.9185**	-0.9354	-0.7363	-0.9584	-0.3919	-0.7256	-0.1870	-0.2833	0.1659	-0.4000	-0.7353	-0.8480	-0.3440	-0.0192	-0.1156	-0.5154	-0.3007
U	**0.8574**	-0.9430	-0.6619	-0.9357	-0.5563	-0.7550	-0.3138	-0.3425	0.3048	-0.4163	-0.6734	-0.8525	-0.4248	-0.1063	-0.1743	-0.5649	-0.2735

Appendix 4 – Matrix of correlation coefficients determined for a feldspar porphyry (Part 2).

	Nb	Cs	Ba	La	Ce	Pr	Nd	Sm	Eu	Gd	Tb	Dy	Ho	Er	Tm	Yb	Lu
SiO₂																	
TiO₂																	
Al₂O₃																	
Fe₂O₃T																	
MnO																	
MgO																	
CaO																	
Na₂O																	
K₂O																	
P₂O₅																	
LOI																	
Sc																	
V																	
Cr																	
Cu																	
Zn																	
Rb																	
Sr																	
Y																	
Zr																	
Nb	-																
Cs	0.3285	-															
Ba	-0.2050	-0.4954	-														
La	0.7031	0.4399	-0.7133	-													
Ce	0.7015	0.4661	-0.7182	0.9975	-												
Pr	0.7324	0.4895	-0.6791	0.9926	0.9965	-											
Nd	0.7439	0.5040	-0.6564	0.9888	0.9934	0.9988	-										
Sm	0.7002	0.5333	-0.6406	0.9619	0.9725	0.9837	0.9848	-									
Eu	0.6614	0.4772	-0.7187	0.9860	0.9877	0.9879	0.9832	0.9801	-								
Gd	0.6368	0.5915	-0.6717	0.9337	0.9505	0.9582	0.9608	0.9874	0.9621	-							
Tb	0.7088	0.5410	-0.5675	0.9124	0.9286	0.9446	0.9506	0.9825	0.9412	0.9870	-						
Dy	0.7995	0.5489	-0.5085	0.8871	0.9027	0.9176	0.9300	0.9366	0.8856	0.9428	0.9675	-					
Ho	0.7786	0.4963	-0.4907	0.8410	0.8585	0.8667	0.8788	0.8802	0.8267	0.8968	0.9238	0.9817	-				
Er	0.7161	0.2975	-0.1842	0.5486	0.5674	0.5805	0.5990	0.6116	0.5296	0.6430	0.7164	0.8300	0.9003	-			
Tm	0.6760	0.0172	0.1916	0.2739	0.2840	0.3021	0.3234	0.3004	0.2184	0.3006	0.3995	0.5669	0.6553	0.8572	-		
Yb	0.5680	0.1199	0.2811	0.0583	0.0753	0.1014	0.1256	0.1139	0.0128	0.1327	0.2292	0.4182	0.5222	0.7878	0.9329	-	
Lu	-0.1089	-0.2095	0.4394	-0.4491	-0.4330	-0.4326	-0.4223	-0.3968	-0.4680	-0.3319	-0.2758	-0.1415	-0.0017	0.3575	0.6068	0.7132	-
Hf	0.7601	0.3054	-0.1954	0.6942	0.6774	0.7009	0.7094	0.6752	0.6662	0.6297	0.6738	0.7269	0.7283	0.6487	0.6336	0.5047	0.0476
Ta	-0.4460	-0.3796	0.5631	-0.7278	-0.7336	-0.7260	-0.7208	-0.7361	-0.7000	-0.7429	-0.7238	-0.7270	-0.7518	-0.5927	-0.4128	-0.2464	-0.0629
Th	-0.6898	-0.3601	0.3790	-0.6310	-0.6267	-0.6261	-0.6317	-0.5711	-0.5370	-0.5451	-0.5567	-0.6803	-0.7276	-0.6532	-0.6286	-0.5145	-0.1375
U	-0.6508	-0.3003	0.3993	-0.6646	-0.6636	-0.6623	-0.6616	-0.6281	-0.5901	-0.6040	-0.6149	-0.7011	-0.7532	-0.6731	-0.6382	-0.5033	-0.1931

Appendix 5 - Per cent changes to bulk composition for feldspar porphyry samples relative to an average least-altered bulk composition (n = 3).

Sample ID	024W	002E	026W	025W	005W	004E	006E	010W	014E	015E
	(% change to bulk composition from a least altered precursor)									
SiO_2	-0.34%	-1.04%	-8.85%	-1.15%	-1.68%	-0.37%	-15.22%	0.43%	5.17%	17.57%
TiO_2	12.17%	5.29%	-2.90%	2.30%	5.95%	-3.24%	22.71%	-30.84%	-47.31%	-90.85%
Al_2O_3	0.46%	0.76%	-8.46%	0.09%	-0.66%	-2.39%	16.80%	-8.69%	-6.68%	-19.76%
Fe_2O_3T	-14.76%	-3.49%	22.30%	-0.01%	-8.76%	0.07%	35.60%	-22.56%	-47.69%	-84.67%
MnO	80.34%	-17.16%	89.84%	-18.19%	5.21%	71.44%	-19.70%	-29.79%	-8.01%	-74.45%
MgO	-6.97%	1.74%	177.87%	-1.02%	0.75%	3.31%	37.88%	-30.67%	-47.68%	-91.94%
CaO	-4.06%	-0.24%	25.28%	-6.62%	7.61%	-55.67%	-82.00%	-65.95%	0.76%	-76.15%
Na_2O	-31.15%	-6.71%	-92.64%	-36.18%	-37.74%	-69.39%	-96.22%	-77.01%	-90.72%	-93.50%
K_2O	29.01%	21.54%	18.33%	25.89%	41.44%	34.96%	100.75%	62.10%	68.79%	54.71%
P_2O_5	3.97%	-3.97%	-11.90%	-7.94%	-2.38%	-7.14%	-7.14%	-34.92%	-43.65%	-100.00%*
LOI	64.62%	-0.79%	347.90%	6.21%	17.48%	54.99%	147.03%	-18.71%	70.41%	-64.88%
	(% change to bulk composition from a least altered precursor)									
Sc	12.49%	8.03%	-27.35%	3.67%	12.11%	-4.77%	13.82%	-21.85%	-45.08%	-89.95%
V	4.01%	7.92%	-13.33%	5.96%	3.73%	12.81%	-21.99%	-34.58%	-50.09%	-100.00%*
Cr	-22.09%	-42.49%	-42.10%	-35.69%	-37.24%	0.45%	-37.44%	-61.53%	-63.67%	-100.00%*
Cu	19.83%	-62.88%	93.42%	-3.40%	-1.66%	-38.13%	-53.98%	-77.42%	-72.87%	41.97%
Zn	5.11%	20.44%	241.06%	-12.96%	13.32%	109.67%	74.64%	-13.50%	-39.23%	-43.61%
Rb	-9.39%	28.15%	-18.97%	22.55%	25.06%	-0.72%	-8.54%	13.56%	-7.10%	-17.40%
Sr	-39.45%	-11.17%	-74.65%	-7.25%	-26.24%	-42.05%	-48.17%	-64.22%	-80.68%	-85.25%
Y	10.02%	-1.94%	-21.73%	-4.89%	4.94%	-10.58%	-6.23%	4.17%	-17.97%	-53.02%
Zr	20.12%	7.17%	4.86%	22.12%	23.67%	-4.00%	15.81%	-14.17%	-18.07%	-49.84%
Nb	-4.20%	-9.46%	-17.77%	-11.76%	-3.75%	-3.79%	12.00%	-6.40%	-17.88%	-41.75%
Cs	-82.90%	99.65%	-50.93%	-1.57%	45.54%	-40.69%	-39.96%	57.24%	-70.82%	-87.35%
Ba	13.75%	-4.06%	22.81%	17.39%	17.56%	47.99%	42.19%	33.95%	46.22%	34.81%
La	5.38%	-1.57%	-61.27%	-9.63%	-13.80%	-26.42%	-30.20%	-53.47%	-76.32%	-91.23%
Ce	2.12%	-1.95%	-62.13%	-10.19%	-16.39%	-25.29%	-33.36%	-49.35%	-74.56%	-92.54%
Pr	-1.54%	-2.14%	-62.72%	-9.73%	-13.69%	-19.14%	-30.41%	-44.67%	-73.05%	-92.34%
Nd	0.25%	-0.33%	-63.55%	-8.06%	-11.33%	-16.71%	-27.08%	-40.37%	-72.37%	-92.24%
Sm	-3.37%	-4.37%	-60.29%	-8.95%	-4.00%	-9.15%	-38.88%	-32.95%	-67.09%	-88.08%
Eu	2.06%	-2.83%	-69.60%	-11.94%	-11.90%	-24.91%	-46.32%	-49.94%	-77.22%	-93.17%
Gd	0.43%	1.16%	-50.40%	-5.95%	-1.39%	-11.37%	-40.78%	-19.05%	-54.85%	-76.11%
Tb	3.10%	-5.99%	-45.43%	-6.45%	2.90%	-4.13%	-30.67%	-12.57%	-46.67%	-71.71%
Dy	7.58%	-0.70%	-29.86%	-6.55%	3.27%	-4.51%	-9.90%	-2.76%	-33.69%	-59.68%
Ho	9.37%	-0.67%	-18.65%	-3.56%	3.43%	-6.13%	-5.72%	-1.51%	-20.93%	-50.36%
Er	15.05%	-5.14%	-4.23%	-3.77%	9.28%	-1.32%	4.21%	10.79%	-2.79%	-37.85%
Tm	19.88%	-2.52%	10.42%	0.81%	2.57%	11.06%	20.60%	15.13%	9.49%	-32.12%
Yb	10.81%	3.45%	12.67%	-3.17%	7.51%	8.54%	22.17%	20.24%	17.07%	-25.13%
Lu	16.85%	6.87%	34.17%	3.75%	6.55%	12.24%	10.62%	23.48%	27.79%	-1.88%
Hf	13.04%	12.71%	-1.29%	9.29%	10.87%	8.20%	12.99%	-6.70%	-6.25%	-31.92%
Ta	-13.11%	-12.29%	-22.93%	-16.38%	-13.27%	-6.41%	28.00%	29.47%	55.33%	77.06%
Th	-2.33%	-4.93%	-13.74%	-7.90%	-2.25%	5.83%	-16.52%	7.11%	24.74%	40.04%
U	-9.61%	-10.05%	-35.55%	-12.45%	-5.02%	-1.98%	-14.83%	31.48%	48.33%	100.85%

* - an asterisk denotes analytical results were below detection limits for a specific element. Listed per cent values are inferred.

Curriculum Vitae

Name: Greg Robinson

Post-secondary   The University of Western Ontario
Education and   London, Ontario, Canada
Degrees: 2013 M.Sc., Geology

                        The University of Western Ontario
                        London, Ontario, Canada
                        2005 B.Sc., Geology

                        Fanshawe College
                        London, Ontario, Canada
                        1996 Dip., Environmental Technology

Related Work   Senior Project Geologist
Experience   Rockcliff Resources Ltd.
                        2012 – 2013

                        Project Geologist
                        Rockcliff Resources Ltd.
                        2011 – 2012

                        Geologist
                        Fortune Minerals Ltd.
                        2011 (winter program)

                        Junior Geologist
                        Fortune Minerals
                        2010 (summer program)

                        Junior Geologist
                        Fortune Minerals
                        2006 (summer program)